A Study of the Design and Synthesis of Polymeric Smart Nanocarriers for Delivering Drugs

Shaifali Sartaliya

A thesis submitted for the partial fulfilment of
the degree of Doctor of Philosophy

Institute of Nano Science and Technology
Knowledge city, Sector-81, SAS Nagar, Manauli PO, Mohali 140306, Punjab, India

Indian Institute of Science Education and Research Mohali
Knowledge city, Sector 81, SAS Nagar, Manauli PO, Mohali 140306, Punjab, India.

March 2023

Dedication

Dedicated to my Parents and Teachers

Declaration

The work presented in this thesis has been carried out by me under the guidance of Dr. Jayamurugan Govindasamy at the Institute of Nano Science and Technology, Mohali. This work has not been submitted in part or in full for a degree, a diploma, or a fellowship to any other university or institute. Whenever contributions of others are involved, every effort is made to indicate this clearly, with due acknowledgment of collaborative research and discussions. This thesis is a bona fide record of original work done by me, and all sources listed within have been detailed in the bibliography.

Shaifali Sartaliya

In my capacity as the supervisor of the candidate's thesis work, I certify that the above statements by the candidate are true to the best of my knowledge.

Dr. Jayamurugan Govindasamy

Pursuing a Ph.D. was a memorable journey of my life. With a lot of experiences and learning, I gathered many memories here. There were always some people to help and guide, without whom I could not have endeavored this. I would like to start my thesis with my gratitude to them.

First and foremost, I would like to express my sincere gratitude to my supervisor **Dr. Jayamurugan Govindasamy** for his thoughtful ideas, support, encouragement, and his priceless suggestions/teaching during my entire Ph.D. tenure. He always stood behind me in every odd and even situation and always helped me in troubleshooting problems whenever I got stuck in my work. The freedom he provided me to execute my research projects in the best possible way is worth remembering. The discussions I had with him have helped me to gain a greater interest in undertaking research in the future. Besides his support for my research, he stood by me during tough times. As a supervisor, his qualities are beyond description, but I can say that this thesis would not have been completed without his guidance and persistent support.

I would like to express my sincere gratitude towards my research advisory committee (RAC), Prof. Asish Pal and Prof. Deepa Ghosh, for their valuable suggestions during the evaluation meetings. Their fruitful suggestions helped me be more focused and push my boundaries.

Especially, I wish to thank Prof. Deepa Ghosh and her group, particularly Vianni Chopra, Himadri Shekhar Roy, and Anjana Sharma, for helping me with antimicrobial studies and conducting biocompatibility tests.

I am thankful to Dr. V. Gowri and Dr. Ritu Mahajan for their informative suggestions during research discussions which helped me to carry out a detailed research analysis of results and made my research more effective. They always motivated me to keep going.

I am also thankful to Dr. Deepika Sharma and her student Amit for allowing and helping me to do hyperthermia studies, respectively.

I thank Dr. Harsimran Kaur and Dr. Deepika Gupta for helping me with HPLC/LC-MS instrument whenever needed.

I thank Dr. Jojo P. Joseph and Chirag Miglani for assisting me in molecular weight determination studies of my samples by size exclusion chromatography.

Many instrument facilities at and around INST were used in my research journey, and I interacted with many people regarding this, some of whom were very generous with their time and assistance. I want to thank Mr. Ashvindar Singh, Ms. Baljeet Kaur, Ms. Neha, Mr. Avtaar Sing (PU), Mr. Manish (PU), Mr. Raj Kumar Sharma (INST), Ritu, Mr. Jitesh (Waters), Avneet, Samraggi, Romi, Debashish, Tashmeen.

I am extremely grateful to my lab members Dr. Arif H. Dar, Dr. Abdul Selim, Ms. Neethu K. M., Raina Sharma (for PXRD studies of my samples), Arun Kumar Solanki (for helping me in NMR studies of my samples), Kritika Nag, Sarita Kumari, Ashish Sharma, and Mithilesh for their efforts to maintain the smooth lab functioning and a healthy work environment. I would mention a special thanks to Ms. Neethu K. M. for the formal and informal discussions during the ups and lows of my Ph. D journey.

I thank all the interns Sindhuja, Namika, Indraraj who joined the lab while my Ph.D. tenure.

I would like to acknowledge all the non-teaching staff including Ms. Gurveen, Ms. Reena, and Mr. Vikram.

I also want to thank my previous roommates, Arpana Jaryal, Gurpreet Kaur, and Sonali Kakkar, for their friendly gesture throughout my stay with them during my Ph.D. tenure. I would give a special thanks to Mrs. Sanchita Shah Jetly, with whom I shared a bond of a friend, roommate, and colleague.

I am also thankful to some people who helped me with my experiences in research at INST Dr. Praveen Kumar PP, Parvati Marandi, Dr. J. Babu, Dr. Neha, Dr. Rohit, Mujeeb, Dr. Jijo, Preeti, Dr. Pooja, Dr. Vijay, Dr. Sonika.

Apart from INST, I would acknowledge my teachers and friends in different institutes at Chandigarh and Mohali, Dr. Jayeeta Bhaumik, Nikhileshwar Reddy, Ritu Kalia, and Ajay, for helping me professionally and personally whenever needed.

This endeavor would not have been possible without my parents (Mrs. Suneeta Chandra Sartaliya and Mr. Rajendra Kumar Sartaliya). My higher education has been made possible by their unconditional love/trust/faith, which inspired me to reach this level.

I would like to acknowledge my maternal uncle (Mr. Dinesh Solanki), who has always inspired me. I am grateful to my brothers (Rishi and Himesh) and cousins (Rishabh,

Ravi, and Gargi) for their moral support. My friends, Tripta, Shivani, and Rajveer, also deserve special thanks.

I am thankful to Prof. Ashok K. Ganguli, Prof. Hirendra N. Ghosh, and Prof. Amitava Patra, founding, former officiating, and current director of INST Mohali, respectively.

I am thankful to INST-Mohali for providing my research fellowship and infrastructure facilities during my Ph.D. Lastly, I would like to thank everyone whose names I have left off here despite their unconditional support to make my journey successful. In a few words...It was a wonderful experience.

θ	Theta
°C	Degree Celsius
µg	Microgram
µL	Microlitre
µm	Micrometer
µM	Micromolar
Å	Angstrom
AFM	Atomic Force Microscopy
AMF	Alternat magnetic field
AP	Antimicrobial polymer
BP	Biocidal polymer
BRP	Biocidal releasing polymer
CC	Column chromatography
CD	Carbon dot
$CDCl_3$	Deuterated chloroform
CFU	Colony forming unit
CH_2Cl_2	methylenechloride
CH_3CN	Acetonitrile
$CHCl_3$	Chloroform
$CHONH_2$	Formamide
CLSM	Confocal laser scanning microscopy
cm	Centimeter
CMC	Critical micellar concentration
COSY	Correlation Spectroscopy
CPD	Carbonized polymeric dot
CQD	Carbon quantum dot
d	Doublet
Da	Daltons
DCFH-DA	Dichloro-dihydro-fluorescein diacetate
dd	Doublet of doublet
DDS	Drug delivery system

DLE	Drug loading efficiency
DLS	Dynamic light scattering
DMF	Dimethyl formamide
DMSO	Dimethyl sulfoxide
DMSO-d_6	Deuterated dimethyl sulfoxide
DNA	Deoxyribonucleic Acid
DOX	Doxorubicin
DSC	Differential scanning calorimetry
dt	Doublet of triplet
EDX	Energy dispersive X-ray
EE	Encapsulation efficiency
Et_3N	Triethylamine
EtOH	Ethanol
FA	Formic acid
FT-IR	Fourier Transform Infrared
h	Hour
HMPA	Hexamethyl phosphoramide
HPLC	High performance liquid chromatography
Hz	Hertz
IC	Initiation concentration
J	Coupling constant
K_2CO_3	Potassium carbonate
KBr	Potassium bromide
KOH	Potassium Hydroxide
LC-MS	Liquid Chromatography Mass Spectrometry
LiBr	Lithium bromide
m	Multiplet
m.p.	Melting point
MeOH	Methanol
MIC	Minimum inhibitory concentration
mL	Millilitre

mm	millimeter
mM	Millimolar
M_n	Number average molecular weight
MNP	Metal nanoparticles
MTCC	Microbial Type Culture Collection and Gene Bank
MTT	3-(4, 5-dimethylthiazolyl-2)-2, 5-diphenyltetrazolium bromide
M_w	Weight average molecular weight
MWCO	Molecular weight cutoff
Na_2SO_4	Sodium Sulphate
NC	Nanocarrier
nm	Nanometer
NMR	Nuclear Magnetic Resonance
NPs	Nanoparticles
OD	Optical density
PB	Polymeric biocide
PBS	Phosphate buffer saline
PDA	Photodiode-Array
PDI	Poly dispersity index
PL	Photoluminescence
PLA	Polylactic acid
PM	Pathogenic microorganisms
pM	Picomolar
PMMA	Polymethylmethacrylate
ppm	Parts per million
P-XRD	Powder X-ray Diffraction
RALS	Right angle light scattering
RGB	Red Green Blue
RI	Refractive index
ROESY	Rotating frame Overhauser Effect Spectroscopy
ROS	Reactive oxygen species

RT	Retention time
SEC	Size exclusion chromatography
SEM	Scanning Electron Microscopy
$SOCl_2$	Thionyl chloride
t	Triplet
TLC	Thin Layer Chromatography
TEM	Transmission Electron Microscopy
TGA	Thermogravimetric analysis
THF	Tetrahydrofuran
ZOI	Zone of inhibition
α	Alpha
δ	Delta
ε	Extinction coefficient
γ	Gamma
λ	Wavelength
π	Pi
σ	Sigma

Abstract

A Study of the Design and Synthesis of Polymeric Smart Nanocarriers for Delivering Drugs

Historically, synthetic polymers have been widely used for a wide range of applications due to their structural and mechanical properties. As a result of their inert nature, these polymers are commonly used in biomedical applications, such as coatings and pharmaceutical excipients (implants, dental materials, sutures, contact lenses, drug delivery, *etc*). Due to the need for highly biocompatible and active materials, polymers from bioactive monomers have been developed, especially antimicrobial and anticancer polymers. Additionally, the current COVID-19 pandemic has prompted a large number of scientists to develop new antimicrobial polymer materials in order to reduce the rise of infections. Due to the lack of new antimicrobial compounds discovered from natural products or novel antimicrobial classes, we have initiated a study to develop drug polymers based on existing antimicrobial compounds.

In a number of reports, antimicrobial drugs have been polymerized with spacers or other polymer backbones to form antimicrobial polymers. To understand the importance of spacers in drug polymers, however, the self-polymerization of such drug units has not been explored. In this thesis work, we envisaged that it is possible to self-polymerize 1-cyclopropyl-6-fluoro-4-oxo-7-piperazine-1-ylquinoline-3-carboxylic acid (ciprofloxacin), a second-generation drug in the class of fluoroquinolones, *via* a simple synthetic approach based on thermally activated self-condensation.

Further, to compare the polymers with and without spacer, we have polymerized the drug (ciprofloxacin) with spacers (**C_2P_2** (29 %) and **$C_{10}P_3$** (53 %)) and without spacers (**C_0P_1** 0%) by condensation reaction and compared the antibacterial activity of both types of polymers. The trend for minimum inhibitory concentration study against Escherichia coli (*E. coli*) and Staphylococcus aureus (*S. aureus*) was observed as **1** > **C_0P_1** > **C_2P_2** = **$C_{10}P_3$**>> **2**. Furthermore, after coating on nylon threads, the non-spacer polymer **C_0P_1** showed an enhanced zone of inhibition (ZOI) than monomer **1** as well as the spacer polymers with a trend **C_0P_1** > **1** > **C_2P_2** > **$C_{10}P_3$**> **2** owing to its superior coating ability and sustained drug release capabilities.

Due to the advantages of precisely controlling the size of nanomaterials and the value-adding transition from highly stable polymeric materials, converting polymeric macromolecules into carbonized polymer nanodots (CPD) has become popular. The process provides the formation of carbon nanomaterial by keeping the surface functionality intact, which maintains the activity of functional groups with the benefit of carbon nanodot properties (photoluminescence, ROS generation, catalysis, sensing).

The adjacent chapter of this thesis discusses the formation of CPD from the true biocidal polymer **C_0P_1**. In general, due to mixed sizes, doping, and surface effects, carbon dots (CDs) generally exhibit excitation-dependent mixed colour photoluminescence. Herein, a biocidal polymer and solvothermal synthesis have been combined to produce an excitation-independent near-white light-emitting polymeric **CPD-C_0P_1**. As opposed to the parent biocidal polymer, the presence of **CPD-C_0P_1** added strong generation of reactive oxygen species (ROS) in dark condition and cell wall degradation for bactericidal activity and 500-fold increased biocompatibility. In addition to this **CPD-C_0P_1** mediated PMMA NF mat was obtained which was further used as antibacterial-anti-adhesivity surface and potential bacterial cell imaging.

As an alternative to traditional drug polymers, smart nanocarriers for controlled, triggered, sustained, cyclic, and tunable release of therapeutic agents have been developed extensively in the last two decades. Stimuli-responsive 'smart' polymeric nanomaterials are of significant interest in drug delivery applications. Moreover, the externally triggered-controlled release of hydrophobic drugs has been a leading challenge in the field of drug delivery.

This thesis also contributes towards the state of art arrangement of polymers in the competitive environment by dynamic self-sorting behavior of the hydrophobic chains of amphiphilic block-copolymer **PEG-PLLA** and hydrophobic polymer poly (*L*-lactide) coated iron oxide nanoparticle **IONP@PLLA**. A core-shell structure in which the hydrophobic **PLLA** part acts as a dense core and **PEG** as an uncrowded shell in **mPEG-PLLA** has been realized by utilizing system chemistry and nanotechnology principles.

The work is a proof-of-concept study, which shows the future possibilities of designing more efficient and improved drug delivery nanocarriers either by changing the

polymeric shell structure (chain length, di/tri/multiblock copolymer) or by replacing the nanoparticles in the core. Overall, this thesis contributes towards the development of highly biocompatible polymers and polymeric nanocomposites with enhanced physical properties, biocidal activity, and controlled drug delivery. We believe that studies in the future may explore the synthesis of cyclic polymers and oligomers of antibacterial molecules and their potential activity against antimicrobial-resistant bacteria.

SYNOPSIS

A Study of the Design and Synthesis of Polymeric Smart Nanocarriers for Delivering Drugs

Shaifali Sartaliya (PH16232)

Chapter 1: Introduction to drug polymers and polymeric smart nanocarrier for drug delivery

The structural and mechanical properties of synthetic polymers have always made them versatile materials suited to a wide range of applications. The inert nature of these polymers has historically facilitated their use in biomedical applications irreversibly, such as coatings and the manufacture of healthcare products (implants, dental materials, sutures, contact lenses, drug delivery, pharmaceutical excipients, *etc*). Presently there is an overwhelming use of polymers in applications where they are expected to be biologically inert and to solely avail/ enhance the delivery of drugs, genes, other small molecules (vitamins, hormones, etc.), and essential macromolecules (polysaccharides, proteins, nucleic acids, enzymes, etc.). Indeed, they contribute to improving drug delivery, such as controlled and tuned drug delivery, reduced drug toxicity, and site-specific drug delivery. The demand for highly biocompatible and bio-active materials has led to the development of polymers from bioactive monomers, especially antimicrobials and anticancer polymers. The lack of discoveries of novel compounds from natural products or novel antimicrobial classes led us to develop drug polymers based on existing antimicrobial compounds. Unlike biologically inactive polymers, which are used heavily for drug delivery, device manufacturing, and coatings, biologically active polymers can also be used for biomedical applications.

In chapter 1, we reviewed the synthetic polymers acting directly or indirectly as bioactive material and classified them according to the arrangement of the bioactive unit within the polymer chain and the mechanism of activity. We have also introduced and defined the term drug polymers briefly and discussed the current scenario in detail. As a new type of polymer, true drug polymers are introduced for biomedical applications that have never been discussed before.

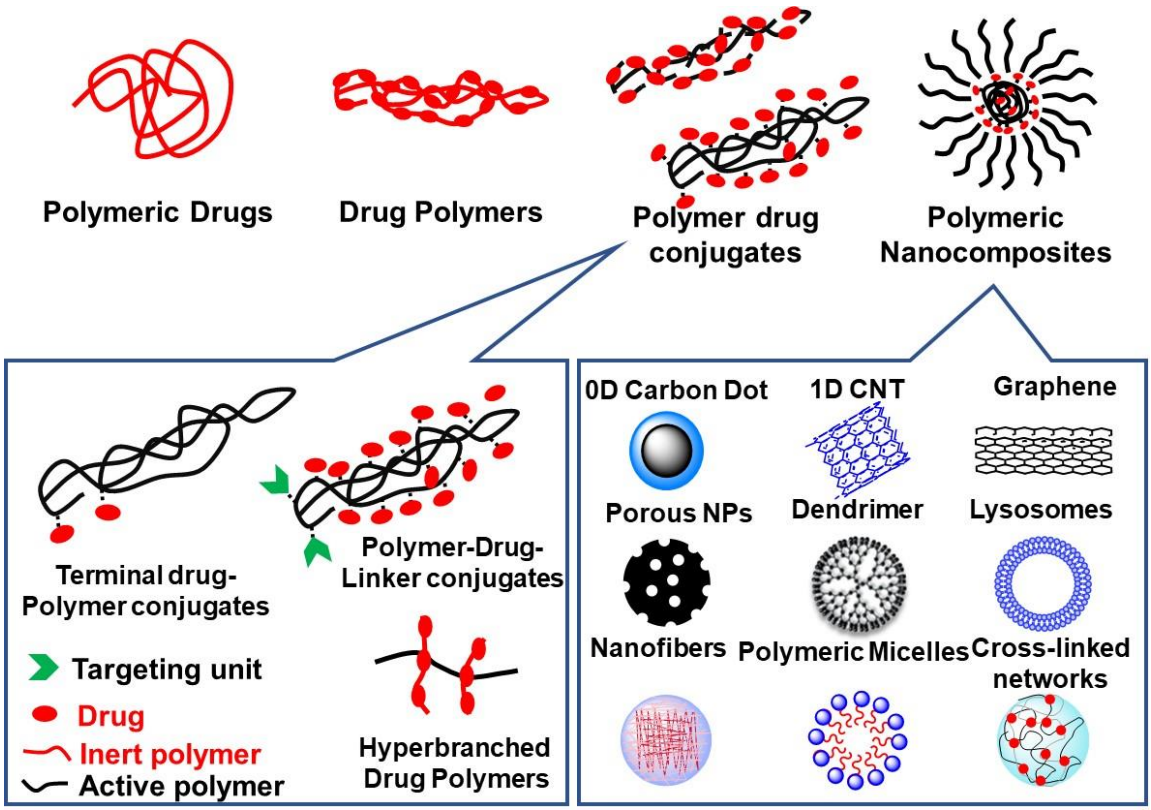

Figure 1. Classification of polymers acting as biologically active units.

****

Chapter 2: Unraveling the Effect of Nondrug Spacers on a True Drug-Polymer and a Comparative Study of Their Antimicrobial Activity.

There have been many reports on the polymerization of antimicrobial drugs with the help of spacers or other polymer backbones to form antimicrobial polymers. However, the self-polymerization of such drug units has not been explored to understand the importance of spacer in drug polymers. In this chapter, we envisaged that it is possible to self-polymerize 1-cyclopropyl-6-fluoro-4-oxo-7-piperazine-1-ylquinoline-3-carboxylic acid (ciprofloxacin), a second-generation drug in the class of fluoroquinolones, *via* a simple synthetic approach based on thermally activated self-condensation. Further, we have tried to polymerize the drug (ciprofloxacin) with spacers (**C_2P_2** and **$C_{10}P_3$**) and without spacers (**C_0P_1**) by condensation reaction and compared the activity of both types of polymers. The trend for minimum inhibitory concentration study against Escherichia coli (*E. coli*) and Staphylococcus aureus (*S. aureus*) was observed as **1** > **C_0P_1** > **C_2P_2** = **$C_{10}P_3$**>> **2**. Furthermore, after coating on nylon threads, the non-spacer polymer **C_0P_1** showed an

enhanced zone of inhibition (ZOI) than monomer **1** as well as the spacer polymers owing to its superior coating ability and sustained drug release capabilities.

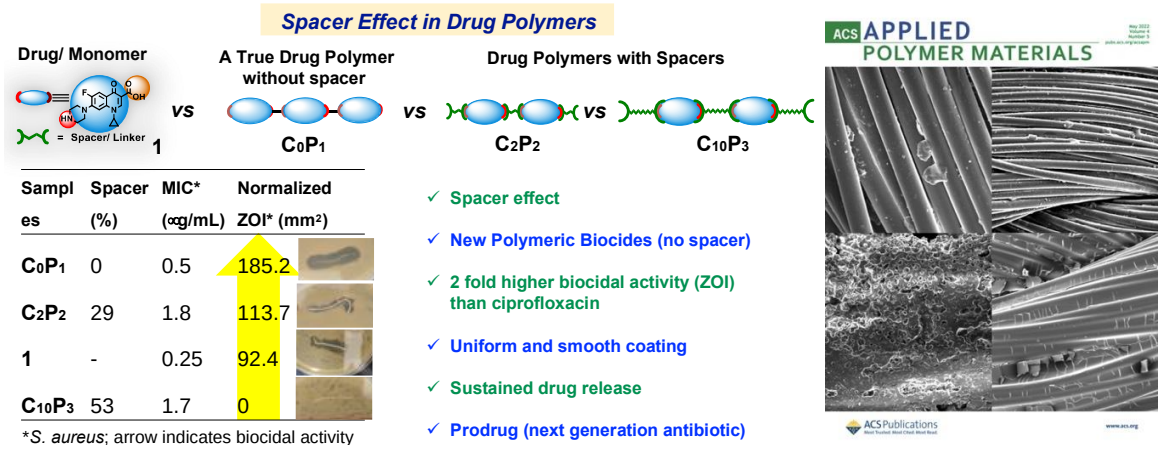

Figure 2. A schematic representation of spacer effect in drug-polymer and further advantages of drug-polymer for coating application.

****

Chapter 3: Biocidal polymer derived near white light-emitting carbonized polymeric dots for antibacterial and bioimaging applications.

As a result of the advantage of being able to precisely synthesize nanomaterials of the right size and the value-adding transition of the existing stable polymeric materials, the process of converting polymeric macromolecules into carbonized polymer nanodots (CPDs) has become more popular in achieving highly biocompatible materials with unique mechanisms of action. This process provides the formation of carbon nanomaterial by keeping the surface functionality intact, which allows the CPDs to retain the activity of functional groups with the advantage of carbon nanodot properties (photoluminescence, ROS generation, catalytic, sensing, *etc*). Chapter 3 of this thesis discusses the formation of CPD from the true biocidal polymer **C_0P_1**. In general, due to mixed sizes, doping, and surface effects, carbon dots (CDs) generally exhibit excitation-dependent mixed colour photoluminescence. Herein, a biocidal polymer and solvothermal synthesis have been combined to produce an excitation-independent near-white light-emitting polymeric CD. As opposed to the parent biocidal polymer, the presence of CD added ROS-mediated bactericidal activity, 500-fold increased cytocompatibility and nanofibers with anti-adhesivity and potential of imaging bacterial cells.

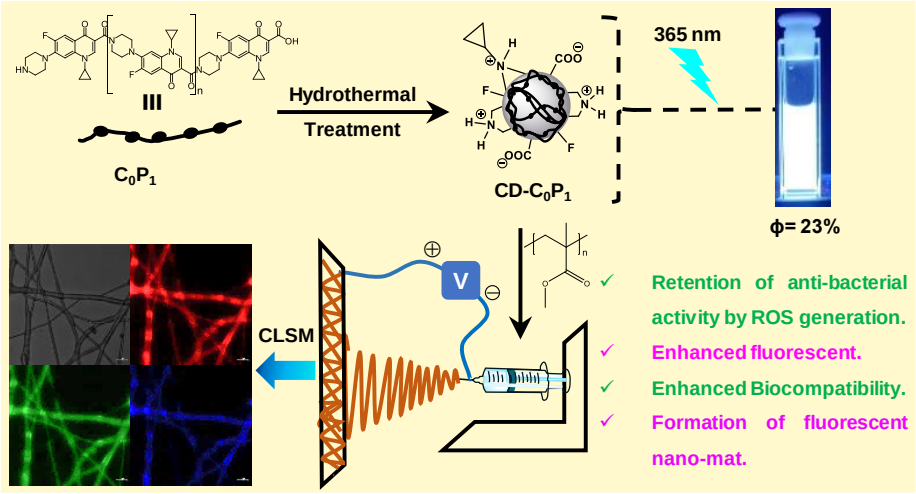

Figure 3. Schematic representation of carbon dot synthesis and transformation to nanofibers.

****

Chapter 4: A new water-soluble magnetic field-induced drug delivery system obtained *via* preferential molecular marriage over narcissistic self-sorting.

Chapter 4 of this thesis describes a unique arrangement of polymers in a competitive environment derived from the dynamic self-sorting behavior of the hydrophobic chains of amphiphilic **mPEG-PLLA** and poly-L-lactic acid (**PLLA**) coated iron oxide nanoparticle **IONP@PLLA** to achieve a core-shell structure in which the hydrophobic **PLLA** part acts as dense core and **PEG** as an uncrowded shell. By using irreversible covalent interactions created by hydrophobic polymer-functionalized on **IONP**, it was possible to selectively form socially self-sorted nanocarriers (**SS-NC**) with a higher hydrophobic core than the hydrophilic shell over narcissistic self-sorted nanocarriers (**NS-NC**), *i.e.*, homo micelles of amphiphilic polymers. The denser hydrophobic core of **SS-NC** is indeed helpful in achieving higher drug (doxorubicin) loading (DLE%)- and encapsulation-efficiencies (EE%) of around 17 and 90%, respectively, over 10.3 and 65.6% for **NS-NC**. Furthermore, due to the presence of **IONP** and the densely packed hydrophobic compartments, the controlled release of doxorubicin (DOX) was facilitated by direct magnetism and temperature stimulation when an alternating magnetic field (AMF) was applied. An appreciably higher rate of drug release ~50% than without AMF (~18%) was achieved at ambient conditions in 24 h. The present study, therefore, proposes a new drug delivery system that exceeds homo micelles and adds the extra feature of manipulating drug release through magnetism and temperature, *i.e.*, hyperthermia.

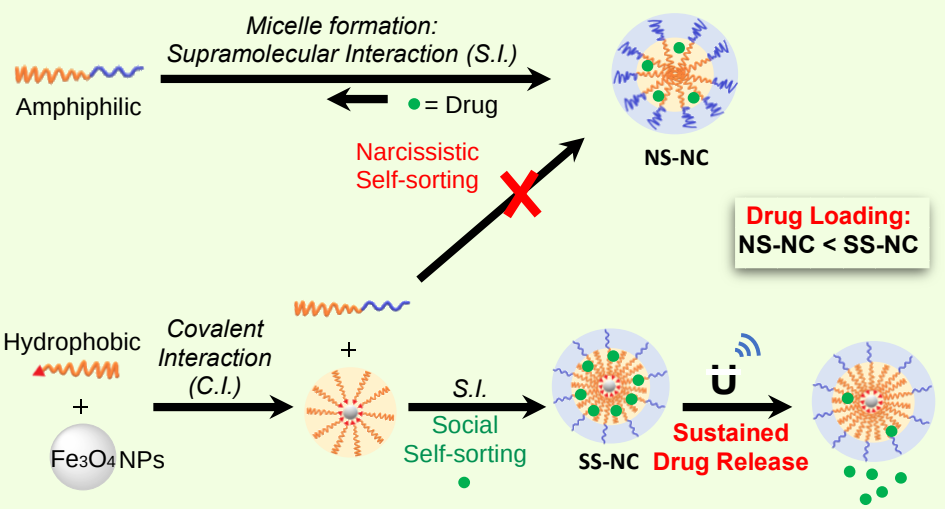

Figure 4. Schematic depiction for the formation of new water-soluble socially self-sorted nanocarrier (**SS-NC**) over narcissistically self-sorted nanocarrier (**NS-NC**).

****

Chapter 5: Summary and conclusion of the overall thesis work.

A brief discussion of drug polymers and their types is presented in Chapter 1.

In chapter 2, we show that a drug polymer can retain and enhance its bioefficacy in the absence of non-bioactive spacer units. As evidenced by the higher melting point (409 °C), better biocompatibility, and excellent coating ability on nylon thread, we expect that **C_0P_1** is a promising candidate for advanced biomaterial and medical applications such as the coating of sutures and other surgical devices. As we have checked only one application for the true drug-polymer (**C_0P_1**), that is, coating on surgical nylon sutures, there is no doubt that the true drug-polymer and possible cyclic oligomers of antimicrobials can open a wide range of new applications, including activity against drug-resistant bacteria.

When biocidal polymers are further converted to nanomaterial, they may offer the dual advantage of possessing a polymeric property with a "nano effect" such as the retention of biocidal activity with excellent bioimaging properties, as shown in chapter 3 by carbonizing the polymer **C_0P_1** into carbonized polymer dots. Even though the field of carbon nanomaterial is emerging to produce promising bioactive materials, we believe that this work can provide a considerable impact on the generation of better and biocompatible antimicrobial materials.

Lastly, a proof-of-concept study of the formation of socially self-sorted nanocarriers over narcissistically self-sorted nanocarriers was presented in chapter 4 of this thesis, showing

that it is possible to create more efficient and improved drug delivery nanocarriers by altering the polymeric shell structure (chain length, di/tri/multiblock copolymer) or by replacing the nanoparticles in the core in the future.

Overall, this thesis contributes towards the development of highly biocompatible polymers and polymeric nanocomposites with enhanced physical properties, biocidal activity, and sustained stimuli (temperature, pH and magnetism) induced drug release capabilities.

Chapter 1: *Introduction: Drug Polymers*

1.0. Bioactive Synthetic Polymers

Synthetic polymers have emerged by far as the broadest and most versatile class of biomaterials for therapeutic applications attributed to their structural and mechanical properties. Polymers with a wide range of architecture can be designed and synthesized with suitable physicochemical properties, which can be utilized further for diverse biomedical applications such as coating and manufacturing of healthcare materials (dental material, sutures, contact lenses, etc.), implants, tissue engineering, drug delivery, therapeutics, diagnostics, sensing and so on. Over the last two decades, the methods of polymerization (synthesis, processing, and characterization) have been developed expeditiously for the production of innumerable novel polymeric materials for biomedical applications. This creates both the opportunities and challenges to develop novel bioactive polymeric materials as well as to understand their interaction within biological system.[1,2]

Presently there is an overwhelming use of polymers in applications where they are expected to be biologically inert and to solely avail/enhance the delivery of drugs, genes, other small molecules (vitamins, hormones, etc.), and essential macromolecules (polysaccharides, proteins, nucleic acids, enzymes, etc.). They contribute to improving the characteristics of drug delivery, such as controlled and tuned drug delivery, reduced drug toxicity, and site-specific drug delivery.[3,4.] Contrary to biologically inactive polymers used highly for drug formulations, polymers acting as biologically active units can also be employed for the advancement in biomedical applications (device manufacturing and coating applications).[5,6] Here, we have classified the synthetic polymers involved directly or indirectly as bioactive materials either by acting as the biologically active entity (polymeric drugs) or by enhancing the activity of the conjugated bioactive unit (drug polymers, polymer drug conjugates and polymeric nanocomposites), (Figure 1.0, Table 1.0).

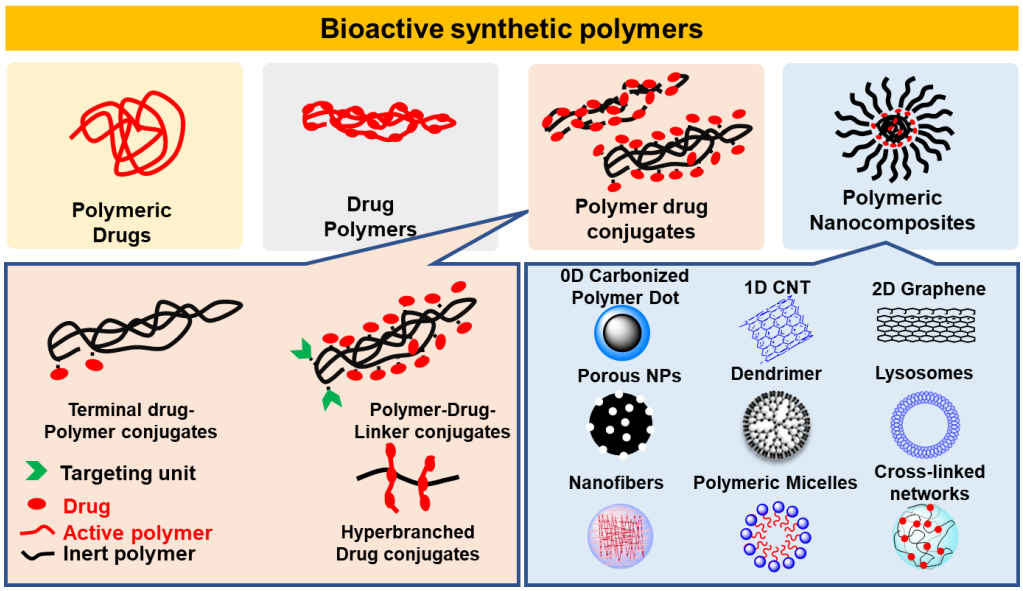

Figure 1.0. Classification of polymers acting as biologically active units. Adapted from[6-8]

Table 1.0. Classification of polymers of therapeutic significance.

Polymers	Drug Polymer	Polymeric Drug	Polymer drug conjugates	Polymeric Nanocomposite
Definition	Synthetic polymers having drugs as a repeating unit in the polymer structure.	Natural or synthetic polymeric materials with biological activity which can further be exploited for therapeutic interest.	Therapeutically active macromolecules consisting of one or more therapeutically active agents comprising drugs, peptides, and proteins covalently interlinked to an inert polymeric moiety	Macromolecular nanocarriers/ polymer transformed nanomaterials used for drug delivery or as a therapeutic agent.
Inert spacer	May or may not present	Absent	Present	May or may not present
Mechanism of action	By release of bioactive monomer unit/ polymer itself show activity.	Whole polymer shows activity (charge/ hydrophobicity, etc.)	Primarily by release of bioactive unite.	Primarily by release of bioactive unit or the nanocomposite/ nanodots act as bioactive agent by its intrinsic mechanism.

Example	**PDOX**[9], **C_0P_1**[10]	Pluronic, PPO[6]	Dextran–methylprednisolone conjugates[48]	PAMAM Dendrimer[52], **CPD-C_0P_1**

1.0.1. Drug Polymers

In recent years, the designing of drug polymers has gained attention and emerged as a promising field in the area of drug delivery.[6,7] Drug polymers are the polymers having drugs as a repeating unit in the polymer structure, which acts similarly to the monomers (drug). Among the various classes of synthetic bioactive polymers listed in Figure 1.0, the drug polymers are a relatively new type of polymers acting as biologically active either as prodrugs (which initially be inert and start acting with time and surrounding conditions (pH, temperature, enzyme and so on)) or the whole polymer acts as a drug even after polymerization, for example, **PDOX** (Figure 1.1a). One such example of drug polymers includes recently reported by our group, i.e., antimicrobial polymer **C_0P_1** of ciprofloxacin, in which ciprofloxacin acts as the repeating unit in the polymeric structure without any non-drug linker/spacer unit (Figure 1.1b).[9] Similarly, Peng Liu and coworkers have reported the acid-triggered degradable polyprodrug type of drug-polymer by conjugating doxorubicin as a repeating unit and *N*-(*tert*-butoxy carbonyl) acryloyl hydrazine as a linker unit.[10]

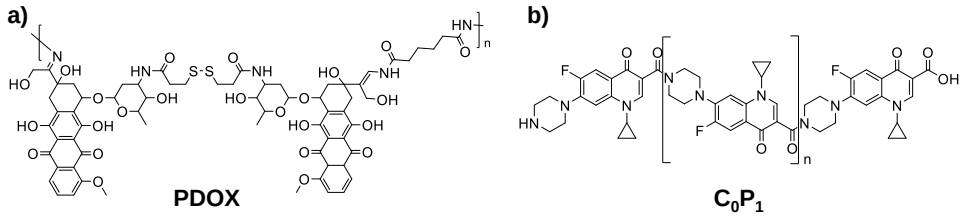

Figure 1.1. Typical structures of drug polymers.

After an adequate literature survey, we have defined the drug polymers with a clearer perspective which may contribute further to the synthesis and investigation of new types of drug polymers.

"Drug polymers are the polymeric materials having bioactive monomer as a repeating unit in its structure bonded via complementary functional groups (of monomer) to obtain the polymeric structure." Small linker or spacer units may or may not contribute to the synthesis of drug polymers. However, releasing a bioactive monomer from the polymer should be the primary objective for any drug polymer. Nevertheless, the

polymeric chain may show bioactivity intrinsically due to certain factors, such as charge, hydrophobicity, etc, on the surface.

As the field of synthesizing new drug polymers using existing drug molecules is in the pioneer stage, a significant amount of drug polymers are yet to be reported. Despite their niche status right now, drug polymers can bring enormous possibilities in the area of new drug discovery and drug delivery not voluntarily accessible with existing small molecule drugs and biologically inert polymer-drug conjugates.

1.0.2. Antimicrobial Polymers

In the wake of the current COVID-19 pandemic, modern science faces a significant challenge in preventing pathogenic microorganisms (PMs) from causing disease.[11-13] Generally, healthcare-associated infections and unhygienic environments are the main causes of infections caused by PM. There has been an increasing gap between the existing antimicrobials and resistant microbial strains since the onset of the antimicrobial crisis, which has negatively impacted microbial infection treatment and management.[14,15] Within the drug polymers, antimicrobial polymers have been highlighted recently as an alternate approach to combat microbial infections in the prevention and treatment using antimicrobial polymers (APs).[16]

APs are generally a class of polymers that are capable of killing/inhibiting the microorganisms on the surface or surrounding environment. In some cases, APs have become so important as an alternative for treating infections that they have started replacing classical antibiotic treatment.[17] The mechanism of action of the various structurally different types of polymers is not fully realized till the current situation. The antimicrobial properties of benzalkonium chloride have been unfolded by Domagk and group in 1935, which made polymers with quaternary ammonium or phosphonium salts as widely used materials for antimicrobial properties.[18] It was Cornell and Dunraruma who reported the first synthesis of AP in 1965, in which they mentioned polymers and copolymers derived from 2-methacryloxytroponones that act as antimicrobials.[19] Many groups in the following years tried to synthesize polymers with antimicrobial properties, including Vogl & Tirrel in 1979 who polymerized salicylic acid.[20] In a review, Timofeeva et al. discuss the effects of various variables on the antimicrobial activity of antimicrobial polymers, including molecular weight, mechanism of action, and charge distribution.[21]

A significant boom has been observed in the total number of FDA-approved disinfectant polymers in the last two decades, which shows the demand for new antimicrobial polymeric materials for the diagnosis, prevention, and treatment of infections.[22,23] Researchers have discovered that AMPs can generally be divided into three categories: (a) biocidal polymer (BP): polymers holding the biocide as a terminal projecting part. (b) polymeric biocide: the biocide unit linked to a polymeric backbone, (PB), and (c) biocidal releasing polymer (BRP): physical encapsulation of the biocide by nanocomposite/polymer cluster (Figure 1.2).

The first class of APs (biocidal polymer) is based on the idea of biocidal groups anchored to a polymeric backbone which acts by acting on drug targets with a similar mechanism of action comparable to low molecular weight biocidal molecules, however, the action becomes slow and steady for targeted and sustained drug release. Also, sometimes due to the sterically hindered polymer backbone or modification in the functional groups due to polymerization, polymeric biocides tend to behave less active than the actual activity of inserted low molecular weight compounds.

On the contrary, in the PB, the active biocidal unit acts as a repeating unit and is covalently embedded in between the whole macromolecule either by using the polymeric moiety as a spacer/ linker group or by using the polymeric unit to attach the biocidal molecules as pendent groups. BRP does not actively involve the polymeric part for the drug action directly, instead, they function as a carrier for biocides delivery in a manner to act on the target site, improving drug solubility, stability, and optimizing *in vivo* drug action time. These polymers are reported to be the most suitable systems presently because of their ability to release the biocides encapsulated close to the cells at a burst release rate. Interestingly, all antimicrobial polymers have at least some non-drug spacer units present alongside the biocidal units in every class reported so far.[24-25]

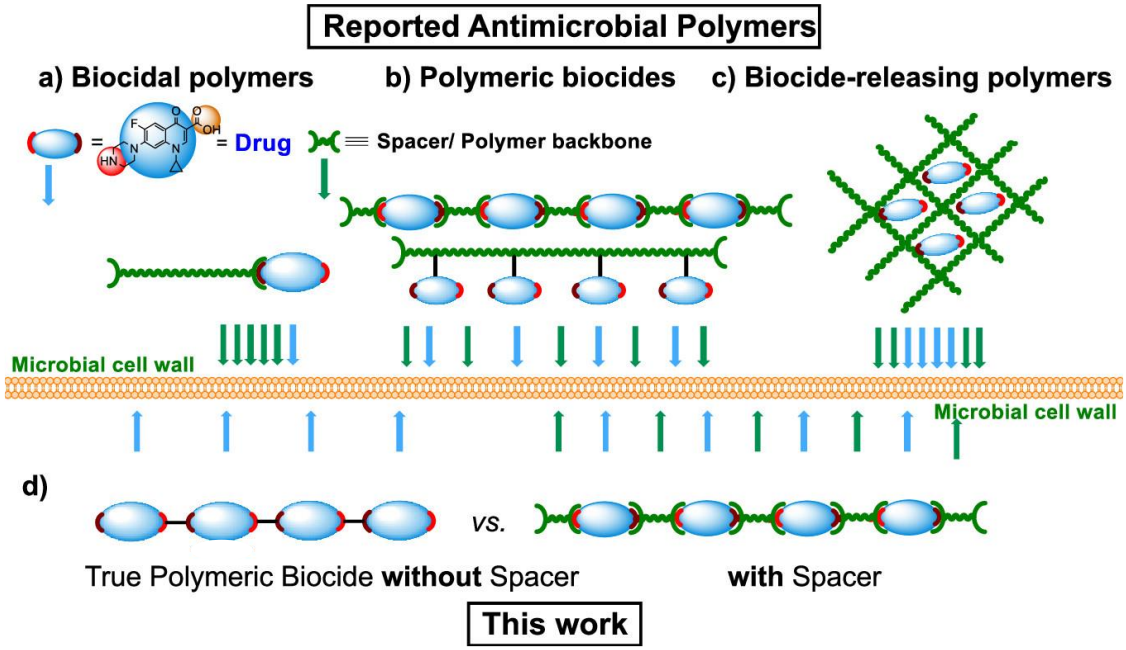

Figure 1.2. This is a schematic representation of previous known AMPs and a new type of true PBs without the spacer. A blue arrow indicates the release of biocide- and a green arrow indicates the release of spacer units, respectively.

PBs have been obtained by polymerizing medicinally essential molecules such as drugs and antimicrobial agents to prevent infections by coating medical devices and hospital surfaces.[27,28] Academic and industrial research have increasingly focused on PB in recent years. Most of the time, they are more effective than monomers because they have enhanced antimicrobial activity, reduced toxicity, minimized environmental hazards, sustained-release activity, and the ability to address antimicrobial resistance.[29-32]

The superiority of this approach is in the fact that the release of an active moiety can be achieved by the fragmentation in chemical linkages (e.g., amide, ester, imine, urethanes)) which links the drug within the macromolecule..[33] Several bioactive compounds such as β-lactams (e.g., penicillin, cephradine), aminoglycosides (e.g., gentamicin), fluoroquinolones (e.g., norfloxacin, ciprofloxacin, levofloxacin), and sulfonamides (e.g., sulphanilamide and sulfamethoxazole) have been reported to be covalently linked to different kinds of polymer backbones.[33] Another approach involves preparing a monomer by modifying a bioactive compound (such as norfloxacin, **1**) and polymerizing it to produce an antibacterial polymer (Figure 1.3).[34] Fluoroquinolone are one such family of broad-spectrum antibiotics which has been widely exploited for synthesizing PB due to their broad-spectrum activity and relatively low cost.[35] In this framework, Das et al. prepared monomers by linking methacrylate to ciprofloxacin **2**

with two distinct linkages, such as phenolic or ester (Figure 1.3).[36] As a result, hydrophilic copolymers or diblock copolymers were produced by copolymerizing the monomers with poly(ethylene glycol) methacrylate (O950) and the chain has been extended from poly(O950) macro chain transfer agent (CTA). Diblock copolymers formed micelles at physiological pH, which disassembled when the pH dropped below six. There was a difference in the release of ciprofloxacin depending on the nature of linkage within the polymer or prodrug, with 50% of the dose being released after 120 hours compared with 50% after 22 days.

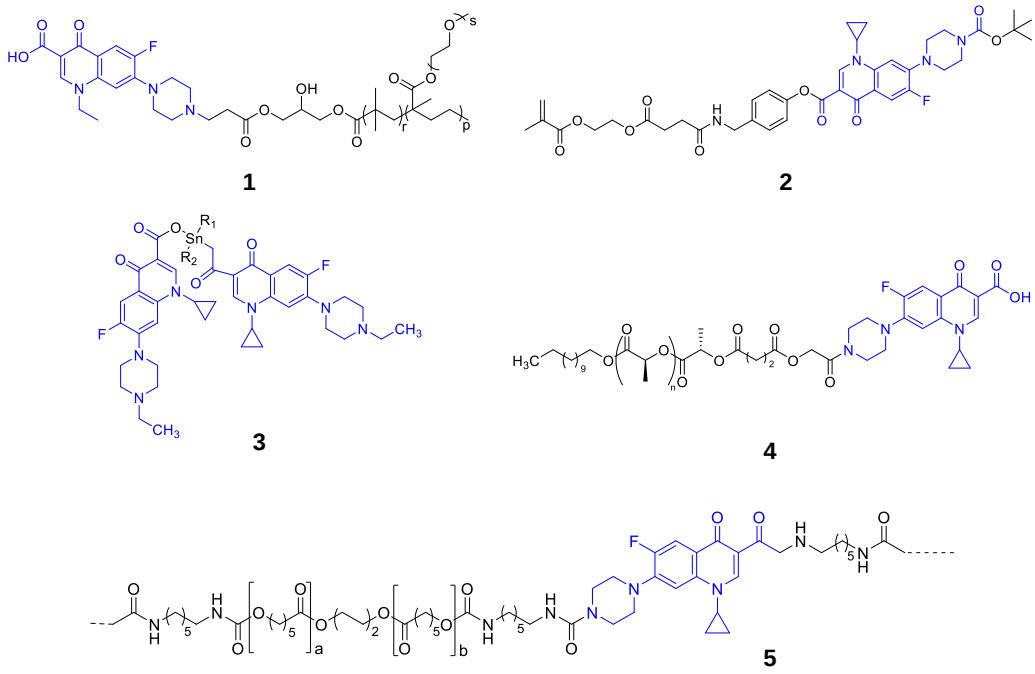

Figure 1.3. Selected examples of reported fluoroquinolone polymers.

A similar approach was used by Parwe et al., who synthesized **4** of a conjugated polylactic acid (PLA)-based nonwoven nanofiber mat with increasing ciprofloxacin content using telechelic PLA polymer as a starting material with two-, three-, four-, six-armed, or star-shaped arms, for example (Figure 1.3). According to their findings, the levels of ciprofloxacin released from the PLA-conjugate nonwoven nanofiber mat could be controlled by both the release medium and the level of drug loading. This indicates that the level of drug content is crucial to achieving better antibacterial outcomes.[37] Similarly, a study published by Woo et al. in 2007 found that 1,6-diisocyanatohexane (DCH) and polycaprolactone diol (PCL) could serve as a spacer in a biodegradable polymer of ciprofloxacin **5**, providing another method of synthesis (Figure 1.3). However, the degradation products, namely, ciprofloxacin and ciprofloxacin bonded to

fragments of PCL and DCH, were found to exhibit both active and inactive forms, respectively, of ciprofloxacin.[38] The results of the study indicate that releasing the actual drug unit upon degradation without conjugating the non-drug counterpart may be a more effective way to release the actual drug unit. It has been demonstrated by Boyer, Wong, and coworkers that the sequence effect may well be important in adjusting the antimicrobial activity of synthetic AMPs.[39] Nevertheless, all these examples clearly illustrate that the non-drug content of a drug can significantly influence the activity of the drug. As a result, as far as we know, far less attention has been paid to developing drugs that can self-polymerize/homopolymerize, at least in the case of those molecule structures that are composed of the AB monomer, as shown in Figure 1.2d.

Therefore, the purpose of this study was to find answers to several questions that we were looking for, such as (i) if the use of non-drug spacers to polymerize the biocide monomers would result in greater or lesser efficacy than drug-polymers, that is, without spacers, (ii) can the antimicrobial drug we are currently using be self-polymerized, and (iii) since the new PB, which is structurally different from its monomer, can it be considered a prodrug and if so, if it will lead to the discovery of new drugs. According to the literature review, we predicted that ciprofloxacin, a drug molecule with an amine secondary and a carboxylic acid end functional group as its end functional group, could be self-sufficient to polymerize without the aid of linkers or spacers.[40,41] There is also an indication that there has not been any report of a covalently linked homopolymer of ciprofloxacin or an oligomer without any linkers yet in the literature. It is presented in Chapter 2 of this thesis that the first ciprofloxacin polymer without a spacer unit has been synthesized *via* self-condensation polymerization of $\mathbf{C_0P_1}$. In this study, we have synthesized two other polymers, $\mathbf{C_2P_2}$ and $\mathbf{C_{10}P_3}$, which have an increased spacer content, with the help of N-formylated 1 (2) and bis-amines (Figure 1.4). Further, we have compared the results of the antibacterial study performed, both in solution and on the surface of the suture coating, of the three polymers against Escherichia coli (*E. coli*) and Staphylococcus aureus (*S. aureus*).

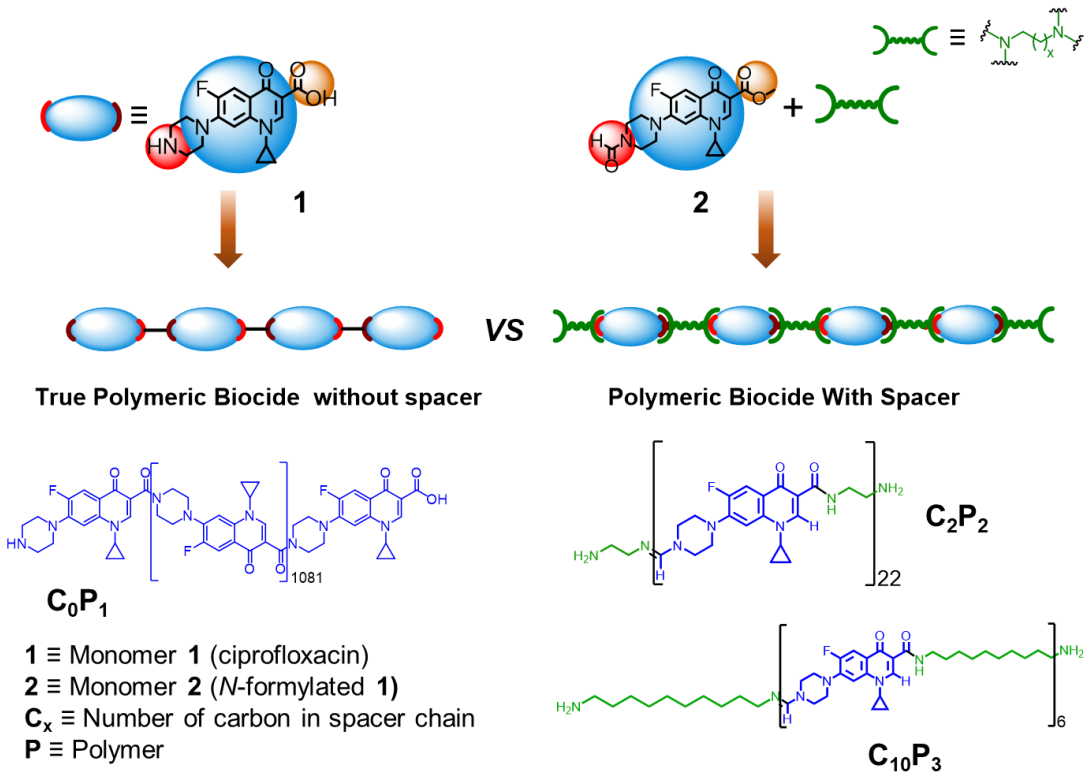

Figure 1.4. Schematic illustration and structural nomenclature of monomers (**1,2**) and polymers (**C_0P_1**, **C_2P_2** and **$C_{10}P_3$**).

1.0.3. Polymeric drugs

Polymeric drugs are natural or synthetic polymeric materials that manifest biological activity which can further be exploited for therapeutic interest.[42] The realization of the biological activity of such polymers has been the result of both pragmatic discoveries as in the case of antimicrobial polymers and sequestrants (Figure 1.5) or the coincidental discoveries, for instance, several pharmaceutical excipients and materials earlier assumed to be biologically inactive examples include Pluronic (amphiphilic block copolymer of poly(ethylene oxide) (PEO) and poly(propylene oxide) (PPO) and *N*-(2-hydroxypropyl) methacrylamide (HPMA) copolymers.[6,43] Many of the biological receptors are complex multivalent macromolecules in nature, which means that they interact with complementary signaling pathways by a complex series of polyvalent associations. Due to their macromolecular size and nature of repeating units, polymers, unlike traditional small bioactive molecules, facilitate easy interaction between multivalent receptors and macromolecular ligands, which is merely possible with a small molecule. Another major advantage of polymeric drugs is that most of these polymers

consist of concentrated charged ions within their structure, which provide them with the predominant mechanism of action and a force to bind with the target.[44]

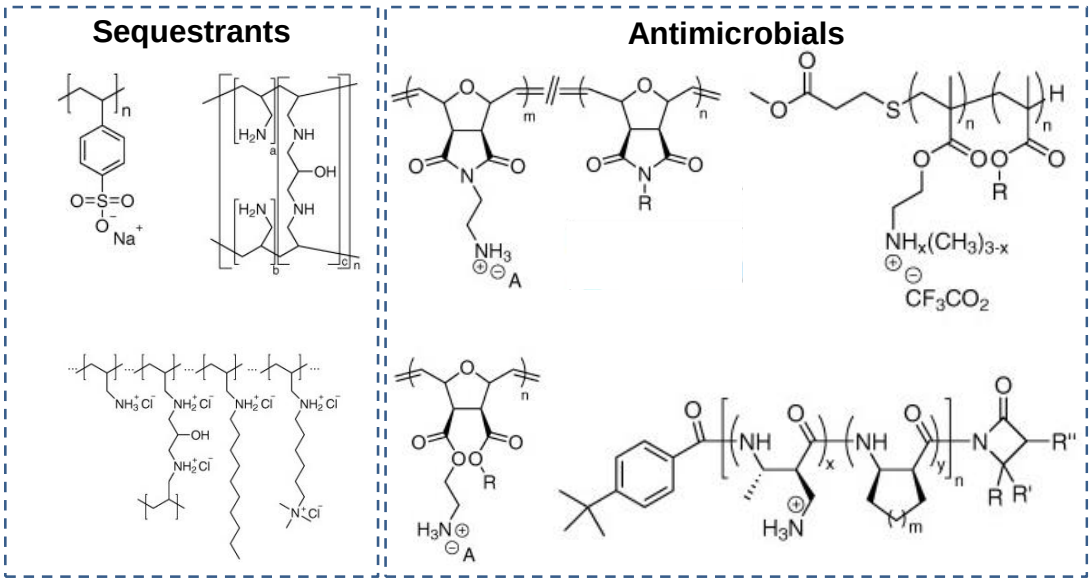

Figure 1.5. Representation of examples in polymeric drugs. Adapted from [6,43]

1.0.4. Polymer drug conjugates

Polymer–drug conjugates or drug-polymer conjugates are therapeutically active macromolecular structures consisting of one or more therapeutically active agents comprising drugs, peptides, and proteins covalently interlinked to an inert polymeric moiety. The conjugates of medicinally active small molecules and polymers extend innumerable benefits, such as improved drug solubility, controlled/triggered/rhythmic drug delivery, escalated drug efficacy and improved pharmacokinetics.[45] As first reported by Jatzkewitz in 1955, a psychedelic alkaloid, mescaline, was hypothesized to provide a controlled release of the bioactive since it was composed of a copolymer of N-vinylpyrrolidone and acrylic acid which was a combination of the alkaloid and acrylic acid. [46] A number of polymer-drug conjugates have been reported including Dox–polymer conjugates with a pH-sensitive trityl spacer[47] and Dextran–methylprednisolone conjugates prepared by coupling 1,1′-carbonyldiimidazole to succinic acid as a coupling agent together with succinic acid as a spacer,[48] (Figure 1.6). Similarly, Lee *et al.* have reported the stable conjugates of rPEG-lysozyme for the rapid release of lysozyme. [49]

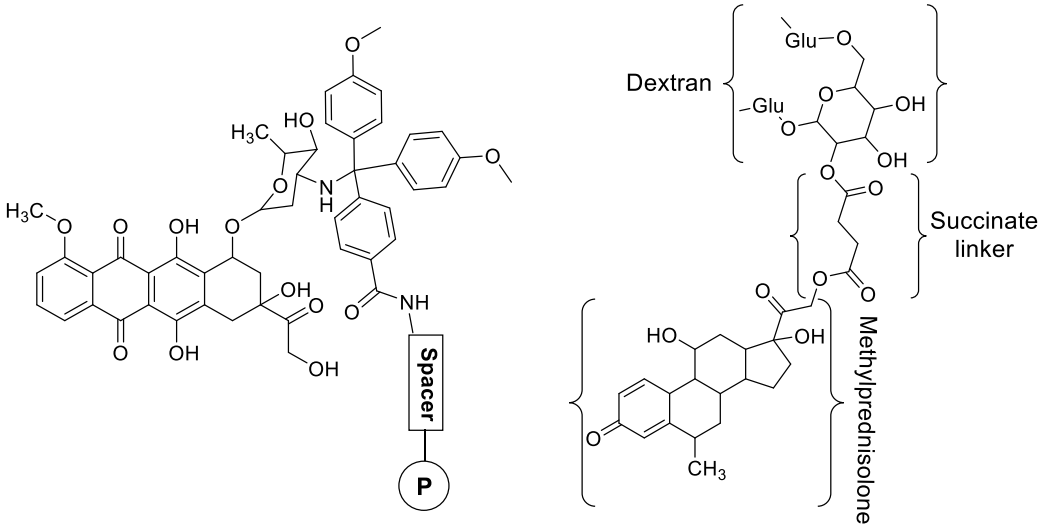

Figure 1.6. Structural representation of polymer-drug conjugate.

1.0.5. Polymeric nanocomposites

Nanomaterials have extensively been used for biomedicine and pharmaceutical purposes because of their specific mechanical, optical, magnetic, and electrical behaviors. The application of polymer-based designing of nanomaterial facilitates applications such as smart drug delivery, diagnostic bio-imaging, biosensing, and in chemotherapy.[50] The factionalized nanoparticles have been widely utilized owing to their easy-to-design and highly biocompatible nature. A diverse range of materials have been used to form nanoparticles, such as metal nanoparticles, polymeric nanocomposites, dendrimers, carbon nanomaterials (carbon dots/CD, carbon quantum dot/CQD, nanotubes, etc.), liposomes, and other supramolecular structures which falls in the range of nanoscale (1-100 nm).[51-54]

Meanwhile, the role of polymers in the design and application of nanomaterials is obvious and invincible at the same time. Designing polymeric nanocomposites transforms the dimension to nanoscale from the polymeric macromolecular structure of polymers to provide the "nano-effect". This transformation boosts the polymeric nanocomposite's ability to be utilized in biomedical applications. Polymeric nanocomposites can encapsulate hundreds of drug molecules inside a single vehicle and can be used for smart drug delivery applications due to their inert and biocompatible nature and state-of-art physical, chemical, and mechanical properties.[55-57]

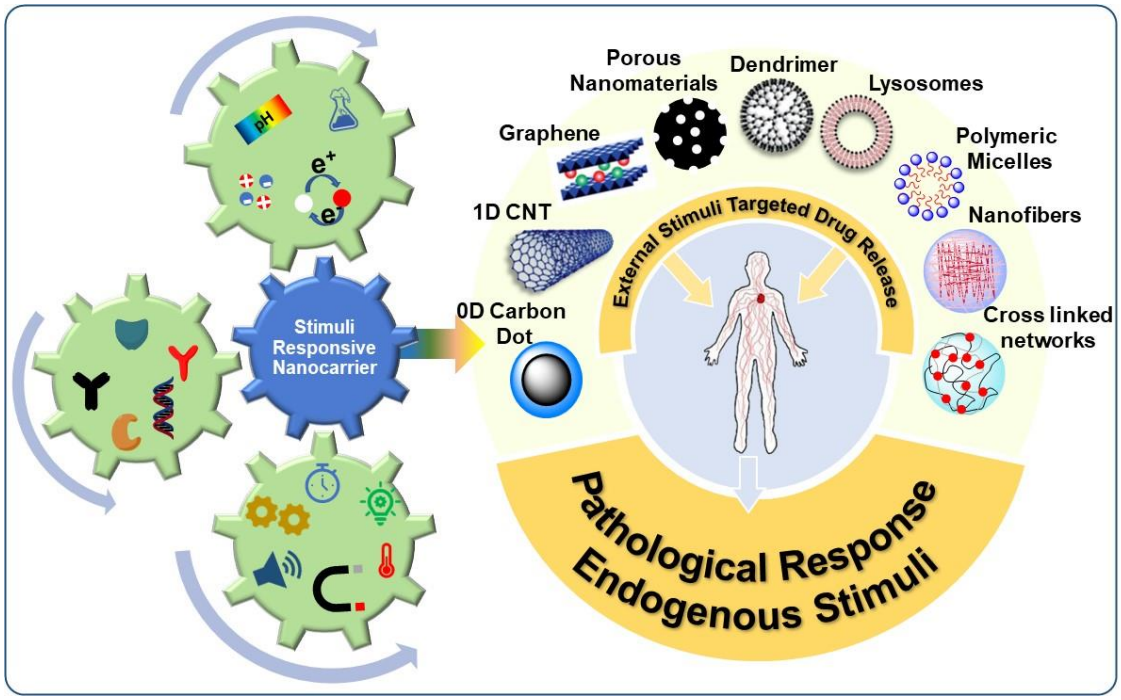

Figure 1.7. Nanomaterial for stimuli-responsive drug delivery.

1.0.5.1. Carbonized polymeric nanomaterials with biocidal activity

In recent times, nanotechnology-assisted antimicrobial applications have emerged as a promising field. Carbon dots (CD) have become a valuable material since their discovery due to their outstanding optoelectronic properties coupled with high biocompatibility and photostability.[58,59] CD has attracted innumerable attention for the antimicrobial application due to the unique mechanism of action overcoming the existing antibiotics i.e., reactive oxygen species (ROS) generation, photosensitization, charge- and photothermal hyperthermia-induced apoptosis, and physical or mechanical cell wall degradation.

Recently, carbonized polymer dots (CPD) among carbon dots (CD) have been propounded to unfold an interesting nature of a different group of CDs and highlighted the importance of polymerization and carbonization for the formation of CPDs originally known as polymer CDs or even polymer dots (PDs).[62-66] A large number of studies are focusing on the selection and regulation of a variety of molecules and polymer precursors to achieve better-performing CPDs(Figure 1.8). As depicted in Figure 1.8, the final product seems to be a core-shell type spherical dot structure, consisting of a carbonized core inside either due to high cross-linking or graphitization, and the outer surface is covered by polymer structure, which justifies the proposed class CPDs. With

superabundant confirmations, tuneable structures, and accordingly synchronized properties, the chances of obtaining diversified CPDs are the same as polymers. In addition to their higher stability, CPDs also have better compatibility due to their reserved polymer chains, which makes them more stable than polymers. Besides combining the advantages of both polymers and CDs, CPDs are also economical, environmentally friendly, and non-toxic.[67]

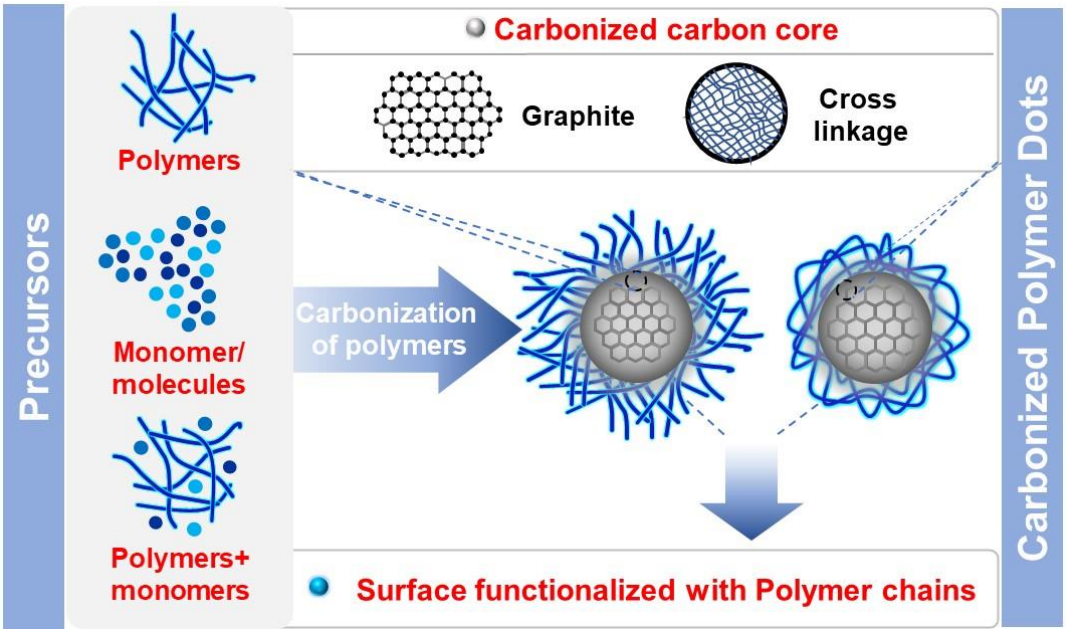

Figure 1.8. Synthesis and structure of CPDs.

CPDs are nontoxic and metabolizable due to carbon being the main constituent element, unlike metals. Additionally, the precursors for CPDs involve a wide range of raw materials as the precursor, including polymers (single chain, branched, hyperbranched), small organic molecules, biomass, and even larger carbon materials (for example graphene sheets). Furthermore, several simple preparation methods have been demonstrated to be effective, including, hydrothermal, solvothermal, and microwave methods. Lastly, the outer surface of CPDs possesses adequate functionalities (polymeric, charged, or small element-specific functional groups), which makes them biocompatible as well as bioactive enough to benefit living organisms without additional modification.

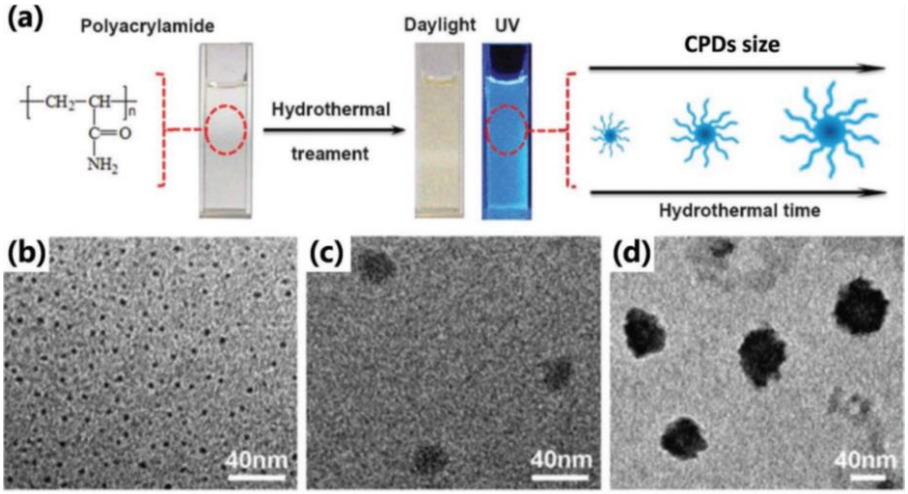

Figure 1.9. a) The diagram illustrates the process of forming CPDs by hydrothermal treatment of polyacrylamide, with digital photos of the aqueous solution of the CPD under day light irradiation and UV illumination. The growth of CPD size with time in hydrothermal conditions. The TEM images of CPDs were prepared with different hydrothermal times b) 24 h, c) 72 h and d) 96 h a–d) Reproduced with permission.[70] Copyright 2013, The Royal Society of Chemistry.

While carbonized polymeric dots (CPD) is being extensively studied as new light emitting materials,[68] the CPD formation using polymers provides the apparent advantage of the ability to control size while synthesis by tuning the applied "cracking force' and to retain the surface functionalities compared to the smaller precursor molecules.[69] For instance, Xi and co-workers have synthesized fluorescent CPD materials with different core sizes in one step by hydrothermal treatment of amide-abundant polyacrylamide for bioimaging purposes (Figure 1.9).[70] Recently, Maruthapandi et al. reported the formation of carbon nanocomposites using positively charged conducting polymers polyaniline and polypyrrole for their antibacterial property.[71] Jijie et al. have conjugated ampicillin antibiotic to post-synthesized CDs and observed retainment of antibacterial activity.[72] However, to the best of our knowledge, CPD of polymeric biocides with retention or enhanced activity has not been reported.

Chapter 3 of this thesis has focused on the use of antimicrobial polymer to obtain antimicrobial nanomaterials, such as the carbonization of biocidal polymer $\mathbf{C_0P_1}$ to obtain fluorescent carbonized polymer dots (CPD) **CPD-$\mathbf{C_0P_1}$** and generation of the antimicrobial surface using electrospinning technique. Also, the emission property and antimicrobial behavior after the transformation of polymers to CPD and embedment of CPD into nano mats have been discussed in detail in chapter 3.

1.0.5.2. Polymeric nanocomposites as a drug nano-carrier

Polymeric nanocomposites serve as an inert scaffold or vehicle for delivering the bioactive substance, be it small biomolecules, drugs, or other diagnostic therapeutics. Polymeric nanocomposites have been thoroughly examined and are still being investigated as nano-carriers for the delivery of bioactive materials. Some examples of organic polymeric nano-carrier include lipids, liposomes, dendrimers, carbon nanomaterials (carbonized polymer dots), emulsions, polymer-based hydrogels, nanofibers, as well as other polymeric biomaterials.[73-76] While being inert, these polymers have been shown to enhance pharmacokinetic characteristics, including solubility and circulation time at the same time, while minimizing nonspecific target effects significantly. The macromolecular structure provides the advantage of an organic interface allowing for the attachment of bioactive units, including imaging agents, and simultaneously designing the nanoarchitectures for diagnosis and disease treatment instantaneously.[77-79]

Synthetic polymeric micelles revealed the enormous potential to assimilate a diversity of bioactive molecules, including drugs, oligonucleotides [80], enzymes, plasmid DNA [81], proteins, and RNAs, photosensitizers [82], by customizing block copolymers' core-forming segments. Recently, synthetic polymers have been highlighted as potential drug nanocarriers (NCs), particularly due to their ability to develop drug delivery systems (DDS) with a triggered/controlled release of drugs [83]. Polymeric micelles have been known as the most common NCs of DDSs as regards the core-shell structure. It is possible to deliver cancer drugs more efficiently by encapsulating them in polymeric micelles modified for targeted drug delivery and triggering release in cancer cells. [84] As a result of being amphiphilic block copolymers, these molecules get self-assembled in water at a critical micelle concentration (CMC) when they are introduced into an aqueous solution. The formation of micellar polymeric units possesses amphiphilic block copolymers, including diblock (A-B), triblock (A-B-A), random block copolymers, and copolymer conjugates. In addition to its ability to encapsulate poorly water-soluble drugs, the hydrophobic core is capable of controlling various important factors such as biodistribution, toxicity profile, stability, and release of the bioactive molecule. The most often used and studied hydrophobic polymers for micellar core formation of NCs in aqueous media are poly(lactic acid) (PLA), poly(ε-caprolactone) (PCL), poly(lactic-*co*-glycolic acid) (PLGA), poly(aspartic acid) (PAsp) and poly(propylene oxide) (PPO)

(Figure 1.10). This figure demonstrates which hydrophilic polymers are the most commonly used and are the most suitable for the formation of the hydrophilic shell of NCs for drug delivery. Examples include poly(vinyl alcohol) (PVA), poly(ethylene glycol) (PEG), poly(ethyleneimine) (PEI), poly(glutamic acid) (PGA), poly(acrylamide) (PAM), as well as N-(2-hydroxypropyl)methacrylamide (HPMA) in the form of polymers (Figure 1.9).[85]

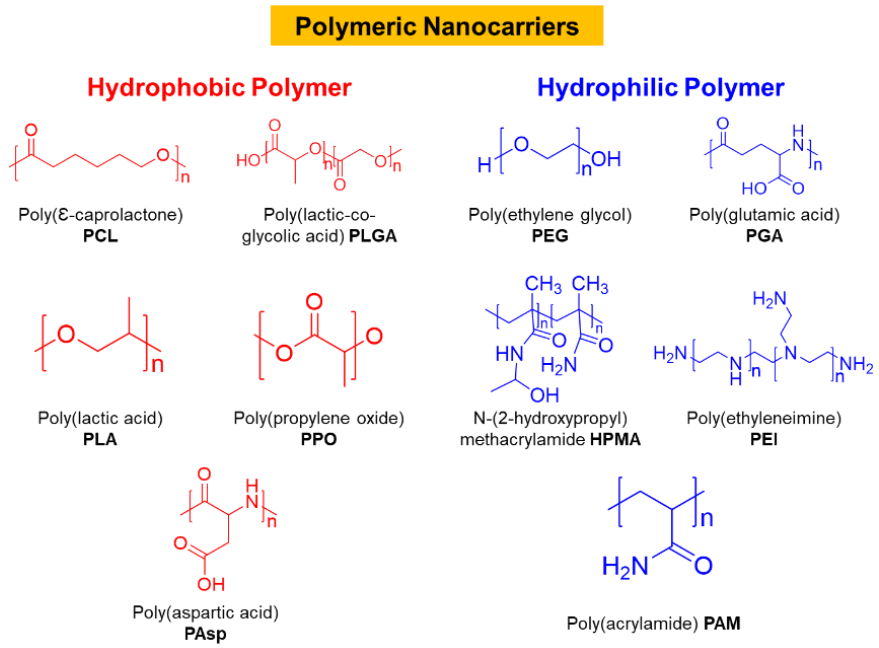

Figure 1.10. Types of polymers for the formation of nano-carriers.[85]

Among the above examples, a frequently used amphiphilic copolymer in DDSs is PEG-PLA which is a combination of hydrophilic PEG and hydrophobic PLA polymer synthesized *via* ring opening polymerization reaction of lactide with PEG. The block copolymer offers apparent stability to NCs by reducing nonspecific interactions with blood proteins and preventing aggregation.[86] Capping these polymers on metal nanoparticles (MNPs) by covalent interactions further provides the ability to develop drug nano-carrier with higher drug encapsulation and loading capacity, stimuli-induced drug delivery, and control of size, shape and stability of nano-carrier.[87,88] As a means of achieving this objective, we have described in chapter 4 a new type of nano-carrier (**SS-NC**) with a highly packed hydrophobic core and a hydrophilic shell, in contrast to the previously reported nano-carriers with a hydrophilic shell. Our new type of core-shell structure (**SS-NC**) is a variation of the conventional narcissistic self-sorted micellar system that uses a hydrophobic polymer PLLA to self-assemble the **IONP** chains

between the amphiphilic chain of **mPEG-PLLA** to provide this new type of core-shell structure. Furthermore, the effect of magnetism and temperature on the release of drugs is also discussed concerning the comparisons of the effects of drug-loading capacity between **SS-NC** and **NS-NC** and the comparison of the effects of magnetism and temperature on the release of drugs.

1.1. Scope of Research

It is perhaps an achievement of polymer research to transform a macromolecule into a standalone bioactive agent. It is clear from the present literature that several synthetic polymers can successfully contribute as an inherent bioactive agent and also for the delivery of bioactive agents. Using antimicrobial polymers as examples, around 5 million deaths globally each year are associated with bacterial infections. [89] Many factors, such as antibiotic resistance bacteria, antibiotic-immune patients, stubborn microbial film formations, etc., are expected to make this problem worse in the future. Antimicrobial polymers among bioactive synthetic polymers are potential candidates to intercept bacterial infections due to their inherent characteristics. Although important scientific advancements have been made in recent years in the field as creative and diverse variants continue to appear in literature in the form of biocidal polymer, polymeric biocide, hyperbranched polymer, dendrimers, polymeric micelles, and carbonized polymeric materials, a great deal of work needs to be done to address some major issues i.e., developing novel broad-spectrum antibacterial material, improving the activity of existing antibiotics, reducing or eliminating the toxicity factor, and fabricate cost-effective materials for antimicrobial applications. Introducing drug polymers in this aspect is an effort to add value to existing small bioactive molecules by their polymerization and/or carbonization. Further extension of this field may provide positive solutions for the challenges mentioned formerly.

Also, the role of polymers for drug delivery applications in the form of nano-carriers is indispensable. Especially as a stimuli-responsive polymeric nano-carrier system, these have the potential to improve drug and gene delivery to targeted areas. As we gain a deep understanding of biological responses towards these nano-carrier systems the chances to enhance stimulus, drug encapsulation, targetability and biodistribution have become favorable by reorganizing the self-assembly of polymeric nano-carrier or by initiating the structural changes to the polymeric chain. Moreover, there are future possibilities for designing more efficient and improved drug delivery nano-carriers either by changing

the polymeric shell structure (chain length, di/tri/multiblock copolymer) or replacing the nanoparticles in the core.

1.2. References

1. Sung, Y. K.; Kim, S. W. Recent advances in polymeric drug delivery systems. *Biomater. Res.* **2020,** *24*, 12.
2. Duncan, R. The dawning era of polymer therapeutics. *Nat. Rev. Drug Discov.* **2003,** *2*, 347–360.
3. Oh, J. K. Polymers in Drug Delivery: Chemistry and Applications. *Mol. Pharm.* **2017,** *14*, 2459–2459.
4. Pillai, O.; Panchagnula, R. Polymers in drug delivery. *Curr. Opin. Chem. Biol.* **2001,** *5*, 447–451.
5. Love, B. Chapter 9-Polymeric Biomaterials. In *Biomaterials*, Love, B., Ed. Academic Press: 2017; pp 205–238.
6. Li, J.; Yu, F.; Chen, Y.; Oupický, D. Advances in the development of pharmacologically active polymers. *J. Control. Release* **2015**, *219*, 369–382.
7. Ekladious, I.; Colson, Y. L.; Grinstaff, M. W. Polymer–drug conjugate therapeutics: advances, insights and prospects. *Nat. Rev. Drug Discov.* **2019,** *18*, 273–294.
8. Senapati, S.; Mahanta, A. K.; Kumar, S.; Maiti, P. Controlled drug delivery vehicles for cancer treatment and their performance. *Signal Transduct. Target. Ther* **2018**, *3*, 7.
9. Sartaliya, S.; Gowri, V.; Chopra, V.; Roy, H. S.; Ghosh, D.; Jayamurugan, G. Unraveling the Effect of Nondrug Spacers on a True Drug-Polymer and a Comparative Study of Their Antimicrobial Activity. *ACS Appl. Polym. Mater.* **2022,** *4*, 3952–3961.
10. Li, X.; Liu, P. Acid-triggered degradable polyprodrug with drug as unique repeating unit for long-acting drug delivery with minimal leakage. *Mater. Sci. Eng. C* **2021,** *128*, 112317.
11. Morens, D. M.; Fauci, A. S. Emerging Pandemic Diseases: How We Got to COVID-19. *Cell* **2020,** *182*, 1077–1092.

12. Hobson, C.; Chan, A. N.; Wright, G. D. The Antibiotic Resistome: A Guide for the Discovery of Natural Products as Antimicrobial Agents. *Chem. Rev.* **2021,** *121*, 3464–3494.
13. Li, W.; Separovic, F.; O'Brien-Simpson, N. M.; Wade, J. D. Chemically modified and conjugated antimicrobial peptides against superbugs. *Chem. Soc. Rev.* **2021,** *50*, 4932–4973.
14. Neu Harold, C. The Crisis in Antibiotic Resistance. *Science* **1992,** *257*, 1064–1073.
15. Payne, D. J.; Gwynn, M. N.; Holmes, D. J.; Pompliano, D. L. Drugs for bad bugs: confronting the challenges of antibacterial discovery. *Nat. Rev. Drug Discov.* **2007,** *6*, 29–40.
16. Jain, A.; Duvvuri, L. S.; Farah, S.; Beyth, N.; Domb, A. J.; Khan, W. Antimicrobial Polymers. *Adv. Healthc. Mater.* **2014,** *3*, 1969–1985.
17. Kenawy, E.-R.; Worley, S. D.; Broughton, R. The Chemistry and Applications of Antimicrobial Polymers: A State-of-the-Art Review. *Biomacromolecules* **2007,** *8*, 1359–1384.
18. Domagk, G. A new class of disinfectants. *Deut. Med. Wochenschr.* **1935,** *61*, 829–832.
19. Cornell, R. J.; Donaruma, L. G. Intermediates for the Synthesis of Biologically Active Polymers. *J. Med. Chem.* **1965,** *8*, 388–390.
20. Vogl, O.; Tirrell, D. Functional Polymers with Biologically Active Groups. *J. Macromol. Sci. Chem.* **1979,** *13*, 415–439.
21. Timofeeva, L.; Kleshcheva, N. Antimicrobial polymers: mechanism of action, factors of activity, and applications. *Appl. Microbiol. Biotechnol.* **2011,** *89*, 475–492.
22. Chattopadhyay, S.; Keul, H.; Moeller, M. Synthesis of Azetidinium-Functionalized Polymers Using a Piperazine Based Coupler. *Macromolecules* **2013,** *46*, 638–646.
23. Tiller, J. C. Antimicrobial Surfaces. In *Bioactive Surfaces*, Börner, H. G.; Lutz, J.-F., Eds. Springer Berlin Heidelberg: Berlin, Heidelberg, 2011; pp 193–217.
24. Kamaruzzaman, N. F.; Tan, L. P.; Hamdan, R. H.; Choong, S. S.; Wong, W. K.; Gibson, A. J.; Chivu, A.; Pina, M. D. Antimicrobial Polymers: The Potential Replacement of Existing Antibiotics? *Int. J. Mol. Sci.* **2019,** *20*, 2747.

25. Kumar, D.; Gihar, S.; Shrivash, M. K.; Kumar, P.; Kundu, P. P. A review on the synthesis of graft copolymers of chitosan and their potential applications. *Int. J. Biol. Macromol.* **2020,** *163*, 2097–2112.
26. Zheng, W.; Anzaldua, M.; Arora, A.; Jiang, Y.; McIntyre, K.; Doerfert, M.; Winter, T.; Mishra, A.; Ma, H.; Liang, H. Environmentally Benign Nanoantibiotics with a Built-in Deactivation Switch Responsive to Natural Habitats. *Biomacromolecules* **2020,** *21*, 2187–2198.
27. Chen, A.; Peng, H.; Blakey, I.; Whittaker, A. K. Biocidal Polymers: A Mechanistic Overview. *Polym. Rev.* **2017,** *57*, 276–310.
28. Banerjee, I.; Pangule, R. C.; Kane, R. S. Antifouling Coatings: Recent Developments in the Design of Surfaces That Prevent Fouling by Proteins, Bacteria, and Marine Organisms. *Adv. Mater.* **2011,** *23*, 690–718.
29. Konai, M. M.; Bhattacharjee, B.; Ghosh, S.; Haldar, J. Recent Progress in Polymer Research to Tackle Infections and Antimicrobial Resistance. *Biomacromolecules* **2018,** *19*, 1888–1917.
30. Li, P.; Li, X.; Saravanan, R.; Li, C. M.; Leong, S. S. J. Antimicrobial macromolecules: synthesis methods and future applications. *RSC Adv.* **2012,** *2*, 4031–4044.
31. Peschel, A.; Sahl, H.-G. The co-evolution of host cationic antimicrobial peptides and microbial resistance. *Nat. Rev. Microbiol.* **2006,** *4*, 529–536.
32. Sasireka, A.; Rajendran, R.; Priya, P.; Raj, V. Ciprofloxacin-Loaded Ceramic/Polymer Composite Coatings on Ti with Improved Antibacterial and Corrosion Resistance Properties for Orthopedic Applications. *ChemistrySelect* **2019,** *4*, 1166–1175.
33. Stebbins, N. D.; Ouimet, M. A.; Uhrich, K. E. Antibiotic-containing polymers for localized, sustained drug delivery. *Adv. Drug Deliv. Rev.* **2014,** *78*, 77–87.
34. Dizman, B.; Elasri, M. O.; Mathias, L. J. Synthesis, Characterization, and Antibacterial Activities of Novel Methacrylate Polymers Containing Norfloxacin. *Biomacromolecules* **2005,** *6*, 514–520.
35. Ergene, C.; Yasuhara, K.; Palermo, E. F. Biomimetic antimicrobial polymers: recent advances in molecular design. *Polym. Chem.* **2018,** *9*, 2407–2427.

36. Das, D.; Srinivasan, S.; Kelly, A. M.; Chiu, D. Y.; Daugherty, B. K.; Ratner, D. M.; Stayton, P. S.; Convertine, A. J. RAFT polymerization of ciprofloxacin prodrug monomers for the controlled intracellular delivery of antibiotics. *Polym. Chem.* **2016,** *7*, 826–837.
37. Parwe, S. P.; Chaudhari, P. N.; Mohite, K. K.; Selukar, B. S.; Nande, S. S.; Garnaik, B. Synthesis of ciprofloxacin-conjugated poly (L-lactic acid) polymer for nanofiber fabrication and antibacterial evaluation. *Int. J. Nanomedicine* **2014,** *9*, 1463–77.
38. Woo, G. L. Y.; Mittelman, M. W.; Santerre, J. P. Synthesis and characterization of a novel biodegradable antimicrobial polymer. *Biomaterials* **2000,** *21*, 1235–1246.
39. Judzewitsch, P. R.; Nguyen, T.-K.; Shanmugam, S.; Wong, E. H. H.; Boyer, C. Towards Sequence-Controlled Antimicrobial Polymers: Effect of Polymer Block Order on Antimicrobial Activity. *Angew. Chem. Int. Ed.* **2018,** *57*, 4559–4564
40. Allen, C. L.; Chhatwal, A. R.; Williams, J. M. J. Direct amide formation from unactivated carboxylic acids and amines. *Chem. Commun.* **2012,** *48*, 666–668.
41. Montalbetti, C. A. G. N.; Falque, V. Amide bond formation and peptide coupling. *Tetrahedron* **2005,** *61*, 10827–10852.
42. Duncan, R.; Vicent, M. J. Polymer therapeutics-prospects for 21st century: The end of the beginning. *Adv. Drug Deliv. Rev.* **2013,** *65*, 60–70.
43. Yeo, Y.; Kim, B.-K. Drug Carriers: Not an Innocent Delivery Man. *AAPS J.* **2015,** *17*, 1096–1104.
44. Yang, Y.; Cai, Z.; Huang, Z.; Tang, X.; Zhang, X. Antimicrobial cationic polymers: from structural design to functional control. *Polym. J.* **2018,** *50*, 33–44.
45. Larson, N.; Ghandehari, H. Polymeric Conjugates for Drug Delivery. *Chem. Mater.* **2012,** *24*, 840–853.
46. Jatzkewitz, H. An ein kolloidales Blutplasma-Ersatzmittel (Polyvinylpyrrolidon) gebundenes Peptamin (Glycyl-L-leucyl-mezcalin) als neuartige Depotform für biologisch aktive primäre Amine (Mezcalin). *Z. Naturforsch. B* **1955,** *10*, 27-31.
47. Ulbrich, K.; Šubr, V. R. Polymeric anticancer drugs with pH-controlled activation. *Adv. Drug Deliv. Rev.* **2004,** *56*, 1023–1050.
48. Mehvar, R.; Dann, R. O.; Hoganson, D. A. Kinetics of hydrolysis of dextran–methylprednisolone succinate, a macromolecular prodrug of methylprednisolone, in rat blood and liver lysosomes. *J. Control. Release* **2000,** *68*, 53–61.

49. Lee, S.; Greenwald, R. B.; McGuire, J.; Yang, K.; Shi, C. Drug Delivery Systems Employing 1,6-Elimination: Releasable Poly(ethylene glycol) Conjugates of Proteins. *Bioconjugate Chem.* **2001,** *12*, 163–169.
50. Paul, D. R.; Robeson, L. M. Polymer nanotechnology: Nanocomposites. *Polymer* **2008,** *49*, 3187–3204.
51. Damodharan, J. Nanomaterials in medicine – An overview. *Mater. Today: Proc.* **2021,** *37*, 383–385.
52. Soleyman, R.; Adeli, M. Impact of dendritic polymers on nanomaterials. *Polym. Chem.* **2015,** *6*, 10–24.
53. Arvizo, R. R.; Bhattacharyya, S.; Kudgus, R. A.; Giri, K.; Bhattacharya, R.; Mukherjee, P. Intrinsic therapeutic applications of noble metal nanoparticles: past, present and future. *Chem. Soc. Rev.* **2012,** *41*, 2943–2970.
54. Pham, S. H.; Choi, Y.; Choi, J. Stimuli-Responsive Nanomaterials for Application in Antitumor Therapy and Drug Delivery. *Pharmaceutics* **2020,** *12*, 630.
55. Singh, A. P.; Biswas, A.; Shukla, A.; Maiti, P. Targeted therapy in chronic diseases using nanomaterial-based drug delivery vehicles. *Signal Transduct. Target. Ther.* **2019,** *4*, 33.
56. Sánchez, A.; Mejía, S. P.; Orozco, J. Recent Advances in Polymeric Nanoparticle-Encapsulated Drugs against Intracellular Infections. *Molecules* **2020**, *25*, 3760.
57. Crosby, A. J.; Lee, J. Y. Polymer Nanocomposites: The "Nano" Effect on Mechanical Properties. *Polym. Rev.* **2007,** *47*, 217–229.
58. Lim, S. Y.; Shen, W.; Gao, Z. Carbon quantum dots and their applications. *Chem. Soc. Rev.* **2015,** *44*, 362–381.
59. Xu, J.-W.; Yao, K.; Xu, Z.-K. Nanomaterials with a photothermal effect for antibacterial activities: an overview. *Nanoscale* **2019,** *11*, 8680–8691.
60. Du, J.; Xu, N.; Fan, J.; Sun, W.; Peng, X. Carbon Dots for In Vivo Bioimaging and Theranostics. *Small* **2019,** *15*, 1805087.
61. Su, W.; Wu, H.; Xu, H.; Zhang, Y.; Li, Y.; Li, X.; Fan, L. Carbon dots: a booming material for biomedical applications. *Mater. Chem. Front.* **2020,** *4*, 821–836.
62. Tao, S.; Zhu, S.; Feng, T.; Xia, C.; Song, Y.; Yang, B. The polymeric characteristics and photoluminescence mechanism in polymer carbon dots: A review. *Mater. Today Chem.* **2017**, *6*, 13–25.

63. Song, Y.; Zhu, S.; Shao, J.; Yang, B. Polymer carbon dots—a highlight reviewing their unique structure, bright emission and probable photoluminescence mechanism. *J. Polym. Sci. A Polym. Chem.* **2017**, *55*, 610–615.
64. Feng, T.; Zhu, S.; Zeng, Q.; Lu, S.; Tao, S.; Liu, J.; Yang, B. Supramolecular Cross-Link-Regulated Emission and Related Applications in Polymer Carbon Dots. *ACS Appl. Mater. Interfaces* **2018**, *10*, 12262–12277.
65. Han, L.; Liu, S. G.; Dong, J. X.; Liang, J. Y.; Li, L. J.; Li, N. B.; Luo, H. Q. Facile synthesis of multicolor photoluminescent polymer carbon dots with surface-state energy gap-controlled emission. *J. Mater. Chem. C* **2017**, *5*, 10785–10793.
66. Vallan, L.; Urriolabeitia, E. P.; Ruipérez, F.; Matxain, J. M.; Canton-Vitoria, R.; Tagmatarchis, N.; Benito, A. M.; Maser, W. K. Supramolecular-Enhanced Charge Transfer within Entangled Polyamide Chains as the Origin of the Universal Blue Fluorescence of Polymer Carbon Dots. *J. Am. Chem. Soc.* **2018**, *140*, 12862–12869.
67. Hill, S. A.; Benito-Alifonso, D.; Morgan, D. J.; Davis, S. A.; Berry, M.; Galan, M. C. Three-minute synthesis of sp3 nanocrystalline carbon dots as non-toxic fluorescent platforms for intracellular delivery. *Nanoscale* **2016**, *8*, 18630–18634.
68. Tao, S.; Feng, T.; Zheng, C.; Zhu, S.; Yang, B. Carbonized Polymer Dots: A Brand New Perspective to Recognize Luminescent Carbon-Based Nanomaterials. *J. Phys. Chem. Lett.* **2019**, *10*, 5182–5188.
69. Liang, J.; Li, W.; Chen, J.; Huang, X.; Liu, Y.; Zhang, X.; Shu, W.; Lei, B.; Zhang, H. Antibacterial Activity and Synergetic Mechanism of Carbon Dots against Gram-Positive and -Negative Bacteria. *ACS Appl. Bio Mater.* **2021,** *4*, 6937–6945.
70. Gu, J.; Wang, W.; Zhang, Q.; Meng, Z.; Jia, X.; Xi, K. Synthesis of fluorescent carbon nanoparticles from polyacrylamide for fast cellular endocytosis. *RSC Adv.* **2013,** *3*, 15589–15591.
71. Maruthapandi, M.; Saravanan, A.; Gupta, A.; Luong, J. H. T. Antimicrobial Activities of Conducting Polymers and Their Composites. *Macromol.* **2022,** *2*, 78-99.
72. Jijie, R.; Barras, A.; Bouckaert, J.; Dumitrascu, N.; Szunerits, S.; Boukherroub, R. Enhanced antibacterial activity of carbon dots functionalized with ampicillin combined with visible light triggered photodynamic effects. *Colloids Surf. B: Biointerfaces* **2018,** *170*, 347–354.

73. Soppimath, K. S.; Aminabhavi, T. M.; Kulkarni, A. R.; Rudzinski, W. E. Biodegradable polymeric nanoparticles as drug delivery devices. *J. Control. Release* **2001,** *70*, 1–20.
74. Su, J.; Chen, F.; Cryns, V. L.; Messersmith, P. B. Catechol Polymers for pH-Responsive, Targeted Drug Delivery to Cancer Cells. *J. Am. Chem. Soc.* **2011,** *133*, 11850–11853.
75. Kumar, S.; Singh, S.; Senapati, S.; Singh, A. P.; Ray, B.; Maiti, P. Controlled drug release through regulated biodegradation of poly(lactic acid) using inorganic salts. *Int. J. Biol. Macromol.* **2017,** *104*, 487–497.
76. Shim, M. S.; Kwon, Y. J. Stimuli-responsive polymers and nanomaterials for gene delivery and imaging applications. *Adv. Drug Deliv. Rev.* **2012,** *64*, 1046–1059.
77. Bharali, D. J.; Lucey, D. W.; Jayakumar, H.; Pudavar, H. E.; Prasad, P. N. Folate-Receptor-Mediated Delivery of InP Quantum Dots for Bioimaging Using Confocal and Two-Photon Microscopy. *J. Am. Chem. Soc.* **2005,** *127*, 11364–11371.
78. Zrazhevskiy, P.; Sena, M.; Gao, X. Designing multifunctional quantum dots for bioimaging, detection, and drug delivery. *Chem. Soc. Rev.* **2010,** *39*, 4326–4354.
79. Kairdolf, B. A.; Smith, A. M.; Stokes, T. H.; Wang, M. D.; Young, A. N.; Nie, S. Semiconductor Quantum Dots for Bioimaging and Biodiagnostic Applications. *Annu. Rev. Anal. Chem.* **2013,** *6*, 143–162.
80. Skatrud, P. L., The impact of multiple drug resistance (MDR) proteins on chemotherapy and drug discovery. In Progress in Drug Research, Glasel, J. A.; Kolb, V. M.; Skatrud, P. L.; Ford, J. W.; Stevens, E. B.; Treherne, J. M.; Packer, J.; Bushfield, M.; Wong, D. T.; Bymaster, F. P.; Gupta, S. P.; Jucker, E., Eds. Birkhäuser Basel: Basel, 2002; pp 99–131.
81. Dai, X.; Tan, C. Combination of microRNA therapeutics with small-molecule anticancer drugs: Mechanism of action and co-delivery nano-carriers. *Adv. Drug Deliv. Rev.* **2015,** *81*, 184–197.
82. Teo, P. Y.; Cheng, W.; Hedrick, J. L.; Yang, Y. Y. Co-delivery of drugs and plasmid DNA for cancer therapy. *Adv. Drug Deliv. Rev.* **2016,** *98*, 41–63.
83. Tran, S.; DeGiovanni, P.-J.; Piel, B.; Rai, P. Cancer nanomedicine: a review of recent success in drug delivery. *Clin. Transl. Med.* **2017,** *6*, 44.

84. Guo, X.; Wang, L.; Wei, X.; Zhou, S. Polymer-based drug delivery systems for cancer treatment. *J. Polym. Sci., Part A-1: Polym. Chem.* **2016,** *54*, 3525–3550.
85. Avramović, N.; Mandić, B.; Savić-Radojević, A.; Simić, T. Polymeric Nanocarriers of Drug Delivery Systems in Cancer Therapy. *Pharmaceutics* **2020**, *12*, 298.
86. Knop, K.; Hoogenboom, R.; Fischer, D.; Schubert, U. S. Poly(ethylene glycol) in Drug Delivery: Pros and Cons as Well as Potential Alternatives. *Angew. Chem., Int. Ed.* **2010,** *49*, 6288–6308.
87. Begines, B.; Ortiz, T.; Pérez-Aranda, M.; Martínez, G.; Merinero, M.; Argüelles-Arias, F.; Alcudia, A. Polymeric Nanoparticles for Drug Delivery: Recent Developments and Future Prospects. *Nanomaterials* **2020**, *10*, 1403.
88. Hu, J.; Qian, Y.; Wang, X.; Liu, T.; Liu, S. Drug-Loaded and Superparamagnetic Iron Oxide Nanoparticle Surface-Embedded Amphiphilic Block Copolymer Micelles for Integrated Chemotherapeutic Drug Delivery and MR Imaging. *Langmuir* **2012,** *28*, 2073–2082.
89. Murray, C. J. L.; Ikuta, K. S.; Sharara, F.; Swetschinski, L.; Robles A. G. et. al. Global burden of bacterial antimicrobial resistance in 2019: a systematic analysis. *Lancet* **2022,** *399*, 629–655.

Chapter 2:

Unraveling the effect of non-drug spacers on a true drug-polymer and a comparative study of their antimicrobial activity

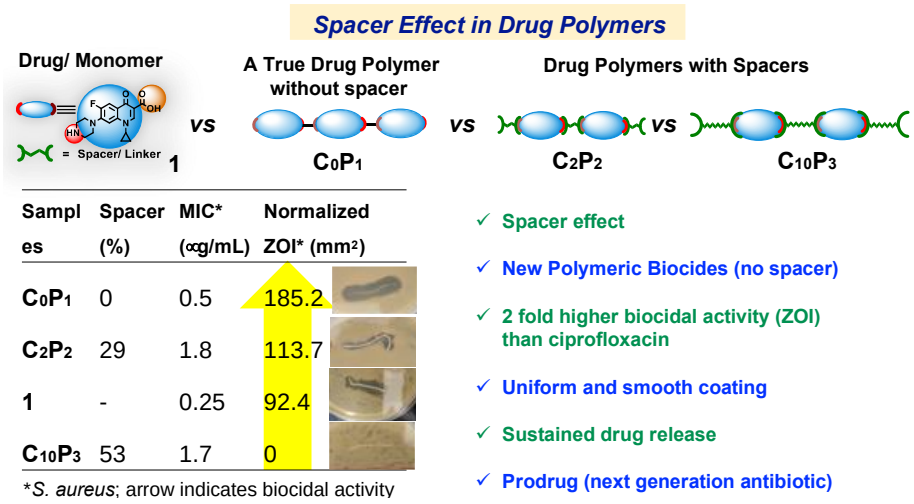

2.0 Introduction

Several studies have been conducted on the polymerization of drug units using spacers or other polymeric units. As discussed in chapter 1 most of the examples of antimicrobial polymers (APs) known so far consist of a significant amount of non-drug parts along with a biocidal unit which on the other hand reveals the consequences of the activity of the drug. According to the best of our knowledge far less attention has been given to the development of self-polymerized/ homopolymerized drugs/ biocide monomers, at least of the molecules comprising the AB monomer. Upon screening the literature on the drug's list, we envisaged that ciprofloxacin, a drug molecule with a secondary amine and a carboxylic acid as end functional groups, can be self-sufficient for polymerization without the need for linkers/spacers or any polymeric unit.[1,2] As a proof of concept, herein, we present a comparative study on the efficacy of antibacterial activity using a polymeric biocide of a widely used drug/antibiotic, second-generation fluoroquinolone 1- cyclopropyl-6-fluoro-4-oxo-7-piperazine-1-ylquinoline-3-carboxylic acid (ciprofloxacin).

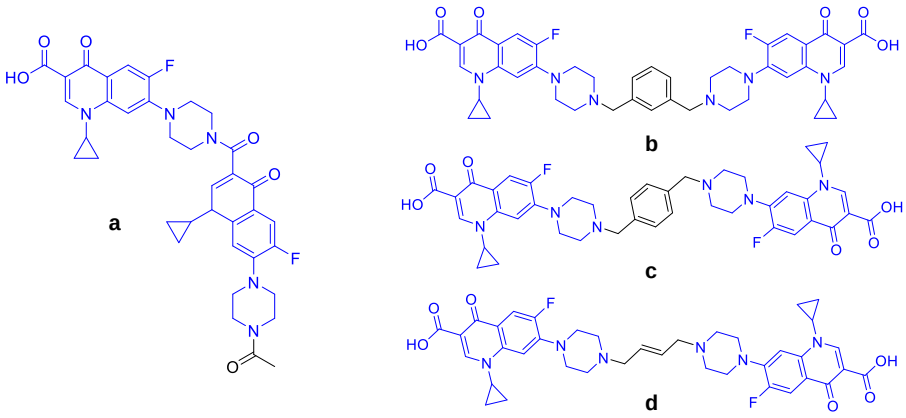

Figure 2.0. Selected examples of dimers of ciprofloxacin.

While the self-condensed polymer of ciprofloxacin is unprecedented, the dimer of acetylated ciprofloxacin (Figure 2.0a) was reported by Turos and co-workers in a patent and demonstrated its activity against drug-resistant bacteria (facultative intracellular bacteria); however, there was no mention of polymerization by covalent bonding or self-condensation reaction.[3] Similarly, Fisher and co-workers have also demonstrated that dimers of ciprofloxacin (Figure 2.0b-d) derivatives synthesized using aryl and alkyl linkers effectively target the gyrase enzyme in Streptococcus pneumoniae.[4]

Mesallati and Tajber reported that it is possible to increase the solubility of ciprofloxacin through polymer-assisted amorphous salt solid dispersions via noncovalent interactions.[5]

As revealed by literature, the covalently linked homopolymer of ciprofloxacin or even an oligomer of ciprofloxacin without any inert linker/spacer has not been reported so far. Although several reports have incorporated the spacers with antimicrobials,[6-8] the concept of the spacer effect on the activity of drug-polymer has not been investigated in detail. Here, we tried to examine the same and found that the non-drug spacer length in the drug-polymer is inversely proportional to the biocidal activity of the polymer, at least in the present case. In this chapter, we report the synthesis of a new kind of PB for the first time, that is, **C_0P_1** ciprofloxacin polymer having no spacer unit via self-condensation polymerization. For comparison purposes, we have also synthesized two other polymers **C_2P_2** and **$C_{10}P_3$**, with an increased spacer content using *N*-formylated **1** (**2**) and bis-amines. These three polymers were studied for their antibacterial activity against Escherichia coli (E. coli), and Staphylococcus aureus (S. aureus), both in solution and after the suture coating and the results have been discussed in detail further.

2.1. Results and discussions

2.1.1. Synthesis and Characterization of Polymeric Biocides and their Monomers

Three polymeric biocides such as **C_0P_1**, **C_2P_2**, and **$C_{10}P_3$**, were designed with the varied ratio of non-drug content of 0, 29, and 53%, respectively, to assess the role/importance of spacer/non-drug content in drug-containing polymers. The general scheme for the synthesis of these three polymers is shown in Scheme 2.0. The synthesis of **C_0P_1** polymer having no spacer was achieved using commercially available ciprofloxacin **1** *via* self-condensation between carboxylic acid and secondary amine activated by $SOCl_2$ and further heating the reaction mixture at 150 °C in DMSO and Et_3N (1 equivalent (equiv.) for 48 h to afford **C_0P_1** in 55% yield. Whereas to synthesize spacer polymers **C_2P_2** and **$C_{10}P_3$** with varying spacer lengths, ciprofloxacin **1** was derivatized to obtain **2** (*N*-formyl and methyl ester functionalized ciprofloxacin) by following reported protocols,[9] to couple *via* imine and amide formation reactions in one pot with *bis*-amines such as ethylenediamine (C_2) and 1,10-diaminodecane (C_{10}), respectively. The alkyl chains C_2 and C_{10} were chosen because they have marked mass differences and minimal/no

antimicrobial activity. For instance, 1,4-diaminobutane is known to have significant antimicrobial activity and toxicity.[10]

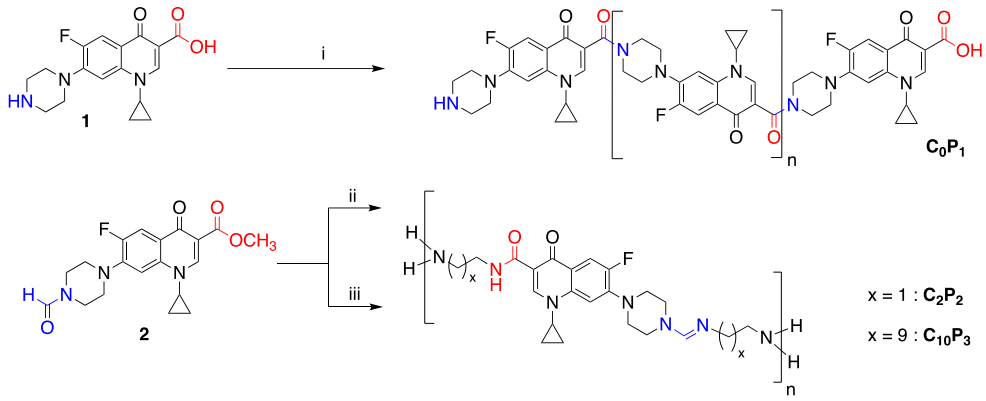

Scheme 2.0. Synthesis of polymers of ciprofloxacin **1** with- and without spacers.[a]

[a]Reagents and conditions: (i) 1. $SOCl_2$, CH_2Cl_2, 40 °C, 6 h, Et_3N, 2. DMSO (10 mL), 150 °C, 48 h, 55% (**C_0P_1**); (ii) ethylenediamine (2 equiv.), CH_3OH, 50 °C, 72 h, 54% (**C_2P_2**); (iii) 1,10-diaminodecane (2 equiv.), CH_3OH, 50 °C, 96 h, 27% (**$C_{10}P_3$**).

The synthesized polymers were characterized by Fourier-transform infrared (FT-IR), nuclear magnetic resonance (NMR), and size exclusion chromatographic (SEC) techniques. The FT-IR spectra of polymer **C_0P_1**, its precursor **1,** the spacer polymers **C_2P_2**, **$C_{10}P_3$**, and their precursor **2** were provided in Figure 2.1. for comparison purposes. In **C_0P_1**, the newly formed peak at 1680 cm^{-1}, which corresponds to an amide carbonyl (C=O stretching), and the decreasing peak at 3388 cm^{-1} and 3239 cm^{-1}, which corresponds to carboxylic acid (O–H stretching) and amine (N–H stretching), respectively, indicate the formation of amide bonds. The spectra of **C_2P_2** and **$C_{10}P_3$** spacer polymers featuring a new merged peak for imine (C=N) and amide (C=O) at ~1660 cm^{-1} and disappearance of the characteristic carbonyl peak for ester and N-CHO at 1724 and 1614 cm^{-1}, respectively, suggest the formation of both amide and imine bonds. More importantly, this indicates that the terminal groups are amine in both cases.

The formation of all polymers was further characterized by NMR spectroscopy and the overlay of ^1H NMR spectra provided in Figure 2.2. The peaks were assigned based on the literature values as well as COSY and ROESY spectra (Section 2.2.3.1, materials and methods).[11-13]

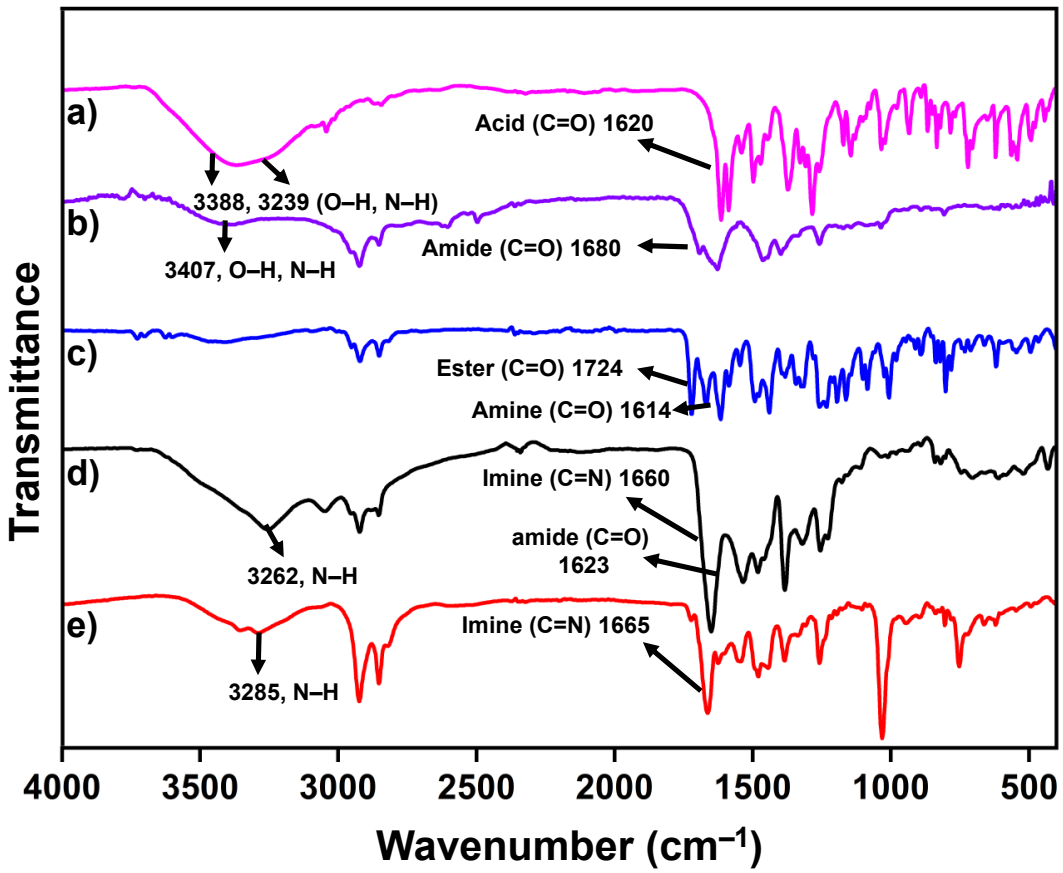

Figure 2.1. FT-IR spectra of a) monomer **1**, b) non-spacer polymer $\mathbf{C_0P_1}$, c) monomer **2**, spacer polymers d) $\mathbf{C_2P_2}$, and e) $\mathbf{C_{10}P_3}$.

H NMR spectrum of $\mathbf{C_0P_1}$ in Figure 2.2.a shows not only the characteristic signals with quite broadened nature, which is probably due to large-molecular-weight as corroborated by SEC data (*vide infra*). In contrast, the $\mathbf{C_{10}P_3}$ polymer showed quite sharp signals relative to $\mathbf{C_0P_1}$ and $\mathbf{C_2P_2}$ owing to the low molecular weight nature (Figure 2.2.b). The complete absence of methyl ester signal at ~3.9 ppm and the simultaneous appearance of amide (9.92–9.99 ppm) and imine (~8.0–8.12 ppm) protons signals in $\mathbf{C_2P_2}$ and $\mathbf{C_{10}P_3}$ with almost equal intensities are affirmative of formation of alternative amide and imine bonds in both the polymers. Interestingly, the absence of additional methylene protons corresponding to amide-amide or imine-imine coupling suggests the observation of orthogonal reactions for both end amine functional groups.

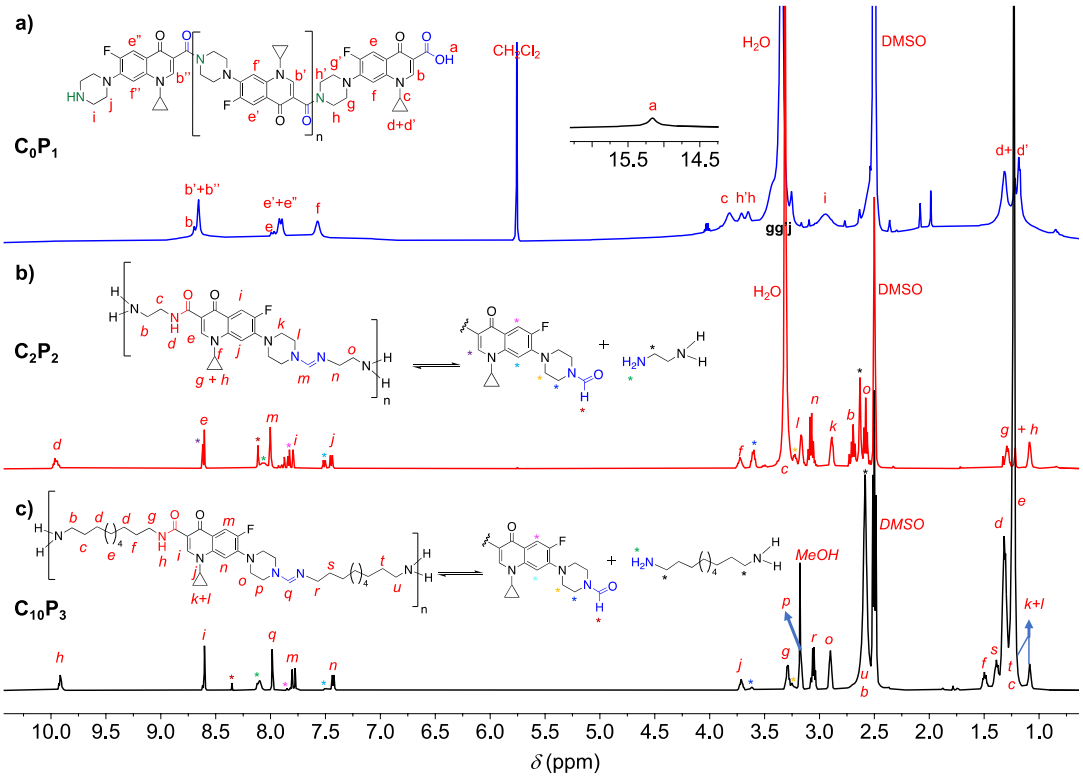

Figure 2.2. ^{1}H NMR spectra of polymers a) $\mathbf{C_0P_1}$ (500 MHz), b) $\mathbf{C_2P_2}$ (400 MHz), and c) $\mathbf{C_{10}P_3}$ (500 MHz) in DMSO-d_6 at 298 K.

The significant downfield shifted amide protons at 9.95 ppm indicate the presence of an H-bonded network. While increasing oligomeric size due to a higher H-bonded network, it has been observed that the amide protons tend to shift towards the downfield region.[14] It was observed that, unlike $\mathbf{C_0P_1}$, the $\mathbf{C_2P_2}$ had shown partial hydrolysis due to a weak imine bond, thus producing aldehyde and ethylene diamine at 8.11 and 2.63 ppm, respectively. Since the IR spectrum did not feature N-CHO stretching at 1614 cm^{-1}, we infer that partial hydrolysis is because of the water content present in DMSO-d_6 solvent and rested for 24 h. Further, the minimal water content in $\mathbf{C_{10}P_3}$ did not result in considerable hydrolysis, though detectable hydrolyzed products were present (Figure 2.2c).

Size exclusion chromatography (SEC) was performed, and the results are provided in Table 2.0 to support the observation of different molecular weight ranges of the polymers as observed by NMR studies. Though $\mathbf{C_2P_2}$ and $\mathbf{C_{10}P_3}$ are soluble in many organic solvents (like MeOH, CH_3CN, THF, DMF, and DMSO, etc.), $\mathbf{C_0P_1}$ solubility is limited with DMF and DMSO probably due to high molecular weight nature. Hence, the SEC was accomplished using DMF as solvent at 50 °C for all polymers. The SEC

analysis revealed that the average molecular weight (M_w) of polymers **C_0P_1**, **C_2P_2**, and **$C_{10}P_3$** were 973.27, 9.61, and 3.74 kDa, respectively. Further, the **C_0P_1** polymer is 42 and 128-fold larger in size than **C_2P_2** and **$C_{10}P_3$**, respectively. The polydispersity index (PDI) values for **C_0P_1**, **C_2P_2**, and **$C_{10}P_3$** were found to be 2.72, 1.13, and 1.29, respectively, indicating the spacer polymers exhibit narrow molecular weights as compared to **C_0P_1**.

Table 2.0. Molecular weights (M_w) and polydispersity index (PDI) of polymers as determined by SEC analysis using DMF at 50 °C and calibrated with linear polystyrene standards.

Polymer	RT (min)[a]	M_n (Kg/mol)[b]	M_w (Kg/mol)[c]	M_w/M_n (PDI)
C_0P_1	09.72	357.9	973.27	2.72
C_2P_2	11.34	8.5	9.61	1.13
$C_{10}P_3$	11.41	2.8	3.74	1.29

[a]RT = retention time, [b]M_n = number average molecular weight (Da), [c]M_w = weight average molecular weight (kDa).

2.1.2. Antibacterial Activity. The antimicrobial activity study was performed against Gram-negative and Gram-positive strains such as Escherichia coli (*E. coli*) and Staphylococcus aureus (*S. aureus*), respectively. The experimental details are described in material and methods (Section 2.2.4., materials and methods).[15,16] The screening was done to estimate drug activity changes to unravel the role of spacer (non-drug unit) upon introducing different spacers in drug-polymers. First, a solution-based minimum inhibitory concentration (MIC_{90}) determination study was performed *via* the turbidity assay method (Table 2.1). Different doses of treatment were used from the stock solutions obtained from 0.1 to 10 μg/mL of all compounds in DMSO. Since the ciprofloxacin monomer is responsible for the antibacterial activity, for a fair comparison, to maintain the number of drug units same for all polymers, the monomer unit in **C_0P_1** was normalized with the repeating unit in spacer polymers for **C_2P_2** and **$C_{10}P_3$** (Table 2.1). To do that, the normalization factor (*NF*) was introduced to calculate the molecular weight difference ratio in the repeating unit drug *vs* non-drug content. The NF values were calculated to be 1, 1.4, and 2.1 for polymers of **C_0P_1, C_2P_2,** and **$C_{10}P_3$**, respectively. The MIC values for **C_0P_1** PB exhibited 50% reduced activity than the ciprofloxacin **1** against both *E. coli* (**1**: 0.5 mg/mL, **C_0P_1**: 1 μg/mL) and *S. aureus* (**1**: 0.25 μg/mL, **C_0P_1**:

0.5 μg/mL). This reduction in activity could be attributed to the end-group modification of ciprofloxacin and the slow hydrolysis nature of **C_0P_1** with stronger tertiary amide bonds as interlinking functional groups. However, it was found that the 0% spacer polymer, *i.e.*, **C_0P_1**, showed ~1.8 times increased biocidal activity against *E. coli* whereas ~3.6 times against *S. aureus* as compared to the spacer polymers of **C_2P_2** and **$C_{10}P_3$**.

Table 2.1. Minimal inhibitory concentration (MIC in μg/mL) of compounds (**C_0P_1, C_2P_2, $C_{10}P_3$, 1, 2, and 3**) against panels of Gram-negative (*E. coli*) and Gram-positive (*S. aureus*) bacterial strains.

entry	Samples	Repeating unit molecular formula	Repeating unit/ monomer molecular weight (Daltons)	Normalization factor (*NF*)[a]	*E. coli*		*S. aureus*	
					MIC (μg/mL)	Normalized MIC[b] (μg/mL)	MIC (μg/mL)	Normalized MIC[b] (μg/mL)
1	**1**	$C_{17}H_{18}FN_3O_3$	331.4	1.0	0.5±0.182	0.5	0.25±0.034	0.25
2	**C_0P_{1s}**	$C_{17}H_{16}FN_3O_2$	313.3	1.0	1.0±0.00778	1.0	0.5±0.0212	0.5
3	**C_2P_2**	$C_{22}H_{26}FN_7O_2$	439.5	1.4	2.5±0.00354	1.8	2.5±0	1.8
4	**$C_{10}P_3$**	$C_{38}H_{58}FN_7O_2$	663.9	2.1	4.0±0.0523	1.9	3.5±0.0438	1.7
5	**2**	$C_{19}H_{20}FN_3O_4$	373.4	1.0	NA[c]	NA[c]	NA[c]	NA
6	**3**	$C_{18}H_{18}FN_3O_4$	359.4	1.0	2.0±0.1039	2.0	1.5±0.0678	1.5

[a] Normalization Factor (*NF*) = molecular weight of monomer unit of **C_2P_2** or **$C_{10}P_3$**/molecular weight of monomer of **C_0P_1**; [b]Normalized MIC = MIC/*NF*; [c] NA = No activity up to 10 μg/mL addition. Experiment was performed in triplicate.

While similar activity trends were observed for both *E. coli* and *S. aureus*, interestingly, in solution, both **C_2P_2** and **$C_{10}P_3$** have shown similar activity of 1.7-1.9 (MIC) for *S. aureus* and *E. Coli*. In contrast, **C_0P_1** has shown significantly increased 0.5 (MIC) activity for *S. aureus* over 1.0 (MIC) for *E. Coli*. This may be because **C_0P_1** contains 100% drug content, whereas the spacer polymers include additional alkyl chains, thus featuring a significantly higher hydrophobic character, which helps the spacer polymers penetrate the hydrophobic regions of bacterial cell wall mediated by

hydrophobic effect, thus facilitating membrane disruption. Similar hydrophobic effect observation has been reported, e.g., Yao and co-workers have observed that *S. aureus* has a higher hydrophobic surface than *E. coli* which helps in the degradation of the hydrophobic compound diethylphthalate.[17] The starting material monomer **2** having formyl and ester functional groups was tested as a positive control sample and found no activity. We inferred that upon hydrolysis of $\mathbf{C_0P_1}$, the polymer catalyzed either by acid or enzyme, and the hydrolyzed product would be the monomer **1**, which makes the $\mathbf{C_0P_1}$ regarded as a prodrug. Whereas for the spacer polymers, if both amide and imine hydrolysis occur, the end hydrolyzed product would be **3**, *i.e.*, *N*-formyl and carboxylic acid functionalized ciprofloxacin. For this purpose, compound **3** was synthesized by following the reported protocol for formylation norfloxacin,[9] which was adopted for **1** and characterized.[18] Upon testing the monomer **3**, found that it retained similar moderate activity against *E. coli* (2.0 μg/mL) and slightly better activity against *S. aureus* (1.5 μg/mL) compared to the spacer polymers $\mathbf{C_2P_2}$ and $\mathbf{C_{10}P_3}$, indicating the end functional group do have a role in biocidal activity as observed for monomer **2** (entry 6, Table 2.1). Overall, according to this study, the trend observed was $\mathbf{1>C_0P_1>3>C_2P_2=C_{10}P_3>>2}$. These results show that the increasing amount of non-drug spacer content in the polymeric biocides reduces the biocidal activity, at least in the present case.

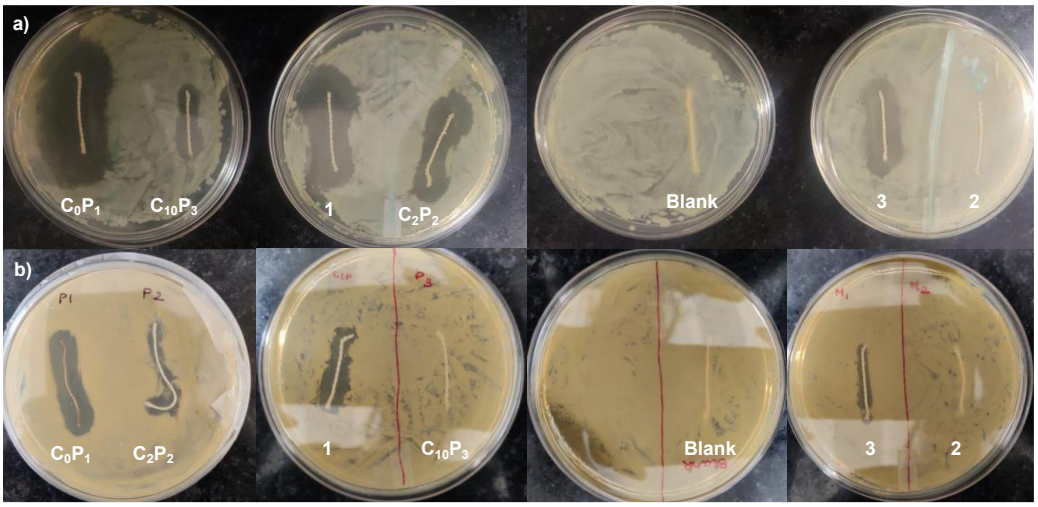

Figure 2.3. Antimicrobial activity of polymers and monomers coated nylon thread against a) *E. coli*. b) *S. aureus.*

After successfully demonstrating antibacterial activities in solution for polymers with varied spacers, we then tested its antibacterial effect on surgical devices since medical device-based infections majorly (60–70%) belong to hospital-acquired

infections.[19,20] Post-surgical incisions can attract bacteria, in particular, via suture materials that can lead to bacterial colonization. To test the efficacy of our polymerized biocides, we coated nylon thread-based sutures with solutions of polymers and monomers and used them as samples for disc diffusion assay.

Figures 2.3a and b show inhibition of *E. coli* and *S. aureus*, respectively, for the polymers and monomers-coated sutures placed in the agar plates. The antibacterial activity results of the coated sutures were obtained as the area of the zone of inhibition (ZOI, mm^2), and the corresponding data are summarized in Table 2.2. Interestingly, the results from the ZOI studies were different from the solution-based MIC determination trend. Figure 2.3a shows the *E. coli* growth inhibition profile on the coated sutures for polymers and monomers after incubation for 24 h, and their corresponding normalized ZOI values are 468.7 mm^2 (**C_0P_1**), 321.9 mm^2 (**C_2P_2**), and 216.1 mm^2 (**$C_{10}P_3$**) and monomers 300.2 mm^2 (**1**), 0 mm^2 (**2**), and 166.5 mm^2 (**3**). Similarly, Figure 2.3b shows the *S. aureus* growth inhibition profiles on the polymers and monomers after incubation for 24 h, and their corresponding normalized ZOI values are 185.2 mm^2 (**C_0P_1**), 113.7 mm^2 (**C_2P_2**), and 2.1 mm^2 (**$C_{10}P_3$**) and monomers 92.4 mm^2 (**1**), 0 mm^2 (**2**), and 42.3 mm^2 (**3**). It was found that the area of the ZOI for **C_0P_1** polymer having no spacer was the most significant, 469 and 185 mm^2 for *E. coli* and *S. aureus*, respectively, whereas for **$C_{10}P_3$** (216.1 and 2.1 mm^2 for *E. coli* and *S. aureus*, respectively) was the lowest for both types of bacteria. At the same time, **2** did not show any significant activity even when twice the amount was added than other compounds. The trend for ZOI determination for *E. coli* and *S. aureus* was observed as **C_0P_1**>**C_2P_2**>**1**>**3**>**$C_{10}P_3$**>**2**. Notably, a couple of interesting facts were observed from this study, i) **C_0P_1** exhibited remarkable activity over both bacteria compared to all PBs as well as the monomers including ciprofloxacin itself, ii) Spacer polymer **$C_{10}P_3$** exhibited significant activity for *E. coli*, but almost no activity was observed for *S. aureus*, iii) There is a clear and distinct activity trend was observed among the polymers, *i.e.*, increasing the spacer content led to reduction of inhibiting activity. These observations support the hypothesis that drug polymers without the spacer can greatly alter the drug's activity. More importantly, in this case, it is possible to obtain better antibacterial activity than the parent ciprofloxacin itself. Thus, this study may open up a new window in drug polymers and may provide

the opportunity to discover a new generation of antibiotics that the world is currently looking for, especially in this pandemic time.

Table 2.2. Zone of inhibition (ZOI in area mm^2) of compounds (**C_0P_1, C_2P_2, $C_{10}P_3$, 1, 2, and 3**) against panels of gram-negative (*E. coli*) and gram-positive (*S. aureus*) bacterial strains.[a]

S.No.	Samples	Spacer content (%)	Normalization factor (*NF*)[b]	*E. coli*		*S.aureus*	
				ZOI (mm^2)	Normalized[c] ZOI (mm^2)	ZOI (mm^2)	Normalized[c] ZOI (mm^2)
1	**C_0P_1**	0	1.0	468.7 ±10.2	468.7	185.2 ±19.2	185.2
2	**C_2P_2**	29	1.4	229.9 ±14.6	321.9	81.2 ±9.2	113.7
3	**$C_{10}P_3$**	53	2.1	102.9 ±16.3	216.1	0	<2.1[d]
4	**1**	-	1.0	300.2 ±18.2	300.2	92.4± 9.7	92.4
5	**2**	-	1.0	0	0	0	0
6	**3**	-	1.0	166.5 ±19.5	166.5	42.3± 4.2	42.3

[a]All samples were coated (4 mg/mL); [b]Normalization Factor (*NF*) = molecular weight of monomer of **C_2P_2** or **$C_{10}P_3$**/molecular weight of monomer of **C_0P_1**; [c]Normalized ZOI = ZOI×NF; [d]If activity considered to be 1.

2.1.3. FE-SEM analysis

An investigation of the coating nature was performed using scanning electron microscopy (SEM) for sutures that had been coated with ciprofloxacin and polymers (Figure 2.4). SEM images of **1** and **C_2P_2** show smooth individual nylon fibers indicating either an insubstantial coating layer or imperfect coating nature.

In contrast, a thick coating layer was observed on the **C_0P_1** and **$C_{10}P_3$**, wherein individual nylon fibers were not visible. However, **C_0P_1** polymer with no spacer showed a smooth and continuous surface, while **$C_{10}P_3$** polymer displayed a porous and rough texture. Further, breakage in the coating was also observed between the inter twinning of yarn in spacer polymer **$C_{10}P_3$** (Figure 2.4d inset). The SEM study suggests that the polymer **C_0P_1**

has better coating efficiency and a uniform coating on the nylon sutures, indicating that **C_0P_1** is more favorable than spacer polymers **C_2P_2** and **$C_{10}P_3$** as well as ciprofloxacin itself. A more uniform coating of **C_0P_1** on nylon thread is possibly due to its highly viscous nature owing to its larger molecular weight (973.27 kDa). Thus, it appears promising for further coating applications in medical devices.

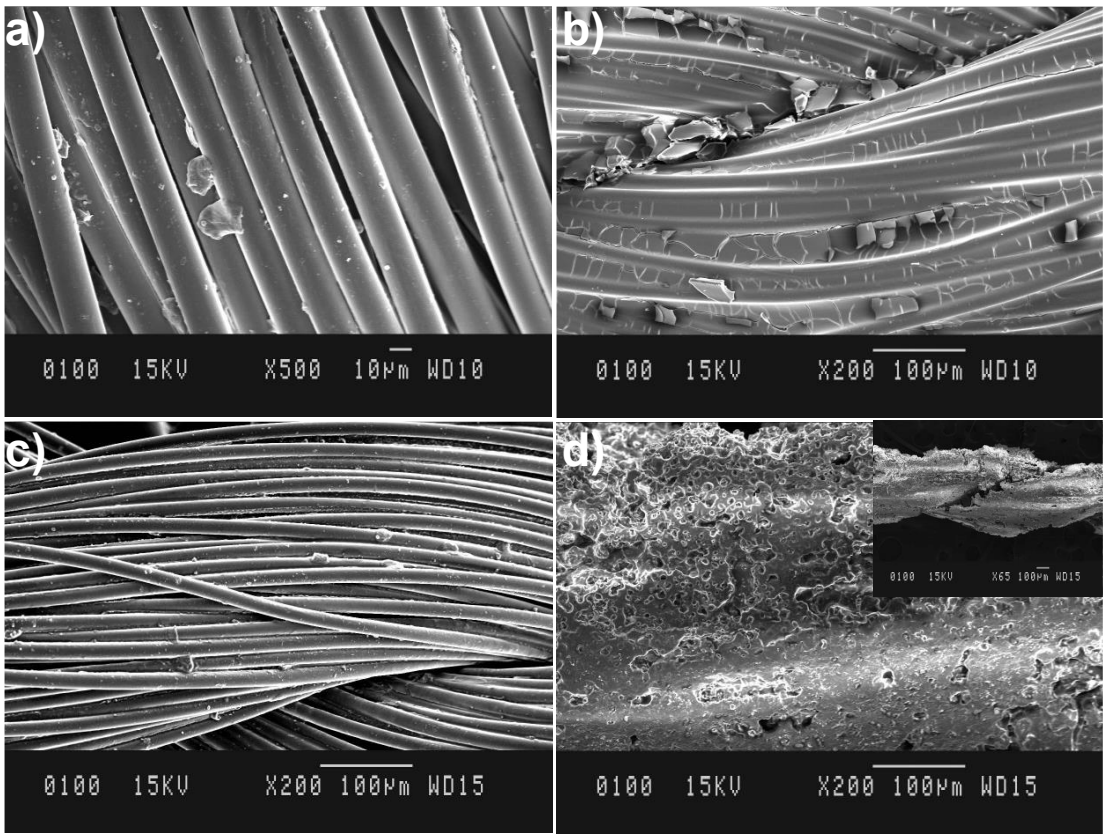

Figure 2.4. SEM images of nylon sutures coated with a) ciprofloxacin **1**, b) **C_0P_1**, c) **C_2P_2**, and d) **$C_{10}P_3$** (inset: zoom scale of X65 showing inter twinning of yarn).

2.1.4. Hydrolysis study of Polymers. The hydrolysis study for PBs such as **C_0P_1**, **C_2P_2**, and **$C_{10}P_3$** was performed by using the HPLC–LCMS technique employing CH_3CN/H_2O 1:1 with a flow rate of 1 mL per minute (min) associated with other parameters such as column temperature (25 °C), sample temperature (37 °C), injection volume (20 µL) and monitored with photodiode array (PDA) detector (for details see Section 2.2.5., materials and methods). Since **C_0P_1** non-spacer polymer does not hydrolyze at neutral pH significantly due to stronger tertiary amide bonds, the release of the drug has been observed by altering the pH into acidic (pH = 3) using 1% (*v/v*) formic acid (FA) addition into all polymer solutions (100 µg/mL for **C_0P_1**, 1 mg/mL for **C_2P_2** and **$C_{10}P_3$**) and the release profiles of all polymers are shown in Figure 2.5.

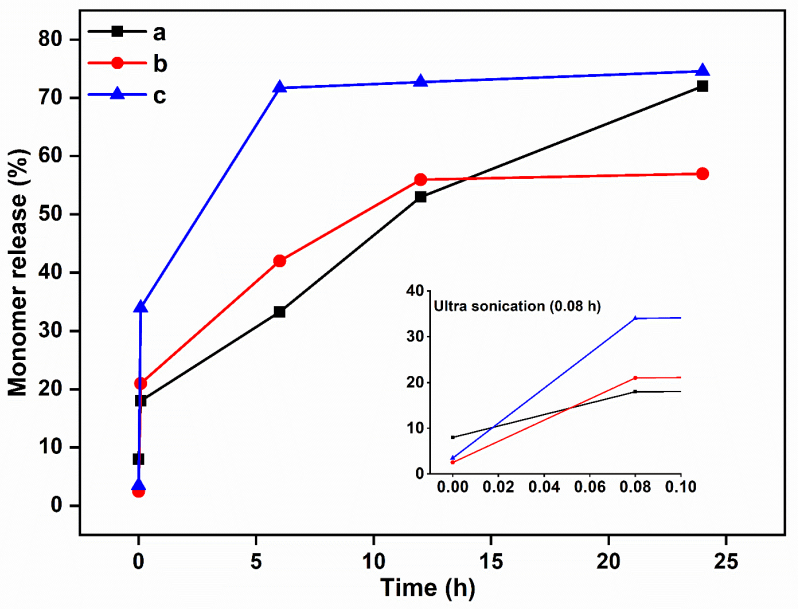

Figure 2.5. Acid-catalyzed hydrolysis of a) $\mathbf{C_0P_1}$, b) $\mathbf{C_2P_2}$, and c) $\mathbf{C_{10}P_3}$ to release the percentage of drug ciprofloxacin **1** and **3**, respectively, *via* under the condition of acidic buffer solution of formic acid (FA) (0.024 M, pH 3), at 37 °C with sampling intervals 0.08, 6,12, and 24 h. Note: the inset shows the initial 0–0.08 h was under sonication and the rest of the time with stirring only.

The HPLC profiles (Figures 2.30–2.37, Section 2.2.5) indicated the release of ciprofloxacin (RT = 3.70 min) and monomer **3** (RT = 5.93 min) from $\mathbf{C_0P_1}$ and spacer polymers ($\mathbf{C_2P_2}$ and $\mathbf{C_{10}P_3}$), respectively, has been observed over time. However, the same rate of release has not been observed with $\mathbf{C_2P_2}$, and the appearance of some new peaks has been observed, which indicates that some degradation or fragmentation occurred due to fast hydrolyzing imine bonds (Figures 2.32, 2.34, Section 2.2.5).

The spacer polymers $\mathbf{C_2P_2}$ and $\mathbf{C_{10}P_3}$ were studied by ^{1}H NMR to further quantify the hydrolysis reaction (Figures 2.38, Section 2.2.5.3). The ^{1}H NMR data of $\mathbf{C_2P_2}$ and $\mathbf{C_{10}P_3}$ indicated a sharp decrease of the amide peaks at 9.90 – 10.05 ppm, i.e., up to 96 and 98%, respectively within 24 h, though 95% of acid-catalyzed hydrolysis occurred within 2 h. Whereas, only partial imine hydrolysis was observed, as indicated by the appearance of aldehyde proton at 8.35 ppm, which showed 10 and 8% for imine hydrolysis after 24 h for $\mathbf{C_2P_2}$ and $\mathbf{C_{10}P_3}$, respectively. We infer that the hydrolyzed amine is in equilibrium with imine due to the presence of acid.

According to our hypothesis, since homo-polymerization of **1** by a condensation reaction to synthesize $\mathbf{C_0P_1}$ does not involve functional group modification on ciprofloxacin, the released monomer would act similar to the established mechanism of ciprofloxacin. The hydrolysis study results do suggest that monomer ciprofloxacin is

being released from the polymer **C_0P_1**. The mechanism of biocidal activity of ciprofloxacin is well-studied, and it is believed to inhibit DNA replication by promoting cleavage of bacterial DNA in the DNA–enzyme complex such as DNA–gyrase and DNA–type IV topoisomerase.[21] This further corroborates the lower activity observed in the solution study for **C_0P_1** compared to **1,** presumably due to slow-release behavior/sustained drug release, *i.e.*, even at pH = 3, only 69% release was achieved after 24 h (Figure 2.5).

2.1.5. Biocompatibility Assay. Ciprofloxacin is not toxic to eukaryotic cells at low concentrations.[22] However, to rule out the possibility of cytotoxicity of the synthesized biocides, a biocompatibility (MTT) assay was carried out using a mouse fibroblast cell line (L929). The antiproliferative effects were assessed employing the EZcount™ MTT cell Assay Kit by treating monomers (**1**, **2**, and **3**) and polymers (**C_0P_1**, **C_2P_2**, and **$C_{10}P_3$**). The assay was performed in triplicate with various test compounds (1µg/mL). Figure 2.6 displays the cell viability (%) after 48 h exposure to the newly synthesized polymers of ciprofloxacin derivatives. The data revealed that the polymers were more biocompatible than their monomers. It was further found that spacer polymers showed significantly higher biocompatibility than **C_0P_1**, presumably due to the weaker hydrolyzable imine and primary amide bonds than relatively stronger tertiary amide bonds in **C_0P_1**.

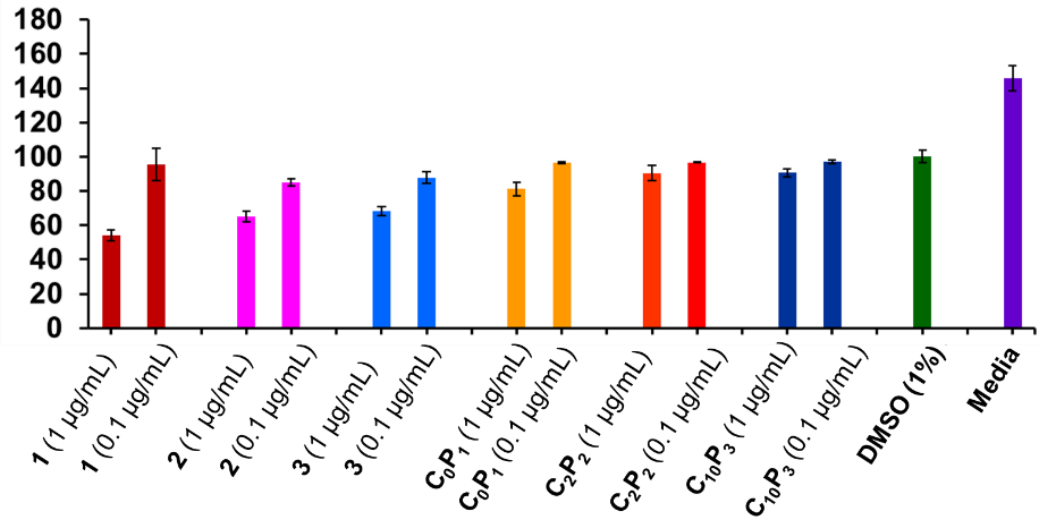

Figure 2.6. Biocompatibility study (MTT assay) of monomers (**1**, **2**, and **3**) and polymers (**C_0P_1**, **C_2P_2**, and **$C_{10}P_3$**) on mouse fibroblast cell lines (L929). Experiment has been performed in triplicate $P<0.05$.

2.2. Materials and methods

2.2.1. General information: Ciprofloxacin **1**, 1,10-diaminodecane, formamide ($CHONH_2$) were purchased from Tokyo Chemical Industry India Pvt. Ltd. Thionyl chloride ($SOCl_2$), ethylenediamine and other chemicals were purchased from Sisco Research Laboratory Pvt. Ltd., India. Formic acid (FA) and phosphate-buffered saline (PBS) were purchased from Sigma-Aldrich. Ethanol (EtOH) and isopropanol (*i*PrOH) were purchased from Renchem India Ltd. Luria Bertani (LB) agar and broth were purchased from HiMedia Laboratories Pvt Ltd. Methylene chloride (CH_2Cl_2) was freshly distilled from CaH_2 under nitrogen atmosphere. DMSO and DMF were further purified by CaH_2 and vacuum distilled for the reaction. Methanol (CH_3OH) was dried by refluxing on magnesium tunings and iodine under an inert atmosphere. Nylon suture thread was purchased from SRL Ltd. 96-well plates (sterile) were purchased from Tarson Ltd. All reagents were used as received without further purification unless otherwise mentioned. Monomers **2** and **3** were synthesized according to a literature procedure.[1] The HPLC grade solvents DMSO, DMF, acetonitrile, and water were procured from Spectrochem and Merck to perform HPLC analysis. Column chromatography (CC) was carried out with either neutral alumina (Al_2O_3) (mesh size 100–300) or silica gel (SiO_2) (mesh size 60–120). Thin-layer chromatography (TLC) was performed on precoated aluminum sheets of silica gel G/UV-254 of 0.2 mm thickness (Macherey Nagel, Germany) or < 60 mm Aldrich neutral Al_2O_3 using appropriate solvent and observed under UV light (λ = 254 nm). *E. coli* (ATCC 25922) and *S. aureus* (ATCC 23235) were cultured overnight at 37 °C in an LB broth before use. All the microbial cultures were procured from Microbial Type Culture Collection and Gene Bank (MTCC), Chandigarh, India.

2.2.2. General experimental details

Melting points (m.p.) were measured in open capillaries with a Stuart (automatic melting point SMP50) apparatus and are uncorrected.

^1H and ^{13}C nuclear magnetic resonance (NMR) spectra were measured on Bruker Avance-II 500 MHz or Bruker Avance Neo 400 MHz spectrometer instruments using DMSO-d_6 or $CDCl_3$ as solvent. Chemical shifts are reported in parts per million (ppm) relative to tetramethylsilane (TMS) as the internal standard. All NMR was done with

fluorine coupling. Coupling constants (*J*) are given in Hz. Data for ^{1}H NMR and ^{13}C NMR are reported as follows: s = singlet, d = doublet, t = triplet, dd = doublet of doublets, m = multiplet, br. = broad.

Transmission spectra were measured using Attenuated total reflection Fourier transform infrared (ATR-FT-IR) Bruker Vertex 70 in a range of 4000–400 cm^{-1}. Signal designations: s (strong), m (medium), and w (weak). Selected absorption bands are reported in wavenumbers (cm^{-1}).

Liquid chromatography and mass spectrometry (LC-MS) was performed using Waters 2489 equipped with Waters 1525 binary HPLC pump, Agilent Eclipse plus 18 (C_{18}) column, (4.6 mm × 25 cm) particle size 5 µm, PDA detector 2998 at 190 nm and range 210-400 nm) was utilized to analyze hydrolysis products from polymers. The injection volume of the sample was 15 µL and the column was thermostated at 30 °C. The isocratic mobile phase CH_3CN/H_2O (1:1 *v/v*) was run at a flow rate of 0.7 mL min^{-1}.

Size exclusion chromatography SEC was performed on a Malvern Viscotek instrument having a refractive index (RI) and right-angle light scattering (RALS) detectors coupled with a D4000 column using 0.05M LiBr in DMF as eluent at 50 °C with a flow rate of 0.7 mL/min. The injection volume was kept as 100 µL of polymer samples having a concentration of 4 mg/mL. The results were analyzed by using Omnisec software. The polymer's peaks were analyzed for absolute M_n, M_w, and PDI values employing the multi-detector calibration method using the PMMA 60k Daltons narrow standard and verified by the PMMA 95k Daltons broad standard.

Scanning electron microscopy (SEM) analysis was performed on model JSM6100 (Jeol) with an image analyzer. The dried coated thread was mounted on stubs with the help of double-stick tape and sputtered with a film of gold.

Differential scanning calorimetry (DSC) analysis: Thermal scanning of polymers was performed on Perkin Elmer Differential Scanning Calorimeter DSC 8000 model and the samples were heated from –4 to 500 °C at an N_2 flow rate of 10 mL/min and a heating rate of 10 °C/min.

Statistics: The biological data presented are mean ± standard deviation. Student's t test and ANOVA were performed for all the data. *P* indicated level of significance.

2.2.3. Synthetic procedures and characterization of the monomers and polymers

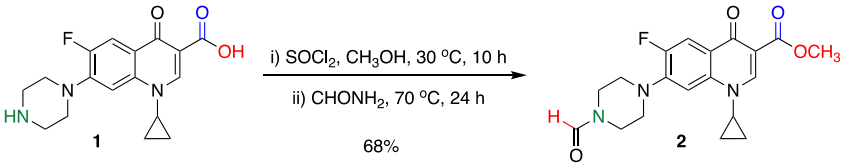

Scheme 2.1. Synthesis of monomer **2.**

***2.2.3.1. Monomer 2*:** A solution of **1** (500 mg, 1.51 mmol) in dry CH_3OH (10 mL) was treated with freshly distilled $SOCl_2$ (1 mL) and stirred at ice bath condition for 5 minutes (min). Then the reaction was brought to room temperature and stirred further for 15 h. Excess $SOCl_2$ was removed by vacuum distillation. The addition of water was followed by subsequent extraction with $CHCl_3$ (3 × 100 mL) and washing of the organic layer with bicarbonate (2% w/v K_2CO_3, 100 mL) solution. The solution was treated with anhydrous Na_2SO_4, and evaporation of $CHCl_3$ afforded solid product which was further treated with formamide in a sealed tube and stirred at 70 °C for 24 h. The residue was diluted with $CHCl_3$ (100 mL) and washed with water (3 × 100 mL). The $CHCl_3$ layer was dried (anhydrous Na_2SO_4) and evaporated at 25 °C. The crude mixture was purified by CC (SiO_2; $CHCl_3$/MeOH
95:5) gave **2**[9] (376 mg, 67 %) as a yellowish-white solid. R_f = 0.7 (SiO_2; $CHCl_3$/MeOH 95:5); m.p. 237 °C.

Characterization data of 2: ^{1}H NMR (400 MHz, $CDCl_3$) δ = 1.11–1.17 (m, 2H), 1.29–1.36 (m, 2H), 3.22 (t, J = 5.1 Hz, 2H), 3.27 (t, J = 5.0 Hz, 2H), 3.39–3.46 (m, 1H), 3.61 (t, J = 5.2 Hz, 2H), 3.79 (t, J = 5.5 Hz, 2H), 3.90 (s, 3H), 7.28 (s, 1H), 8.05 (d, $J_{H\text{-}F}$ = 12.9 Hz, 1H), 8.12 (s, 1H), 8.54 ppm (s, 1H). ^{13}C NMR (101 MHz, $CDCl_3$) δ = 8.3, 34.7, 45.6, 49.6 (d, J_{CF} = 3.2 Hz), 51.2 (d, J_{CF} = 4.9 Hz), 52.3, 77.4, 105.5 (d, J_{CF} = 2.6 Hz), 110.4, 113.8 (d, J_{CF} = 22.9 Hz), 123.9 (d, J_{CF} = 7.1 Hz), 138.1, 144.2 (d, J_{CF} = 10.8 Hz), 148.7, 152.3, 154.8, 161.0, 166.4, 173.1 ppm (d, J_{CF} = 2.9 Hz); LC-MS (*m/z*): calcd for $C_{19}H_{21}FN_3O_4^+$: $[M+H]^+$, 374.15; found, 374.41.

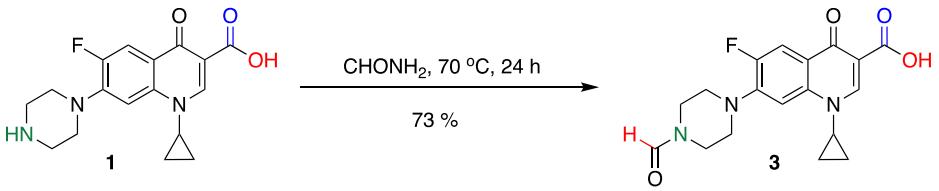

Scheme 2.2. Synthesis of monomer **3.**

***2.2.3.2. Monomer 3*:** Formamide (10 mL) was added to **1** (500 mg, 1.51 mmol) in a sealed tube and stirred at 80 °C for 24 h. Then the reaction was brought to room temperature, and the residue was diluted with $CHCl_3$ and washed with water (3 × 100 mL) and brine solution. The $CHCl_3$ layer was dried (anhydrous Na_2SO_4) and evaporated at 25 °C to afford **3**[23] (396 mg, 73 %) as a yellowish-white solid. R_f = 0.4 (SiO_2; CH_2Cl_2/MeOH 95:5); m.p. 263 °C. ^{1}H

Characterization data of 3: NMR (400 MHz, $CDCl_3$) δ = 1.18–1.24 (m, 2H), 1.37–1.44 (m, 2H), 3.29 (t, J = 5.2 Hz, 2H), 3.37 (t, J = 5.0 Hz, 2H), 3.50–3.59 (m, 1H), 3.64 (t, J = 5.0 Hz, 2H), 3.82 (t, J = 5.1 Hz, 2H), 7.39 (d, J = 7.1 Hz 1H), 8.06 (d, $^3J_{H\text{-}F}$ = 12.6 Hz, 1H), 8.14 (s, 1H), 8.77 (s, 1H), 14.85 ppm (s, 1H); ^{13}C NMR (101 MHz, $CDCl_3$) δ = 8.4, 35.5, 45.5, 49.4 (d, J_{CF} = 3.7 Hz), 51.0 (d, J_{CF} = 5.3 Hz), 77.4, 105.6 (d, $^4J_{CF}$ = 2.6 Hz), 108.5, 112.8 113.1, 120.9 (d, J_{CF} = 7.8 Hz), 139.1, 145.5, 145.6, 147.8, 160.9, 167.0, 177.3 ppm (d, $^4J_{CF}$ = 2.9 Hz); LC-MS (*m/z*): calcd for $C_{18}H_{19}FN_3O_4^+$: $[M+H]^+$, 360.13; found, 360.35; LC-MS (*m/z*): calcd for $C_{18}H_{19}FN_3O_4^+$: $[M+H]^+$, 360.36; found, 360.13.

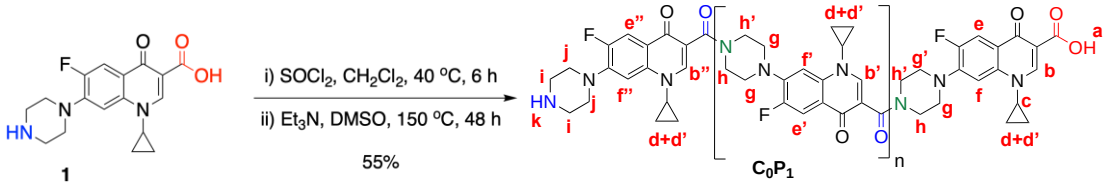

Scheme 2.3. Synthesis of $\mathbf{C_0P_1}$ Polymer.

***2.2.3.3. C_0P_1*:** Synthesis of $\mathbf{C_0P_1}$ polymer was carried out in 2 steps. The intermediate (acid chloride of ciprofloxacin) was synthesized by adding $SOCl_2$ (3 equiv) to a suspension of ciprofloxacin (500 mg, 1.509 mmol) in dry CH_2Cl_2/DMF 10:1 (10 mL) and stirred at ice bath condition for 5 min. Then the reaction was brought to 40 °C and stirred further for 6 h. Evaporation of solvent and $SOCl_2$ was carried out by vacuum distillation. The reaction mixture was transferred to a sealed tube using dry DMSO (10 mL) under an inert atmosphere followed by the addition of triethylamine (Et_3N) (2 equiv.) and stirred at 150 °C for 48 h. The addition of CH_2Cl_2 (150 mL) resulted in the precipitation of a brown solid which was collected and washed with isopropanol/water 1:1 (50 mL) and isopropanol (50 mL), dried under vacuum at 45 °C to give $\mathbf{C_0P_1}$ (271 mg, 55 %) as a light brown colored floppy solid. m.p. 382–390 °C. IR (ATR) $\tilde{\nu}$ = 3396 (w), 3078 (m), 2923 (m), 2862 (w), 1710 (s), 1616 (s), 1452 (s), 1323 (m), 1232 (m), 1254 (m), 1022 (m), 729 cm^{-1} (m).

Characterization data of C_0P_1 Polymer: ^{1}H NMR (500 MHz, DMSO-d_6) δ = 1.09–1.41 (m, 5H; d,d',k), 2.93 (br., 4H; i), 3.22–3.50 (br.m, 8H; g,g',j), 3.57–3.90 (br.m, 5H; c,h',h), 7.56 (br.s, 1H; f'), 7.65 (br. S, 1H; f), 7.91 (br.d, J_{CF} = 11.5 Hz, 1H; e',e"), 7.98 (br.d, J_{CF} = 13.3 Hz; 1H; e), 8.66 (s, 1H; b',b"), 8.70 (s, 1H; b), 15.18 (bs, 1H; a);^{13}C NMR (101 MHz, DMSO-d_6) δ= 8.0, 25.7, 36.4, 42.5, 43.4, 45.0, 47.4, 51.1, 53.0, 60.7, 107.06, 107.14, 107.3, 111.3, 111.5, 111.7, 119.6, 119.7, 13.5, 145.4, 145.5, 161.8, 166.7, 176.8 ppm; HPLC RT = 2.816 min in CH_3CN/H_2O 2:8 with flow rate of 1 mL/min. SEC analysis (DMF, PMMA triple detection standard): M_n = 357.95 KDa; M_w =973.27 KDa; M_w/M_n = 2.71, RT = 9.67 min.

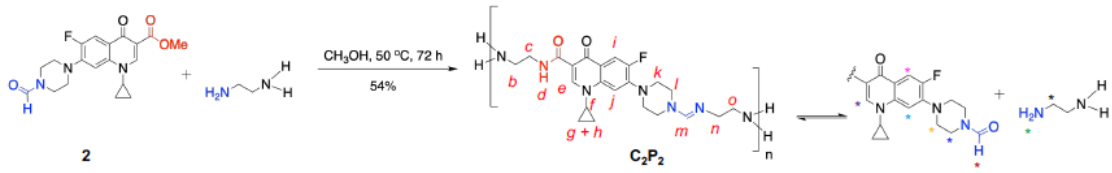

Scheme 2.4. Synthesis of C_2P_2 Polymer.

2.2.3.4. C_2P_2: A solution of **2** (200 mg, 0.535 mmol) in dry CH_3OH (10 mL) was treated with ethylenediamine (120 mg, 1.07 mmol) under N_2 and stirred at 50 °C for 72 h. The CH_3OH was evaporated at 25 °C. The crude mixture was purified by CC (Al_2O_3; CH_2Cl_2/CH_3OH 9:1) and gave **C_2P_2** (108 mg, 54 %) as CC as a light-yellow sticky solid. R_f = 0.1 (Al_2O_3; CH_2Cl_2/CH_3OH 9:1); IR ($\tilde{\nu}$) 3249 (m), 3052 (w), 2923 (m), 2846 (m), 1651 (s), 1529 (m), 1470 (m), 1384 (m), 1246 (m);

Characterization data of C_2P_2 Polymer : ^{1}H NMR (400 MHz, DMSO–d_6) δ = 1.05–1.12 (m, 2H) & 1.25–1.33 (m, 2H) [g & h], 2.55–2.61 (m, 2H; o), 2.63 (s, 4H; *), 2.66–2.73 (m, 2H; b), 2.86–2.90 (4H; k), 3.02–3.12 (m, 2H; n), 3.13–3.19 (4H; l), 3.20–3.25 (m; 2H, *), 3.27–3.31 (2H; c), 3.56–3.64 (1H; m, 4H; *), 3.68–3.76 (1H; f), 7.45 (d, J = 7.4 Hz, 1H; j), 7.51 (d, J = 7.4 Hz, 1H; *), 7.81 (d, J = 13.6 Hz, 1H; i), 7.86 (d, J = 13.2 Hz, 1H; *), 8.0 (s, 1H; m), 8.06 (br s, 1H; *), 8.11 (s, 1H; *), 8.60 (s, 1H, e), 8.62 (s, 1H; *), 9.90–9.99 ppm (m, 1H; d); ^{13}C NMR (101 MHz, DMSO–d_6) δ = 7.96, 35.40, 35.47, 40.9, 41.47, 41.74, 41.92, 42.58, 43.12, 45.89, 46.38, 49.72, 51.33, 106.26, 107.18, 110.66, 110.76, 111.45, 111.68, 138.79, 138.91, 144.37, 145.24, 145.34, 147.03, 147.19, 152.27, 154.41, 161.63, 164.49, 164.56, 165.2, 174.7 ppm; HPLC RT = 3.5 min in CH_3CN/H_2O 1:1 with flow rate of 1 mL/min. SEC analysis (DMF, PMMA triple detection standard): M_n = 8.5 KDa; M_w = 9.6 KDa; M_w/M_n = 1.13, RT= 11.339 min

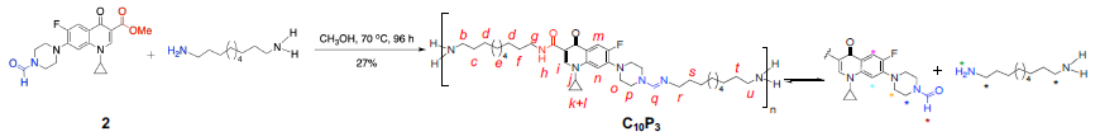

Scheme 2.5. Synthesis of $\mathbf{C_{10}P_3}$.

2.2.3.5. $C_{10}P_3$: A solution of **2** (200 mg, 0.535 mmol) in dry CH_3OH (10 mL) was treated with decane-1,10-diamine (277 mg, 1.61 mmol) under N_2 and stirred at 70 °C for 96 h. The CH_3OH was evaporated at 25 °C. The crude mixture was purified by CC (Al_2O_3; CH_2Cl_2/CH_3OH 9:1) and gave $\mathbf{C_{10}P_3}$ (54 mg, 27 %) as CC as a light-yellow sticky solid. R_f = 0.05 (Al_2O_3; CH_2Cl_2/CH_3OH 9:1).

Characterization data of $\mathbf{C_{10}P_3}$ Polymer: IR ($\tilde{\nu}$) 3284 (m), 2923 (s), 2846 (s), 1667 (s), 1478 (w), 1258(w), 1032(s), 747 cm^{-1} (w). ^{1}H NMR (400 MHz, DMSO–d_6) δ = 1.05–1.12 (m, 2H) & 1.19–1.25 (m, 2H) [k & l], 1.20–1.27 (m, 4H; t, c), 1.28–1.35 (m, 8H; d), 1.36–1.43 (m, 2H; s) 1.45–1.54 (m, 2H; f), 2.47–2.54 (quint), 2.59 (br.s, 8H; u,b,*), 2.88–2.93 (m, 4H; o), 3.03–3.10 (m, 2H; r), 3.15–3.19 (m, 4H; p), 3.23–3.26 (m, 2H; *), 3.26–3.32 (m, 2H; g), 3.59–3.64 (m, 4H; *), 3.68–3.74 (m, 1H; j), 7.43 (d, J = 7.5 Hz, 1H; n), 7.50 (d, J = 7.4 Hz, 1H; *), 7.79 (d, J = 13.6 Hz, 1H; m), 7.84 (d, J = 13.3 Hz, 1H; *), 7.99 (s, 1H; q), 8.10 (br.s, 2H; *), 8.35 (s, 1H; *), 8.60 (s, 1H; i), 9.85–9.94 (m, 1H; h);^{13}C NMR (101 MHz, DMSO–d_6) δ = 7.54, 25.96, 26.45, 26.55, 26.62, 28.74, 28.80, 28.85, 29.07, 29.10, 29.13, 29.19, 29.34, 30.98, 33.35, 34.91, 37.11, 38.35, 40.90, 41.69, 45.49, 48.52, 50.86, 50.89, 79.29, 105.57, 105.59, 110.22, 111.06, 111.24, 120.51, 120.57, 138.42, 144.82, 144.90, 146.39, 151.70, 151.76, 153.67, 153.73, 160.89, 163.90, 164.43, 174.34, 174.36 ppm; HPLC RT = 2.487-2.850 (3 peaks) in CH_3CN/H_2O 1:1 with flow rate of 1 mL/min. SEC analysis (DMF, PMMA triple detection standard): M_n = 2.829 KDa; M_w =3.745 KDa; M_w/M_n = 1.29, RT = 11.41 min.

2.2.3.1. *^{1}H- and ^{13}C-NMR spectral profiles of monomers and polymers*

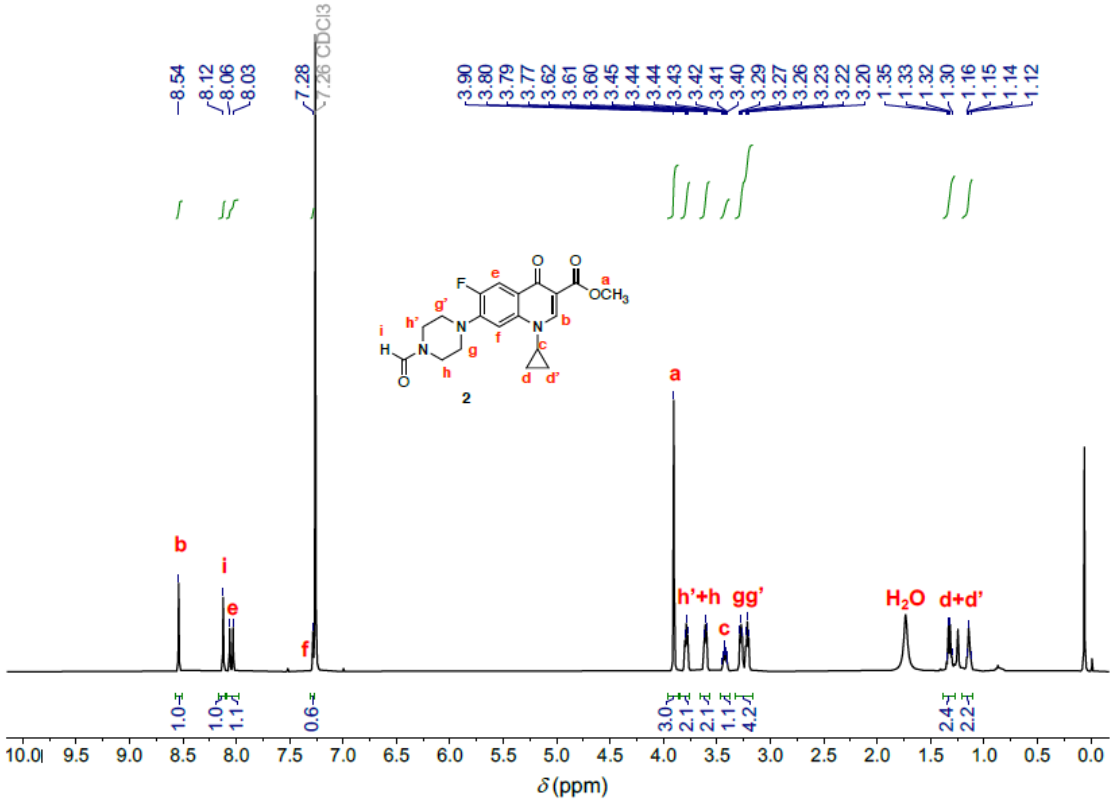

Figure 2.7. 400 MHz ^{1}H NMR spectrum of **2** in $CDCl_3$ at 298 K.

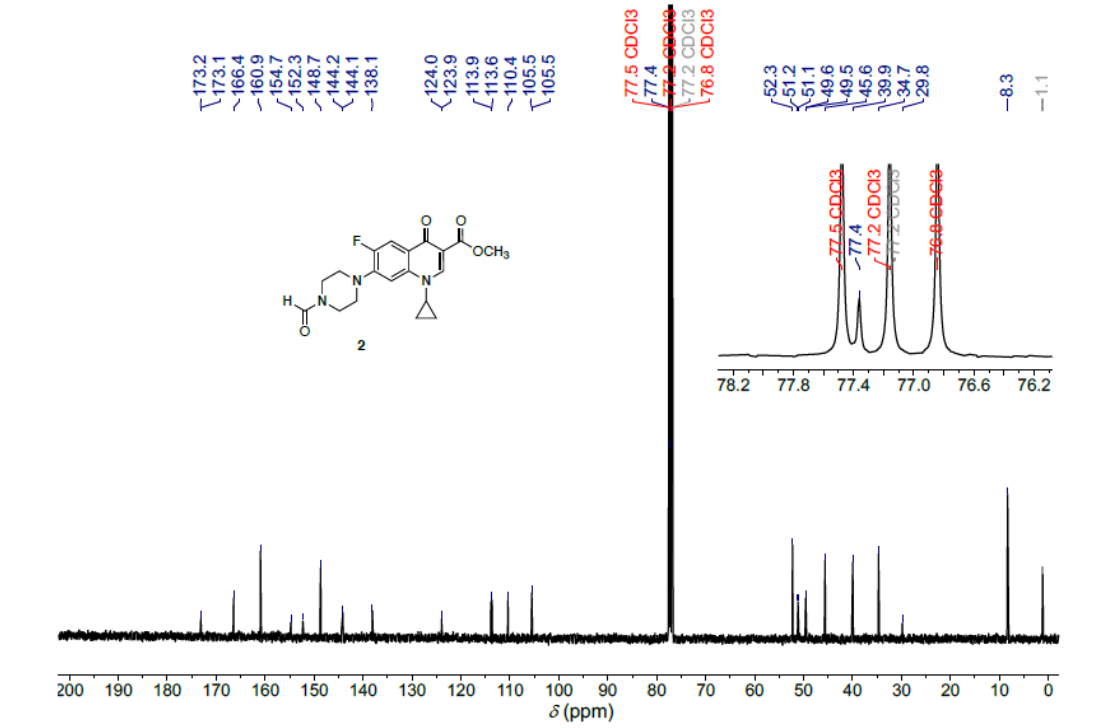

Figure 2.8. 101 MHz ^{13}C NMR spectrum of **2** in $CDCl_3$ at 298 K.

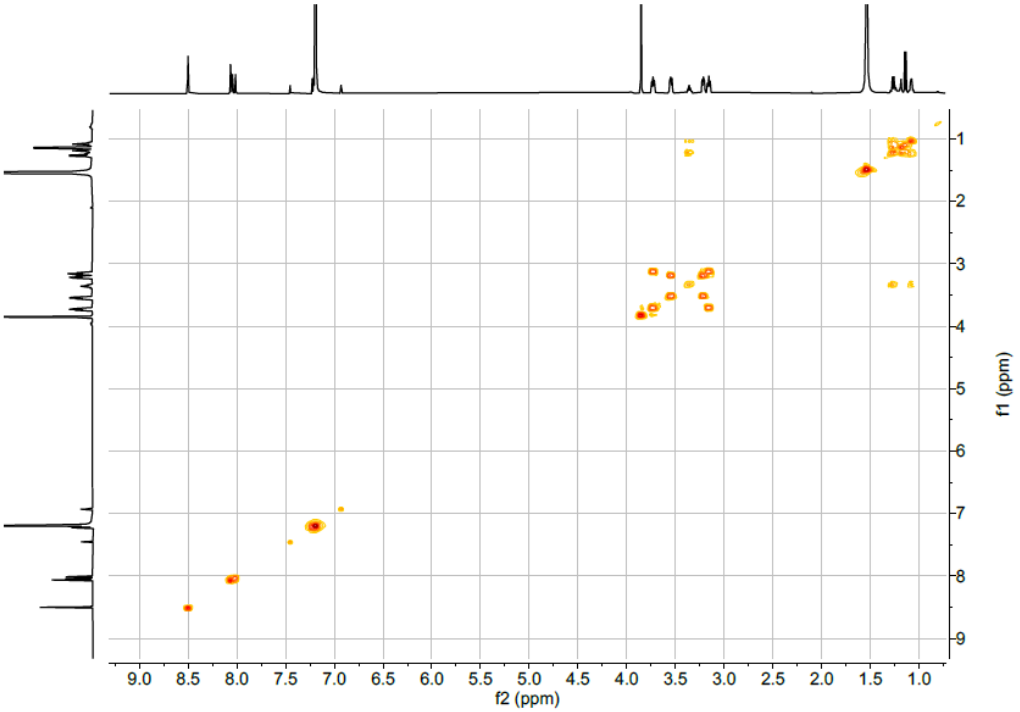

Figure 2.9. 400 MHz ^{1}H-COSY NMR spectrum of **2** in $CDCl_3$ at 298 K.

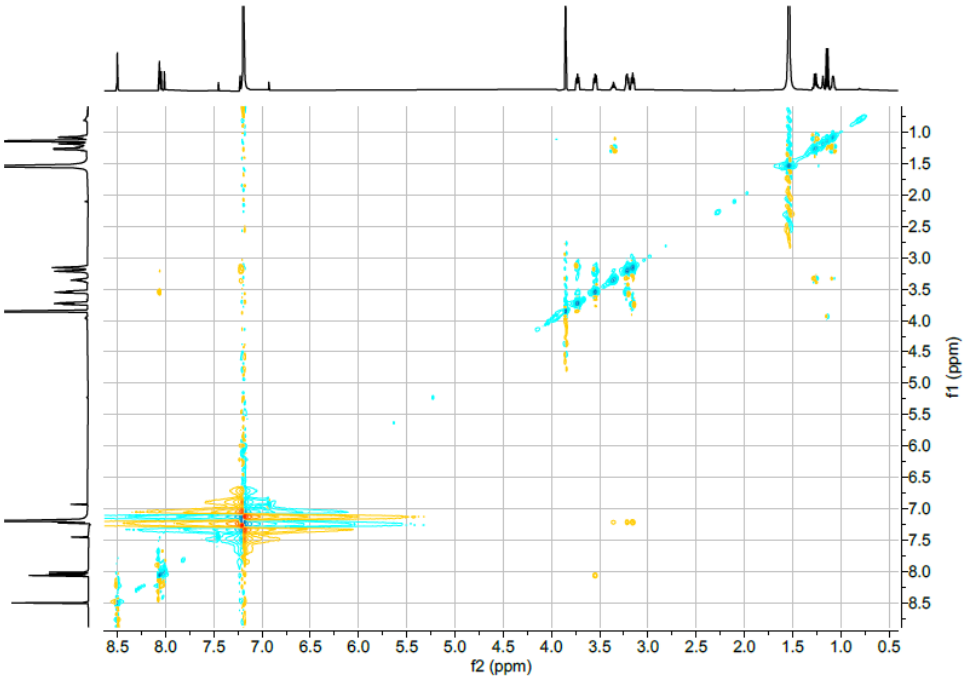

Figure 2.10. 400 MHz ^{1}H-ROESY NMR spectrum of **2** in $CDCl_3$ at 298 K.

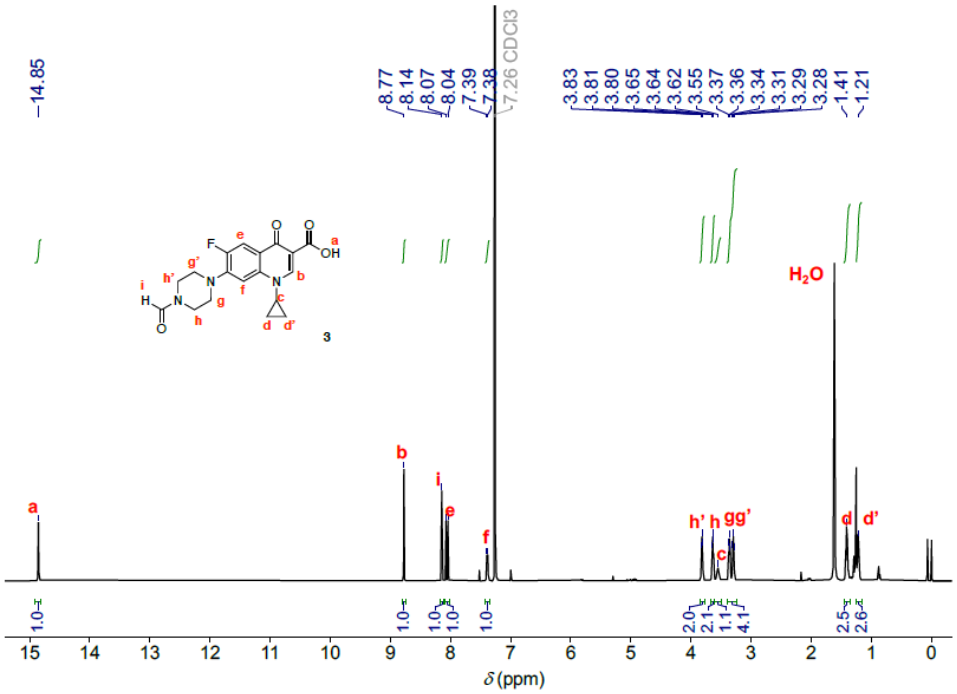

Figure 2.11. 400 MHz ^{1}H NMR spectrum of **3** in $CDCl_3$ at 298 K.

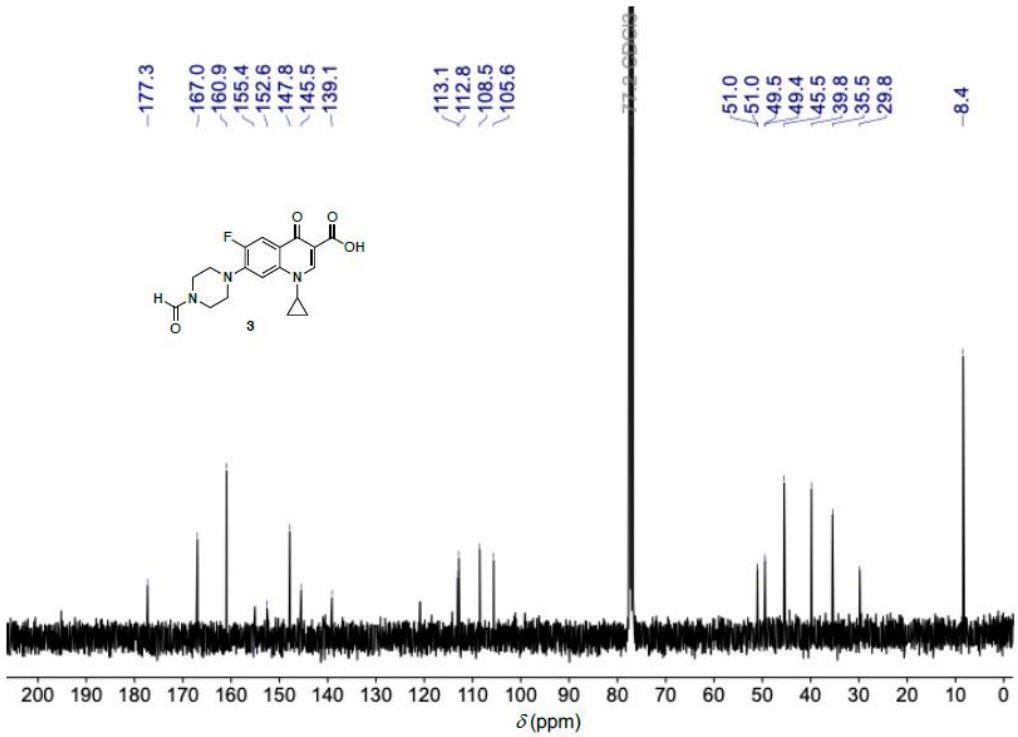

Figure 2.12. 101 MHz ^{13}C NMR spectrum of **3** in $CDCl_3$ at 298 K.

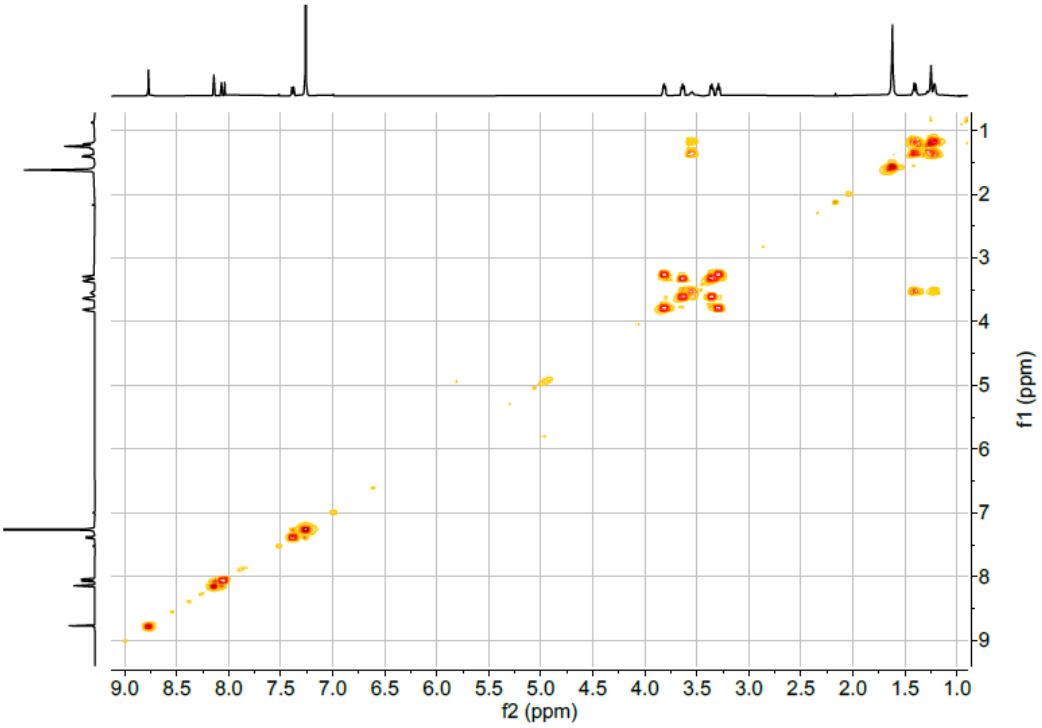

Figure 2.13. 400 MHz ^{1}H-COSY NMR spectrum of **3** in $CDCl_3$ at 298 K.

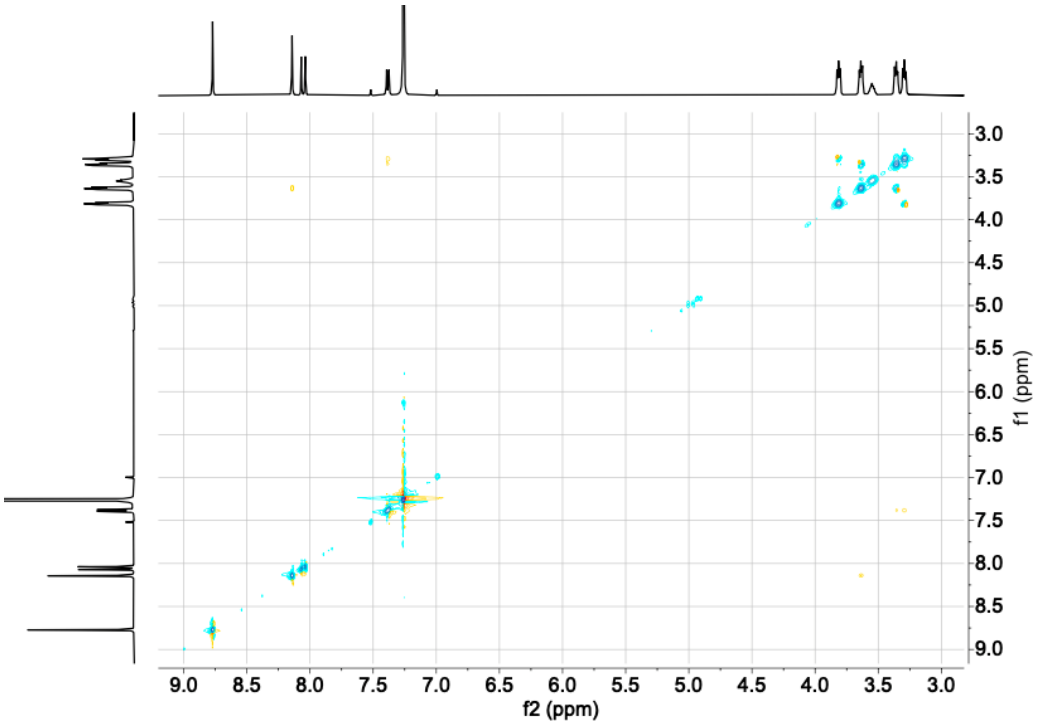

Figure 2.14. 400 MHz ^{1}H-ROESY NMR spectrum of **3** in $CDCl_3$ at 298 K.

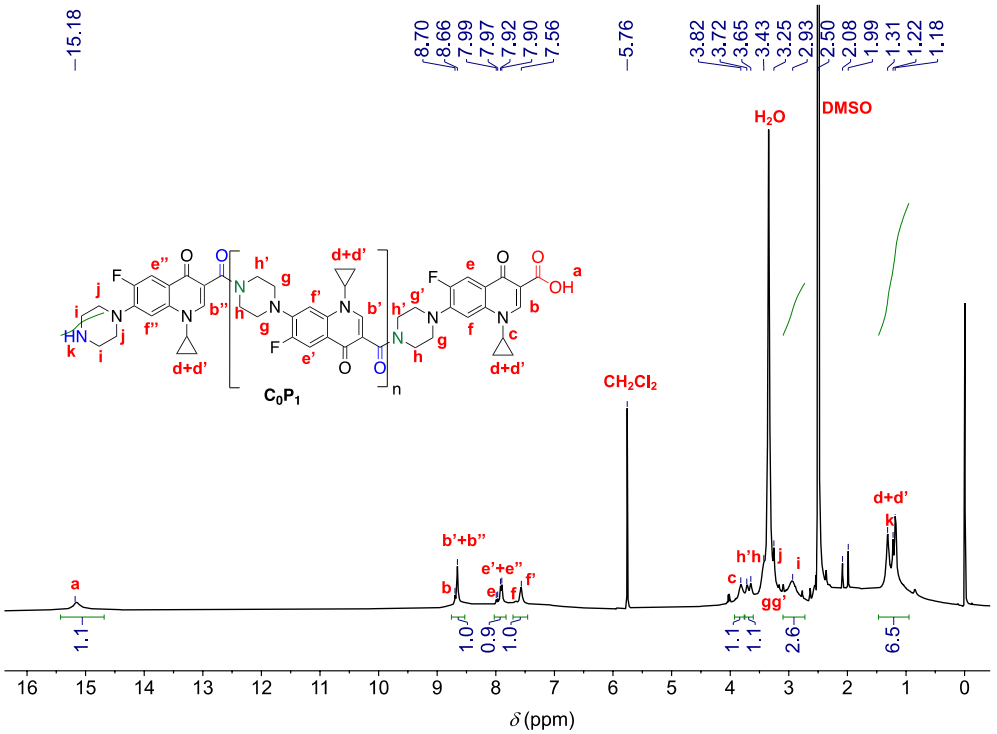

Figure 2.15. 500 MHz ^{1}H NMR spectrum of $\mathbf{C_0P_1}$ in DMSO-d_6 at 298 K.

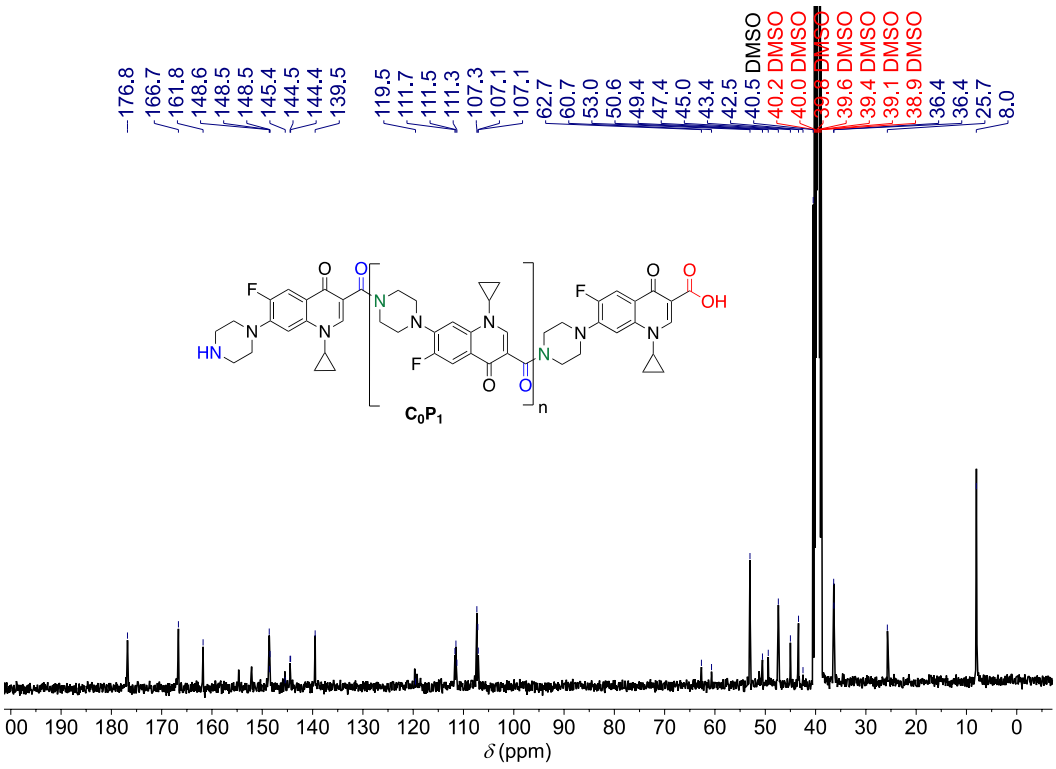

Figure 2.16. 101 MHz ^{13}C NMR spectrum of $\mathbf{C_0P_1}$ in DMSO-d_6 at 298 K.

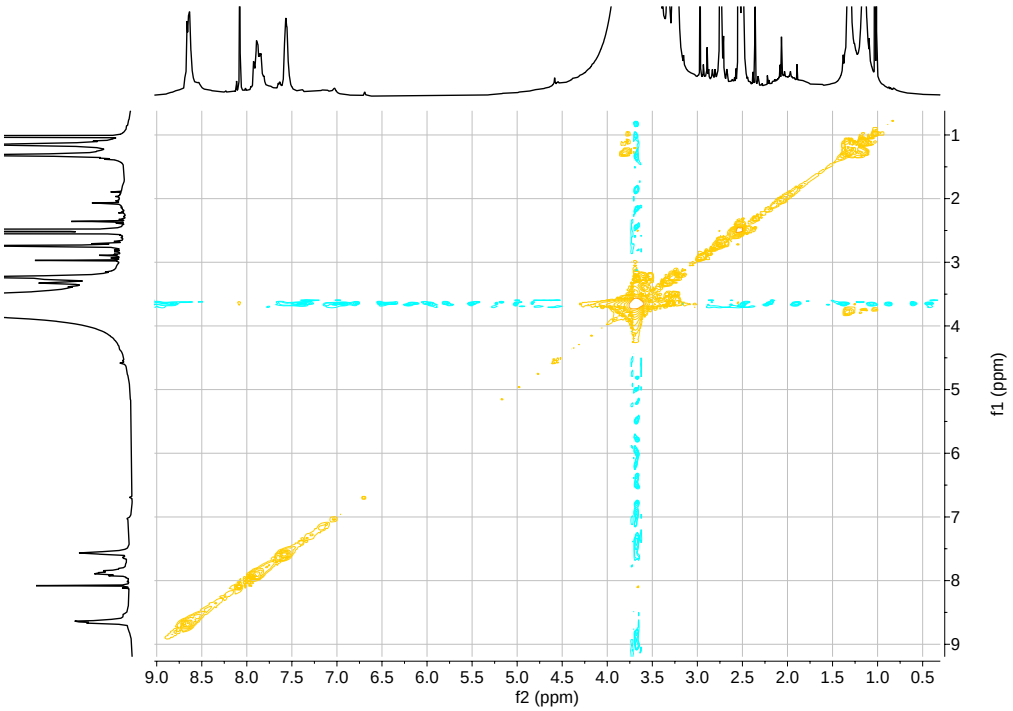

Figure 2.17. 400 MHz ^{1}H-COSY NMR spectrum of $\mathbf{C_0P_1}$ in DMSO-d_6 at 298 K.

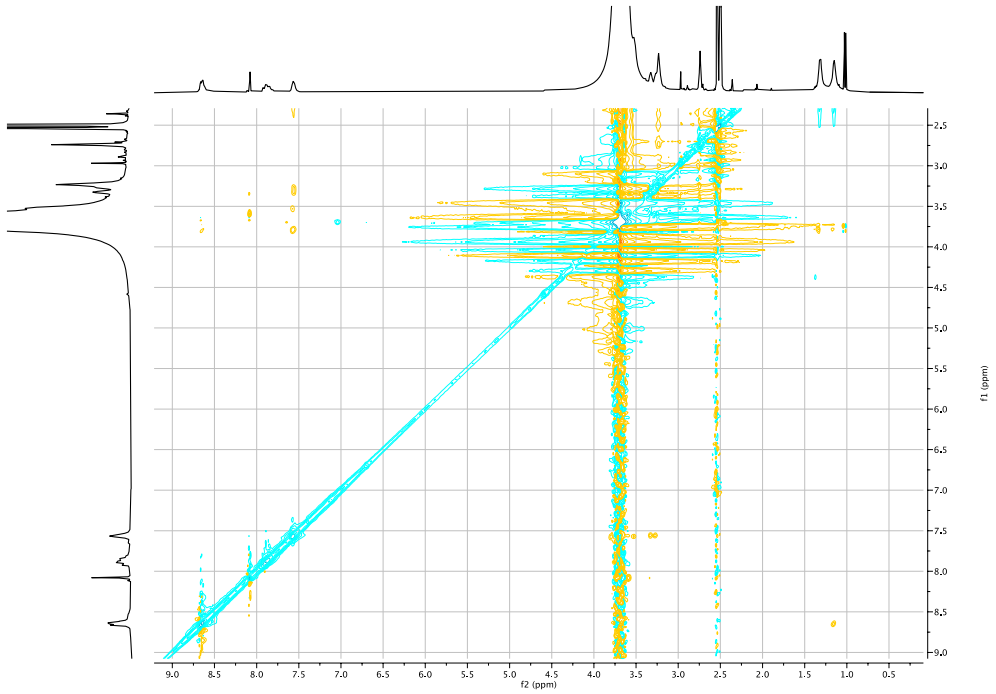

Figure 2.18. 400 MHz ^{1}H-ROESY NMR spectrum of $\mathbf{C_0P_1}$ in DMSO-d_6 at 298 K.

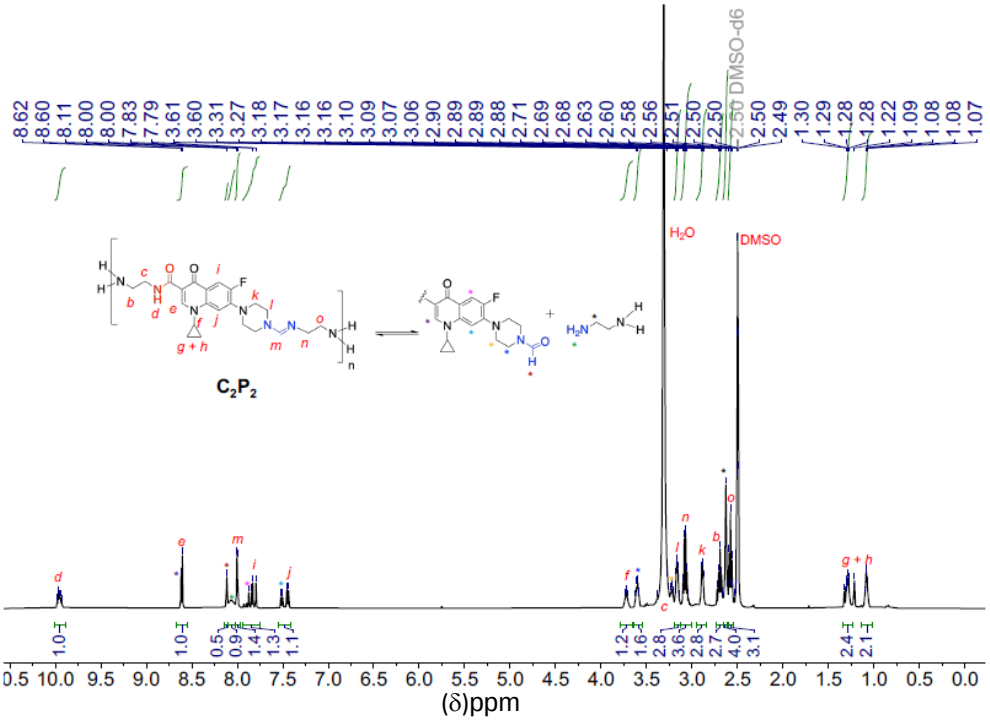

Figure 2.19. 400 MHz ^{1}H NMR spectrum of $\mathbf{C_2P_2}$ in DMSO-d_6 at 298 K.

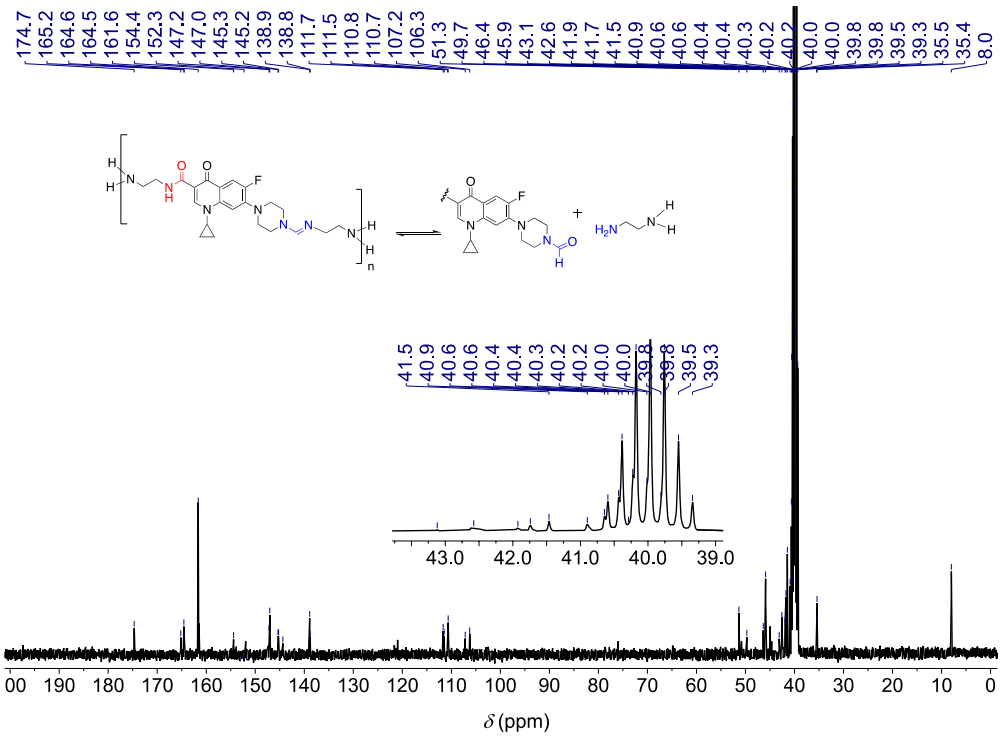

Figure 2.20. 101 MHz ^{13}C NMR spectrum of $\mathbf{C_2P_2}$ in DMSO-d_6 at 298 K.

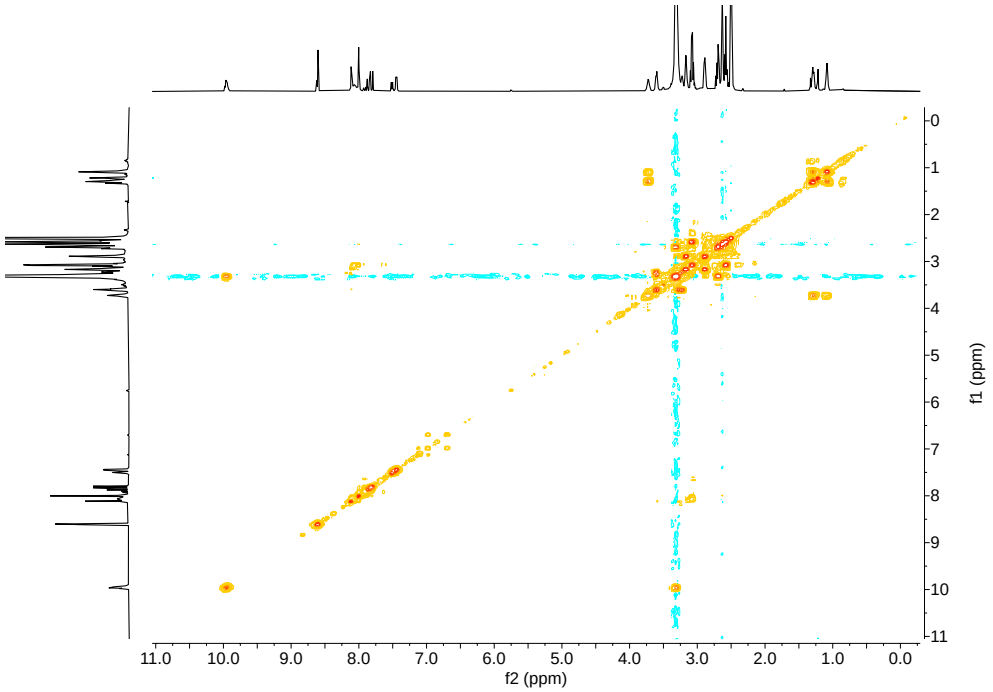

Figure 2.21. 400 MHz ^{1}H-COSY NMR spectrum of $\mathbf{C_2P_2}$ in DMSO-d_6 at 298 K.

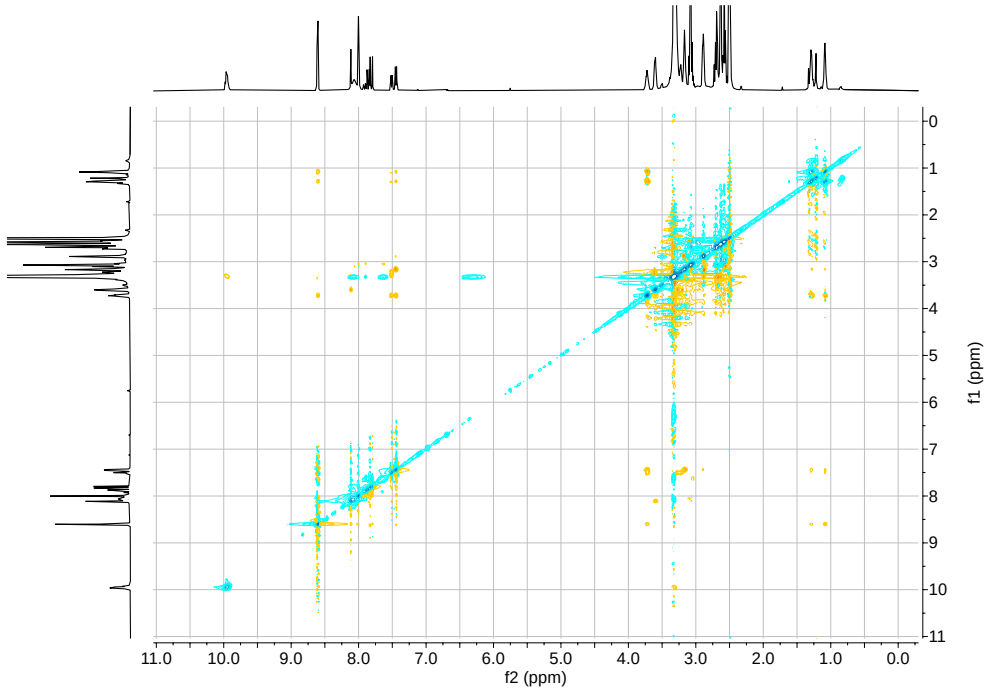

Figure 2.22. 400 MHz ^{1}H-ROESY NMR spectrum of $\mathbf{C_2P_2}$ in DMSO-d_6 at 298 K.

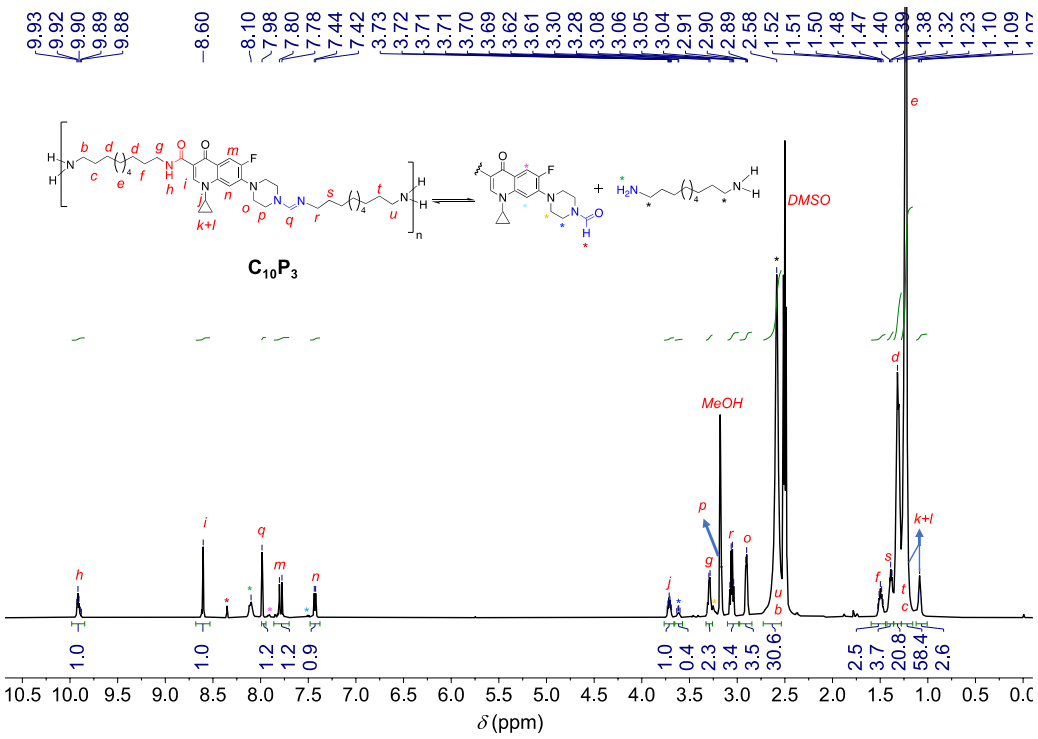

Figure 2.23. 500 MHz ^{1}H NMR spectrum of **$C_{10}P_3$** in DMSO-d_6 at 298 K.

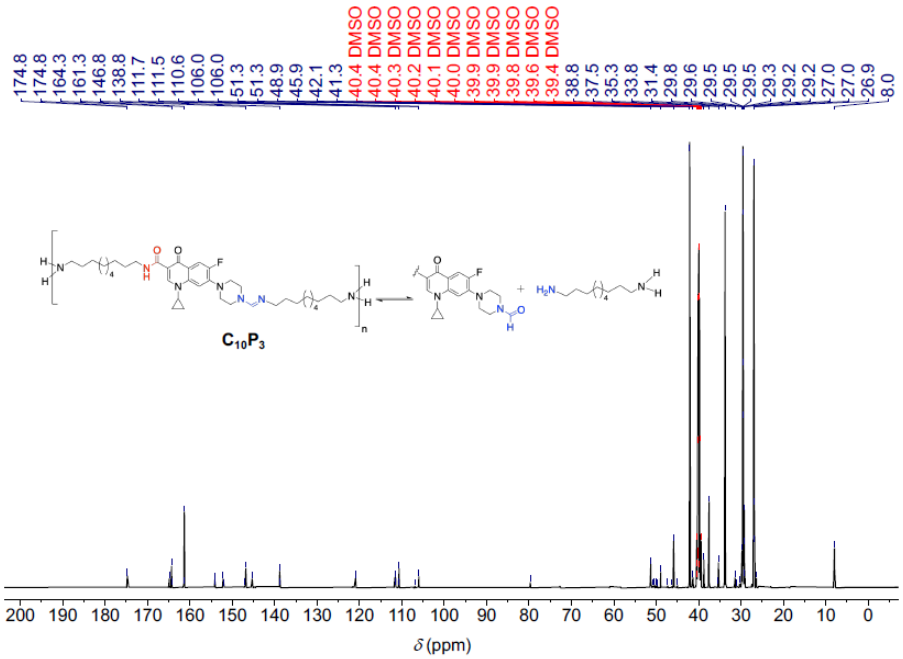

Figure 2.24. 125 MHz ^{13}C NMR spectrum of **$C_{10}P_3$** in DMSO-d_6 at 298 K.

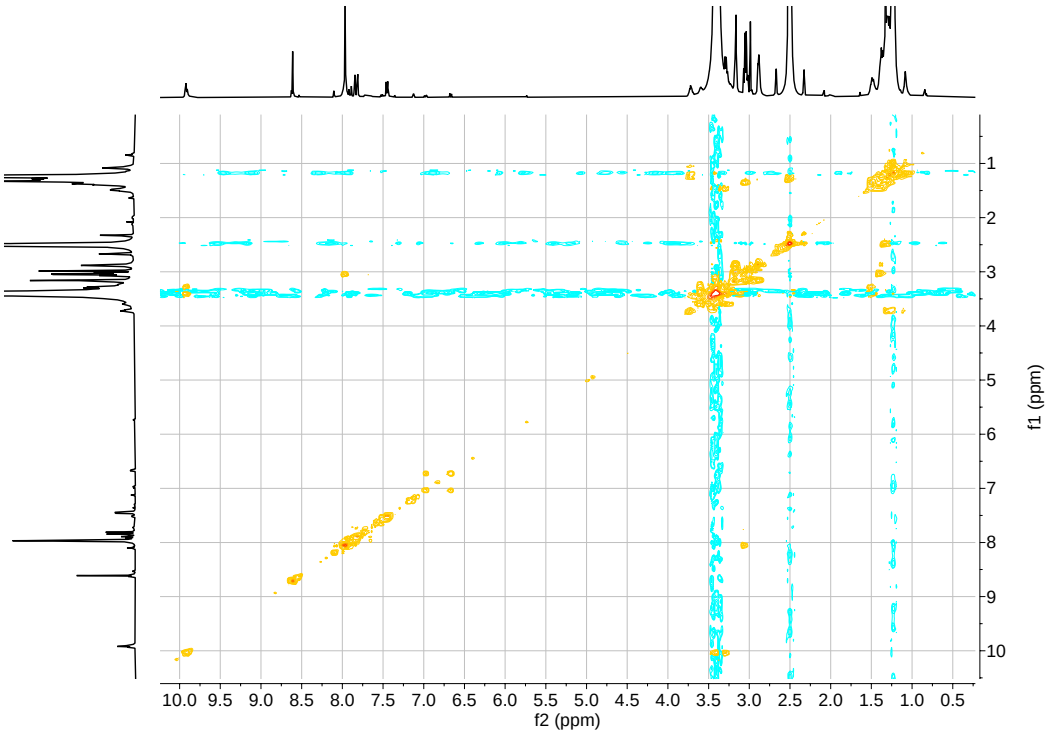

Figure 2.25. 400 MHz ^{1}H-COSY NMR spectrum of $\mathbf{C_{10}P_3}$ in DMSO-d_6 at 298 K.

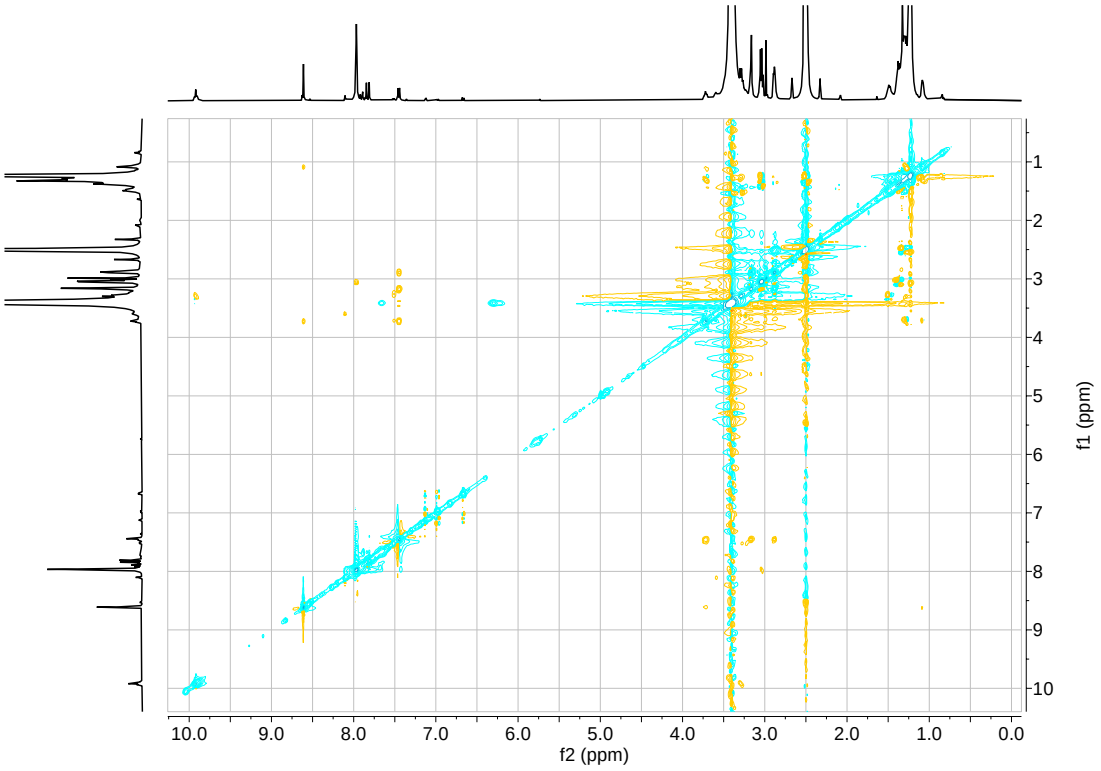

Figure 2.26. 400 MHz ^{1}H-ROESY NMR spectrum of $\mathbf{C_{10}P_3}$ in DMSO-d_6 at 298 K.

2.2.3.2. Characterization by Size exclusion chromatography (SEC)

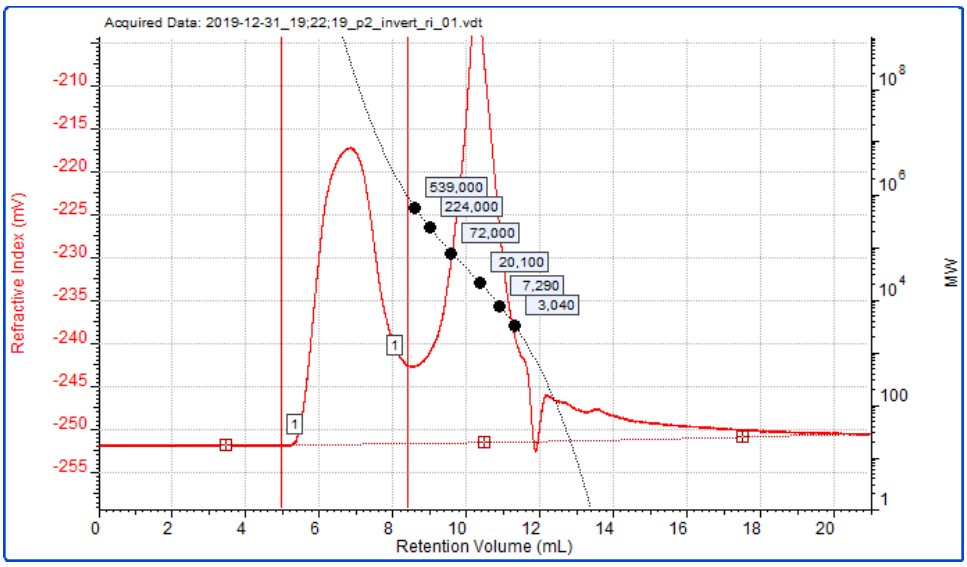

Figure 2.27. SEC chromatogram of $\mathbf{C_0P_1}$ monitored using RI detector.

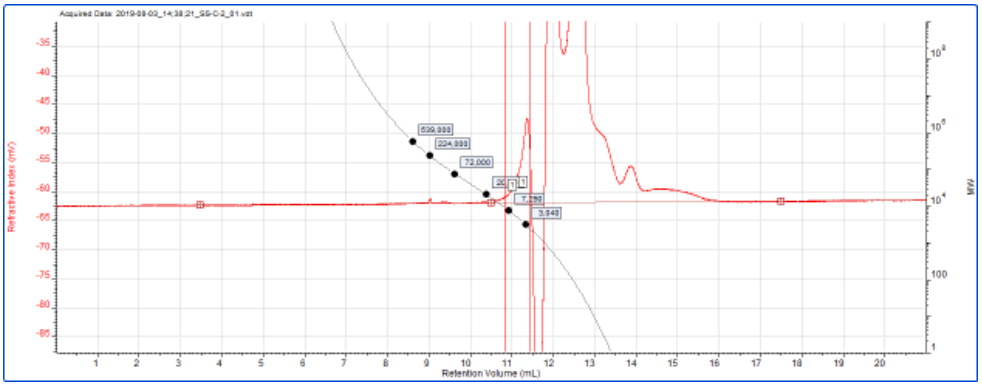

Figure 2.28. SEC chromatogram of $\mathbf{C_2P_2}$ monitored using RI detector.

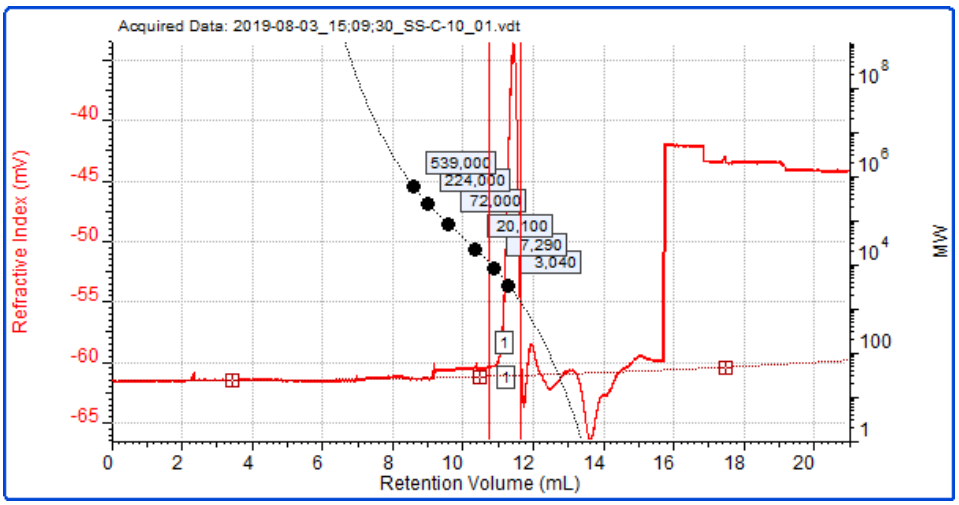

Figure 2.29. SEC chromatogram of $\mathbf{C_{10}P_3}$ monitored using RI detector.

2.2.4. Antibacterial assay and biocompatibility

2.2.4.1. ***MIC determination of polymers and monomers*** was carried out using the turbidity assay method.[24] The samples were dissolved in either DMSO or media to prepare a stock solution. As **1** suffered solubility issue, a suspension was made in media by ultrasonication as stock solution and further diluted to the desired concentration. All solutions were filtered with PTFE 0.2 μm sterile syringe filter. The stock solution was then put into 96-well plates and diluted with nutrient broth by adding the desired concentration of 0.1–10 μg/mL, the volume was kept constant. Both *E. coli* and *S. aureus* (1×10^7–10^8 CFU/mL) were transferred to 96-well plates 200 μL in each well. The plates were incubated for 24–48 h at 37 °C. Then the MIC was determined by visual turbidity readout (Bioteck Synergy HTX Multimode Reader) at 600 nm. Vehicle and reference agents (**1**, **2**, and **3**) were used in every test as negative and positive controls. Assays were performed in triplicate. Readings were recorded in different time intervals (6, 12, 24, 48 h). MIC values reported are the minimum concentration necessary to inhibit 90% of the cell growth. MIC was determined by measuring cell growth at OD600 after 12 h by following standard protocols. All reported values represent a minimum of triplicate experiments.

2.2.4.2. ***Agar disc diffusion assay*** was used to evaluate the zone of inhibition of manually coated nylon sutures with polymers and monomers. Experiments were performed according to the reported procedure.[25] All the samples were dissolved in DMSO/media solution at a concentration of 4 mg/mL and manually dip-coated on commercially available nylon sutures (length: 2.5 cm). As **1** was not soluble at this concentration in either DMSO or media, sutures were coated by the suspension. Coated sutures were dried in a vacuum oven at 70 °C for 24 h. For *S. aureus* and *E. coli*, the agar plates were prepared by adding Luria-Bertani (LB) medium to Petri plates and left to solidify, and the strains 10 μL of 1×10^7–10^8 CFU/mL were spread on solidified agar plates and left for 30 min. Nylon-6 threads coated with samples were placed on the surface of Petri plates. Bacterial growth over the surface was monitored for 24 h at 37 °C. After 24 h of incubation, the area of the zone of inhibition was measured using ImageJ software in terms of area millimetre square (mm^2). The positive controls for this experiment were **1**, **2**, and **3** (for both *S. aureus* and *E. coli*). The blank suture was used as a negative control.

2.2.4.3. ***Biocompatibility*** was assessed using a fibroblastic cell line L929. The cell viability for biocompatibility studies was measured at 570 nm using a 3-(4,5-dimethylthiazol-2-yl)-2,5-diphenyltetrazoliumbromide (MTT) assay. Cells were cultured on 96-well plates for 24 h in DMEM with 10% v/v FBS and 1% v/v penicillin−streptomycin at 37 °C in a 5% CO_2 incubator. The test samples were incubated at a concentration of 1 mg/mL in DMEM for a period of 72 h at 37 °C. The extracts were added to cells and treated for 48 h. MTT was added and incubated for 4 h. DMSO was added and incubated for 30 min. The optical density of dissolved formazans crystals was quantified at 570 nm using spectrophotometric analysis (Tecan Infinite M Plex). The cytotoxicity effect in each treatment can be expressed as a percentage of cell viability relative to the untreated control cells and is defined as,

Cell viability % = [Absorbance of treated cells]/[Absorbance of control cells] × 100.

2.2.5. Hydrolysis study of polymers

2.2.5.1. ***HPLC data for monomers 1 & 3 and polymers C_0P_1, C_2P_2, and $C_{10}P_3$.*** The hydrolysis study for monomers **1** & **3** and polymers $\mathbf{C_0P_1}$, $\mathbf{C_2P_2}$, and $\mathbf{C_{10}P_3}$ has been performed by using the HPLC–LCMS technique. Agilent Eclipse plus 18 (C_{18}) column was used. The standard and sample solutions were prepared by dissolving in CH_3CN/H_2O 1:1 with the addition of 10% DMSO for better solubility and filtered through a 0.22 μm pore size filter (Hydrophobic PTFE Syringe Filter - Non-Sterile). The eluent used for the release of ciprofloxacin **1** from $\mathbf{C_0P_1}$ is CH_3CN/H_2O 2:8, whereas, for the release of the monomer **3** from $\mathbf{C_2P_2}$ and $\mathbf{C_{10}P_3}$ was observed by using CH_3CN/H_2O 1:1 with a flow rate of 1 mL/min associated with other parameters such as column temperature (25 °C), sample temperature (37 °C), injection volume (20 μL). The standard ciprofloxacin **1** was detected at 3.71 min, whereas **3** was detected at 5.925 min by a photodiode array (PDA) detector. The method run time was 15 min. Since, no degradation was observed at neutral pH at 37 °C for $\mathbf{C_0P_1}$ (100 μg/mL) polymer at 0 h, to expedite the hydrolysis reaction or the release of monomer **1**, the pH of the solution was adjusted to acidic condition at pH 3 using 1% (*v/v*) FA. However, the solution was sonicated for 5 min (0.08 h) to make the solution homogenous before the first injection, and subsequent injections were performed only with stirring at 6, 12, and 24 h) readings.

For spacer polymers, $\mathbf{C_2P_2}$ and $\mathbf{C_{10}P_3}$ (1mg/mL) also were performed under similar conditions to monitor the release of monomer **3**.

It has been observed that the $\mathbf{C_0P_1}$ peak at RT 2.82 min slowly reduced synchronously with the appearance of monomer **1** peak at 3.7 min for up to 24 h (Figures 2.30. and 2.31, materials and methods). The release percentage was calculated by area under the curve of both peaks which was detected at 277 nm with different time intervals. The release percentage of 69% was observed for **1** from $\mathbf{C_0P_1}$ after 24 h. The release of monomer *via* hydrolysis polymer $\mathbf{C_0P_1}$ was indicated by the new peak appearance at 3.7 min with a time-dependent increase in intensity. It appears that the $\mathbf{C_0P_1}$ polymer is degraded into monomer **1** under acidic conditions since this new peak RT matches that of monomer (Figure 2.30), suggesting that the polymer undergoes degradation into monomer **1** under acidic conditions. Similarly, Figures 2.32 and 2.34 depict the HPLC profile of $\mathbf{C_2P_2}$ and $\mathbf{C_{10}P_3}$.

It was found that for both $\mathbf{C_2P_2}$ and $\mathbf{C_{10}P_3}$ due to weak imine bond presence fragmentation even at neutral pH in aqueous conditions as depicted in Figures 2.32a and 2.34a, respectively. A significant amount of monomer **3** was observed at RT 5.6 min after adding FA (1%). The release percentage was calculated by the area under the curve of both peaks detected at 277 nm with different time intervals. The area under the curve of degraded peaks corresponding to the release of monomer **3** for $\mathbf{C_2P_2}$ and $\mathbf{C_{10}P_3}$ was estimated to be 57 and 75%, respectively, after 24 h. The release of monomers **1** and **3** was corroborated by LC-MS analysis of the standards as depicted in Figures 2.33, 2.35, 2.36, and 2.37.

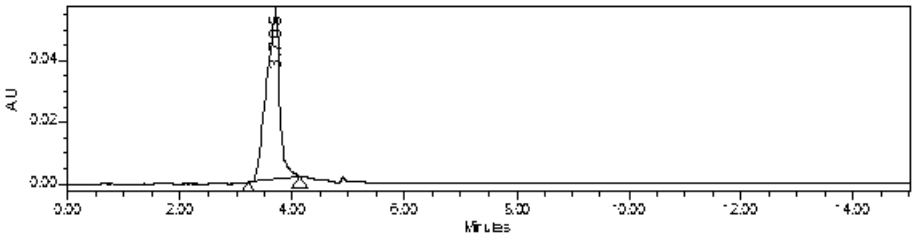

Figure 2.30. HPLC-LCMS profile for ciprofloxacin **1** with 1% FA.

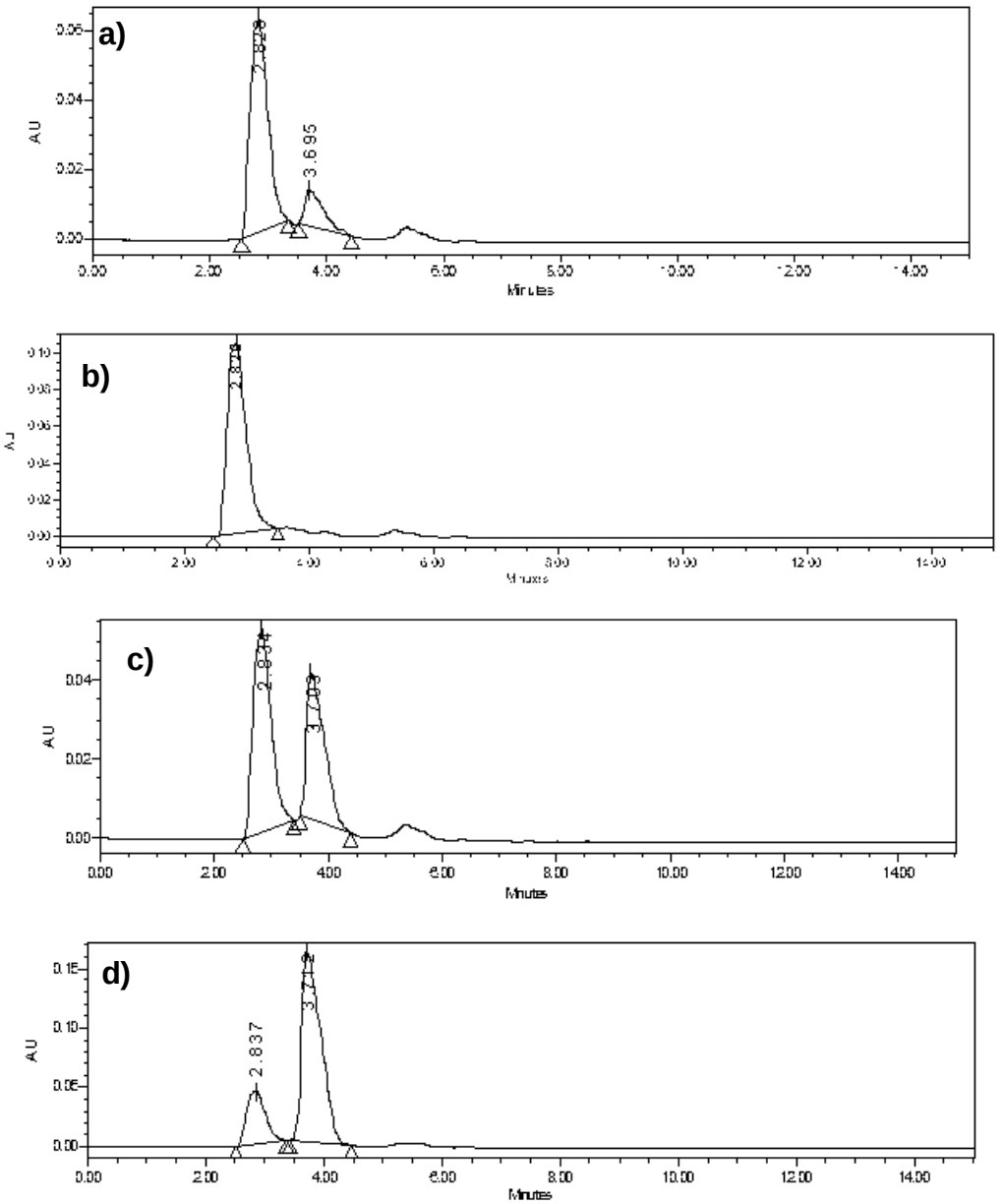

Figure 2.31. HPLC chromatograms for monomer **1** release profile of a) $\mathbf{C_0P_1}$ without FA, and $\mathbf{C_0P_1}$ with 1% FA b) 0 h, c) 12 h, d) 24 h. The HPLC profiles were monitored using a PDA detector at 277 nm.

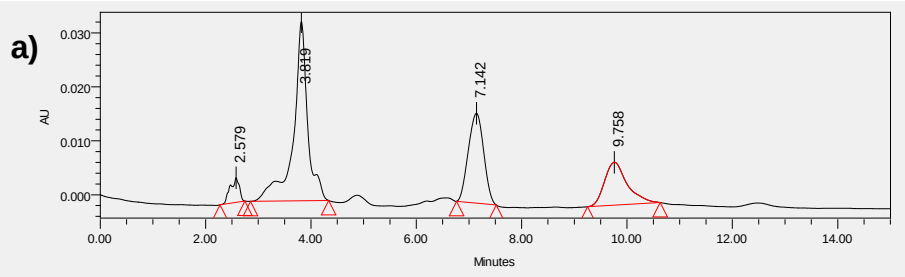

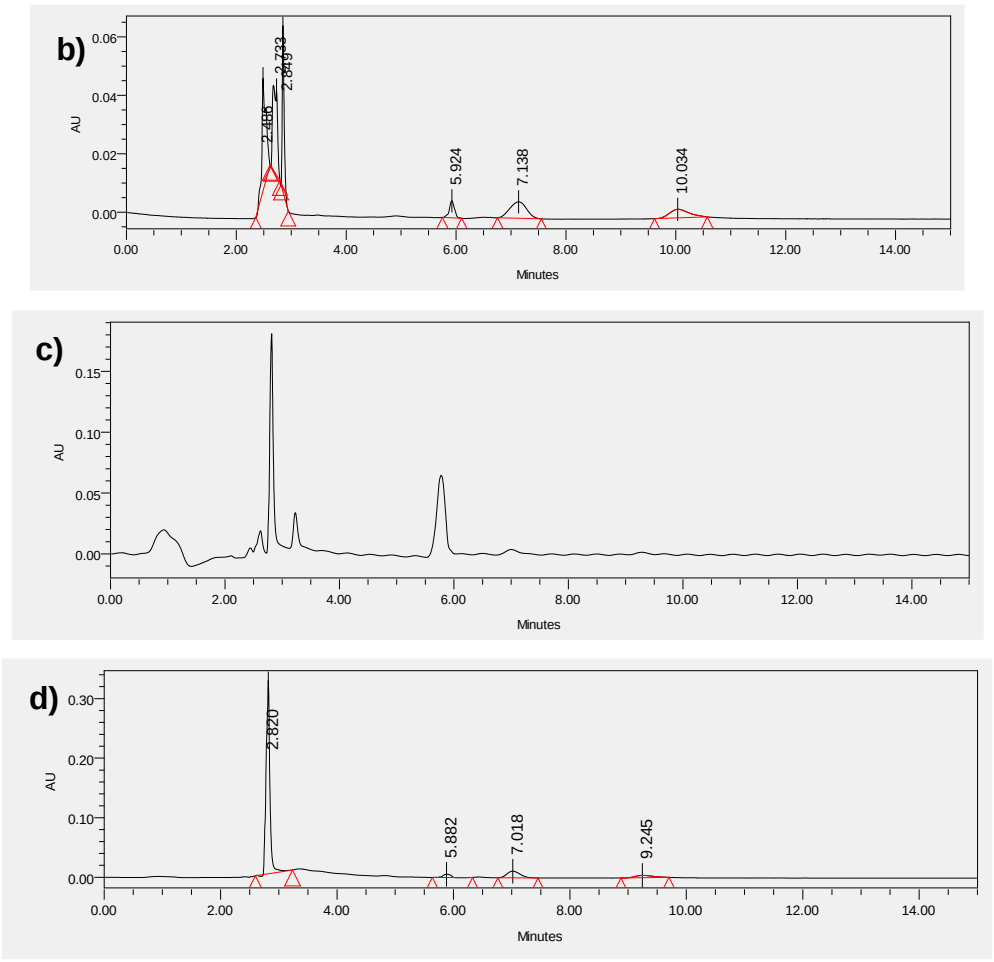

Figure 2.32. Polymer degradation profiles of **C_2P_2** monitored by HPLC. a) C_2P_2 without FA; C_2P_2 with 1% FA b) 0 h, c) 12 h d) 24 h (monitored using PDA detector at 277 nm).

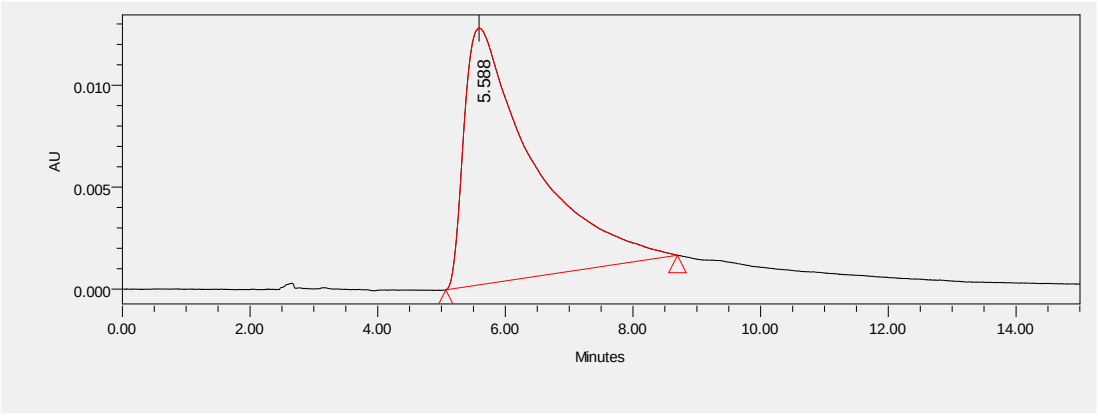

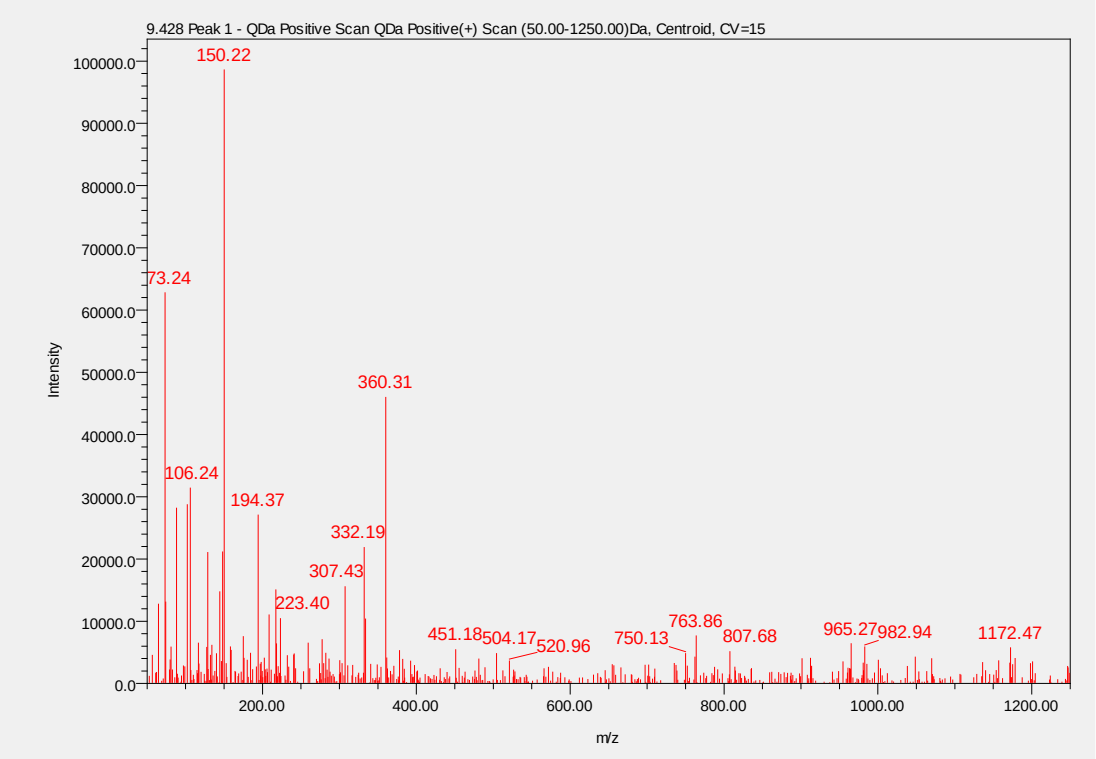

Figure 2.33. HPLC-LCMS profile for monomer **3** with 1% FA (monitored using PDA detector at 277 nm). LC-MS after degradation of $\mathbf{C_2P_2}$.

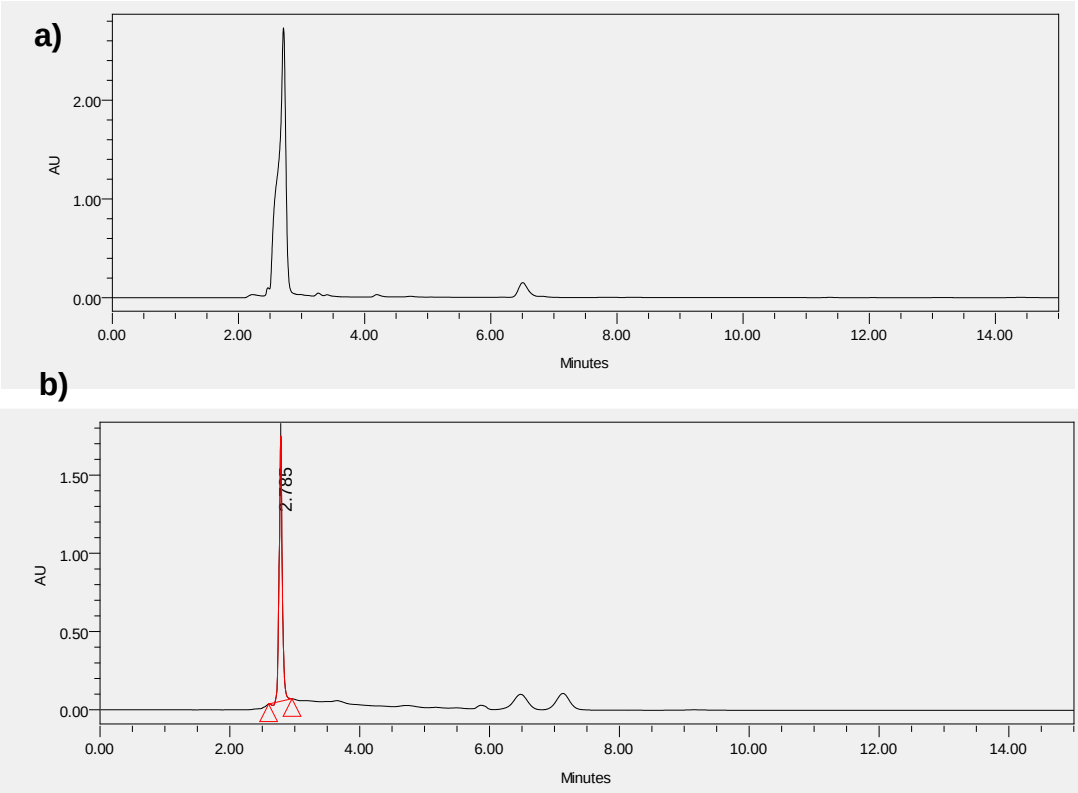

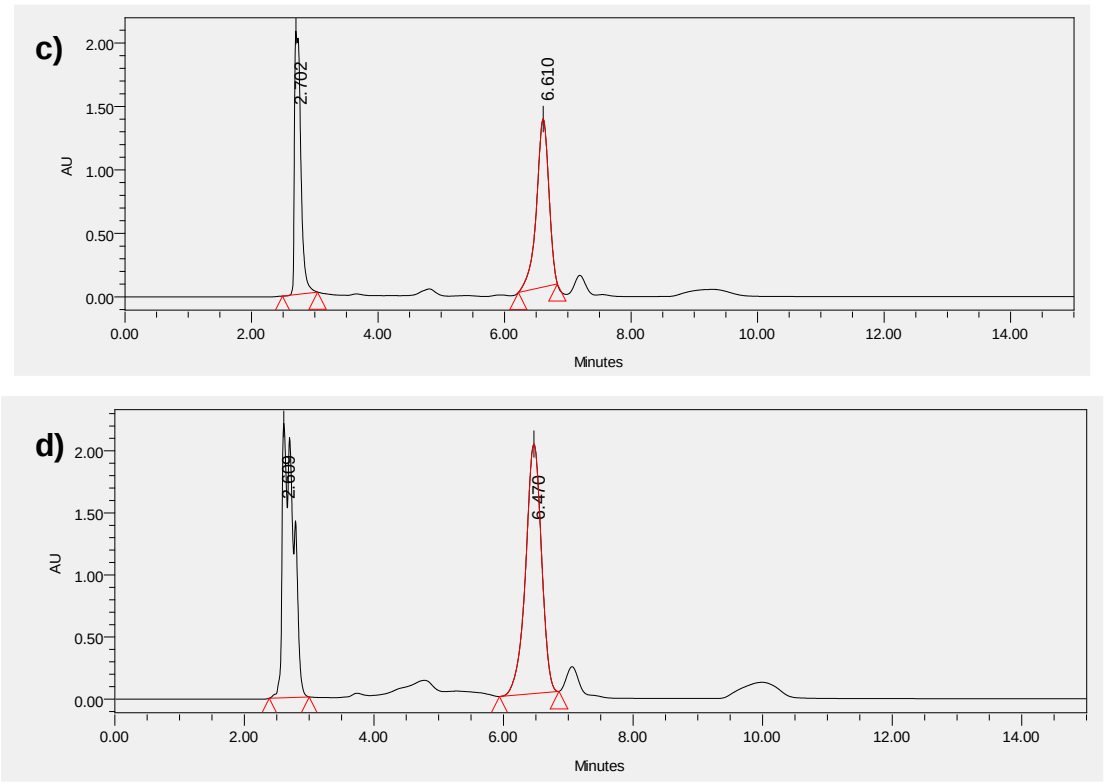

Figure 2.34. Polymer degradation profiles of $\mathbf{C_{10}P_3}$ monitored by HPLC. a) $\mathbf{C_{10}P_3}$ without FA, $\mathbf{C_{10}P_3}$ with 1% FA b) 0 h, c) 12 h, d) 24 h (monitored using PDA detector at 277 nm).

2.2.5.2. *LC-MS data for monomers 2 and 3.*

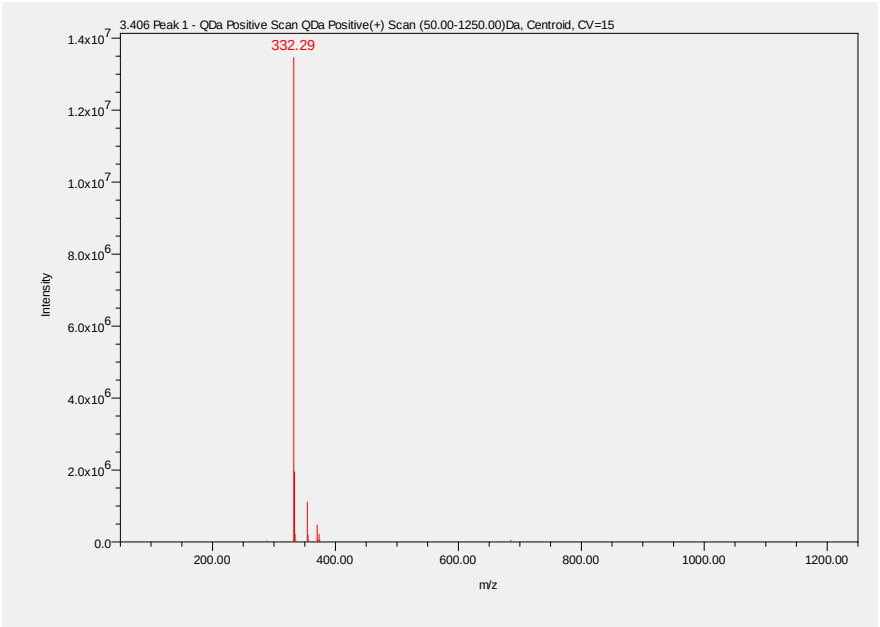

Figure 2.35. LC-MS (*m/z*) spectrum for **1**: calcd for $C_{17}H_{19}FN_3O_3^+$: $[M+H]^+$, 332.14; found, 332.29.

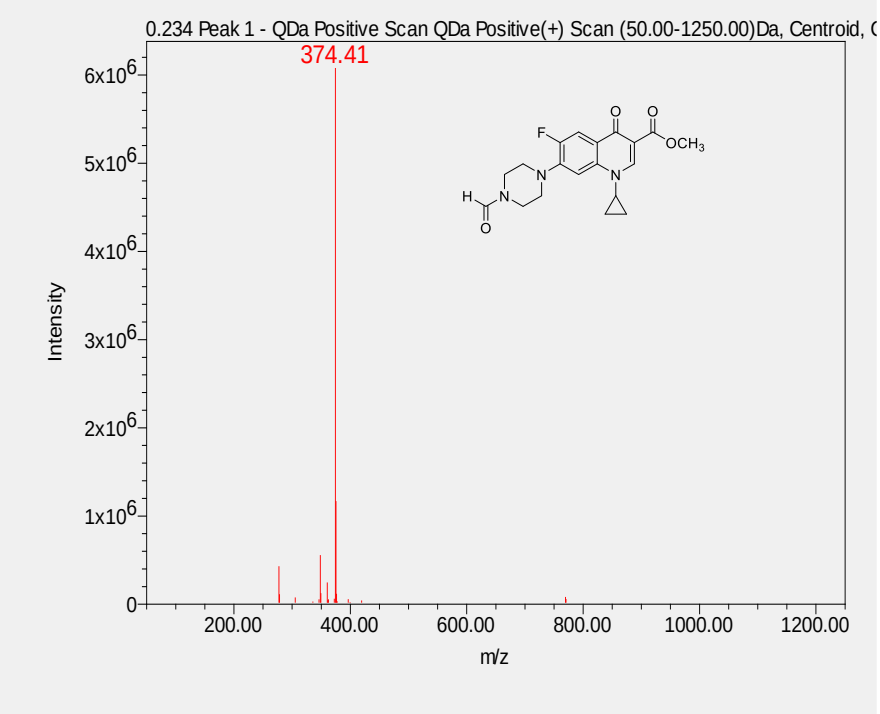

Figure 2.36. LC-MS (*m/z*) spectrum for **2**: calcd. for $C_{19}H_{21}FN_3O_4^+$: $[M+H]^+$, 374.15; found, 374.41.

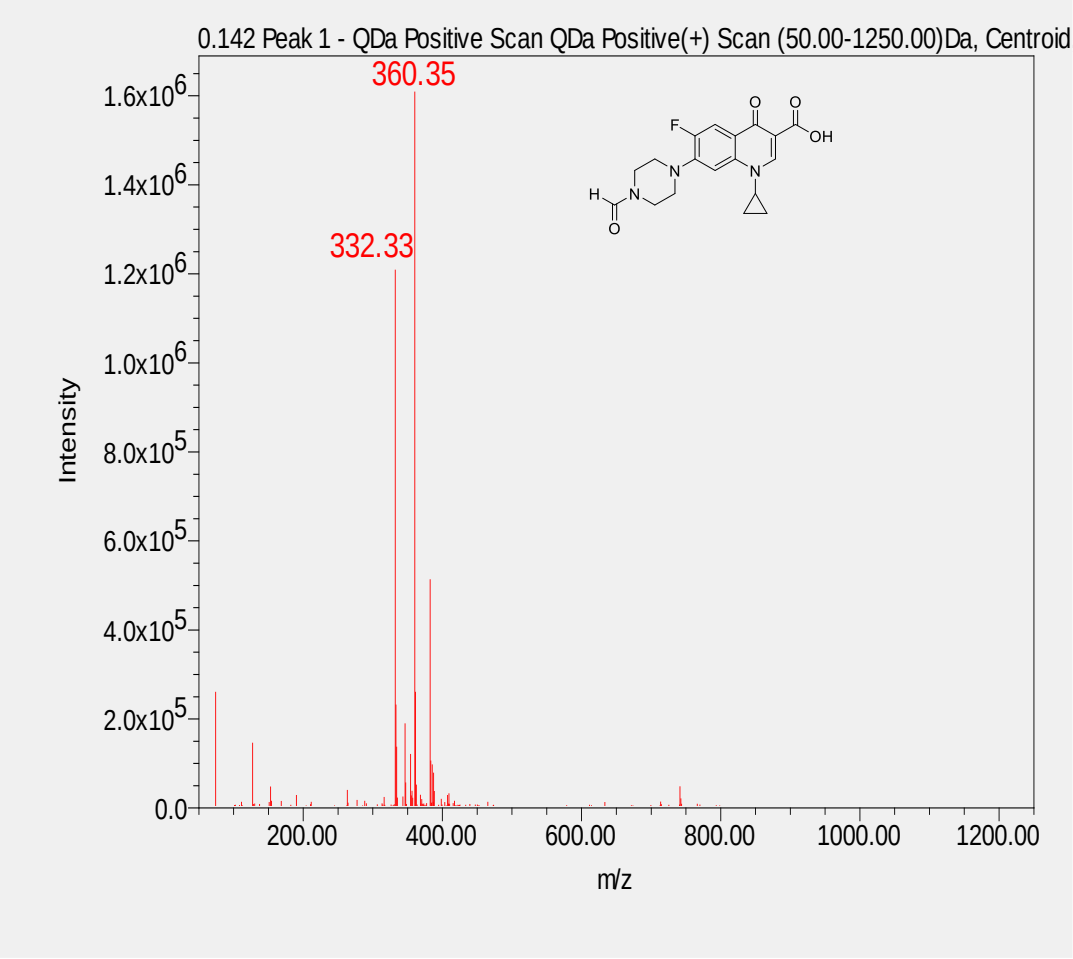

Figure 2.37. LC-MS (*m/z*) spectrum for **3**: calcd. for $C_{18}H_{19}FN_3O_4^+$: $[M+H]^+$, 360.14; found, 360.35.

2.2.5.3. ***^{1}H NMR data for polymers C_2P_2, and $C_{10}P_3$.*** The hydrolysis study for 10 mg of spacer polymers **C_2P_2** (Figure 2.38) and **$C_{10}P_3$** (Figure 2.39) has been performed by using the 2 μL of HCOOH in 0.7 mL of DMSO/D_2O 5:2. The reaction was monitored after adding FA up to 24 h.

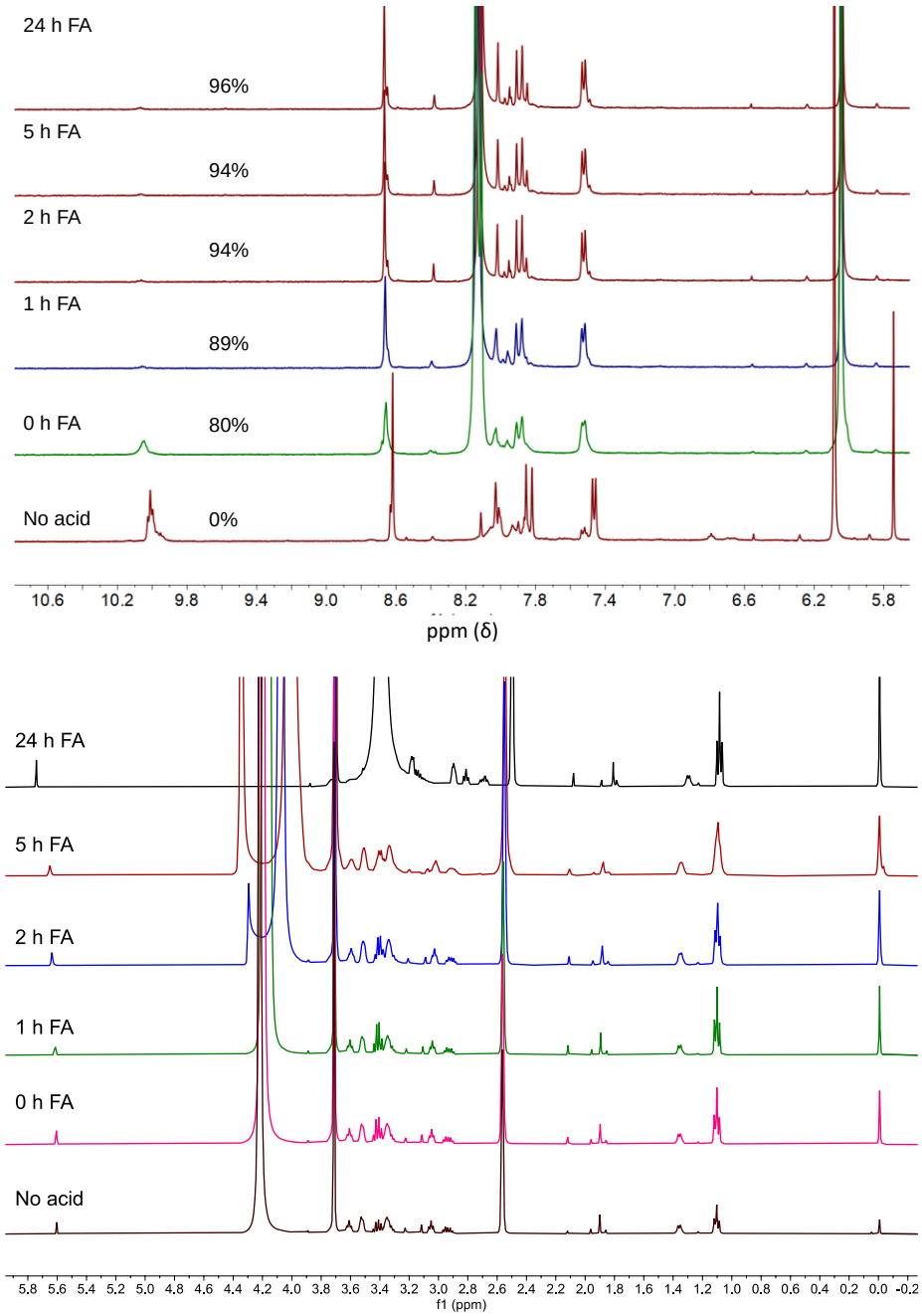

Figure 2.38. Time-dependent 400 MHz ^{1}H NMR spectra of **C_2P_2** in 0.7 mL of DMSO/D_2O 5:2 upon addition of FA.

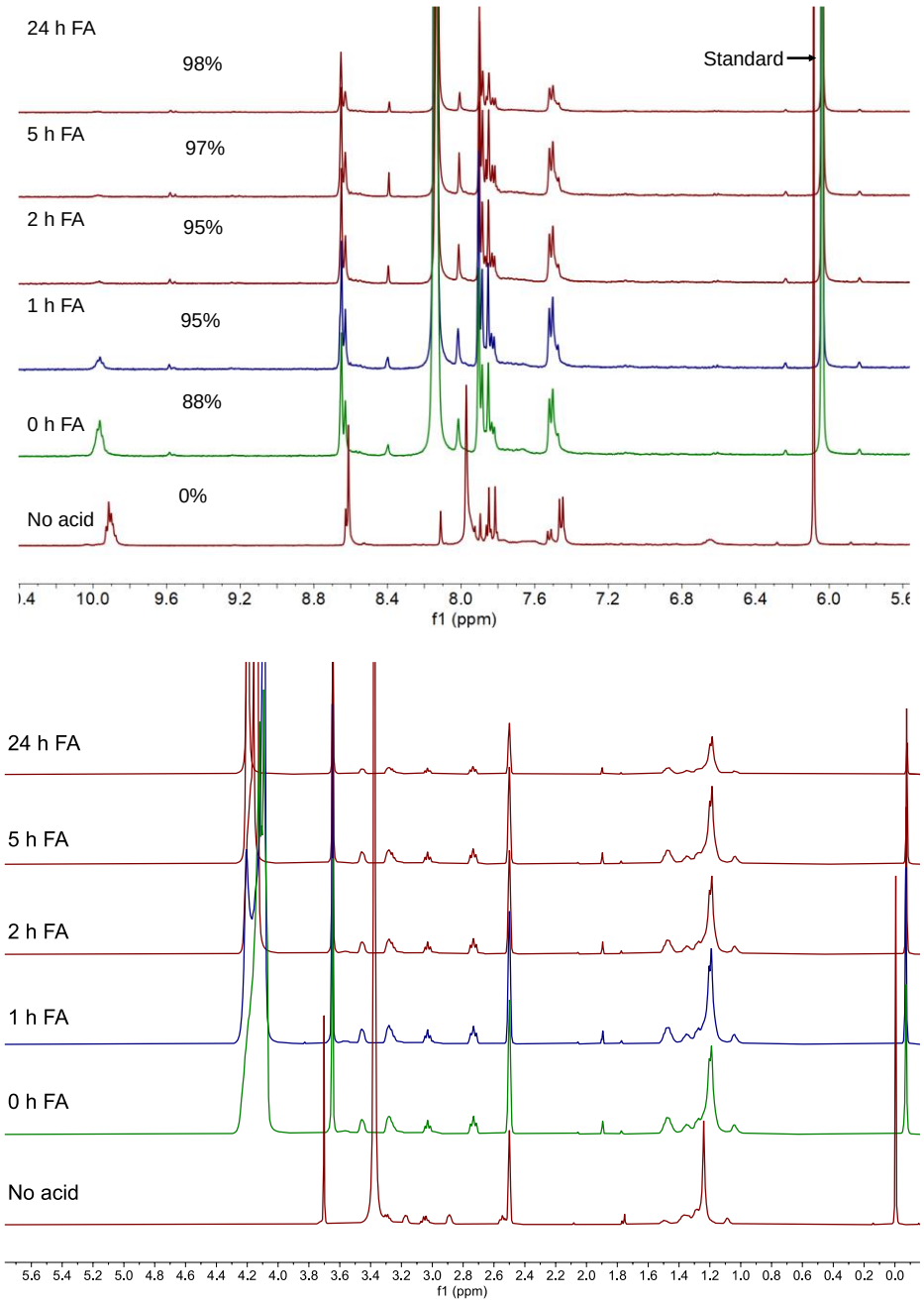

Figure 2.39. Time-dependent 400 MHz ^{1}H NMR spectra of $\mathbf{C_{10}P_3}$ in 0.7 mL of DMSO/D_2O 5:2 upon addition of FA.

2.2.6. Thermal analysis of Polymers by DSC (differential scanning calorimetry).

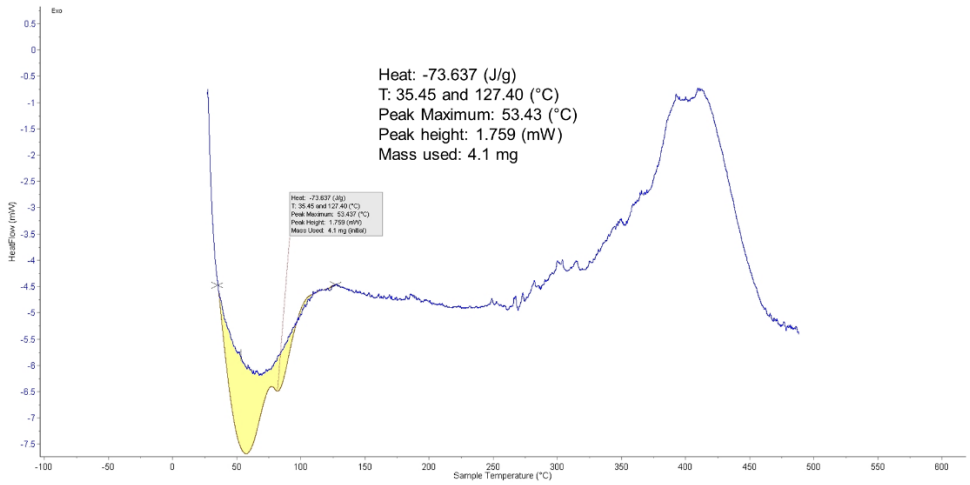

Figure 4.40. DSC thermograms of $\mathbf{C_0P_1}$.

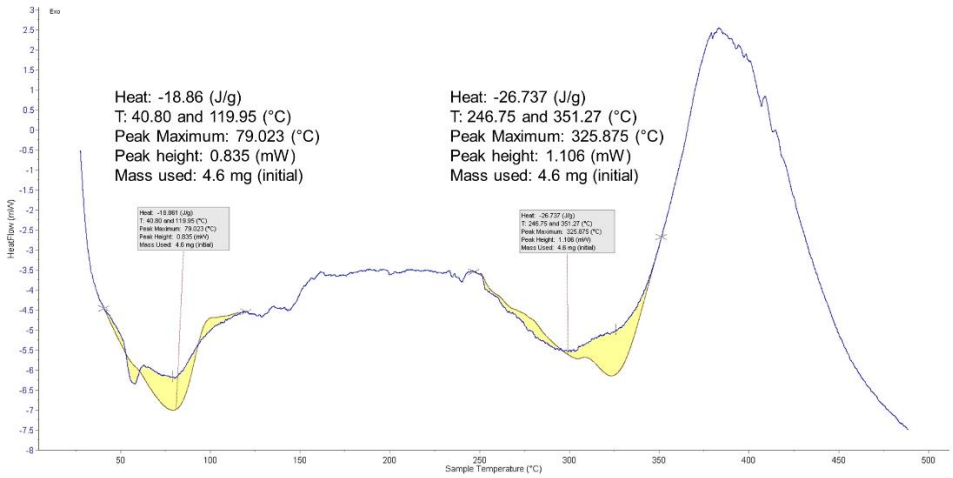

Figure 4.41. DSC thermograms of $\mathbf{C_2P_2}$.

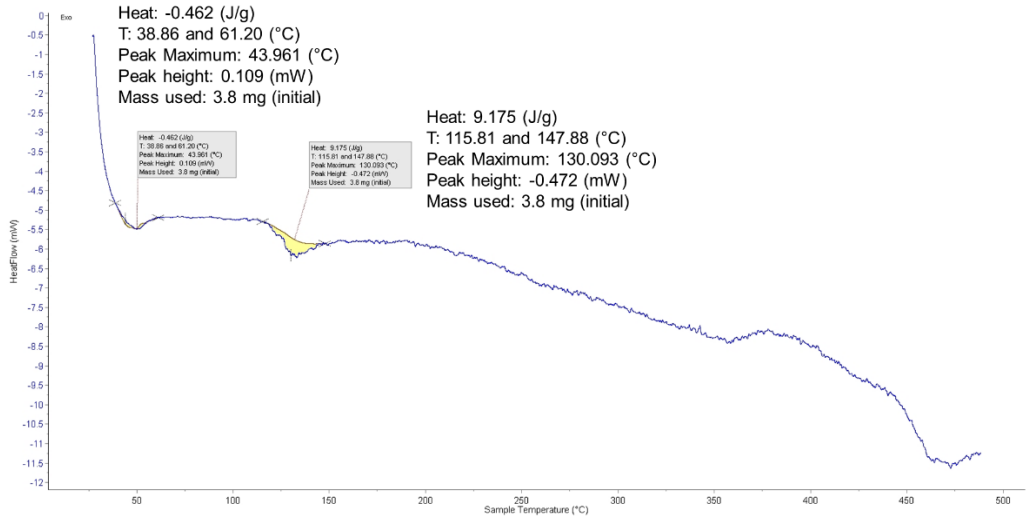

Figure 4.42. DSC thermograms of $\mathbf{C_{10}P_3}$.

2.2.7. Bacterial growth curves

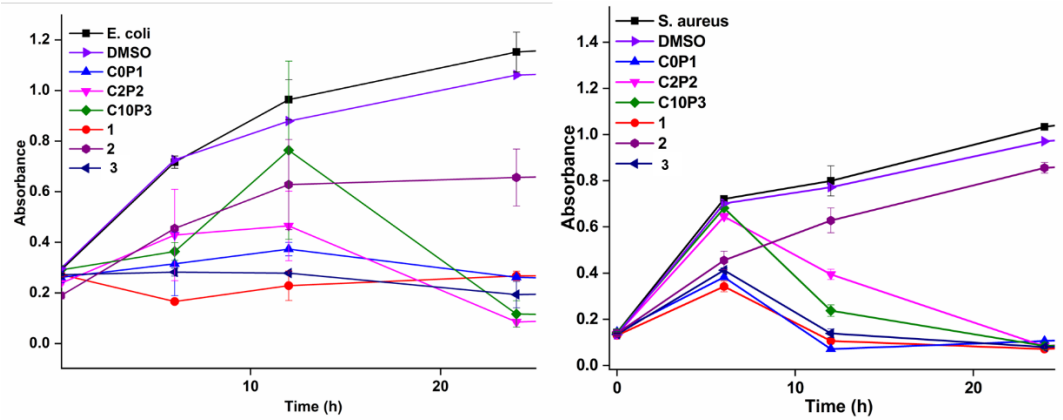

Figure 2.43. Growth curve of *E. coli* and *S. aureus* with and without treatment of 10 µg/mL of **1**, **2**, **3**, $\mathbf{C_0P_1}$, $\mathbf{C_2P_2}$, $\mathbf{C_{10}P_3}$.

2.3. Summary and conclusion

To unravel the role of the spacer effect, we have designed and synthesized a new type of polymeric biocides (PB) $\mathbf{C_0P_1}$, which we refer to as a true drug-polymer because upon hydrolysis/degradation, only the monomer drug units are released with no other extra mass. This not only enables more drug release in lesser amounts but also obviates the toxicity of non-drug parts. As a proof of concept, a well-known antibiotic molecule having AB-type monomer, *i.e.*, ciprofloxacin, was polymerized for the first time to obtain a large molecular weight (973.27 kDa) PB having 0% non-drug content. This true drug-polymer was compared with two other new polymers $\mathbf{C_2P_2}$ and $\mathbf{C_{10}P_3}$, with increased non-drug spacer content of 29 and 53%, respectively. Antibacterial inhibition studies by both solution and suture coating revealed a clear trend, *i.e.*, improved activity when the non-drug spacer content decreased even when the activity was normalized with the spacer content ratio. Spacer polymers exhibited comparatively lower activity even with fast-releasing capability due to imine and primary amide bonds.

Interestingly, the non-spacer polymer $\mathbf{C_0P_1}$ showed decreased activity in solution against monomer **1,** probably due to the slow hydrolysis nature, whereas increased activities of 1.5 and 2.2 times for E. coli and 1.6 and 88 times for S. aureus against spacer polymers $\mathbf{C_2P_2}$ and $\mathbf{C_{10}P_3}$, respectively, were observed in suture coating application. The uniform coating ability for $\mathbf{C_0P_1}$ to adhere to nylon thread was achieved effectively using polymerization, without which monomer **1** suffers from poor solubility and coating

ability. The hydrolysis study suggests that the **C_0P_1** polymer shows sustainable monomer release over the other two spacer PBs due to stronger tertiary amide bonds. As evidenced by the higher melting point (409 °C), better biocompatibility and excellent coating ability on nylon thread, we expect **C_0P_1** is a promising candidate for advanced biomaterial and medical applications such as coating of sutures and other surgical devices. As we have checked only one application for the true drug-polymer (**C_0P_1**), *i.e.*, coating on surgical nylon sutures, there is no doubt that the true-drug polymer of antimicrobials can open a wide range of new applications, including activity against drug-resistant bacteria. Our lab is currently exploring this direction of research.

2.4. References

1. Allen, C. L.; Chhatwal, A. R.; Williams, J. M. J. J. Direct Amide Formation from Unactivated Carboxylic Acids and Amines. *Chem. Commun.* **2012,** *48*, 666–668.
2. Montalbetti, C. A. G. N.; Falque, V. Amide Bond Formation and Peptide Coupling. *Tetrahedron* **2005,** *61*, 10827–10852.
3. Turos, E.; Anderson, B. E.; Cormier, R. S.; Thomas, J. C.; Kapolka, R. J.; Roma, G. Activity of New N-acylated Ciprofloxacin Derivatives Against Faculative Intracellular Bacteria. US Patent, US8143398B1, March 27, 2012.
4. Gould K. A.; Pan, X. S.; Kerns R., J.; Fisher, L. M. Ciprofloxacin Dimers Target Gyrase in Streptococcus pneumoniae. *Antimicrob. Agents Chemother*. **2004,** *4*, 2108–2115.
5. Mesallati, H.; Tajber, L. Polymer/Amorphous Salt Solid Dispersions of Ciprofloxacin. *Pharm. Res.* **2017,** *34*, 2425–2439.
6. Lawson, M. C.; Shoemaker, R.; Hoth, K. B.; Bowman, C. N.; Anseth, K. S. Polymerizable Vancomycin Derivatives for Bactericidal Biomaterial Surface Modification: Structure-Function Evaluation. *Biomacromolecules* **2009,** *10* 2221–2234.
7. Zhang, R.; Jones, M. M.; Moussa, H.; Keskar, M.; Huo, N.; Zhang, Z.; Visser, M. B.; Sabatini, C.; Swihart, M. T.; Cheng, C. Polymer-Antibiotic Conjugates as Antibacterial Additives in Dental. *Biomater. Sci.* **2019,** *7*, 287–295.
8. Duncan, R.; Vicent, M. J. Polymer therapeutics-prospects for 21st century: the end of the beginning. *Adv. Drug Deliv. Rev.* **2013,** *65*, 60–70.

9. Zhang, L.; Addla, D.; Ponmani, J.; Wang, A.; Xie, D.; Wang, Y. N.; Zhang, S.-L.; Geng, R.-X.; Cai, G.-X.; Li, S.; Zhou, C. H. Discovery of membrane active benzimidazole quinolones-based topoisomerase inhibitors as potential DNA-binding antimicrobial agents. *Eur. J. Med. Chem.* **2016,** *111*, 160–182.
10. Tabor, C. W.; Tabor, H. 1,4-Diaminobutane (putrescine), spermidine, and spermine. *Annu. Rev. Biochem.* **1976,** *45*, 285–306.
11. Porcheddu, A.; Giacomelli, G.; Piredda, I. Synthesis of Trisubstituted Formamidines: A Facile and Versatile Procedure. *J. Comb. Chem.* **2009,** *11*, 126–130.
12. Kim, H.; Rajamanickam, R.; Park, J.-W. Carbonation and Decarbonation of Non-aqueous Solutions with Different Compositions of Ethylene Glycol and Various Amidines. *Int. J. Greenh. Gas Control.* **2017,** *59*, 91–98.
13. Golub, T.; Dou, G.-Y.; Zeng, C.-C.; Bsecker, J. Y. One-Pot Anodic Conversion of Symmetrical Bisamides of Ethylene Diamine to Unsymmetrical gem-Bisamides of Methylene Diamine. *Org. Lett.* **2019,** *21*, 7961–7964.
14. Chandrasekhar, S.; Reddy, G. P. K.; Kiran, M. U; Nagesh, C.; Jagadeesh, B. Nucleoside Derived Amino Acids (NDA) in Foldamer Chemistry: Synthesis and Conformational Studies of Homooligomers of Modified AZT. *Tetrahedron Lett*. **2008,** *49*, 2969–2973.
15. Ramalingam, B.; Parandhaman, T.; Das, S. K. Antibacterial Effects of Biosynthesized Silver Nanoparticles on Surface Ultrastructure and Nanomechanical Properties of Gram-Negative Bacteria viz. Escherichia coli and Pseudomonas aeruginosa. *ACS Appl. Mater. Interfaces* **2016,** *8*, 4963–4976.
16. Lee, E.-Y.; Choi, D.-Y.; Kim, D.-K.; Kim, J.-W.; Park, J. O.; Kim, S.; Kim, S.-H.; Desiderio, D. M.; Kim, Y.-K.; Kim, K.-P.; Gho, Y. S. Gram Positive Bacteria Produce Membrane Vesicles: Proteomics-Based Characterization of Staphylococcus Aureus-Derived Membrane Vesicles. *Proteomics* **2009,** *9*, 5425–5436.
17. Gogra, A.B.; Yao, J.; Sandy, E.H.; Zheng, S; Zaray, G.; Koroma, B. M.; Hui, Z. Cell Surface Hydrophobicity (CSH) of Escherichia coli, Staphylococcus aureus and Aspergillus niger and the Biodegradation of Diethyl Phthalate (DEP) Via Microcalorimetry. *J. Am. Sci*. **2010,** *6*, 78–88.

18. Vavříková, E.; Polanc, S.; Kočevar, M.; Horváti, K.; Bősze, S.; Stolaříková, J.; Vávrová, K.; Vinšová, J. New fluorine-containing´ hydrazones active against MDR-tuberculosis. *Eur. J. Med. Chem.* **2011,** *46*, 4937–4945.
19. Ilyas, S.; Srivastava, R. R.; Kim, H. Disinfection Technology and Strategies for COVID-19 Hospital and Bio-medical Waste Management. *Sci. Total Environ.* **2020,** *749*, 141652.
20. Vilchez, F.; Martínez-Pastor, J. C.; García-Ramiro, S.; Bori, G.; Maculé, F.; Sierra, J.; Font, L.; Mensa, J.; Soriano, A. Outcome and Predictors of Treatment Failure in Early Post-Surgical Prosthetic Joint Infections Due to Staphylococcus Aureus Treated with Debridement. *Clin. Microbiol. Infect*. **2011,** *17*, 439–444.
21. Campoli-Richards, D. M.; Monk, J. P.; Price, A.; Benfield, P.; Todd, P. A.; Ward, A. Ciprofloxacin. A review of its antibacterial activity, pharmacokinetic properties and therapeutic use. *Drugs* **1988,** *35*, 373–447.
22. Wolfson, J. S.; Hooper, D. C. Fluoroquinolone Antimicrobial Agents. *Clin. Microbiol. Rev.* **1989,** *2*, 378–424.
23. Ross, A. G.; Benton, B. M.; Chin, D.; De Pascale, G.; Fuller, J.; Leeds, J. A.; Reck, F.; Richie, D. L.; Vo, J.; LaMarche, M. J. Synthesis of ciprofloxacin dimers for evaluation of bacterial permeability in atypical chemical space. *Bioorg. Med. Chem. Lett*. **2015,** *25*, 3468–3475.
24. Andrews, J. M. Determination of minimum inhibitory concentrations. *J. Antimicrob. Chemother*. **2001,** *48*, 5–16.
25. Li, Y.; Kumar, K. N. New Bactericidal Surgical Suture Coating. *Langmuir* **2012,** *28*, 12134–12139.

Chapter 3:

Biocidal polymer derived near white light-emitting carbonized polymeric dots for antibacterial and bioimaging applications

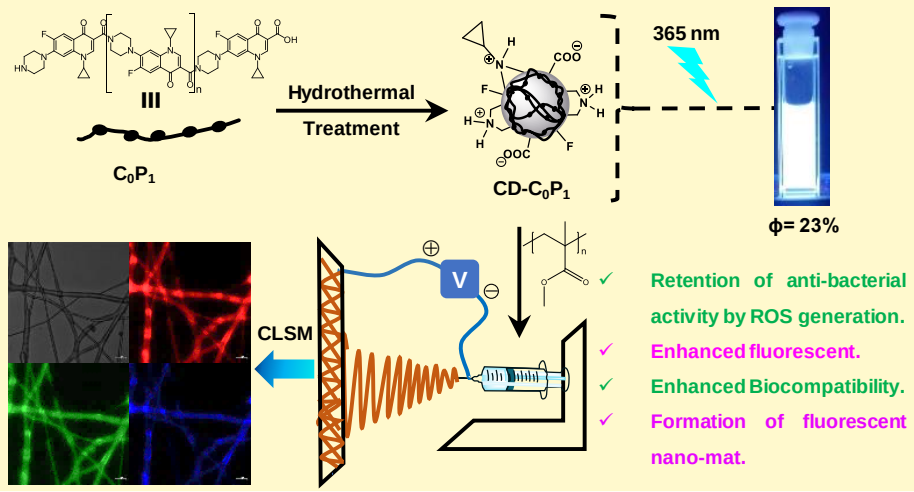

3.0. Introduction

Modern medicine has evolved since penicillin was discovered, and antibiotics have saved millions of lives.[1] Developing new antimicrobial drugs with low toxicity, significant biocompatibility, and excellent antimicrobial activity with newer mechanisms of action is urgently needed in an era of antibiotics- resistant bacteria.[2,3] Meanwhile, utilizing and improving existing antimicrobials is also essential.[4] Antimicrobial nanotechnology has emerged as a promising field recently.[5] In which carbon dots (CD) have been discovered to be a valuable material due to their outstanding optoelectronic properties and high biocompatibility.[6,7] CDs have emerged as new antimicrobial agents with a novel and complex mode of action which involve strong ROS generation, cell wall degeneration, photosensitization, electrostatic interaction and photothermal hyperthermia-induced programmed bactericidal activity, *etc*.[8,9,10]

While carbonized polymeric dots (CPD) is being extensively studied as new light emitting materials,[11] the CPD formation using polymers provides the apparent advantage of the ability to control size while synthesis by tuning the applied 'cracking force' and to retain the surface functionalities compared to the smaller precursor molecules.[12] For instance, Xi and co-workers have synthesized fluorescent CPD materials with different core sizes in one step by hydrothermal treatment of amide-abundant polyacrylamide for bioimaging purposes.[13] Recently, Maruthapandi *et al.* reported the formation of carbon nanocomposites using positively charged conducting polymers polyaniline and polypyrrole for their antibacterial property.[14] Jijie *et al.* have conjugated ampicillin antibiotic to post-synthesized CDs and observed retainment of antibacterial activity.[15] However, to the best of our knowledge, CPD of polymeric biocides with retention or enhanced activity has not been reported.

Recently, we have reported a true polymeric biocide **C_0P_1** having only drug units of a broad-spectrum antibiotic ciprofloxacin **1** *via* self-condensation reaction for antibacterial coating application.[16] In an attempt to synthesize highly biocompatible and fluorescent material with bioimaging application derived from true polymeric biocide, herein, we synthesized the CPD of **C_0P_1**[16] (**CPD-C_0P_1**) and optimized its synthesis for white light (WL) emission property (Scheme 3.0). Due to its higher molecular weight (973 KDa; DLS size: 1 µm (Figure 3.16, Section 3.2.3.2), biocidal polymer **C_0P_1** has been chosen as a carbon source for the synthesis of carbon nanocomposites that is capable of ROS for bacterial cell death.

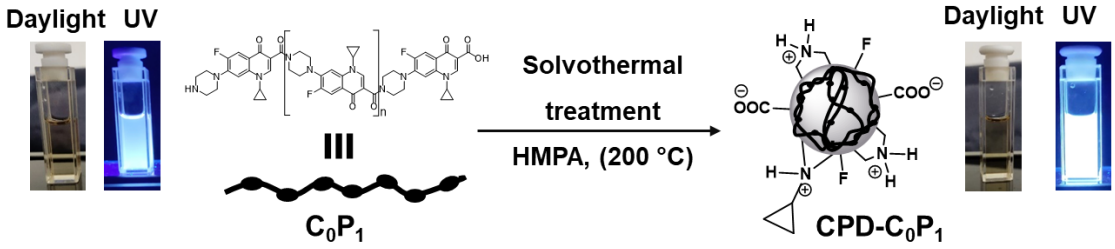

Scheme 3.0. Solvothermal mediated conversion of biocidal polymer to carbonized polymeric dot **CPD-C_0P_1.**

3.1. Results and Discussion

3.1.1. Synthesis of CPD-C_0P_1

For the optimization of solvothermal reaction conditions (Table 3.0), the polymer **C_0P_1**[16] was thermally treated along with different high boiling solvents (DMSO, EtOH,

and HMPA) at varying temperatures (150–220 °C) and time periods (24–72 h). After completion of the time, the reaction mixtures were scanned for the presence of emission (Table 3.0, Figure 3.0) and the size of the CPD through DLS analysis. The results revealed that DMSO and EtOH did not provide emissive CPD due to larger particles and precipitation, respectively (entries 1–9, Table 3.0). Interestingly, hexamethylphosphoramide (HMPA) has provided relatively smaller-sized CPDs with emissive nature (entries 10–14). A **CPD-C_0P_1** with a size of 120–270 nm was obtained under entry 11 (200 °C for 24 h), which was selected as an optimized condition due to its near WL color and higher emission intensity. The fluorescence intensity was observed to be affected by the reaction temperature and time period, even with HMPA. **CPD-C_0P_1** obtained under the entry 11 condition was taken forward for further characterization and antibacterial studies.

Synthetic procedure: Typically, 10 mg of **C_0P_1** was dissolved in 2 mL of hexamethylphosphoramide (HMPA) and stirred well for 10–15 min to obtain a homogenous solution. The resultant solution was then transferred to a 25 mL teflon-lined hydrothermal reactor and heated in the oven at 200 °C for 24 h. After cooling down to room temperature naturally to obtain a dark brown homogenous solution, the solution was diluted with H_2O (20 mL) and kept in a dialysis bag with MWCO 1000 Da against H_2O (250 mL × 2) water for 24 h to remove the HMPA, and the inner part of dialysis bag was lyophilized and recovered as a brownish powder (4.21 mg) **CPD-C_0P_1**. The best reaction condition was optimized by following the fluorescence generation and size of carbonized polymeric dots (DLS study) of the reaction mixture (Table 3.0).

Table 3.0. Optimization table for the generation of fluorescent **CPD-C_0P_1** from **C_0P_1**.[a]

Entry	*Reaction mixture*	*Solvent*	*Temperature (°C)*	*Time (h)*	*Emission*[b]	*DLS Particle size (nm)*
1.	**CPD-C_0P_1**	DMSO	180	24	No	500-1000
2.	**CPD-C_0P_1**	DMSO	200	24	No	500-1000
3.	**CPD-C_0P_1**	DMSO	220	24	No	450-1350
4.	**CPD-C_0P_1**	DMSO	200	48	No	600-1000

5.	**CPD-C_0P_1**	DMSO	200	72	No	550-1120
6.	**CPD-C_0P_1**	DMSO	220	48	No	520-1830
7.	**CPD-C_0P_1**	EtOH	150	24	No	ppt[c]
8.	**CPD-C_0P_1**	EtOH	150	48	No	ppt[c]
9.	**CPD-C_0P_1**	EtOH	180	24	No	ppt[c]
10.	**CPD-C_0P_1**	HMPA	180	24	360–570 nm λ_{max} = 436 nm Blue	426–860
11.	**CPD-C_0P_1**	HMPA	200	24	380–754 nm λ_{max} = 500 nm White-light	120–270
12.	**CPD-C_0P_1**	HMPA	220	24	-	340–672
13.	**CPD-C_0P_1**	HMPA	200	48	370–650 nm λ_{max} = 465 nm green	350–690
14.	**CPD-C_0P_1**	HMPA	200	72	375–560 nm λ_{max} = 478 nm green	260–760

[a]Concentration (0.5 mg/mL) of the reaction mixture was kept constant for all reactions, [b]excitation wavelength used was 365 nm, [c]precipitation was observed.

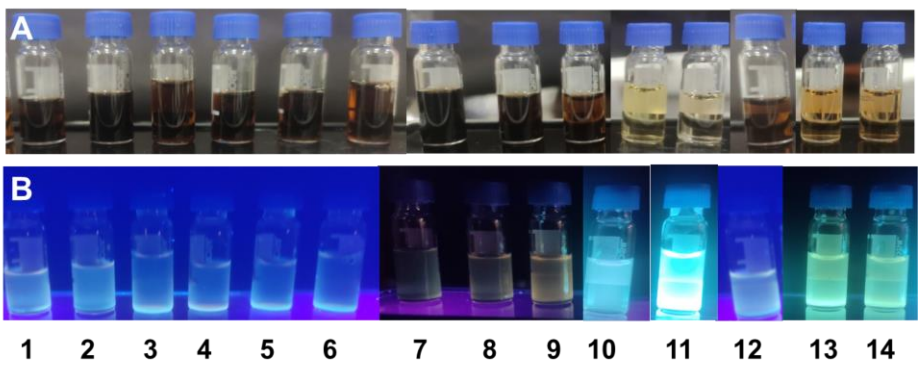

Figure 3.0. a) Daylight and b) under UV lamp irradiated imaging of reaction mixture at different optimization conditions (entries 1–14 in Table 3.0).

3.1.2. Characterization of CPD-C_0P_1:

The **CPD-C_0P_1** obtained from the biocidal polymer of ciprofloxacin **C_0P_1** has been characterized by a series of methods to analyze the structure and morphology (Figure 3.1). To figure out the composition and functionality present in the **CPD-C_0P_1**, a comparative ATR-FT-IR analysis of compounds **1**, **C_0P_1**, and **CPD-C_0P_1** were carried out (Figure 3.1a). The characteristic peaks of O–H, N–H, C=O (amide), and C=O (carboxylate) were observed at 3412, 3244, 1630, and 1467 cm^{-1}, respectively, indicating the fragmentation of ciprofloxacin unit in **C_0P_1**, thus generating both 3° and 2° amines and carboxylic acid which are in zwitterionic form. The peaks at 1486 and 1392 cm^{-1} indicate the formation of graphitic carbons (C=C).[17] Interestingly, the peak intensity significantly reduced at 1296 cm^{-1}, whereas the new peak at 1060 cm^{-1} was accredited to the presence of covalent C–F in residual polymer and semi-ionic C–F bond.[12] The peaks at 972 and 737 cm^{-1} indicate the C–C and C–H (bending), respectively.

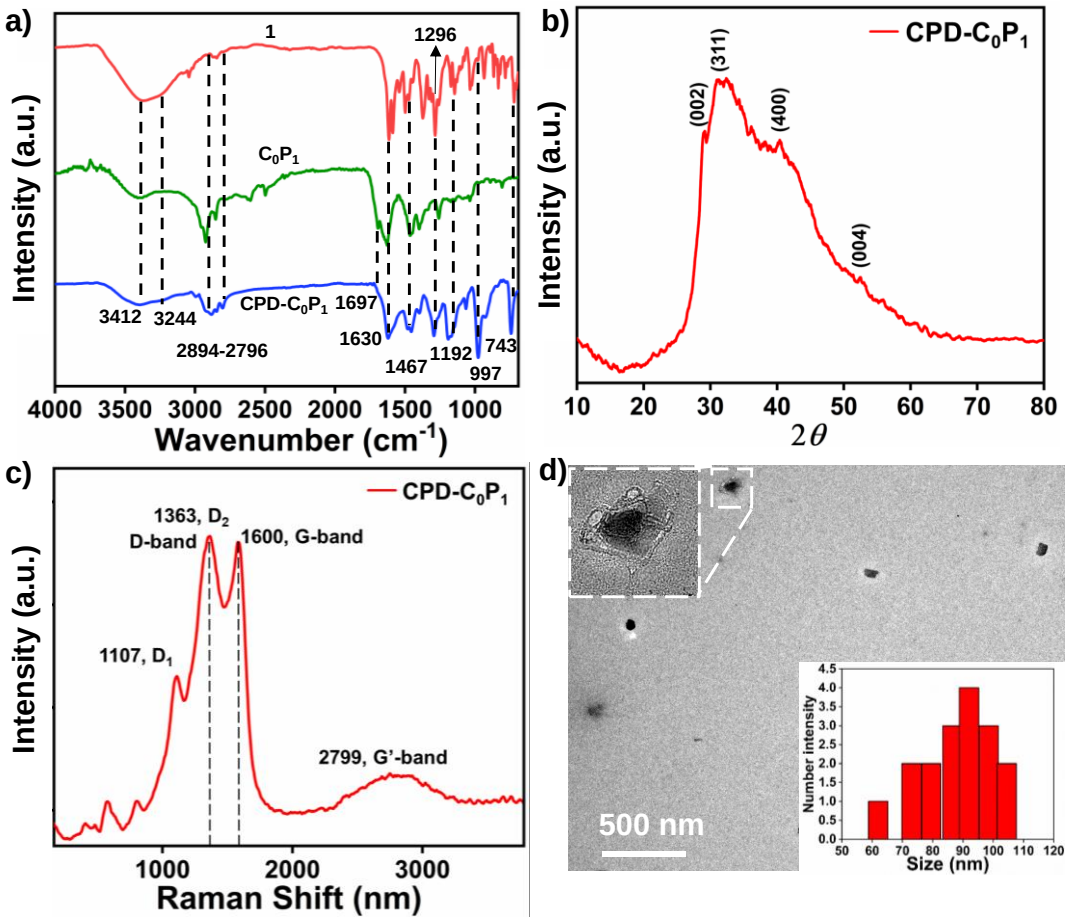

Figure 3.1. Characterization data of a) FT-IR of **1**, **C_0P_1**, **CPD-C_0P_1**, b) Raman, c) P-XRD, d) TEM imaging of **CPD-C_0P_1** (inset: particle size distribution graph).

The p-XRD spectrum of **CPD-C_0P_1** shows broad peaks with 002, 311, 400, and 004 plane peaks, where 002 corresponds to graphitic carbon in CD (Figure 3.1b). These peaks suggest that **CPD-C_0P_1** has an amorphous nature with a certain degree of crystallinity.[18] Additionally, **CPD-C_0P_1**'s Raman spectrum showed characteristic G- and D-bands, indicating the presence of both graphitic and amorphous carbon in CPD (Figure 3.1c). **CPD-C_0P_1** was examined by TEM for the size of the CPD particles (50–100 nm) and defects on the surface, suggesting the presence of polymers on the surface (Figure 3.1d), while HR-TEM confirmed the crystalline structure of **CPD-C_0P_1** (Section 3.2.3). The DLS analysis further corroborated the size of **CPD-C_0P_1** as ~50-120 nm (Figure 3.16, Section 3.2.3.2). Although the size of **CPD-C_0P_1** in the reaction mixture (size mentioned in table 3.0) and the separated solution was found to be different due to the presence of multispecies (carbon nanotube, polymer) in the reaction mixture after carbonization (Section 3.2.3, Figure 3.14). Further, the elemental composition was detected using TEM equipped with energy dispersive X-ray (EDX) spectrum for the elements carbon (C, 78%), nitrogen (N, 13%), oxygen (O, 9.3%), and fluorine (F, 0.23%) (Figure 3.15, Table 3.1).

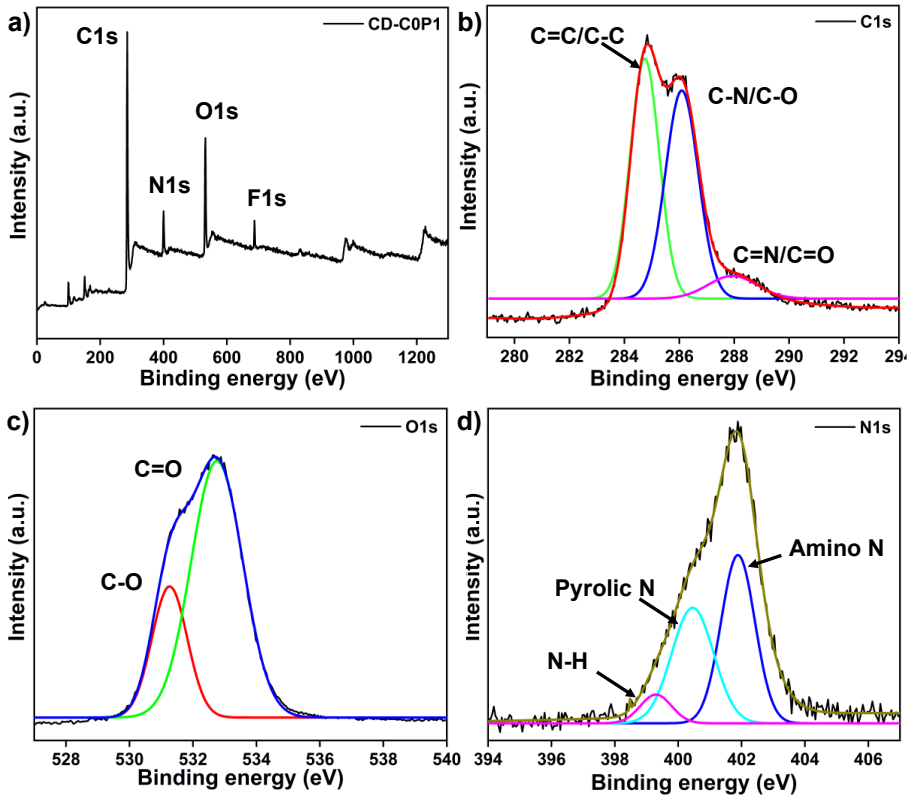

Figure 3.2. XPS survey of **CPD-C_0P_1** a) broad XPS scan, and the individual high-resolution spectra of b) C 1s, c) O 1s, d) N 1s.

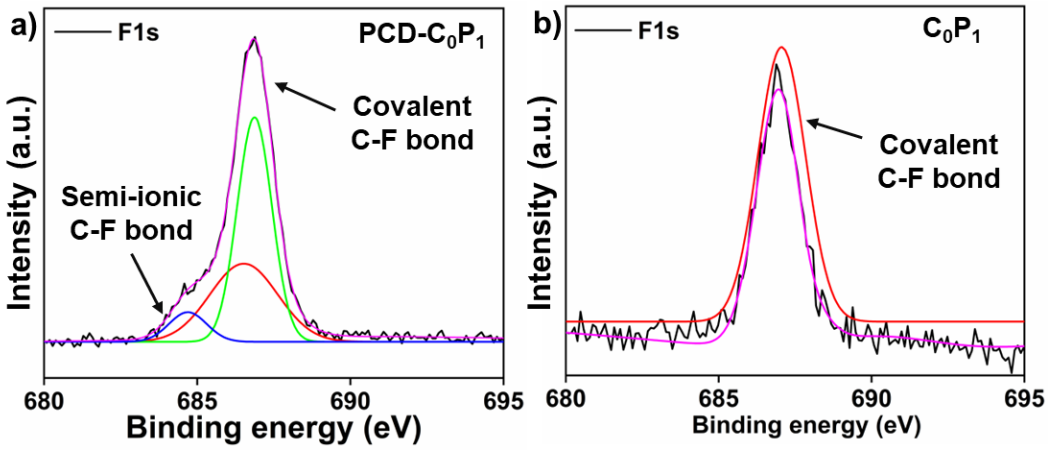

Figure 3.3. Individually fitted high-resolution XPS spectra of F1s for a) **CPD-C_0P_1**, b) **C_0P_1**.

In corroboration with EDX-spectrum, XPS data also indicate the presence of C 1s, N 1s, O 1s and F 1s elements present in CPD (Figures 3.2 and 3.3). In deconvoluted data for the C 1s, the binding energies for C=C/C–C at 284.71 eV, C–N/C–O at 286.14 eV, and C=N/C=O at 288.02 eV suggest the presence of sp^2 hybridized carbon, while the peaks at 286.14 and 288.02 eV indicate the presence of retentive polymer at the surface of **CPD-C_0P_1** (Figure 3.2b).[19,20] Similarly, individual curve fittings showed the binding energies for C–O and C=O at 531.22 and 532.77 eV, respectively, indicating the presence of carboxylate functional groups (Figure 3.2c).[21] A curve fitting for N 1s revealed that amino-, amido-, and positively-charged-N have binding energies at 399.2, 400.4, and 401.8 eV, respectively, ascribed to the polymeric structure of **C_0P_1** and the surface functional group present on its surface (Figure 3.2d,).[22,23] Moreover, the full scan spectrum of **C_0P_1** (Section 3.2.3.3, Figure 3.17) shows a trace amount of fluorine as indicated by F 1s peak intensity which has been observed to increase after the formation of **CPD-C_0P_1** (Figure 3.2a). Further, individually fitted F1s data also revealed semi-ionic C-F bond formation in **CPD-C_0P_1** which was found absent in **CPD-C_0P_1** spectra (Figure 3.3).[24]

To illustrate the unique emissive nature of CPD, the photophysical properties of **CPD-C_0P_1** were compared with **C_0P_1**. All the spectra were recorded in DMF (50 µg/mL). The UV−vis spectrum of precursor polymer **C_0P_1** has shown absorption at 320–400 nm, while the **CPD-C_0P_1** exhibited broad absorption at 320–500 nm (Figure 3.4a). The broad absorption in the visible region is due to CPD while the two peaks observed at 345 and 368 nm correspond to π–π* and n–π* transitions. The peak at 281 nm has disappeared for **CPD-C_0P_1**, possibly due to the carbonization of the polymeric structure.

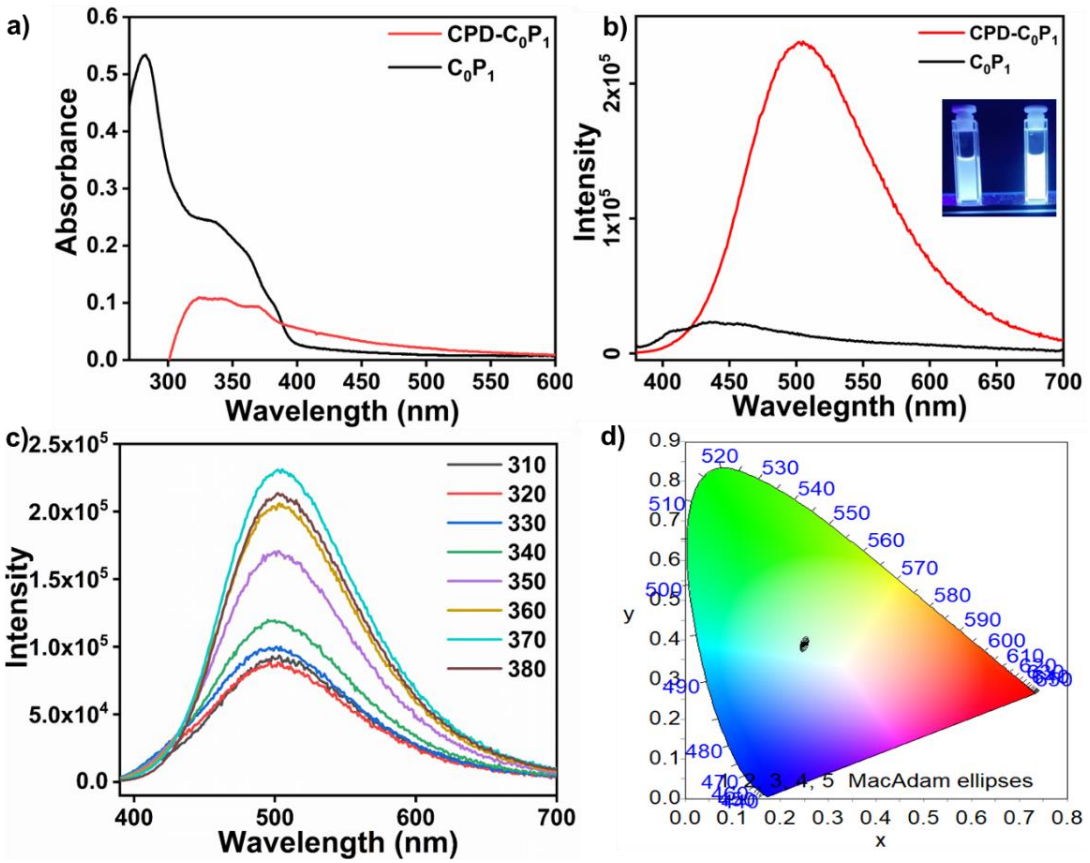

Figure 3.4. a) The UV–vis and b) fluorescence (λ_{ex} = 370 nm) spectra of **C_0P_1** and **CPD-C_0P_1** (Inset: digital photo of solutions under UV lamp), c) fluorescence spectra at different excitation wavelengths for **CPD-C_0P_1**. d) CIE plot for **CPD-C_0P_1**. Concentration 50 µg/mL in DMF.

The fluorescence spectra of **C_0P_1** showed a very weak emission (400–500 nm), whereas the **CPD-C_0P_1** showed a strong and broad emission peak (400–700 nm), owing to the CPD (Figure 3.4b). Interestingly, the emission was found to show WL with excitation-independent (310–380 nm) emission, unlike typical CDs (Figure 3.4c). The near WL emission was illustrated by the CIE chromaticity diagram with CIE coordinates of 0.25 and 0.38 (Figure 3.4d). Lifetime measurement was performed for the emission of **CPD-C_0P_1** using a time-correlated single photon counting method for further analysis of steady-state fluorescence emission. The decay kinetics was successfully fitted to the sum of three exponential components with different time decay of τ_1, τ_2, and τ_3 representing 2.12, 7.49, and 0.26 ns, respectively (Figure 3.18, Table 3.2, Section 3.2.4.1). The quantum yield estimation revealed a moderate value of 23% against quinine sulfate as the reference (Section 3.2.4.2, quantum yield calculation).

3.1.3. Antibacterial Activity

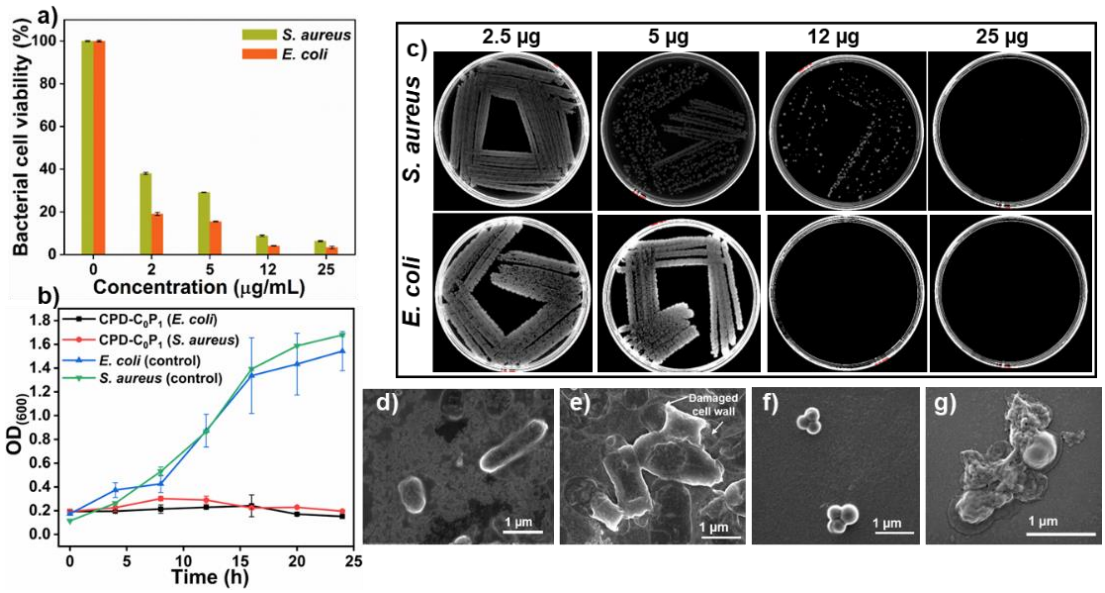

Figure 3.5. a) Bacterial cell viability (%) of *E. coli* and *S. aureus* evaluated after treatment with different concentrations of **CPD-C_0P_1** after 24 h. b) Time-dependent antibacterial activity of **CPD-C_0P_1** at MIC (12 and 25 μg/mL) against *E. coli* and *S. aureus*. c) Photographs of *E. coli* and *S. aureus* after treatment with different concentrations of **CPD-C_0P_1** for 24 h. FE-SEM imaging of d) *E. coli* (control), e) after **CPD-C_0P_1** treatment, f) S. aureus (control), and g) after **CPD-C_0P_1** treatment.

The antibacterial activity of **CPD-C_0P_1** was evaluated against *Staphylococcus aureus (S. aureus) and Escherichia coli (E. coli)* (for experimental details, see materials and methods) with minimum inhibitory concentration (MIC_{90}) of 25 and 12 μg/mL, respectively (Figure 3.5a). A time-dependent bacterial growth inhibition study was performed by taking the corresponding MIC of **CPD-C_0P_1** and further monitored by optical density (OD_{600}) values measured for cultured bacteria at different times (Figure 3.5b). While *S. aureus* and *E. coli* in the control group increased significantly at the 4^{th} and 8^{th} h, respectively, and reached a peak at the 16^{th} h for both cases. In contrast, the growth rate of both types of bacteria co-cultured with **CPD-C_0P_1** showed no apparent OD_{600} increase. This suggests that the **CPD-C_0P_1** shows broad-spectrum activity. For further confirmation, the standard colony counting method was performed to determine the survival of bacteria treated with **CPD-C_0P_1** for 24 h (Figure 3.5c). The results indicated an apparent decline in bacterial growth with an increasing dose of **CPD-C_0P_1**. At the MIC values, complete bacterial growth inhibition was found. Cellular damage caused by **CPD-C_0P_1** was examined by FE-SEM analysis of the **CPD-C_0P_1** treated

bacteria. This indicated the bacteria were killed by ruptured cell walls (Figure 3.5d-g). Additionally, the **CPD-C_0P_1** was observed to have adhered specifically to the cell wall of bacteria governed by surface adherence phenomena,[26] which may contribute to its biocidal and bacterial-specific properties (Figure 3.19a,b, mechanism of action). The ability of **CPD-C_0P_1** to damage cell walls and produce ROS may be attributed to several mechanisms, including electrostatic interactions between bacteria and **CPD-C_0P_1**. This has been observed by the difference in the surface zeta potential of bacteria before and after treatments suggesting the adherence of CPDs to the bacterial cell wall (Figure 3.19c).[11] To verify the ROS generation, a time-dependent ROS determination study was performed using DCFH-DA[25] (for details, see material and methods). Intrinsic generation of ROS has been observed as the major apoptotic factor for bacterial killing in the presence of **CPD-C_0P_1** (Figure 3.20, mechanism of action of **CPD-C_0P_1**).

3.1.4. Cytocompatibility Assay:

Cytocompatibility assay was conducted on mouse fibroblast cells and data are provided in Figure 3.6. Our previous study showed that the precursor biocidal polymer **C_0P_1** has higher cytocompatibility than ciprofloxacin **1** at a concentration of 1 µg/mL.[16] Interestingly, the **CPD-C_0P_1** has shown higher biocompatibility even at unexpectedly higher concentrations *i.e.*, 500 µg/mL as up to 90% of cells are non-affected. Intriguingly, the **CPD-C_0P_1** was found to be highly biocompatible with 10 and 20 times higher concentrations against bioactive concentrations of *S. aureus* and *E. coli*, respectively. Hence, as originally hypothesized, the biocompatibility of biocidal polymers could be greatly improved by using carbonized polymeric dots.[27]

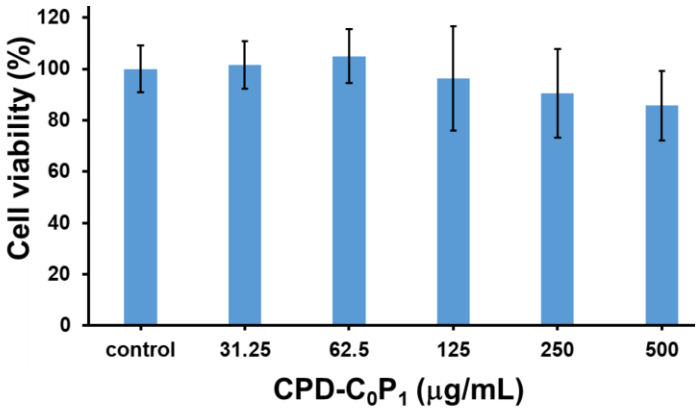

Figure 3.6. Cytocompatibility assay of **CPD-C_0P_1** at different concentrations on mouse fibroblast cells.

3.1.5. Embedding CPD-C_0P_1 in PMMA matrix for fiber formation and their antibacterial profile

To demonstrate the practical applications and to fabricate the antimicrobial nanofibers (NF) mat with bio-imaging (RGB colors) capability, the **CPD-C_0P_1** was combined with polymethylmethacrylate (PMMA) matrix and electrospun to obtain nanofibers (for details, see Section 3.2.7).[28] The NF were prepared by a DMF solution (with the optimized concentration of 100 mg in 1 mL) containing PMMA/**CPD-C_0P_1** (93:7 *w/w*) as well as only PMMA as control. NF containing PMMA blue fluorescence minimally under confocal microscopy (Figure 3.7a), whereas, NF containing **CPD-C_0P_1** fluoresced red, green, or blue based on the excitation filter used (TRITC, FITC, and DAPI) and emerged as near WL emitting NF (Figure 3.7b). The morphology and size of both NFs were characterized by FE-SEM and AFM analysis (Section 3.2.7). Nanofibers with smooth surfaces with a width and height of 200-400 and ~300-500 nm, respectively have been found for both PMMA and PMMA/**CPD-C_0P_1**. These results imply that the presence of **CPD-C_0P_1** in PMMA did not affect the nanofiber formation significantly.

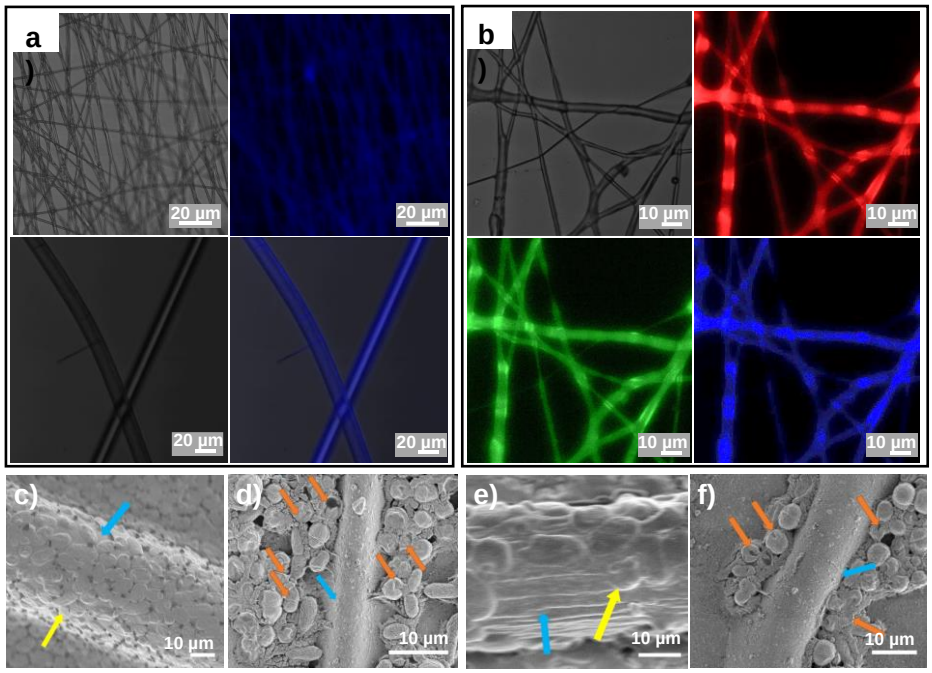

Figure 3.7. Confocal microscopy images of electrospun nanofibers of a) PMMA, b) PMMA/**CPD-C_0P_1** 93:7 wt ratio (Red, Green, Blue excitation wavelength 560, 495, 365 nm respectively). FE-SEM imaging (c) *E. coli* with PMMA NF, (d) *E. coli* with PMMA/**CPD-C_0P_1** NF, (e) *S. aureus* with PMMA NF, and (f) *S. aureus* with PMMA/**CPD-C_0P_1** NF.

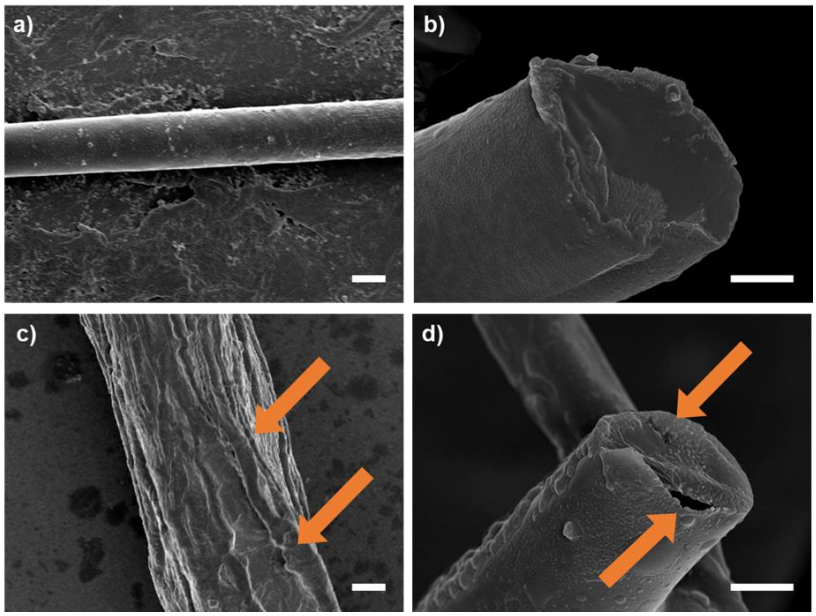

Figure. 3.8. Morphology of PMMA/**CPD-C$_0$P$_1$** fibres a),b) at 0 h, c),d) at 12 h of release. Scale bar, 1 µm.

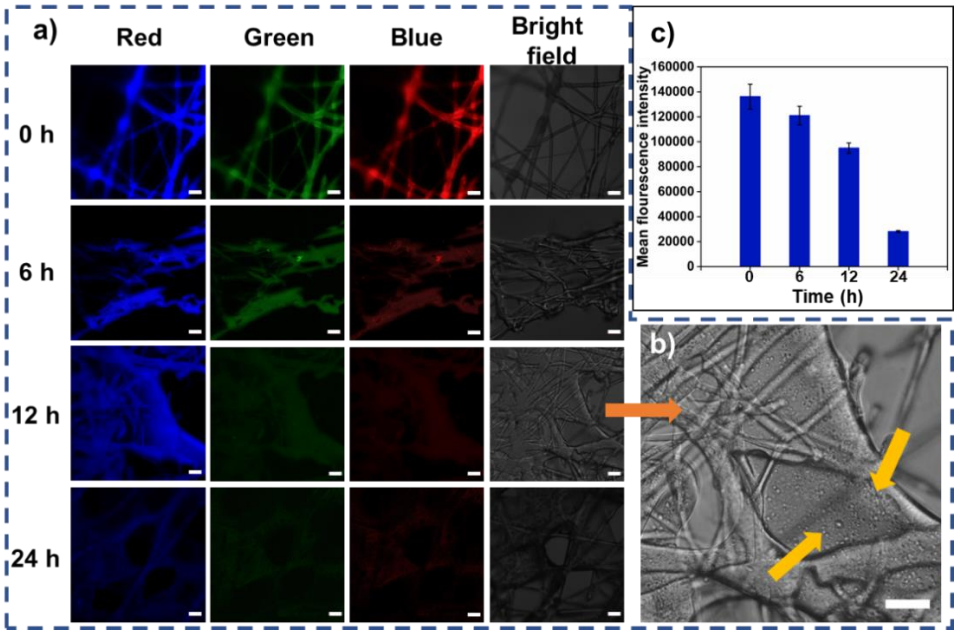

Figure 3.9. a) confocal laser scanning microscopy (CLSM) images of PMMA/**CPD-C$_0$P$_1$** NF with time after stirring with PBS buffer for 24 h. b) Zoomed image of fibers in a bright field after 12 h stirring in PBS buffer, yellow arrow indicates porosity in the fibers after the release of **CPD-C$_0$P$_1$**. All scale bars, 10 µm. c) Mean fluorescence intensity profile of fibers depicted in (a). (Red, Green, Blue excitation wavelength 560, 495, 365 nm respectively).

The antibacterial activity of PMMA/**CPD-C$_0$P$_1$** was determined by the release of **CPD-C$_0$P$_1$** from the NF using FE-SEM (Figure 3.8) and CLSM (Figure 3.9) and bacterial growth inhibition measured by visual turbidity readout of **CPD-C$_0$P$_1$** (Figure 3.9). For

the release study, the fibers were kept for continuous stirring for 24 h in PBS buffer and the fragments of the fibers were collected with respect to time (0, 6, 12, and 24 h) and observed for fluorescence intensity by using CLSM, as the fluorescence in the fibers indicates the presence of **CPD-C_0P_1**. The fluorescence intensity of the fibers reduced gradually with time (figure 3.9a,c). Further, the zoomed image of fibers collected at 12 h intervals revealed the porosity in fibers which may be due to the release of preblended **CPD-C_0P_1** (Figure 3.9b). Further, in both cases *S. aureus* and *E. coli*, the NFs with **CPD-C_0P_1** showed higher biocidal activity by inhibiting bacterial growth at different time points (0, 6, and 12 h) with regards to $OD_{(600)}$ (Figure 3.10). However, rapid growth of bacteria was observed with bare PMMA fibers. Moreover, over 90% of bacterial colonies were inhibited within 12 h by the aliquots of PMMA/**CPD-C_0P_1** streaked on solidified agar plates (Figure 3.11), suggesting that **CPD-C_0P_1** is constantly released from PMMA/**CPD-C_0P_1**. After 12 h of incubation in a bacterial medium, fiber-bacterial interactions between PMMA and PMMA/**CPD-C_0P_1** were visualized by FE-SEM. It is shown in Figure.3.7c and e that *E. coli* and *S. aureus* soak through a bare PMMA NF. However, PMMA/**CPD-C_0P_1** exhibits biocidal and antiadhesive properties since no bacteria were found to adhere to it (Figures 3.7d,f). In addition, all the bacteria present around PMMA/**CPD-C_0P_1** NFs displayed damaged cell walls. It appears that the presence of **CPD-C_0P_1** in inert PMMA NF may confer antibacterial activity to PMMA/**CPD-C_0P_1** NF. The *E. coli* and *S. aureus* treated with PMMA/**CPD-C_0P_1** NFs were further checked with fluorescence microscopy which indicated that **CPD-C_0P_1** was successfully taken up by the bacterial cells showing the potential to be used as a fluorescent imaging agent for bacterial cells (Figure 3.12 a,b).

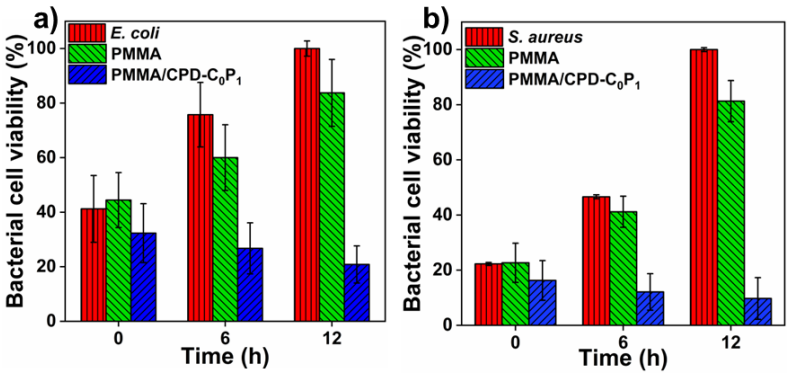

Figure 3.10. Antibacterial activity of PMMA and PMMA/**CPD-C_0P_1** against a) E. coli and b) S. aureus. Experiment has been performed in triplicate. Experiment performed in triplicate $P<0.05$

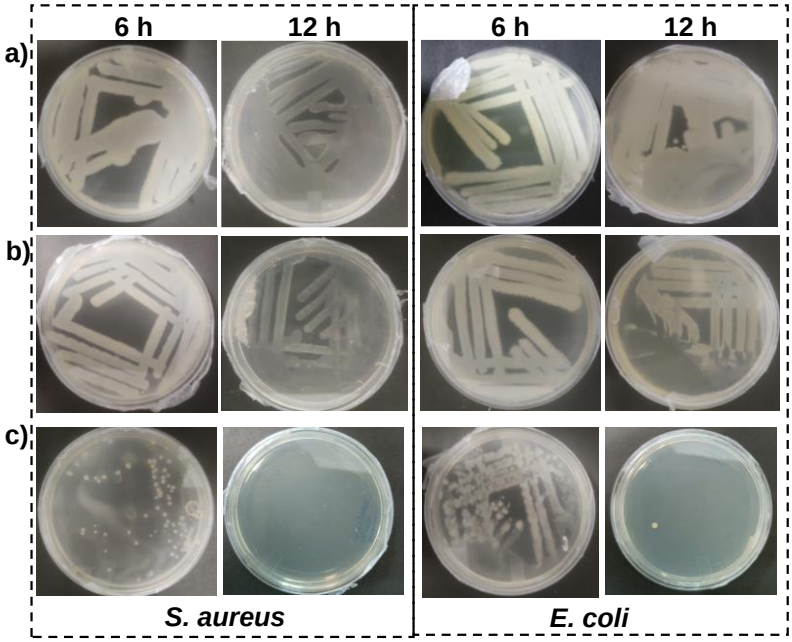

Figure 3.11. Agar disc diffusion assay of aliquots at different time intervals (6 and 12 h) of a) control b) PMMA and c) PMMA/**CPD-C_0P_1** fibers against *E. coli* an *S. aureus.*

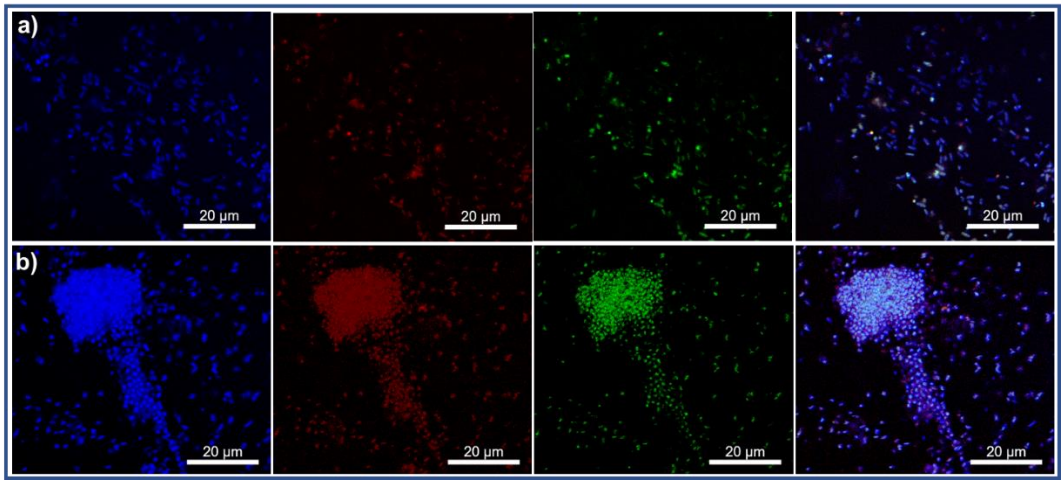

Figure 3.12. CLSM images of PMMA/ **CPD-C_0P_1** treated a) *E. coli* and b) *S. aureus* after 6 h. Scale bar 20 µm.

3.2. Materials and methods:

3.2.1. General Information

Ciprofloxacin and hexamethylphosphoramide (HMPA) were purchased from TCI chemicals India Ltd. Phosphate-buffered saline (PBS), lysogenic broth (LB), and Luria−Bertani agar (LB agar) were purchased from Himedia. Polymer **C_0P_1** was synthesized as given in the previous report.[16] AR grade dimethylformamide (DMF), dimethyl sulfoxide (DMSO), and ethanol (EtOH) were purchased from Merck India Ltd.

was purchased from Spectrochem India Ltd. Dialysis membrane used of MWCO ~ 1000 Da, 20 mm dry was purchased from Spectrum labs. *S. aureus* ATCC 25923 and *E. coli* ATCC 25922 were purchased from Microbial Type Culture Collection and Gene Bank (MTCC), Chandigarh, India.

3.2.2. General experimental details

Transmission spectra were measured using Attenuated total reflection Fourier transform infrared (ATR–FT–IR) Bruker Vertex 70 in a range of 4000–400 cm^{-1}. Selected absorption bands are reported in wavenumbers (cm^{-1}). Signal designations: s (strong), m (medium), and w (weak).

X-ray diffraction (XRD) was carried out on Eco D8 Advance Bruker powder X-ray diffraction (PXRD) with a Cu Kα radiation source (λ = 0.15406 nm). The instrument was operated at 40 kV and 25 mA at scanning steps of 0.02 in the 2θ.

Raman spectroscopy was carried out using a WITec 300R Raman spectrometer. A 532 nm Nd:YAG laser has been used to irradiate the nanodots using a 100X objective with a numerical aperture (NA) of 0.9 um.

Dynamic light scattering (DLS) was performed to determine the particle size distribution using Zetasizer Nano ZSP; Model−ZEN5600; Malvern Instruments LTD., Worcestershire, UK. First, a stock solution of 1 mg/ mL of **CPD-C_0P** was prepared in DD water which was further diluted 10 times before DLS measurement. Measurement was performed in a quartz cuvette of 3 mL capacity. The concentration of **CPD-C_0P_1** for TEM and DLS measurement was the same. The experiment was done with 30 seconds of equilibrium time and 30 seconds of measurement with 3 times repeating the cycle for each sample.

Transmission Electron microscopy (TEM) images were acquired on a JEOL, JEM−2100, (Tokyo, Japan) operating at 200 kV. Samples for TEM were prepared by drop-casting 7 µL of diluted sample suspension on a 300 mesh TEM grid, and excess solution was gently wicked off with filter paper. Samples were dried under an IR lamp for 7 h and stored under vacuum conditions before measurement. Size analysis of images has been done using the software image *J*.

Scanning electron microscopy (SEM) analysis was performed on model JSM6100 (JEOL) with an image analyzer. The dried coated thread was mounted on stubs with the help of double-stick tape and sputtered with a film of gold.

Confocal microscopy for the fibers was done to visualize the fluorescence intensity and RGB emission by using a Zeiss LSM880 confocal microscope (Carl Zeiss, Thornwood, New York).

UV–visible (UV–vis) spectra were recorded using Shimadzu UV−vis spectrophotometer. The absorption maxima (λ_{max}) are reported in nm. The spectra were evaluated in a quartz cuvette of 1 cm at 298 K.

Photoluminescence (PL) measurements were carried out on Edinburg FS 5 spectrofluorometer.

Time correlated single-photon counting (TCSPC) study was carried out using a Deltaflex modular fluorescence lifetime system (HORIBA Scientific).

X-ray photoelectron spectroscopy (XPS) experiments were performed using a Thermofisher scientific kα surface analysis spectrometer, using monochromatic Al Kα radiation (1486.6 eV) operating at an accelerating X-Ray power of 50W15KV. Before the measurement, the sample was outgassed at 25 °C in a UHV chamber (<5 x10^{-7} Pa). The sample charging effects were compensated by calibrating all binding energies (BE) with the adventitious C 1s peak at 284.6 eV. This reference gave BE values with an accuracy of ±0.1 eV. The sample was prepared by film formation in silicon wafers.

3.2.3. Size and morphology analysis of CPD-C_0P_1

3.2.3.1. *TEM, HR-TEM & TEM-EDX data*

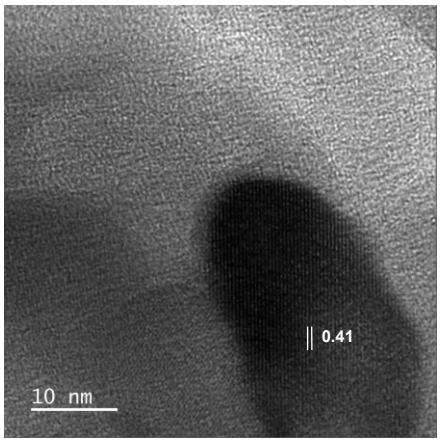

Figure 3.13. HR-TEM images of **CPD-C_0P_1**.

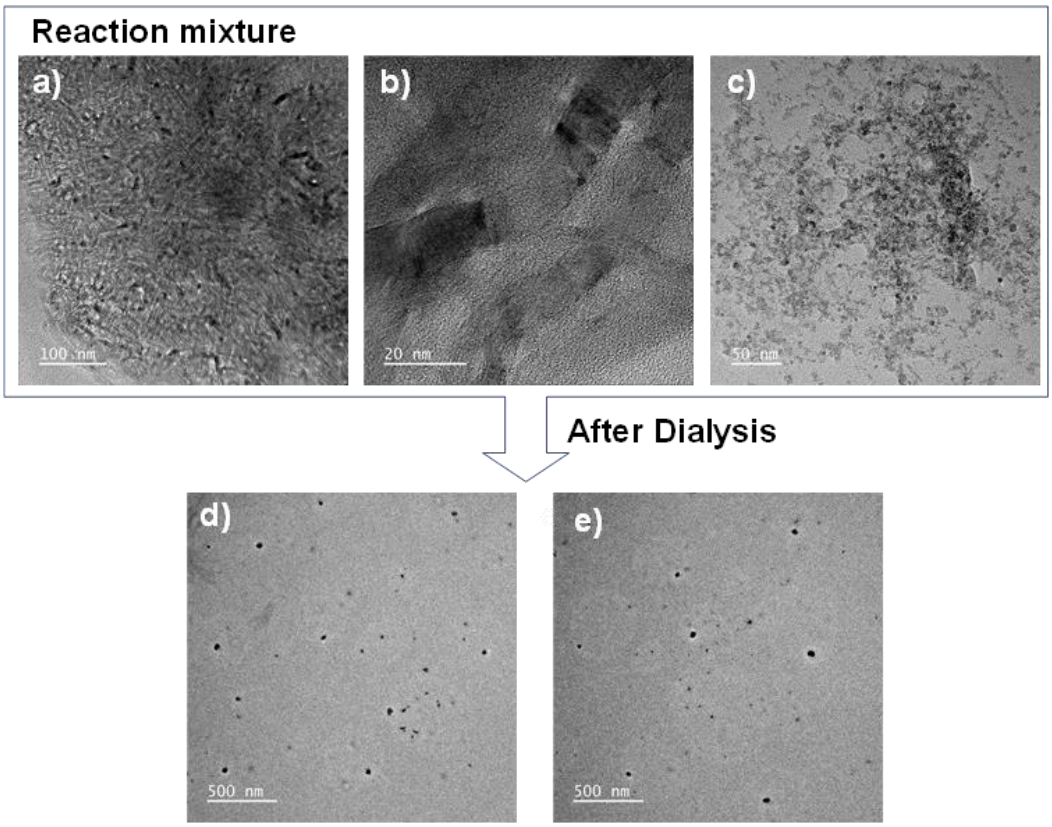

Figure 3.14. TEM images of samples from the reaction mixture and dialysis-separated mixture. a) Carbon nanotubes, b) HR-TEM of carbon nanotubes, c) carbon dot polymer mixture, d) and e) Carbon nanodots.

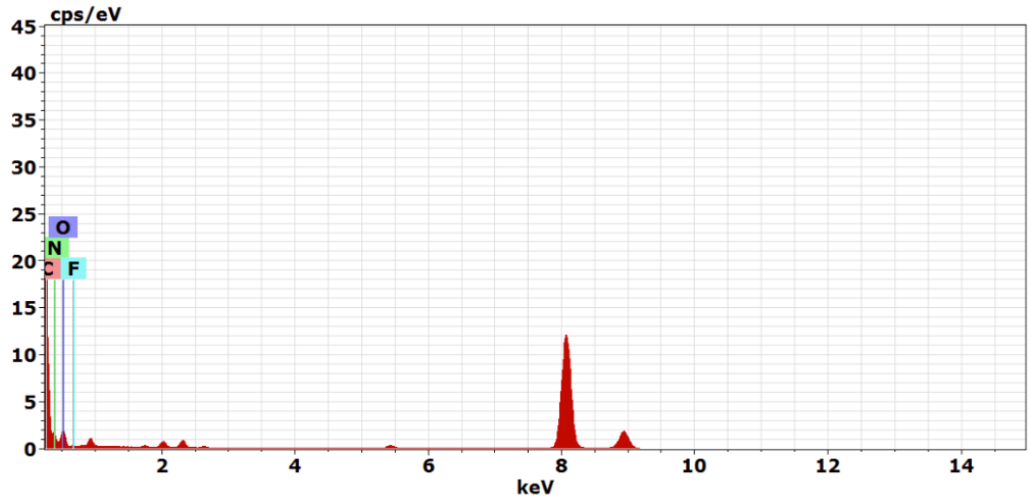

Figure 3.15. Elemental scanning of **CPD-C_0P_1**.

Energy dispersive X–ray (EDX) spectrum was measured using a transmission electron microscope (TEM) equipped with an EDX facility. The elemental composition and relative abundance are given in Table 3.1.

Table. 3.1. Elemental scanning ratio (%) of **CPD-C_0P_1**.

Element	series	[wt.%]	[norm. wt.%]	[norm. at.%]	Error in wt.% (1 Sigma)
Carbon	K-series	77.58	77.58	81.01	4.32
Nitrogen	K-series	12.87	12.87	11.52	0.74
Oxygen	K-series	9.33	9.33	7.31	0.54
Fluorine	K-series	0.23	0.23	0.15	0.04

3.2.3.2 DLS data

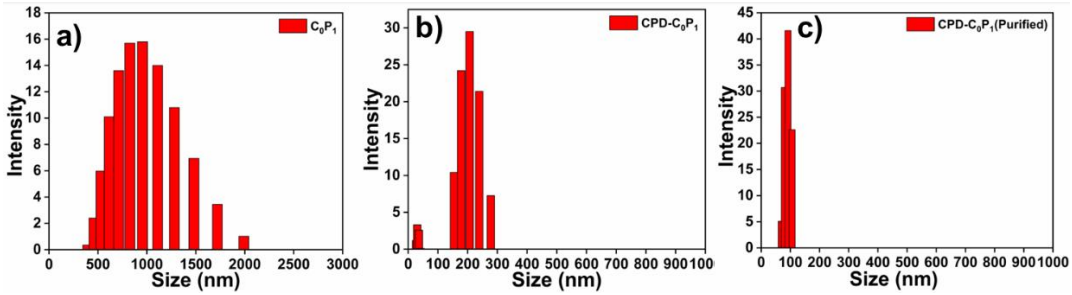

Figure. 3.16. Number distribution graphs of a) **C_0P_1** and b) **CPD-C_0P_1** (reaction mixture) c) **CPD-C_0P_1** (after purification) generated by DLS analysis.

3.2.3.3. XPS data

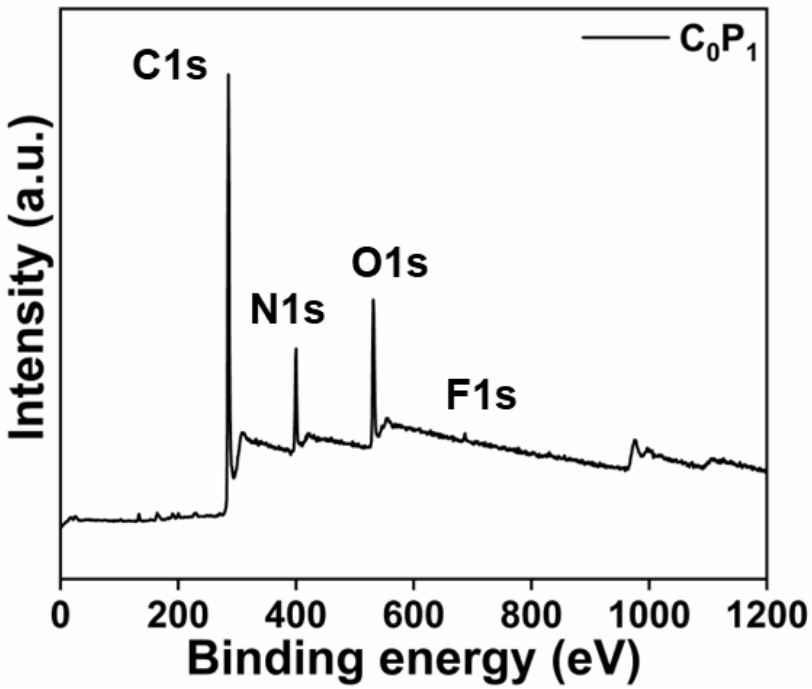

Figure 3.17. XPS survey of **CPD-C_0P_1** a) broad XPS scan, and the individual high-resolution spectra of b) C 1s, c) O 1s, d) N 1s.

3.2.4 Photophysical study

3.2.4.1. Lifetime decay study

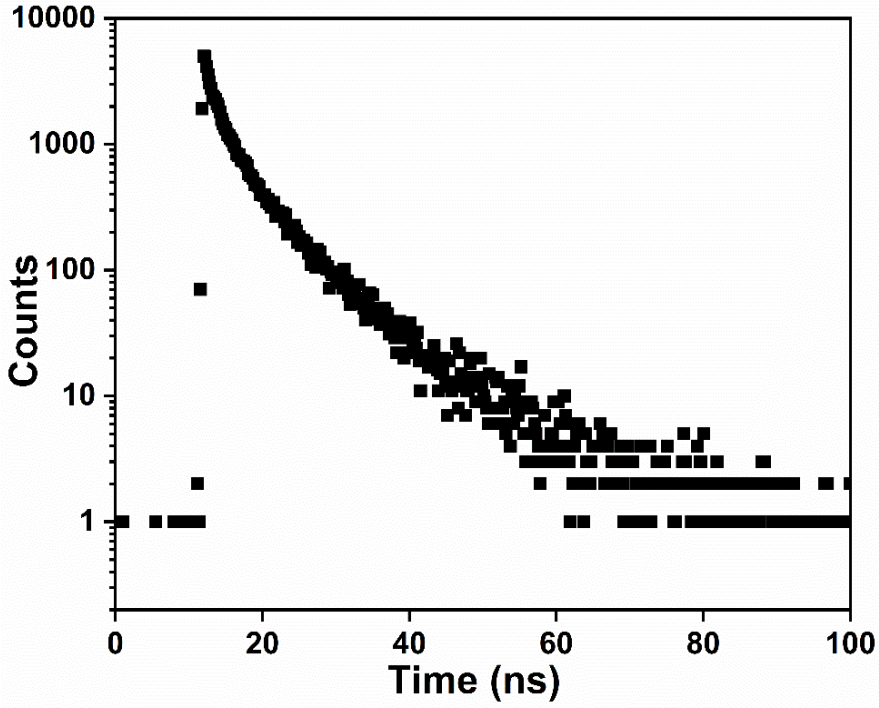

Figure 3.18. Photoluminescence lifetime intensity decay of **CPD-C_0P_1** in DMF solution (excitation at 370 nm, emission at 400 nm).

Table 3.2. The photoluminescence decay of **CPD-C_0P_1**

	τ/ns	**A_i/%**
τ_1	2.12	41.45
τ_2	7.48	45.08
τ_3	0.26	13.47

The average photoluminescence lifetime was obtained by the below-mentioned formula (eq. 3.0).

$$\tau = \frac{A_1\tau_1+A_2\tau_2+A_3\tau_3}{A_1+A_2+A_3} \qquad \text{(eq. 3.0)}$$

3.2.4.2. Quantum yield Calculation

The quantum yield calculation was determined by the comparative method with quinine sulfate (Φ_F = 0.54 in 0.1 M H_2SO_4)[29,30] as a standard using the below equation (eq. 3.1).

$$QY_{ref} = QY_{ref} \times \frac{OD_{ref}}{OD_{sam}} \times \frac{I_{sam}}{I_{ref}} \times \frac{\eta_{sam}}{\eta_{ref}} \quad \text{(eq. 3.1)}$$

3.2.5. Experimental procedures for antimicrobial assay and biocompatibility study

3.2.5.1. MIC_{90} determination of **CPD-C_0P_1** was performed by taking turbidity measurements and colony counting methods. All the samples were either well dispersed or dissolved in media to prepare the stock solution (1 mg/mL) using DMSO (not more than 5%) and nutrient media for the dissolution of **CPD-C_0P_1** and **C_0P_1**. All the solutions were then further diluted by nutrient broth media in 96 well plates from 2 to 50 µg/mL. And checked for any absorbance at 600 nm. Both *E. coli* and *S. aureus* were then transferred to the 96 well plates 250 µL in each well (1.5×10^7 to 1.5×10^8 CFU/ mL). The plates were incubated for 12–24 h at 37 °C. Then the MIC_{90} was determined by visual turbidity readout (BioTeck Synergy HTX Multimode Reader) at 600 nm. Vehicle and reference agents (ciprofloxacin **1** and **C_0P_1**) were used in every test as negative and positive controls. Readings were recorded with different time periods (4, 8, 12, 16, 20, 24 h). MIC values reported are the minimum concentration needed to inhibit 90% of bacterial growth. MIC was determined by measuring bacterial growth at OD_{600} after 12 h by following standard protocols. All reported values represent a minimum of triplicate experiments. Bacterial viability was calculated using the below formula (eq. 3.2) where BV stands for bacterial cell viability and $BVOD'_{600}$ and $BVOD_{600}$ correspond to the OD_{600} of the bacterial culture with different concentrations of **CPD-C_0P_1** and without **CPD-C_0P_1**, respectively.[31]

$$\tau = \frac{BVOD'_{600}}{BVOD_{600}} \quad \text{(eq. 3.2)}$$

Further, to evaluate the bacterial survival rate, the inoculum with different concentrations of **CPD-C_0P_1** from 96 well plates was streaked on solidified LB agar Petri plates and placed for incubation at 37 °C for 24 h. Colonies were counted per cm^2.

3.2.5.2. Biocompatibility study. The cytocompatibility of **CPD-C_0P_1** was evaluated on the fibroblasts cell lines L929 using 3-(4,5-dimethylthiazol-2-yl)-2,5-diphenyltetrazolium bromide (MTT) assay. Cells were cultured in 96 well plates for 24 h in Dulbecco's modified Eagle medium (DMEM) with 10% v/v FBS and 1% v/v penicillin−streptomycin at 37 °C in a 5% CO_2 incubator. DMEM containing the **CPD-C_0P_1** with different concentrations (0, 31.25, 62.5, 125, 250, and 500 µg/mL) was

incubated for 72 h at 37 °C, then added to the cells and treated for 48 h. MTT was added and incubated for 4 h. The optical density of dissolved formazans crystals was quantified at 570 nm using spectrophotometric analysis (Tecan Infinite M Plex). The cytotoxicity effect in each treatment can be expressed as a percentage of cell viability relative to the untreated control cells and is defined as,

Cell viability % = [Absorbance of treated cells]/[Absorbance of control cells] × 100.

3.2.6. Mechanism of antibacterial activity

3.2.6.1. Identification of electrostatic interaction by surface zeta potential.

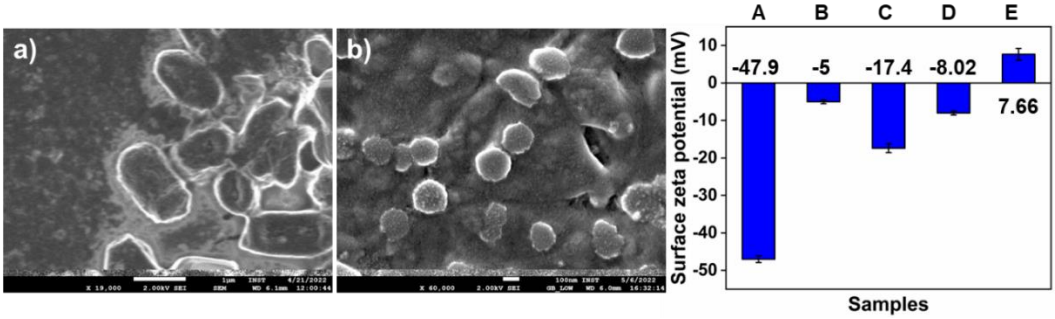

Figure 3.19. FE-SEM images of **CPD-C_0P_1** treated a) *E. coli*. and b) *S. aureus* after 1 h of incubation at 37 °C. c) Surface zeta potential measurement for A) *E. coli* B) **CPD-C_0P_1** treated *E. coli* C) *S. aureus* D) **CPD-C_0P_1**treated *S. aureus* E) **CPD-C_0P_1** in PBS Buffer.

3.2.6.2. Procedure for time-dependent ROS determination assay was performed by using a 2′,7′-dichlorodihydro fluorescein diacetate (DCFH-DA) probe. DCFH-DA was ideally diffused through the bacterial cell membrane into the cell and was deacetylated by esterases to form non-fluorescent 2,7-dichlorofluorescein (DCFH). The DCFH reacted with ROS to form the fluorescent product 2,7-dichlorofluorescein (DCF), which was trapped inside the cell making a fluorescence cell.[25] To understand this mechanism by **CPD-C_0P_1** the bacterial cell suspensions (25 mL) of both *E. coli* and *S.aureus* were treated with **CPD-C_0P_1** (100 μg) and incubated for 30 min at 37 °C and then treated with DCFH-DA (100 μL, 100 mM) kept for further incubation at 37 °C for 6 h in the dark. The aliquots were collected at different time intervals 6, 12, and 24 h. The residual DCFH-DA probe was removed from the suspension by centrifugation and washed three times with PBS. The pellets were then resuspended in PBS. For control, bacteria with DCFH-DA only and DCFH-DA with H_2O_2 were cultures simultaneously. Finally, the fluorescence spectra of DCFH-DA were recorded at the excitation and emission

wavelength of 480 and 520 nm, respectively by using a Bioteck synergy HTX microplate reader.

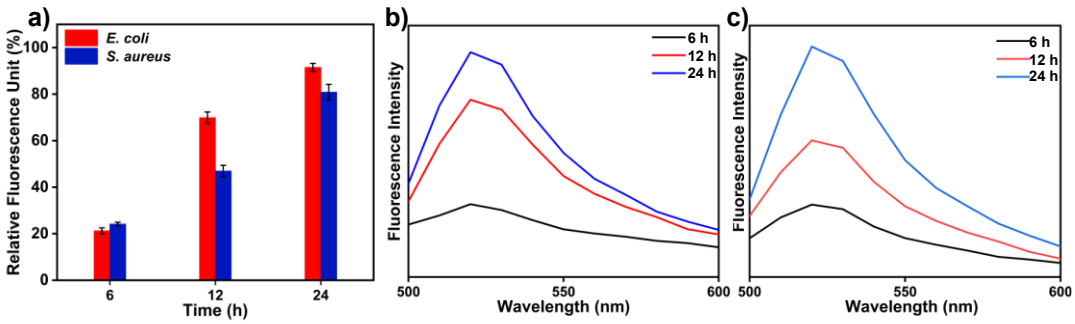

Figure 3.20. a) Time-dependent fluorescence emission spectra of ROS generation in bacterial cells after removing the supernatant, individual fluorescence intensity with time after treatment of **CPD-C_0P_1** with b) *E. coli* c) *S. aureus.*

3.2.7. Characterization and antibacterial profile of PMMA/CPD-C_0P_1 nanofibers

*3.2.7.1. Characterization of PMMA/**CPD-C_0P_1** nanofibers*

To generate the fibers, the **CPD-C_0P_1** was embedded in a polymer matrix of PMMA (polymethyl methacrylate) and transformed into nanofibers to enhance their biocompatibility. The nanofibers were prepared by electrospinning after adding 7% **CPD-C_0P_1** and 93% PMMA (total 200 mg/ 2 mL) in DMF as a solvent and kept for stirring overnight at 30 °C. The nanofibers were then electrospun at 10 keV using a 2 mL syringe with a 15 cm distance between the syringe and collector. The NFs were then collected as smooth yellowish brown color fibers with 750 rpm speed on the aluminum foil covered on the rotor as a nanofiber mat (NFM). The NFM were collected after drying in a hot air oven at 70 °C for 12 h. For control purpose, bare PMMA fibers with no **CPD-C_0P_1** was also prepared by taking 9.3% PMMA with respect to DMF by keeping the same parameters.[32]

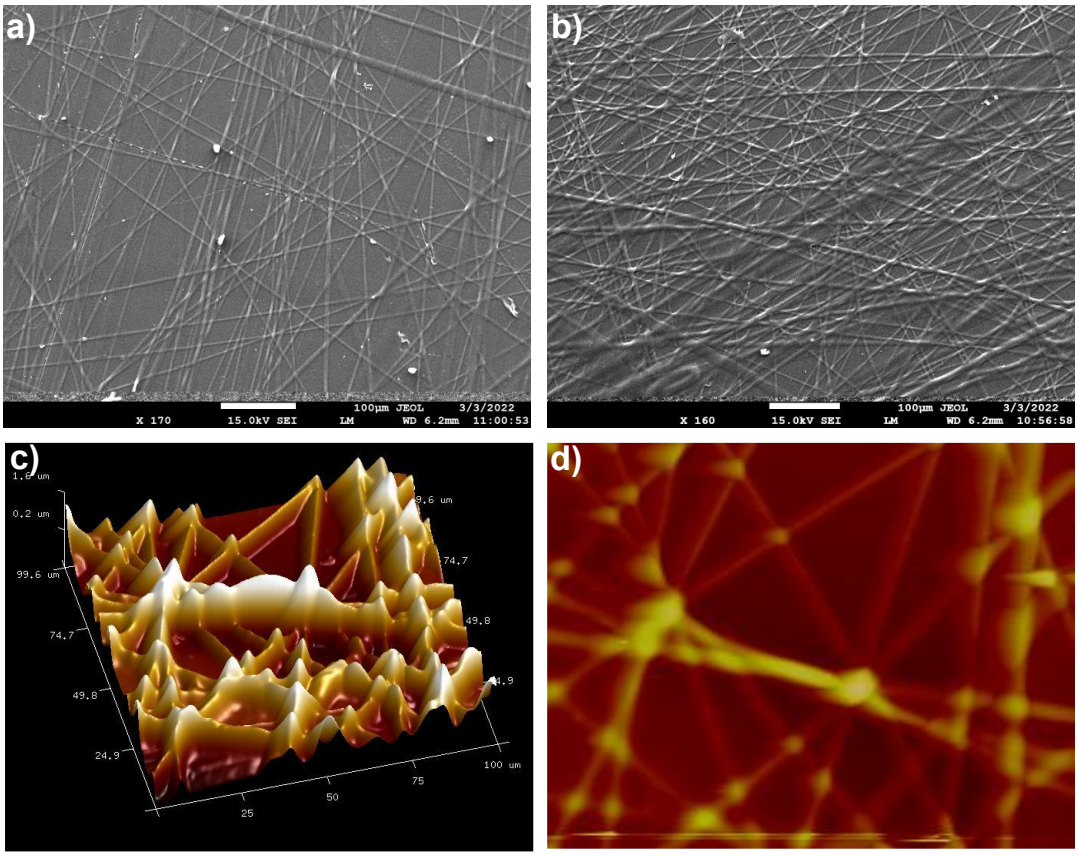

Figure 3.21. FE-SEM images of electrospun nanofibers of a) PMMA (100%). B) PMMA/**CPD-C_0P_1** 93:7 wt ratio. AFM images of c) and d) fibers with PMMA/**CPD-C_0P_1**.

*3.2.7.2. Antimicrobial activity of PMMA/**CPD-C_0P_1***

Fibers consisting of **CPD-C_0P_1** (PMMA/**CPD-C_0P_1**) and PMMA fibers (control) were cut out from a nanofiber mat (1:1 cm^2) and dispersed in bacterial media solution separately (both *e. coli* and *s. aureus*), (1 mL in each well, 1.5×10^7 to 1.5×10^8 CFU/ mL). in 6 well plates. The plates were incubated for 12–24 h at 37 °C. To determine the bacterial growth inhibition, the aliquots (250 µL) were isolated from the 6 well plates with different time intervals (0, 6, and 12 h) and measured for OD by visual turbidity readout (Bioteck Synergy HTX Multimode Reader) at 600 nm. All reported values represent a minimum of triplicate experiments. Further, to evaluate the bacterial survival rate the aliquots with different time intervals (0, 6, 12 h) were streaked on solidified LB agar petri plates and placed for incubation at 37 °C for 24 h (Figure 3.11). Colonies were counted per cm^2.

3.3. Summary and Conclusion

In summary, by utilizing the top-down approach, we optimized the condition to provide excitation independent near WL emitting carbon dots **CPD-C_0P_1** with 23% quantum yield. The resulting antimicrobial **CPD-C_0P_1** not only retained the broad-spectrum antibacterial effect but also exhibited a 500-fold increase in biocompatibility. Further, we demonstrated a successful fabrication of nanofibers using PMMA as the matrix to provide RGB emissive antimicrobial NF mat. **CPD-C_0P_1** was found to be intrinsically generating the ROS and resulting in programmed bacterial cell death. Although the field of carbon nanomaterial is emerging to produce promising bioactive materials, we believe that this work can provide a considerable impact on the generation of better and biocompatible antimicrobial materials.

3.4. References

1. Cunha, B. R.; Fonseca L. P.; Calado, C. R. C. Antibiotic Discovery: Where Have We Come from, Where Do We Go? *Antibiotics* **2019**, *8*, 45.
2. Toprak, E.; Veres, A.; Michel, J. B.; Chait, R.; Hartl D. L.; Kishony R. Evolutionary paths to antibiotic resistance under dynamically sustained drug selection. *Nat. Genet.* **2012**, *44*, 101–105.
3. Laxminarayan, R.; Matsoso, P.; Pant, S.; Brower, C.; Røttingen, J. A.; Klugman K.; Davies, S. Access to effective antimicrobials: a worldwide challenge. *Lancet* **2016**, *387*, 168–175.
4. León-Buitimea, A.; Garza-cárdenas, C. R.; Garza-cervantes, J. A.; Lerma-Escalera, J. A.; Morones-Ramírez, J. R. The Demand for New Antibiotics: Antimicrobial Peptides, Nanoparticles, and Combinatorial Therapies as Future Strategies in Antibacterial Agent Design. *Front. Microbiol*. **2020**, *11*, 1.
5. Paladini, F.; Pollini, M. Antimicrobial Silver Nanoparticles for Wound Healing Application: Progress and Future Trends. *Materials* **2019**, *12*, 2540.
6. Lim, S. Y.; Shen, W.; Gao, Z. Carbon quantum dots and their applications. *Chem. Soc. Rev*. **2015**, *44*, 362–381.
7. Xu, J. W.; Yao, K.; Xu, Z. K. Nanomaterials with a photothermal effect for antibacterial activities: an overview. *Nanoscale* **2019**, *11*, 8680–8691.
8. Du, J.; Xu, N.; Fan, J.; Sun W.; Peng, X. Carbon Dots for In Vivo Bioimaging and Theranostics. *Small* **2019**, *15*, 1805087.

9. Su, W.; Wu, H.; Xu, H.; Zhang, Y.; Li, Y.; Li, X.; Fan, L. Carbon dots: a booming material for biomedical applications. *Mater. Chem. Front.* **2020**, *4*, 821–836.
10. Varghese M.; Balachandran, M. Antibacterial efficiency of carbon dots against Gram-positive and Gram-negative bacteria: A review. *J. Environ. Chem. Eng.* **2021**, *9*, 106821.
11. Tao, S.; Feng, T.; Zheng, C.; Zhu S.; Yang, B. Carbonized Polymer Dots: A Brand New Perspective to Recognize Luminescent Carbon-Based Nanomaterials. *J. Phys. Chem. Lett.* **2019**, *10*, 5182–5188.
12. Liang, J.; Li, W.; Chen, J.; Huang, X.; Liu, Y.; Zhang, X.; Shu, W.; Lei, B.; Zhang, H. Antibacterial Activity and Synergetic Mechanism of Carbon Dots against Gram-Positive and -Negative Bacteria. *ACS Appl. Bio Mater.* **2021**, *4*, 6937–6945.
13. Gu, J.; Wang, W.; Zhang, Q.; Meng, Z.; Jia, X.; Xi, K. Synthesis of fluorescent carbon nanoparticles from polyacrylamide for fast cellular endocytosis. *RSC Adv.* **2013**, *3*, 15589–15591.
14. Maruthapandi, M.; Saravanan, A.; Gupta, A.; Luong J. H. T.; Gedanken, A. Antimicrobial Activities of Conducting Polymers and Their Composites. *Macromol*. **2022**, *2*, 78–99.
15. Jijie, R.; Barras, A.; Bouckaert, J.; Dumitrascu, N.; Szunerits S.; Boukherroub, R. Enhanced antibacterial activity of carbon dots functionalized with ampicillin combined with visible light triggered photodynamic effects. *Colloids Sur. B: Biointerfaces*, **2018**, *170*, 347–354.
16. Sartaliya, S.; Gowri, V.; Chopra, V.; Roy, H. S.; Ghosh, D.; Jayamurugan, G. Unraveling the Effect of Nondrug Spacers on a True Drug-Polymer and a Comparative Study of Their Antimicrobial Activity. *ACS Appl. Polym. Mater.*, **2022**, *4*, 3952–3961.
17. Tan, J.; Zou, R.; Zhang, J.; Li, W.; Zhang, L.; Yue, D. Large-scale synthesis of N-doped carbon quantum dots and their phosphorescence properties in a polyurethane matrix. *Nanoscale* **2016**, *8*, 4742–4747.
18. Li, H. T.; Kang, Z. H.; Liu, Y.; Lee, S.-T. Carbon nanodots: synthesis, properties and applications. *J. Mater. Chem.* **2012**, *22*, 24230–24253.

19. Niu, Q.; Gao, K.; Lin, Z.; Wu, W. Amine-capped carbon dots as a nanosensor for sensitive and selective detection of picric acid in aqueous solution via electrostatic interaction. *Anal. Methods* **2013**, *5*, 6228–6233.
20. Chen, W.; Li, D.; Tian, L.; Xiang, W.; Wang, T.; Hu W.; Dai, Z. Synthesis of graphene quantum dots from natural polymer starch for cell imaging. *Green Chem.* **2018**, *20*, 4438–4442.
21. Gaashani, R. A.; Najjar, A.; Zakaria, Y.; Mansour, S.; Atieh, M. A. XPS and structural studies of high quality graphene oxide and reduced graphene oxide prepared by different chemical oxidation methods. *Ceram. Int.* **2019**, *45*, 14439–14448.
22. Yuan, S.; Xiong, G.; He, F.; Jiang, W.; Liang, B.; Choong, C. Multifunctional REDV-conjugated zwitterionic polycarboxybetaine–polycaprolactone hybrid surfaces for enhanced antibacterial activity, anti-thrombogenicity and endothelial cell proliferation. *J. Mater. Chem. B* **2015**, *3*, 8088–8101.
23. Bleu, Y.; Barnier, V.; Christien, F.; Bourquard, F.; Loir, A.; Garrelie, F.; Donnet, C. Dynamics of carbon diffusion and segregation through nickel catalyst, investigated by in-situ XPS, during the growth of nitrogen-doped graphene. *Carbon* **2019**, *155*, 410–420.
24. Lee, J.-W.; Jeong, S.-P.; You, N.-H.; Moon, S.-Y. Tunable Synthesis of Predominant Semi-Ionic and Covalent Fluorine Bonding States on a Graphene Surface. *Nanomaterials* **2021**, *11*, 942.
25. Bing, W.; Sun, H.; Yan, Z.; Ren J.; Qu, X. Programmed Bacteria Death Induced by Carbon Dots with Different Surface Charge. *Small* **2016**, *12*, 4713–4718.
26. Wang, B. B.; Quan, Y. H.; Xu Z. M.; Zhao, Q. Preparation of highly effective antibacterial coating with polydopamine/chitosan/silver nanoparticles via simple immersion. *Prog. Org. Coat.* **2020**, *149*, 105967.
27. Zhang, J.; Yu, S. H. Carbon dots: large-scale synthesis, sensing and bioimaging. *Mater. Today* **2016**, *19*, 382–393.
28. Dar, A. H.; Gowri, V.; Mishra, R. K.; Khan R.; Jayamurugan, G. Nanotechnology-Assisted, Single-Chromophore-Based White-Light-Emitting Organic Materials with Bioimaging Properties. *Langmuir* **2022**, *38*, 430–438.

29. Zhou, J.; Booker, C.; Li, R.; Zhou, X.; Sham, T.-K.; Sun, X.; Ding, Z. An Electrochemical Avenue to Blue Luminescent Nano- crystals from Multiwalled Carbon Nanotubes (MWCNTs). *J. Am. Chem. Soc.* **2007**, *129*, 744−745.
30. Eaton, D. F. Reference Materials for Fluorescence Measurement. *Pure Appl. Chem.* **1988**, *60*, 1107−1114.
31. Wiegand, I.; Hilpert, K.; Hancock, R. E. W. Agar and broth dilution methods to determine the minimal inhibitory concentration (MIC) of antimicrobial substances. *Nat. Protoc*. **2008**, *3*, 163–175.
32. Altun, E.; Aydogdu, M. O.; Koc, F.; Crabbe-Mann, M.; Brako, F.; Kaur-Matharu, R.; Ozen, G.; Kuruca, S. E.; Edirisinghe, U.; Gunduz O.; Edirisinghe, M. Novel Making of Bacterial Cellulose Blended Polymeric Fiber Bandages. *Macromol. Mater. Eng*. **2018**, *303*, 1700607.

Chapter 4:

A new water-soluble magnetic-field induced drug delivery system obtained via preferential molecular marriage over narcissistic self-sorting

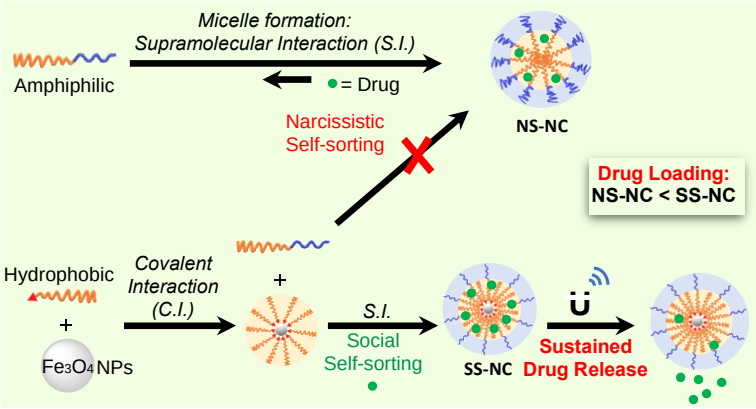

4.0 Introduction

Capping ligands in metal nanoparticles (MNPs) are indispensable due to their role in stabilizing and maintaining the structural and physical properties (size, shape, and morphology) of MNPs.[1,2] Polymer-capped MNPs have been investigated for decades for a variety of applications, including sensing,[3,4] drug delivery,[5–10] photodynamic therapy,[11] antimicrobials,[12] contrast agents for magnetic resonance imaging,[13] catalysis,[14] and molecular electronics.[15] Among these, drug delivery has drawn the most attention due to its additional therapeutic properties when combined with chemotherapy, for instance, hyperthermia,[16–21] and radiation therapy,[22,23] using polymer functionalization on iron oxide and gold nanoparticles have been studied.

In polymer-capped MNPs for drug delivery, polymers primarily serve four functions: i) to preclude nanoparticle agglomeration, ii) encapsulate drugs in a hydrophobic environment, iii) make metal nanoparticles water-soluble, and iv) provide functionalization of materials for targeted delivery. The water-soluble core-shell-type structure-based nanocarrier with hydrophobic and hydrophilic functionalization is

traditionally formed *via* covalent bond formation using complementary metal anchoring groups functionalized amphiphilic block copolymers (Figure 4.0.a).[24] The random amphiphilic copolymers with hydrophilic main chains and hydrophobic pendant groups also exhibited such core-shell architectures upon solvent-dependent self-folding (Figure 4.0.b).[25–28] Conventional nanocarriers *i.e.*, polymeric micelles based on amphiphilic surfactants have also been used (Figure 4.0.c).[29] However, given the weak supramolecular interactions based on self-assembly in water, it is challenging to keep the micelle and self-folding polymers in their spherical shape to hold the drug compartment. As a solution, the cross-linking strategy is applied either in the core or the shell upon the formation of micelles.[30] In their study, Bao and co-workers demonstrated a clever way of converting hydrophobic capping ligands into water-soluble iron oxide nanoparticles by exchanging them with polymers that contain water-soluble functional groups.[31] Unfortunately, this approach does not provide a sufficient hydrophobic environment for encapsulating water-insoluble drugs. Although linking polymer to metal NPs *via* covalent interaction (C.I.) provides stability, it does not allow exchange with other polymers. Therefore, we infer that combining both S.I. and C.I. interactions would provide a better water-soluble nanocarrier (Figure 4.0.d). To achieve molecular marriage (social self-sorting), one must overcome narcissistic self-sorting.

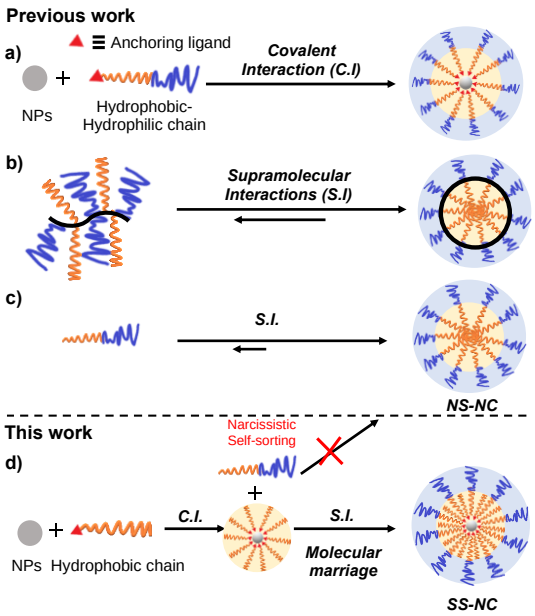

Figure 4.0. (a–c) Different methods for preparing water-soluble polymeric nanocarriers. Multi-layer vesicles are not considered here. **(d)** Schematic representation of the new type of nanocarrier presented in this work.

Self-sorting is the science of studying networks of interacting molecules belonging to system chemistry. A considerable amount of research has been conducted to design macromolecules,[32,33] peptides,[34] polymers,[35] nanomaterials,[36] and metal-organic complexes[37,38] to allow the formation of well-organized self-assembled compartments under complex circumstances *via* intermolecular physical interactions (e.g., solvophobic, hydrogen bonding, charge-transfer, metal-ligand coordination)[39] or discriminatory recognition dependent on size, morphology, chirality, and stereoselectivity.[40,41] Imai et al. recently reported that using different types of polymers to form micelles led to narcissistic self-sorting. Even with a dynamic exchange, they were able to recognize the same types for an amphiphilic random copolymer containing hydrophilic poly(ethylene glycol) (PEG) and hydrophobic alkyl pendants in aqueous media.[42] A number of groups have investigated the delivery of hydrophobic drugs using self-assembled polymeric nano-micelles (e.g., amphiphilic PEG-PLA micelles encapsulating doxorubicin and paclitaxel drugs[9,10,19,20,22,23,43,44] and PEGylated phospholipid-based block copolymers for the encapsulation of paclitaxel, diazepam, and vasoactive intestinal peptide[45,46]) in an aqueous environment for site-specific drug delivery. They discussed the role that hydrophobic interactions play in drug-PLA interactions.

The possibility of building extremely packed hydrophobic core-based self-sorted structures in an aqueous environment to load more drug molecules has not been explored. A combination of chemotherapy and magnetic hyperthermia is desired for a more versatile therapeutic efficacy, especially in the treatment of cancer.[19,20,22,23,47] For this purpose, materials with high magnetic saturation and higher drug loading efficiency are needed. Toward this objective, we report herein the development of a new nanocarrier (**SS-NC**, Figure 4.0.d) that contains every single amphiphilic polymer chain (shell), surrounded by multiple crowded hydrophobic polymer chains in comparison with existing core-shell type nanocarriers (Figure 4.0.a-c). In achieving the new type of core-shell structure (**SS-NC**), we have overcome the conventional narcissistic self-sorted micellar system of **mPEG-PLLA** by using **IONP@PLLA** coated with hydrophobic polymer to self-assemble them between the hydrophobic chains. In addition, we discuss the results obtained from comparisons of the drug-loading capacity of **SS-NC** versus **NS-NC** and studies on the effect of magnetism and temperature on drug release. Drug release induced by magnetism and temperature is discussed below.

4.1 Results and Discussion

4.1.1. Synthesis and characterization of polymers and nanoparticles

A socially self-sorted nanocarrier (**SS-NC**) with a core and outer shell is proposed by preferential molecular marriage over narcissistic self-sorting using a combination of amphiphilic polymer-coated iron oxide nanoparticles (**IONP@PLLA**) and hydrophobic polymer-coated block copolymers (**MPEG-PLLA**) (Scheme 4.2). The synthesis of **mPEG-PLLA** polymer was followed by the published procedure (Scheme 4.0).[48]

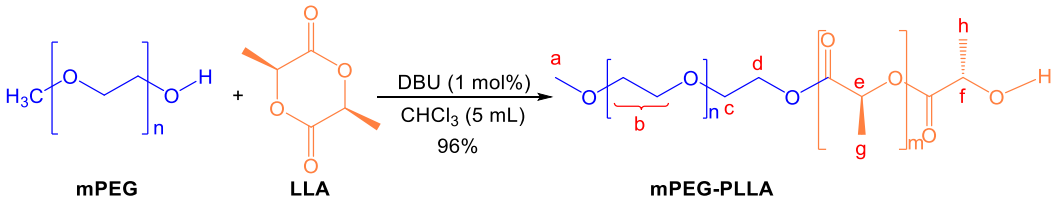

Scheme 4.0. Synthesis of **mPEG-PLLA** copolymer.

The formation of the block copolymer can be indicated by the disappearance of the CH_2OH (4.56 ppm, *m*) functional group of **mPEG** to CH_2OCO (4.20 ppm, *m*) of **mPEG-PLLA** as observed in the ^1H NMR spectra comparison of Figures 4.12 and 4.8 (Section 4.2.5.1), respectively. Additionally, the NMR pattern obtained also matches well with previously reported **mPEG**$_{10000}$-**PLLA**$_{2000}$ and **mPEG-PLLA** polymers.[48,49] In addition to NMR analysis, FT-IR (Figure 4.1A) also corroborates the functional group conversion indicating the block copolymer composition and purity of both polymers. Whereas the synthesis of **IONP@PLLA** has not been reported. Thus, the hydrophobic polymer-coated iron oxide nanoparticles (**IONP@PLLA**) were obtained by functionalizing the **IONP** with **PLLA** chains. The synthetic details are provided in Scheme 4.1.

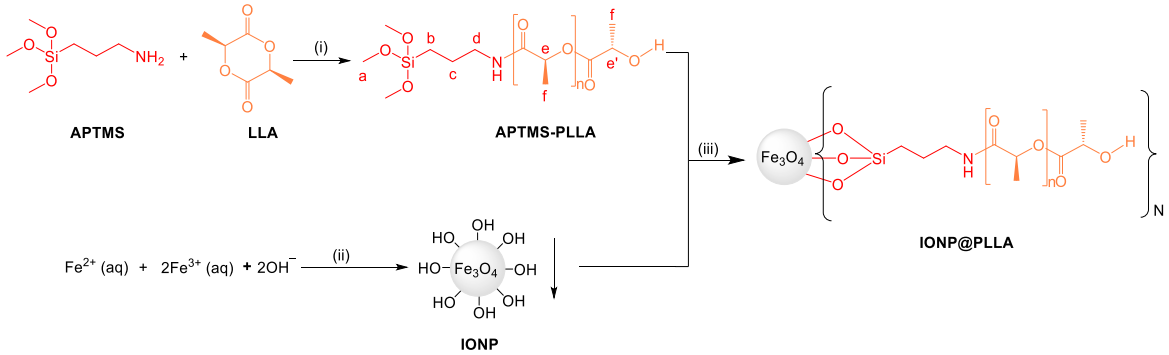

Scheme 4.1. Synthesis of **APTMS-PLLA**, **IONP**, and **IONP@PLLA**. [a]Reagents and conditions (i) DBU, CH_2Cl_2, 30 °C, (ii) 2M NaOH, 75°C, (iii) acetone, 25 °C.

The functionalization of PLLA chains was accomplished by using a ring-opening polymerization involving 2-aminopropyl trimethoxy silane (**APTMS**) as an anchoring

group. Accordingly, **APTMS-PLLA** was synthesized by treating **APTMS** with *L*-lactide by ring-opening polymerization using DBU as a catalyst (0.2 equiv.). For producing **IONP@PLLA** with a core-shell structure, freshly synthesized **IONP** (0.5 g, via coprecipitation) was coated with **APTMS-PLLA** (1 g) in the presence of acetone/H_2O 2:1 to produce 1.12 g of **IONP@PLLA** with good conversion.

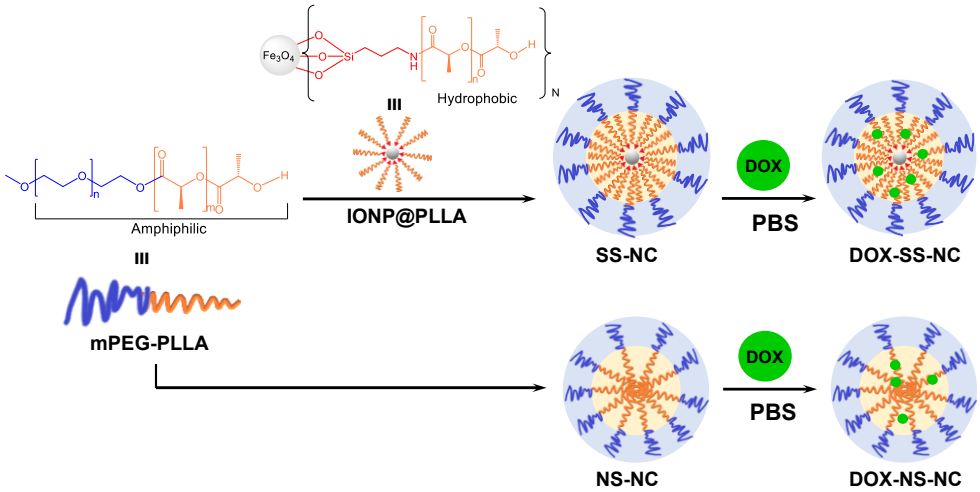

Scheme 4.2. Synthetic scheme for producing doxorubicin-loaded socially self-sorted nanocarrier (**DOX-SS-NC**) and narcissistic self-sorted nanocarrier (**DOX-NS-NC**).

Both amphiphilic **mPEG-PLLA** and hydrophobic **APTMS-PLLA** polymers were characterized using attenuated total Fourier transform infrared (AT-FT-IR), nuclear magnetic resonance (NMR), and size exclusion chromatography (SEC) techniques. FT-IR spectra of **mPEG-PLLA**, **APTMS-PLLA**, **IONP**, and **IONP@PLLA** are shown in Figure 4.1A. The presence of two kinds of functional groups in **mPEG-PLLA** corresponding to C=O (ester; PLLA) and C–O (ether; mPEG) are observed at 1750 and 1088 cm^{-1}, respectively indicating both PEG and PLLA polymeric chains are coupled (Figure 4.1A(a)). Likewise, the presence of amide carbonyl stretching frequency at 1671 cm^{-1} (Figure 4.1A(b)) indicates the formation of a second amide bond between **APTMS** and *L*-lactide. **mPEG-PLLA** and **APTMS-PLLA** polymers were further characterized by ^{1}H and ^{13}C–NMR spectroscopy and the characteristic signals are observed (characterization data, material and methods).

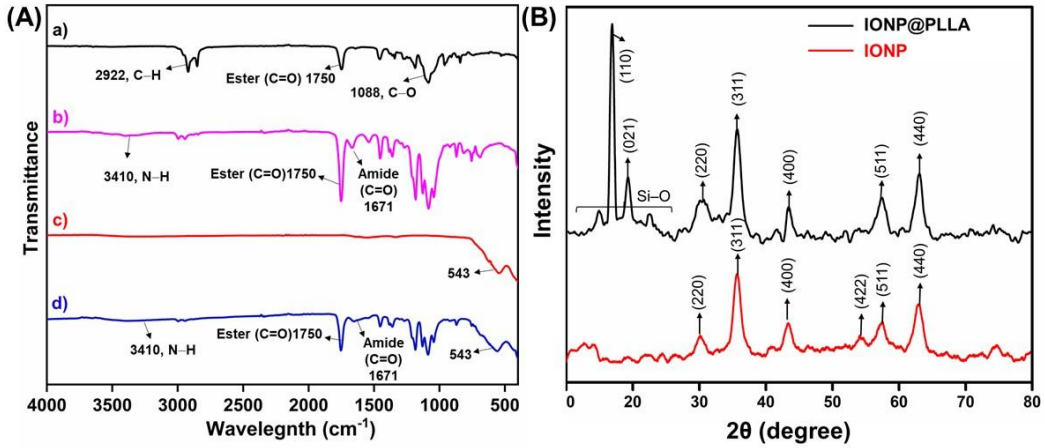

Figure 4.1. (A) FT-IR spectra of a) **mPEG-PLLA**, b) **APTMS-PLLA**, c) **IONP**, d) **IONP@PLLA**; (B) XRD spectra of **IONP** and **IONP@PLLA**.

SEC was performed on both polymers to determine their size and polydispersity index (PDI) and the data are summarized in Table 4.0. The average molecular weights (M_w) of the amphiphilic polymer **mPEG-PLLA** and hydrophobic polymer **APTMS-PLLA** were found to be around 18500 and 19700 Daltons (Da), respectively (characterization data, material and methods). The PDI values of **mPEG-PLLA** and **APTMS-PLLA** were found to be 1.5 and 1.4, respectively, suggesting that they are somewhat broader.[50,51] Omitting the M_n value of the PEG chain in **mPEG-PLLA**, the hydrophobic part of **IONP@PLLA** was found to be ~1.4 times higher than the hydrophobic part of **mPEG-PLLA**, which represents the structural organization of the PLLA part of amphiphilic polymer which may penetrate up to 75% through **IONP@PLLA** because the PEG chain would prefer to stay in the water environment. The nanocarrier structure would then create two distinct compartments, which may affect the kinetics of drug release (*vide infra*).

Table 4.0. Average molecular weights (M_n, M_w) and polydispersity index (PDI) of polymers as determined by SEC analysis using DMF at 35 °C. Calibrated with linear polystyrene narrow standards.

Polymer	M_n (g/mol)[a]	M_w (g/mol)[b]	M_w/M_n (PDI)	DP[c]
mPEG-PLLA	11900	18500	1.5	128
APTMS-PLLA	14000	19700	1.4	136.6

[a]M_n = number average molecular weight (Da), [b]M_w = weight average molecular weight (Da). [c]DP = degree of polymerization.

A variety of tools were used to characterize **IONP** and **IONP@PLLA**, including FT-IR, powder X-ray diffraction (PXRD), transmission electron microscopy (TEM) coupled with EDX, thermogravimetric analysis (TGA), and dynamic light scattering (DLS). It was observed that stretching frequencies associated with **IONP** (543 cm^{-1}) and **PLLA** peaks were present, suggesting that **PLLA** was functionalized on **IONP** (Figure 4.1A(c,d)). Further, the PXRD pattern of **IONP** showed peaks at 220, 311, 400, 422, 511, and 440 planes indicating that magnetite Fe_3O_4 NPs were formed (Figure 4.1B).[52] Additionally, the **IONP@PLLA** also showed these planes along with 110 and 021 planes indicating the presence of **PLLA** chains. **APTMS-PLLA** caused an overlapping hump between 13 and 28°, which contained amorphous silanized surfaces of Fe_3O_4 NPs. All peaks were well matched from the reported literature.[52,53] Fe_3O_4 NPs were confirmed by fringes of 0.32 nm and a particle size distribution of 3-9 nm in the HR-TEM of **IONP** (Figures 4.2a, 4.17(a,b)). We observed a significant increase in size for **IONP@PLLA** after coating with PLLA (Figures 4.2b, 4.17(c,d), and 4.22) indicating that ~4-6 (Figure 4.30, Section 4.3) particles of aggregates were coated with hydrophobic PLLA polymer driven by coercive forces.[54]

In order to assess the content of organic and magnetite in **IONP** and **IONP@PLLA**, the thermogravimetric analysis (TGA) was used by heating the samples at a rate of 10 °C/min for a heating range of 25 to 800 °C (Figure 4.20, 4.2.5.5). There was a 9% decomposition for **IONP** due to the removal of absorbed moisture content. In the case of **IONP@PLLA**, there was a sharp decrease in weight loss between 200 and 360 °C, presumably due to the decomposition of the organic coating of **PLLA**, followed by a slow decrease due to the removal of **APTMS** from the surface of **IONP** after 360 °C. The total degradation in **IONP@PLLA** was observed to be ~70% at 800 °C. Which indirectly referred towards the 30 % residual presence of **IONP** in **IONP@PLLA**. The results matched well with the TEM-EDX analysis where the amount of iron (Fe) is 26% in **IONP@PLLA** (Figure 4.16, Figure 4.18, Table 4.4, Section 4.2.5.3). Further, the chemical composition and elemental valence state of **IONP@PLLA** were also determined by X-ray photoelectron spectroscopy (XPS) based on the specific binding energies (Figure 4.19, Section 4.2.5.4). The presence of both Fe $2p_{3/2}$ and Fe $2p_{1/2}$ has been identified corresponding to the characteristic doublets located at 709.6−710.7 and 723.2−724 eV, respectively in Fe2p XPS spectra (Figure 4.19b). This suggests that Fe^{2+}

and Fe^{3+} together are present in the magnetite nanostructure. These results match well with the reported XPS spectra of Fe_3O_4 NPs.[55]

4.1.2. Formation and characterization of socially self-sorted (SS-NC) and narcissistically self-sorted nanocarrier (NS-NC)

After the successful synthesis and characterization of both precursors **IONP@PLLA** and **mPEG-PLLA,** we wanted to test the hypothesis that whether the socially self-sorted nanocarrier (**SS-NC**), *i.e.*, molecular marriage between **IONP@PLLA** and **mPEG-PLLA** would preferentially be formed over the narcissistic self-sorting (**NS-NC**), *i.e.*, homo micelles of **mPEG-PLLA**. Given that **IONP@PLLA** has a pseudo-micelles-like structure obtained *via* covalently fixing of hydrophobic chains on the **IONP**, **SS-NC** is expected to form, thereby avoiding reversible random self-assembled structures. Prior to the synthesis of **SS-NC**, we have determined the CMC of **mPEG-PLLA** *i.e.*, 0.02 mg/mL using pyrene as a fluorescent probe in PBS which has been extracted from fluorescence spectra as the intensity ratio between I_1 (366) and I_3 (377) (Figure 4.3(c,d)).[56] This is crucial because above the CMC of **mPEG-PLLA**, the **NS-NC** may tend to form even in the presence of **IONP@PLLA**. To unravel the selective formation ability and to identify the initiation concentration (IC) of **SS-NC**, we have first fixed a concentration of **IONP@PLLA** (0.05 mg/mL) and tested a wide concentration range of **mPEG-PLLA** (0.001 – 5 mg/mL) below and above the CMC. The I_1/I_3 graph shows the **SS-NC** formation starting to appear from the ratio of 0.05:0.01 mg (w/w) **IONP@PLLA/mPEG-PLLA** (Figure 4.3a,b). Interestingly, **SS-NC** has a lower IC than **NS-NC**. This is because **SS-NC** has a higher hydrophobic component than **NS-NC** and the cooperative effect of multiple hydrophobic chains may also help **SS-NC** to form before **NS-NC**.[57,58]

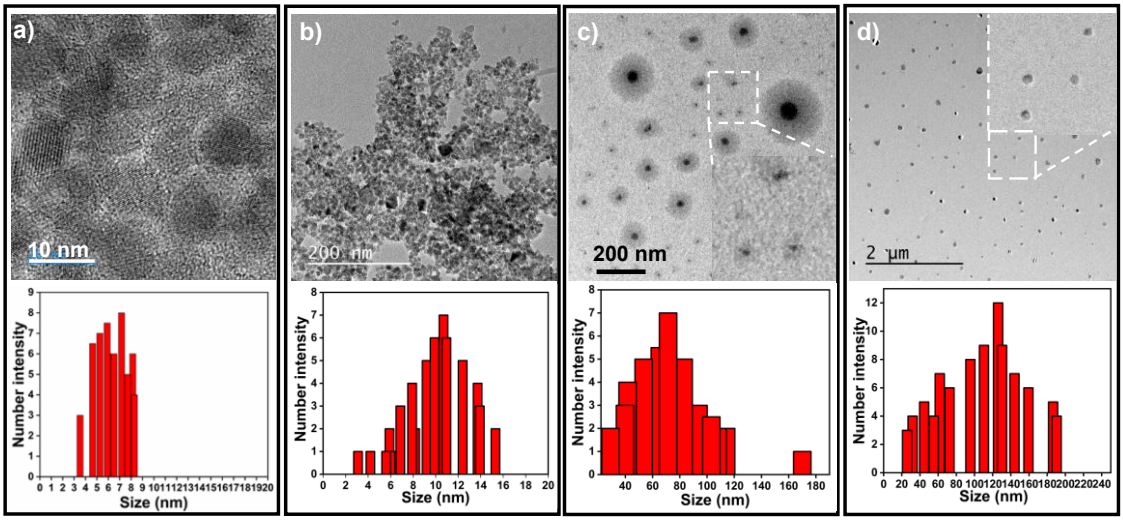

Figure 4.2. TEM images and corresponding particles size distribution histograms of a) **IONP**, b) **IONP@PLLA**, c) **SS-NC** (**IONP@PLLA/mPEG-PLLA** 0.05:0.15 mg/mL (*w/v*)), and d) **NS-NC** (**mPEG-PLLA** 0.02 mg/mL (*w/v*)).

In addition, the increasing weight ratio of **mPEG-PLLA** to 0.05 mg/mL and 0.1 mg/mL (*w/v*) over **IONP@PLLA** (0.05 mg/mL) has resulted in increased formation of **SS-NC**, while **IONP@PLLA** has decreased, as observed in TEM images (Figure 4.22, Section 4.2.6). The core-shell structure of **SS-NC** can be seen clearly in the TEM image in Figure 4.2c. The core corresponds to the **IONP@PLLA** whereas the shell consists of the organic PEG polymeric moiety. It was found that the size range for the core was 4–50 nm, presumably because of the aggregation of **IONP@PLLA** in the core of a few **SS-NC** elements. The shell size appeared to be 20–90 nm. In addition, TEM imaging revealed that **NS-NC** size ranges from around 20 to 200 nm (Figure 4.2d). However, when **mPEG-PLLA** was added at 0.15 mg/mL (*w/v*), it formed **SS-NC** without any **IONP@PLLA**. Further increasing the weight of **mPEG-PLLA** to 0.3 mg/mL (*w/v*) and above resulted in the formation of **SS-NC** along with increasing **NS-NC** indicating that 0.3 mg/mL is the saturation weight ratio for 0.05 mg/mL of **IONP@PLLA** above which it cannot accommodate **mPEG-PLLA**. Thus, the excess **mPEG-PLLA** is likely to form **NS-NC** since the concentration is above the CMC. As it is clear that a higher concentration of **mPEG-PLLA** leads to form a mixture of **SS-NC** and **NS-NC**, it would be interesting to study and verify whether the **SS-NC** can be easily separated by using an external magnet. For this, we have conducted a special experiment wherein the external magnet was kept on the vial to attract the freshly prepared **SS-NC** solution which was made using 0.05:05 mg/mL of **IONP@PLLA/mPEG-PLLA**. It was found that the

magnet could hold complete **SS-NC** particles by leaving the **NS-NC** in solution. This was verified by performing TEM images of the isolated particles and the solution samples (Figure 4.29, Section 4.2.10). From these results, we infer that in the presence of hydrophobic moiety **IONP@PLLA**, amphiphilic polymer **mPEG-PLLA** gets arranged around hydrophobic moiety through hydrophobic interactions between PLLA chains from both moieties to obtain a different-sized nanocarrier **SS-NC** due to aggregated and non-aggregated **IONP@PLLA**.

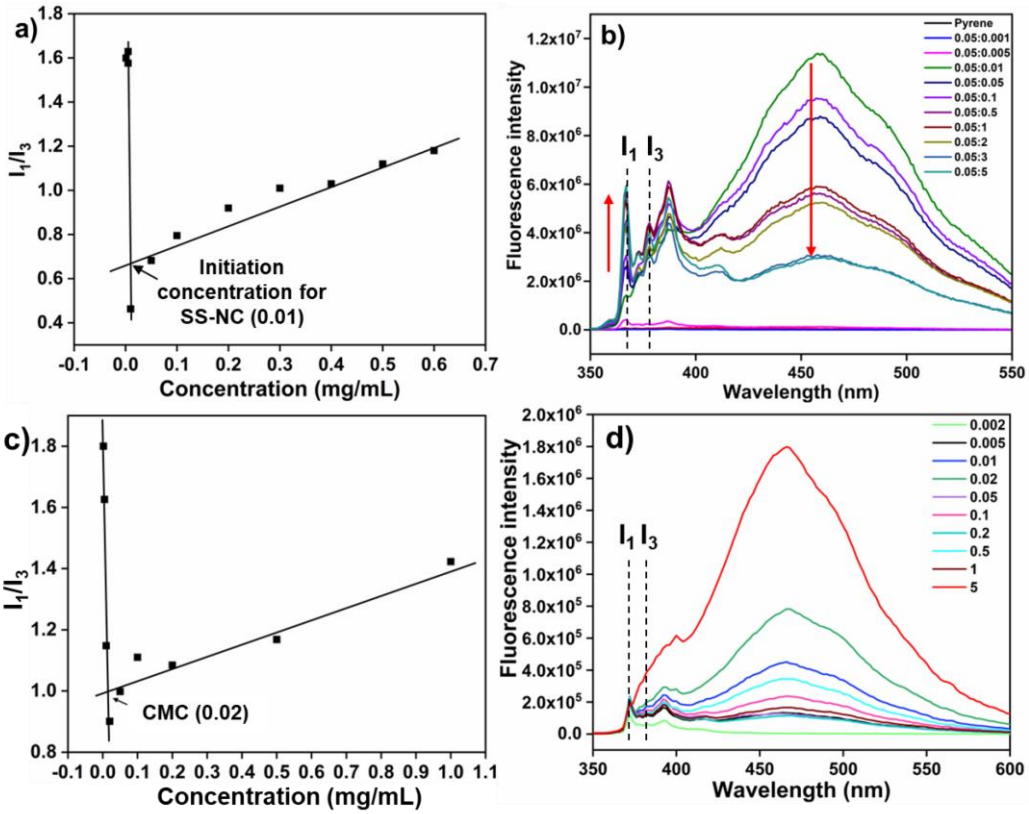

Figure 4.3. a) Effect of **mPEG-PLLA** concentration on I_1/I_3 ratios of pyrene in aqueous **IONP@PLLA** mixture. b) fluorescence intensity graph of pyrene in **SS-NC** solution. c) Effect of **mPEG-PLLA** concentration on I_1/I_3 ratios of pyrene in aqueous mixture d) fluorescence intensity graph of pyrene in **NS-NC** solution.

Given the CMC for **mPEG-PLLA** being 0.02 mg/mL, which is greater than the IC for **SS-NC**, we have examined the concentration-dependent size analysis by using the dynamic light scattering (DLS) technique to identify changes in the self-assembled structure's size of **mPEG-PLLA** with and without **IONP@PLLA** (Figure 4.4). It is interesting to note that the changes in size for both are different. In the absence of **IONP@PLLA**, multiple species have been observed to form when **mPEG-PLLA** is

increased. As opposed to this, the **SS-NC** is largely formed through a broad range of increasing **mPEG-PLLA** concentrations, indicative of its robustness due to the fixed size of **IONP@PLLA** as its core. These results indicate that the size of **mPEG-PLLA** is highly influenced by concentration due to no size-controlling factor in **NS-NC** and reversible multiple transient self-assembled structures.

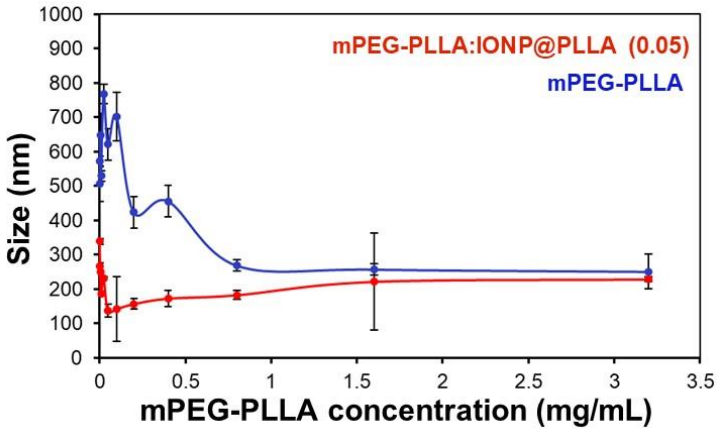

Figure 4.4. Concentration-dependent size analysis of **mPEG-PLLA** with and without **IONP@PLLA** (0.05 mg/mL) by DLS.

The above studies demonstrate that the **SS-NC** with ~ size 80 nm can be formed at the ratio of 0.05:0.15 mg/mL (*w/w*) **IONP@PLLA/mPEG-PLLA** (Figure 4.2c). It has been reported that nanocarriers with a size range of 100−200 nm are highly desirable for drug delivery in tumor-affected areas because of their ability to retain the drug and good permeability-mediated accumulation in tumor cells.[59,24] In addition, we have probed the magnetic properties of **IONP**, **IONP@PLLA**, and **SS-NC** and M-H hysteresis loop diagrams at 300 K using a physical property measurement system (PPMS, closed cycle based cryogen-free system) to utilize the presence of **IONP** and its magnetic property *via* hyperthermia (Figure 4.27, Section 4.2.8). Table 4.1 summarizes saturation magnetization (M_s), remanent magnetization (M_r), and coercivity field (H_c) data. In all cases, superparamagnetic properties have been observed to be present since they do not retain magnetism after removing the magnetic field. There is a significant decrease (4-13 times) in saturation magnetization of **IONP** in **IONP@PLLA** and **SS-NC** which may be due to the presence of non-magnetic polymer on the surfaces of **IONP**.[60] Despite the superparamagnetic character observed in all compounds, the **SS-NC** has exhibited slight diamagnetic properties in the higher magnetic field range in contrast to **IONP** and

IONP@PLLA. This is due to the decreased mass ratio of the magnetic core to the diamagnetic polymer shell.[61]

Table 4.1. Magnetic parameters (M_s, M_r, M_r/M_s, H_c) have been calculated from M-H loop at 300 K.

Sample name	M_s (emu/g)	M_r (emu/ g)	M_r/M_s	$+H_c$ (T)	$-H_c$ (T)
IONP	2.9	1.87	1.55	0.003	-0.006
IONP@PLLA	0.72	0.12	0.16	0.004	-0.007
SS-NC	0.22	0.016	0.05	0.006	-0.008

4.1.3. SS-NC for drug delivery application

Due to the presence of a relatively crowded hydrophobic core surrounded by a fairly uncrowded hydrophilic shell, this nanocarrier is more stable as a colloidal dispersion when compared to the **IONP** and **NS-NC** (Figure 4.23f, Section 4.2.6), and ideal for encapsulating hydrophobic drug molecules while remaining water dispersible. As a means of unraveling this property, we compared the hydrophobic drug loading and encapsulation efficiencies of **SS-NC** with **NS-NC**. For this purpose, a pyrene probe was used to investigate the hydrophobic nature of the nanocarriers before using doxorubicin (DOX) drug. We thus studied pyrene encapsulation in **SS-NC** and **NS-NC** using confocal microscopy (Figure 4.5). For both **SS-NC** and **NS-NC**, specific fluorescent globules were observed in an aqueous solution. The fluorescent globules in **IONP@PLLA** with pyrene are also clearly visible due to the aggregation of the pyrene molecules over the hydrophobic chains in **IONP@PLLA**. Studying the encapsulation of hydrophobic pyrene in **SS-NC** further clarified its functional properties and led us to explore the encapsulation and drug delivery of the anticancer hydrophobic drug.

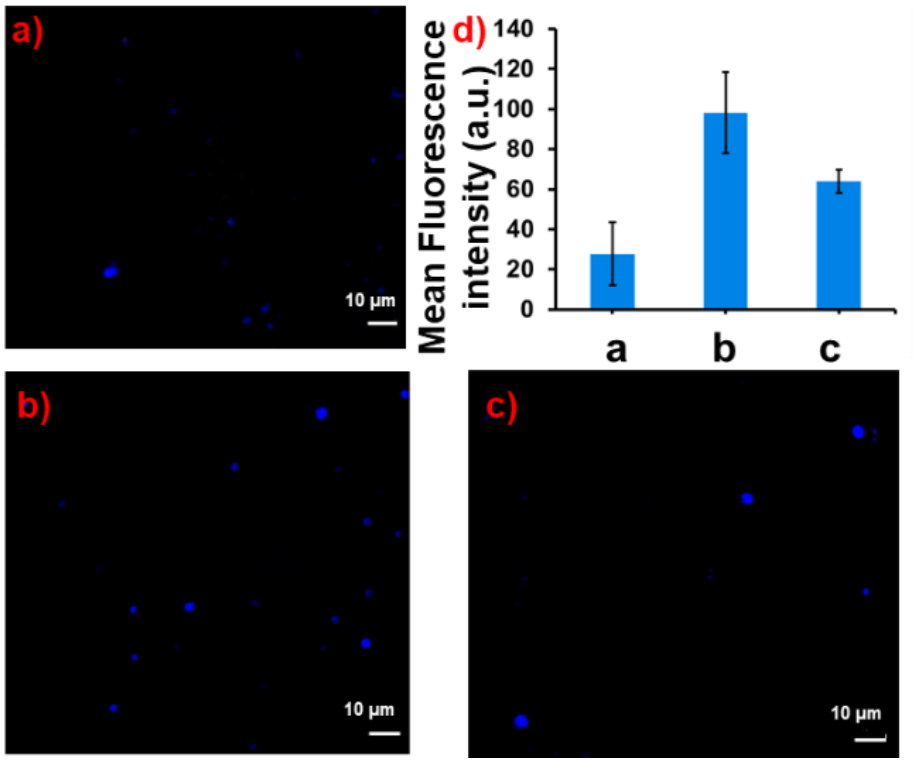

Figure 4.5. Imaging of fluorescent probe (pyrene) encapsulated in a) **IONP@PLLA**, b) **SS-NC**, c) **NS-NC** and d) mean fluorescence intensity graph of a, b, and c.

Drug loading was carried out to demonstrate the efficacy of crowded core and uncrowded shell nanocarrier i.e., **SS-NC,** as a new type of drug delivery system that encapsulates a widely used anticancer drug, *i.e.*, doxorubicin (DOX). The drug loading efficiency (DLE%) and encapsulation efficiency (EE%) of **SS-NC** by using UV–vis spectroscopy and the formula used to calculate these are mentioned in materials and methods (Section 4.2.7.). The drug loading was performed using the optimized concentration range of 0.05:0.15 mg/mL of **IONP@PLLA/mPEG-PLLA** in 1 mL PBS for **SS-NC** and the estimated DLE and EE were found to be 17 and 90%, respectively (Figure 4.25). Interestingly, the **NS-NC** with the same concentration (0.15 mg/mL) of **mPEG-PLLA** in the absence of **IONP@PLLA** has shown a reduced DLE (10.3%) and EE (65.6%), respectively. This may be due to the presence of a more crowded hydrophobic core and less crowded hydrophilic shell that is absent in **NS-NC** micelles due to hydrophobic interactions.

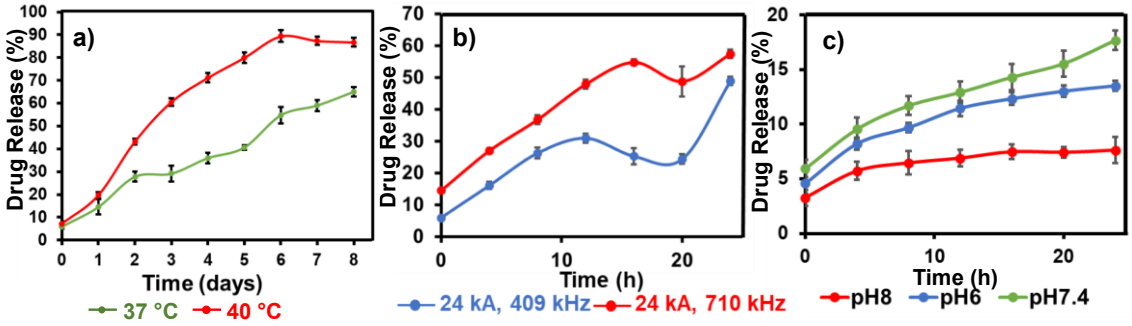

Figure 4.6. DOX release from **DOX-SS-NC** at a) different temperatures (37 and 40 °C), b) after applying 30 min of AMF, c) the effect of different pH at 37 °C.

Any nanocarrier which is intended for practical use must have stimuli-controllable release capability and sustained slow release as prerequisite properties.[62] Considering the advantages of having **IONP** and a crowded hydrophobic core (hydrophobic interaction), the DOX encapsulated **SS-NC** (**DOX-SS-NC**) is expected to show magnetism-induced drug release with an applied magnetic field (AMF) controlled slow release to be applied in magnetic hyperthermia. We have varied the amplitude and frequency of the artificial magnetic field to obtain the optimal hyperthermia temperature (45–47 °C)[63] in the hyperthermia instrument (Figure 4.28, Section 4.2.9). As a result of the initial experiment without AMF, it was observed that a minimal drug release of up to 6–12% was observed at 37 and 40 °C for 12 h, but a high dose of 18–20% was observed at 40 °C for 24 h (Figure 4.6a).

Likewise, differential scanning calorimetry (DSC) has been used to study the thermal sensitivity of the polymers, which showed that the T*g* of **mPEG-PLLA** and **APTMS-PLLA** are lower, *i.e.*, ~40 and 28 °C, respectively. Therefore, the obtained nanocarrier might be susceptible to heat (40 to 50 °C), which could result in chain movement and have an effect on the drug release profile (Figure 4.21, Section 4.2.5.6). To achieve the maximum release, AMF with 24 kA/m and a frequency of 409 kHz was used to trigger the nanocarrier to open up and release the drug. When **SS-NC** was exposed to AMF for 30 min and then kept at 37 °C for 0 to 24 h (Figure 4.6b), we observed sustained drug release of up to 47% with biphasic release profile, which is likely due to PLA chain mobility under magnetic stimulation and the presence of two types of compartments (*vide supra*). It is expected that the biphasic release profile would occur since drugs present close to the inner core and outer polymeric shell may have different binding strengths with the hydrophobic chains, thus releasing at different times. After

observing the AMF-triggered sustained drug release, we also altered the pH of the media at pH 6, 7.4, and 8 to examine the drug release effects (Figure 4.6c). At pH closer to neutral, *i.e.*, 7.4, 6 and 8 showed a maximum drug release of 18% over 24 h, indicating that the **SS-NC** is quite stable and does not open up to release the drug. Considering cancer cells have a pH between 6.4 and 7.0,[64] these studies revealed that the **SS-NC** structure is quite stable at neutral, slightly acidic, and basic conditions (pH 6 and 8) till 24 h and can be considered a promising candidate for the application of sustained drug release therapy for cancer.

4.1.4. Drug release kinetics

Drug release kinetics for **DOX-SS-NC** was interpreted by fitting the release parameters in different release kinetics models using different equations by DD solver software,[65,66] and the best fitting models with R^2 closest to one were selected as ideal drug release kinetics model (Tables 4.2 and 4.3). For drug release at 40 and 37 °C and pH 7.4, the drug release parameters were best fitted in the Makoid-Banakar model having R^2 values of 0.976 and 0.916, respectively (Figure 4.7a,c). The Makoid-Banakar model is based on the principle of diffusion which indicated the slow diffusion of the drug from **SS-NC** with time for sustained drug release.[67] For stimulation-induced biphasic release under AMF, the Hopfenberg model was considered to be the best-fitting model with the R^2 value of 0.7644, indicating surface erosion leads to biphasic release.[68–70] Drug release profiles at different conditions suggest that **SS-NC** are composed of two different compartments, allowing for rapid burst release during stimulus-response, followed by a sustained diffusion-mediated release at 37 °C.

Table 4.2. Drug release kinetics for **DOX-SS-NC** at different conditions using different equations by DD solver software.

S. No.	Drug release condition Temp. (°C)	Best fit drug release model	R^2
1.	40	Makoid-Banakar model	0.976
2.	37	Makoid-Banakar model	0.916
3.	37 (AMF, 30 min)	Hopfenberg model	0.764
4.	37	Peppas-Sahlin	0.90

We observed the R^2 adjusted values among all the models for release kinetics and the R^2_adj value was used for the model selection criterion, with the best model exhibiting the R^2 adjusted value closest to one.

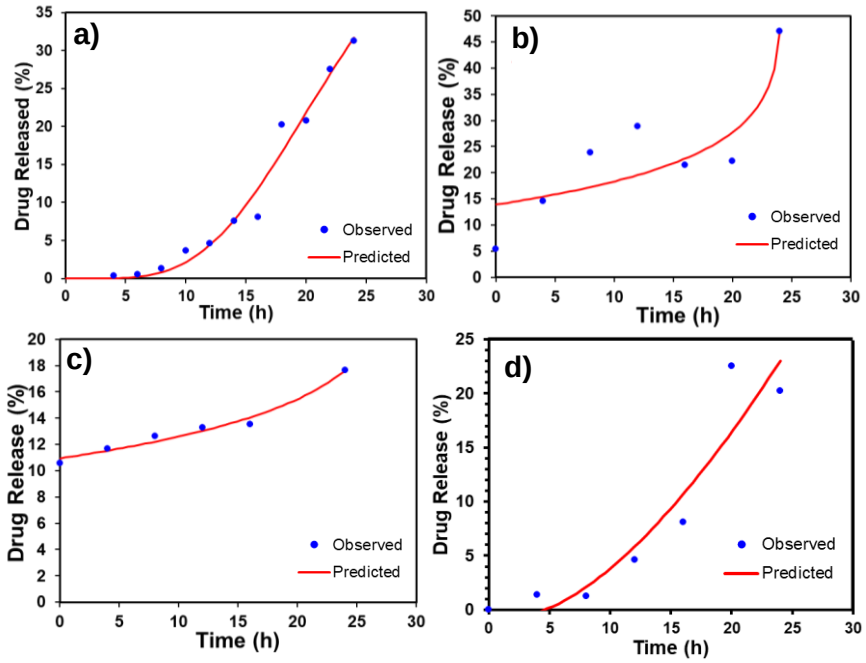

Figure 4.7. Drug release kinetics for 24 h, a) at pH 7.4 with 40 °C from Makoid–Banakar model, b) at AMF from Hopfenberg with tlag model, c) at pH 7.4 with 37 °C from Makoid–Banakar with tlag model, d) at pH 7.4 with 37 °C from Peppas-Sahlin model at 37 °C.

Table 4.3. The goodness of fit constant from fitting the empirical equations 4.0–4.3 (below Table 4.3) to release data for (a)–(d) from Makoid–Banakar, Hopfenberg, and Peppas-Sahlin models.

Graph No.	Release Model	R^2	R^2_adj.	MSE	MSE root	SS	WSS	AIC	MSC
a)	Makoid Banakar Model (eq. 4.0)	0.976	0.970	3.8833	1.970	31.0666	31.0666	43.797	3.184
b)	Hopfenberg with tlag Model	0.764	0.646	58.859	7.672	235.438	235.438	44.230	0.589

	(eq. 4.1)								
c)	Makoid-Banakar with tlag Model (eq. 4.2)	0.916	0.790	40.980	6.401	81.961	81.961	34.437	1.147
d)	Peppas-Sahlin with tlag Model (eq. 4.3)	0.90	0.88	14.210	3.77	56.86	56.86	34.28	1.226

DD Solver software was used to simulate the drug release kinetics.[64,65] The equations for fitting models for drug release kinetics are as below:

F=100*{1-[1-kHB*(t-Tlag)]^n} (eq. 4.0)

F=kMB*(t-Tlag)^n*Exp[-k*(t-Tlag)] (eq. 4.1)

F=k1*(t-Tlag)^m+k2*(t-Tlag)^(2*m) (eq. 4.2)

F=k1*t^m+k2*t^(2*m) (eq. 4.3)

4.2. Materials and methods

4.2.1. General Information

Poly(ethylene glycol) methyl ether (mPEG), (3S)-cis-3.6-dimethyl-1,4-dioxane-2,5-dione (L-Lactide), 3-(trimethoxysilyl)-propylamine (APTMS), 1,8-diazabicyclo [5.4.0]undec-7-ene (DBU), phosphate buffer saline (PBS) tablet, doxorubicin were purchased from Sigma-Aldrich. Polyethylene glycol (2000 g mol^{-1}) was purchased from the Tokyo chemicals industry (TCI). Iron (III) chloride hexahydrate ($FeCl_3.6H_2O$) and iron (II) chloride tetrahydrate ($FeCl_2.4H_2O$) were purchased from Alfa Aesar. All raw chemicals such as sodium chloride, sodium sulfate, sodium hydroxide, benzoic acid, etc. were purchased from Merck and used as received. Dichloromethane (CH_2Cl_2) and chloroform ($CHCl_3$) were freshly distilled using phosphorous pentoxide, and ethanol was dried by refluxing on magnesium tunings and iodine under a nitrogen atmosphere. HPLC grade DMF was purchased from Spectrochem India Ltd. Dialysis membrane used of

MWCO ~3.5 kDa, 35 mm dry was purchased from Thermo Scientific. TLC was performed on a pre-coated aluminum sheet of silica gel G/UV–254 of 0.2 mm thickness (Macherey Nagel, Germany) using suitable solvents and observed under UV light (λ = 254 nm).

4.2.2. General experimental details

^{1}H and ^{13}C nuclear magnetic resonance (NMR) spectra were measured on Bruker Advance II 400 and 500 MHz spectrometers using DMSO–d_6 or $CDCl_3$ as solvent at 298 K Residual solvent signals in ^{1}H and ^{13}C NMR spectra were assigned as the internal reference. Chemical shifts (δ) have been reported in part per million (ppm) downfield from tetramethylsilane (TMS) as the internal standard. Coupling constants (J) are given in Hz. The apparent resonance multiplicity is described as s (singlet), d (doublet), q (quartet), and m (multiplet).

Transmission spectra were measured using Attenuated total reflection Fourier transform infrared (ATR–FT–IR) Bruker Vertex 70 in a range of 4000–400 cm^{-1}. Selected absorption bands are reported in wavenumbers (cm^{-1}). Signal designations: s (strong), m (medium), and w (weak).

X-ray diffraction (XRD) was carried out on Eco D8 Advance Bruker powder X-ray diffraction (PXRD) with a Cu Kα radiation source (λ = 0.15406 nm). The instrument was operated at 40 kV and 25 mA at scanning steps of 0.02 in the 2θ.

Dynamic light scattering (DLS) was performed to determine the particle size distribution using Zetasizer Nano ZSP; Model–ZEN5600; Malvern Instruments LTD., Worcestershire, UK.

Transmission Electron microscopy (TEM) images were acquired on a Jeol, JEM–2100, (Tokyo, Japan) operating at 200 kV. Samples for TEM were prepared by drop-casting 7 µL of diluted sample suspension of **IONP** and **IONP@PLLA** and undiluted samples of **SS-NC** and **NS-NC** on 300 mesh TEM copper grid, and excess solution was gently wicked off with filter paper. Samples (**IONP** and **IONP@PLLA**) were dried under an IR lamp for 7 h and **SS-NC** and **NS-NC** were dried at 25 ^{o}C and stored under vacuum conditions before measurement. Size distribution histograms were made by three different areas of images with an average count Size of 78-110 particles and the analysis of images have been done using the software image *J*.

The calorimetric magnetic hyperthermia efficiency was evaluated using the DM2 applicator-equipped DM100 system (nB nanoscale Biomagnetics, Zaragoza, Spain) at a frequency of 409 kHz and field amplitude of 24 kA/m).

Confocal microscopy was done to visualize the results after encapsulation by using a Zeiss LSM880 confocal microscope (Carl Zeiss, Thornwood, New York). A suspension without further dilution of samples was drop cast on a glass slide and trapped using a glass coverslip.

UV–visible (UV–vis) spectra were recorded using Shimadzu UV–vis spectrophotometer. The absorption maxima (λ_{max}) are reported in nm. The spectra were evaluated in a quartz cuvette of 1 cm at 298 K.

Photoluminescence (PL) measurements were carried out on a Fluorolog 3–221 fluorimeter equipped with a 450 W xenon lamp.

Thermogravimetric analysis: Thermogravimetric analysis (TGA) was performed to determine the degradation/decomposition behaviour of samples using thermogravimetric (TG) analyzer-Perkin Elmer STA 8000) at an N_2 flow rate of 10 mL/min and a heating rate of 10 °C/min.

Differential scanning calorimetry (DSC) analysis: Thermal scanning of polymers was performed on Perkin Elmer Differential Scanning Calorimeter DSC 8000 model and the samples were heated from –4 to 200 °C at an N_2 flow rate of 10 mL/min and a heating rate of 10 °C/min. Polymers were analyzed for glass transition temperature (T*g*).

X-ray photoelectron spectroscopy (XPS) experiments were performed using a Thermo fisher scientific k alpha surface analysis spectrometer, using monochromatic Al Ka radiation (1486.6 eV) operating at an accelerating X-Ray power of 50W15KV. Before the measurement, the sample was outgassed at 25 °C in a UHV chamber ($<5 \times 10^{-7}$ Pa). The sample charging effects were compensated by calibrating all binding energies (BE) with the adventitious C 1s peak at 284.6 eV. This reference gave BE values with accuracy at ±0.1 eV. The sample was prepared by film formation in silicon wafers.

4.2.3. Synthetic procedures of polymers and nanoparticles

4.2.3.1. The synthesis procedure for mPEG-PLLA was adopted from the reported procedure.[48] To a 5 mL solution of (3S)-cis-3.6-dimethyl-1,4-dioxane-2,5-dione (*L*-Lactide, 100 mg, 2.26 mmol) and poly(ethylene glycol) methyl ether (**mPEG** ~ Mw 2000 Da, 100 mg, 0.05 mmol) in $CHCl_3$, diazabicyclo[5.4.0]undeca-7-ene (DBU) (1 mg, 1

mol%) was added and stirred for 1 h. After completion of the reaction, hydrochloric acid (HCl) (1 N, 20 mL) was added immediately and the mixture was washed with brine. After evaporation of $CHCl_3$ by vacuo, the residue was dissolved in *i*PrOH (2 mL), and the solution was treated with $CHCl_3$ (1mL) to obtain the precipitation of the polymer. Decantation was followed by vacuum drying at 50 °C overnight, afforded white sticky solid **mPEG-PLLA** (192 mg, 96%). ^{1}H NMR (400 MHz, DMSO–d_6) (Figure 4.8) δ = 1.25–1.30 (d, J = 6.8 Hz, 3H; h), 1.43–1.49 (d, J = 7.08 Hz, 3H; g), 3.23 (s, 3H), 3.34 (s, 4H; b), 4.12–4.26 (m, 4H; c, d), 5.08–5.14 (q, J = 7.08 Hz, 1H; f), 5.15–5.24 ppm (q, J = 7.04 Hz, 1H; e); ^{13}C (101 MHz, DMSO–d_6) δ (ppm) (Figure 4.9) 16.49, 16.53, 16.57, 16.60, 16.68, 20.36, 20.37, 58.08, 60.27, 64.33, 65.45, 65.65, 65.84, 67.80, 67.92, 68.07, 68.56, 68.98, 69.84, 71.33, 169.25, 169.32, 169.59, 169.75, 173.99, 174.08, ppm 174.15. IR (ATR) $\tilde{\nu}$ = 2922 (s), 2854 (m), 1750 (s), 1457 (w), 1347 (w), 1191 (m), 1088 (s), 956 (w).

***4.2.3.2. Synthesis of APTMS-PLLA*:** The synthesis procedure for the synthesis of **APTMS-PLLA** was adopted from the reported procedure.[71] A solution of APTMS, 1 equiv., (100 mg) in 2 mL CH_2Cl_2 was added to a solution of *L*-lactide (30 equiv., 2.4 g) in CH_2Cl_2 (5 mL), and the mixture was stirred at 30 °C for 30 min to ensure complete consumption of amine. Then, a solution of DBU (0.2 equiv., 17 mg) in 1 mL CH_2Cl_2 was added to the reaction mixture. The completion of the reaction was indicated by TLC after 30 min, and then the excess DBU was quenched with benzoic acid. The reaction mixture was washed with cold solutions of 1N HCl, saturated solution of $NaHCO_3$, and brine. Finally, the CH_2Cl_2 was dried over anhydrous sodium sulfate. Following filtration, the removal of solvent was done by distillation under reduced pressure to yield white powder (1.75 g, 72%) ^{1}H NMR (500 MHz, $CDCl_3$) (Figure 4.10)δ = 1.42–1.47 (m, 2H; b), 1.47–1.51 (m, 2H; c), 1.52–1.62 (m, 6H; f, f'), 2.2–2.5 (bs, 2H; d), 3.74 (s, 9H; a), 4.32–4.39 (q, J = 6.95 Hz, 1H, e'), 5.09–5.23 ppm (q, J = 7.15 Hz, 1H, e); ^{13}C (125 MHz, $CDCl_3$) (Figure 4.11) δ = 1.1, 16.8, 16.9, 20.2, 20.6, 29.8, 52.6, 66.9, 69.2, 69.5, 69.6, 77.4, 128.6, 130.2, 133.6, ppm 169.7. IR (Wavenumber, $\tilde{\nu}$) = 3410 (b, m), 3001 (s), 2941 (s), 1750 (s), 1671 (m), 1545 (m), 1457 (m), 1375 (m), 1193 (s), 1090 (s), 1038 (s), 872 (w), 756 (w), 688 (w).

4.2.3.3. Synthesis of IONP: Magnetic Fe_3O_4 nanoparticles were synthesized by the coprecipitation method.[24] 2:1 molar ratio $FeCl_3.6H_2O$ (1.35 g, 5 mmol) and $FeCl_2.4H_2O$ (0.5 g, 2.5 mmol) were dissolved into 50 mL of degassed DD water and stirred for 30 minutes. Chemical precipitation was observed at 25 °C under stirring (500 revolutions per minute) by adding 2 M NaOH solution in the nitrogen atmosphere. Then stirring was continued further for 3 h at 70 °C. The reaction was cooled to 25 °C, and the precipitated particles were washed with DD water (3 × 100 mL) and vacuum dried at 50–60 °C for 15 h.

***4.2.3.4. Synthesis of IONP@PLLA*:** 0.5 g of **IONP** (50 wt%) was kept in a vacuum oven at 120 °C for 90 min and dispersed in 10 mL acetone by 1 h stirring at ambient temperature and finally was sonicated for 30 min after addition of 5 mL water. Then, **APTMS-PLLA** (1 g) was gently added to the dispersed solution and stirred for a further 24 h at 30–37 °C. Finally, it was centrifuged, and the residue was further washed with acetone (3 × 20 mL). The washing was repeated 3 times, and the residual precipitate was dried under vacuum conditions at 70 °C for 72 h to obtain 1.12 g of light brown solid IR (Wavenumber, $\tilde{\nu}$) = 3410 (b, m), 1750 (s), 1671 (m), 1546 (w), 1450 (w), 1372 (w), 1272 (w), 1194 (m), 1126 (m), 990 (b, m), 543 (s).

4.2.4. Preparation and CMC/IC determination of self-sorted micelles of mPEG-PLLA and IONP@PLLA (SS-NC): The self-sorted micellar structures (**SS-NC**) were prepared by the solvent evaporation method. Firstly, the different mixtures of a fixed concentration (0.5 mg/10 mL) of **IONP@PLLA** in PBS solution were prepared. Different concentrations of **mPEG-PLLA** ranging from 0.05 to 70 mg/mL were added from a stock solution of 100 mg/ mL in acetone to the different mixtures of **IONP@PLLA**. All the solutions were then kept for 7 h stirring for acetone evaporation at 30 °C.

After acetone evaporation, 809 μg/100 μL of pyrene from a stock solution of 4×10^{-4} M in acetone was added to all the 10 mL solutions and kept for stirring for another 7–10 h. To compensate for the simultaneous water loss, the final volume of all the solutions was maintained at 10 mL and kept for stirring for a further 1 h. Further, the fluorescence spectra for all the solutions were measured using a Fluorolog 3–221 fluorimeter equipped with a thermostat at an excitation wavelength of 310 nm. Excitation and emission slit widths were 2 nm. Similarly, the CMC of **NS-NC** was determined by

taking the same concentrations of **mPEG-PLLA** in 1 mL PBS as in the above case in the absence of **IONP@PLLA**.

4.2.5. Characterization data of polymers and nanoparticles

4.2.5.1. ^{1}H- and ^{13}C-NMR spectral profiles of polymers

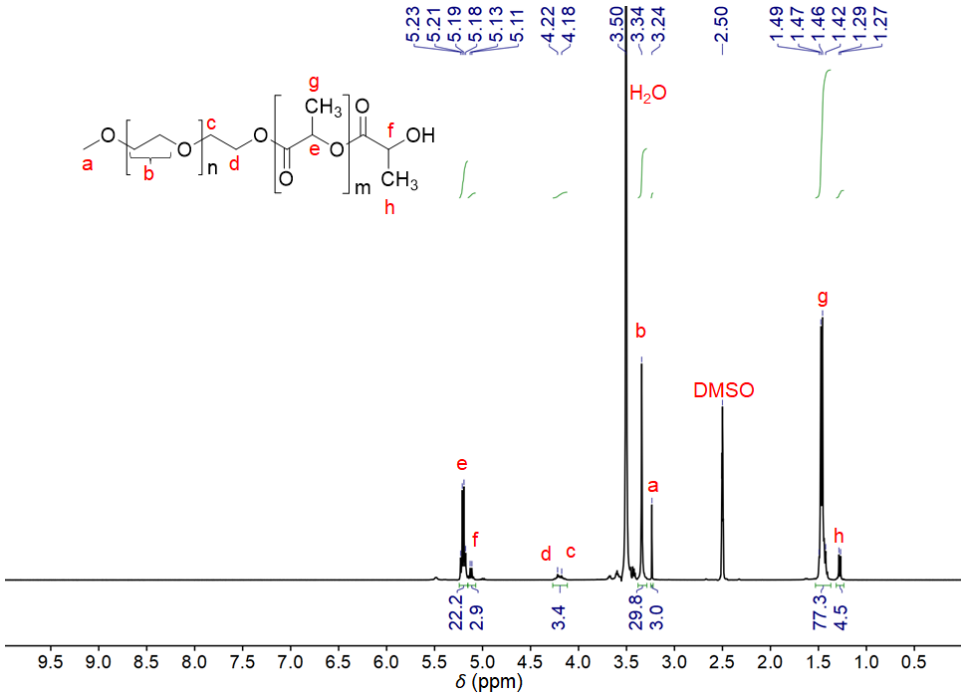

Figure 4.8. 400 MHz ^{1}H-NMR spectrum of **mPEG-PLLA** in DMSO–d_6 at 298 K.

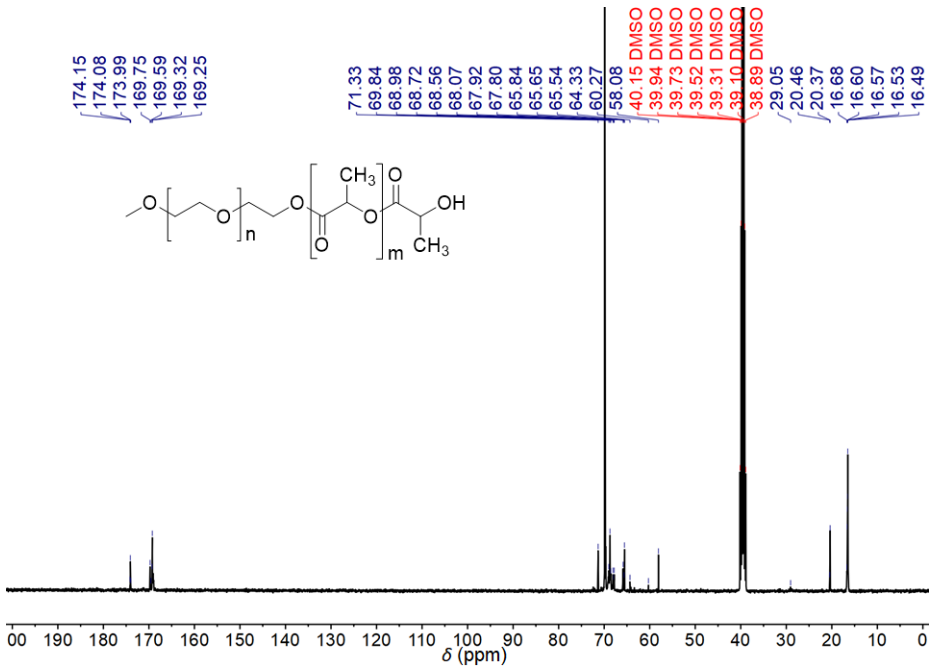

Figure 4.9. 400 MHz ^{13}C-NMR spectrum of **mPEG-PLLA** in DMSO–d_6 at 298 K.

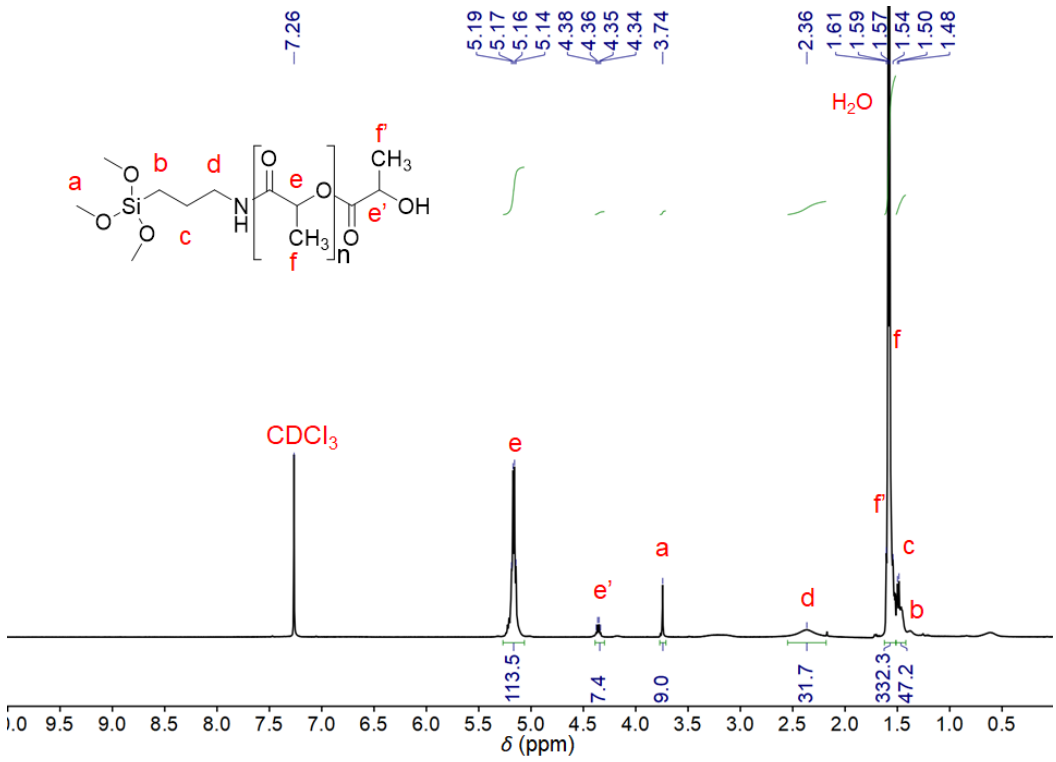

Figure 4.10. 500 MHz ^{1}H-NMR spectrum of **APTMS-PLLA** in $CDCl_3$ at 298 K.

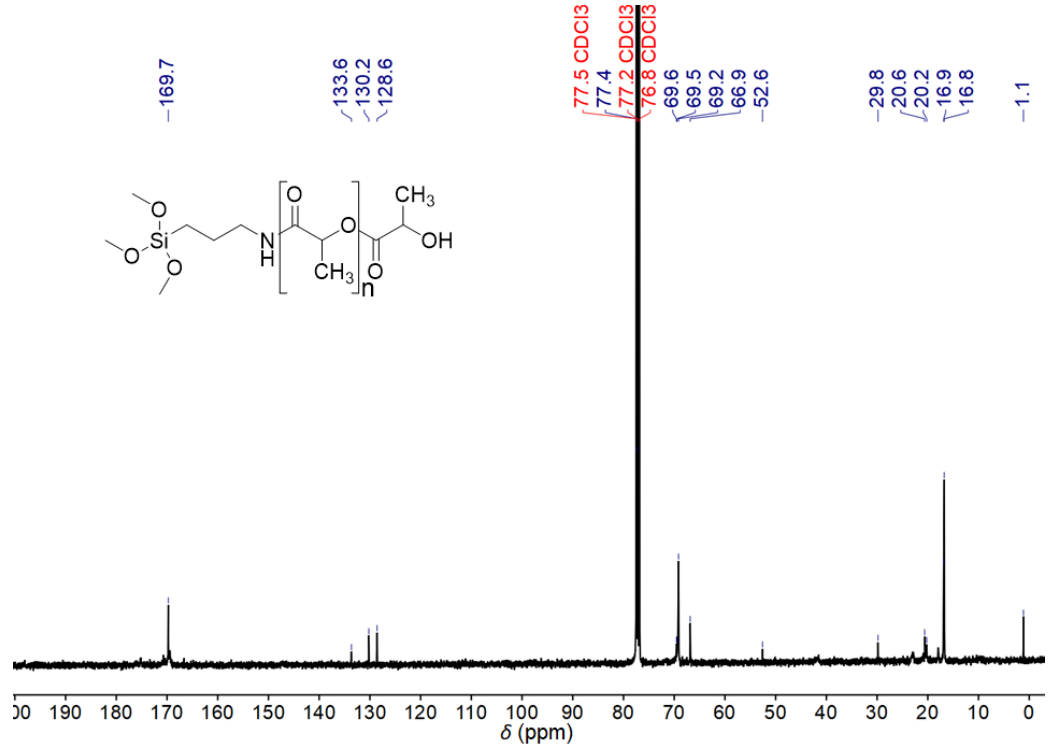

Figure 4.11. 500 MHz ^{13}C-NMR spectrum of **APTMS-PLLA** in $CDCl_3$ at 298 K.

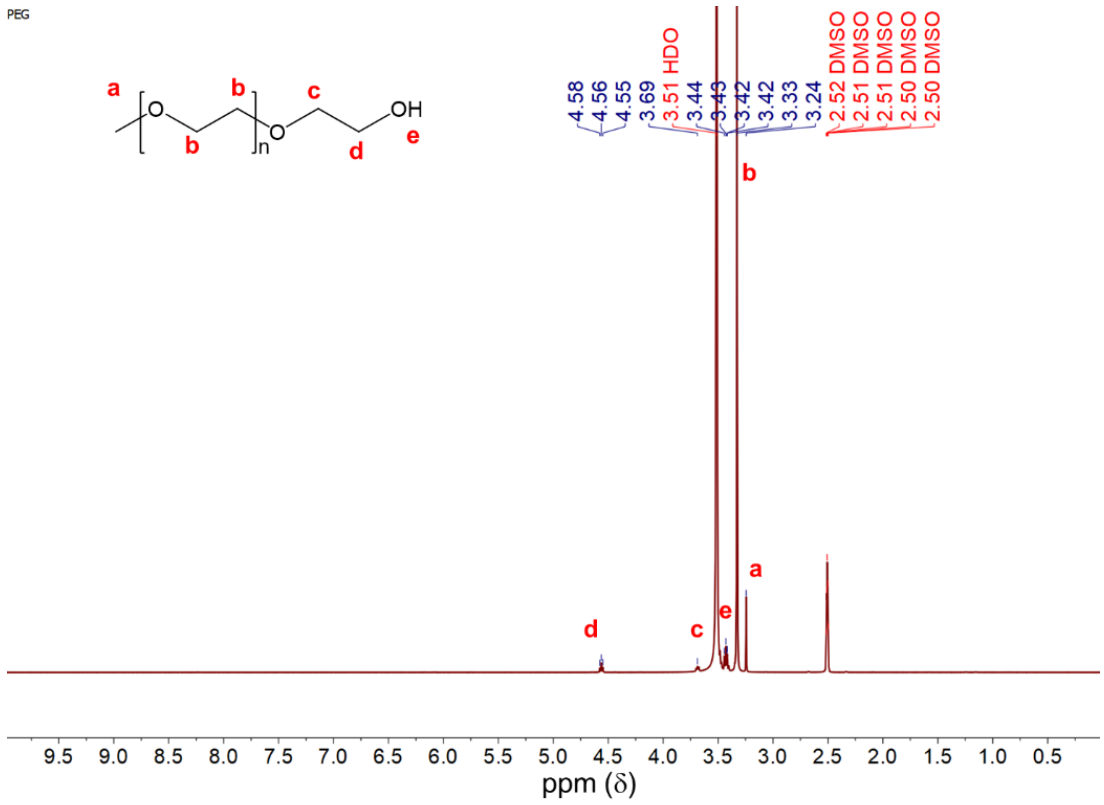

Figure 4.12. 400 MHz ^{1}H-NMR spectrum of **mPEG** in DMSO-d_6 at 298 K.

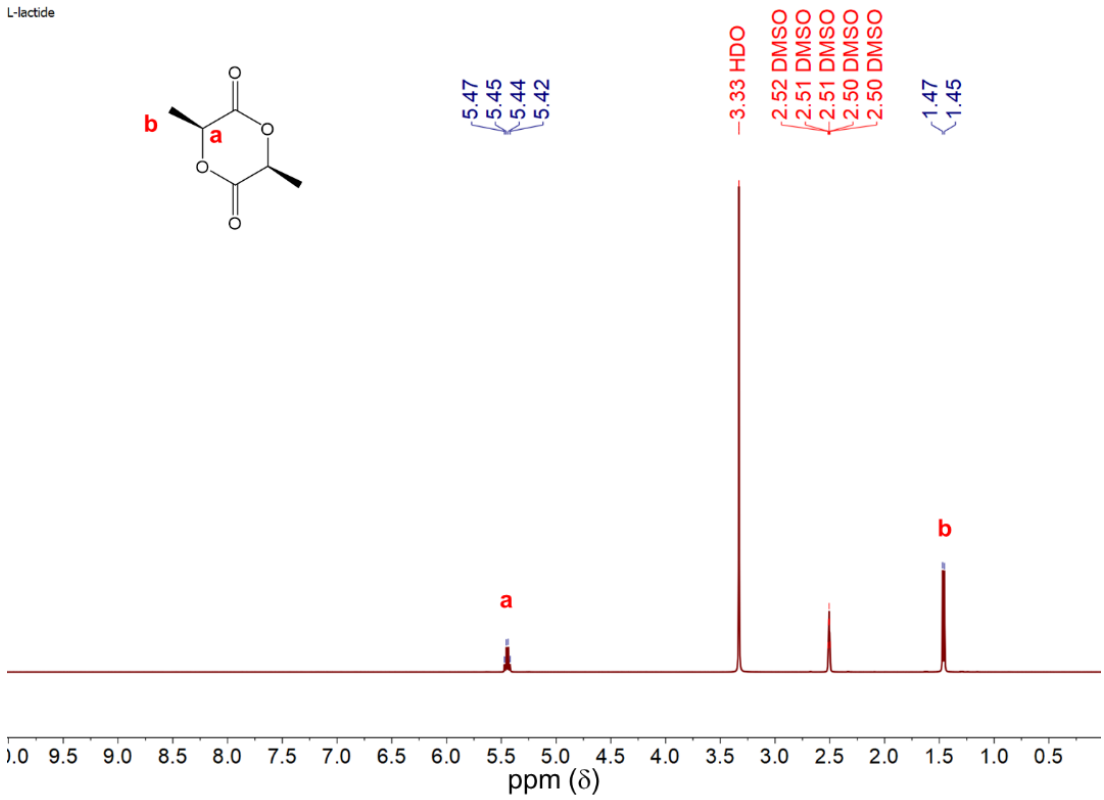

Figure 4.13. 400 MHz ^{13}C-NMR spectrum of *L*-lactide in DMSO-d_6 at 298 K.

4.2.5.2. SEC data of polymers

Size exclusion chromatography (SEC) was performed using the Waters system equipped with Waters 1525 binary HPLC pump, Waters STYRAGEL HR 1 DMF column, (4.6 mm × 25 cm) particle size 5 μm, UV detector 2489 with range 210–400 nm and refractive index (RI) detector 2414 were utilized to detect the retention time for peaks. The injection volume was kept at 100 μL for polymer samples with a 5 mg/mL concentration. The flow rate was 1 mL/min at 35 °C temperature. The results were analyzed by using EMPOWER software. The polymer's peaks were analyzed for absolute M_n, M_w, and PDI values employing the universal calibration method using polystyrene (500–30000 g/mol) as narrow standards.

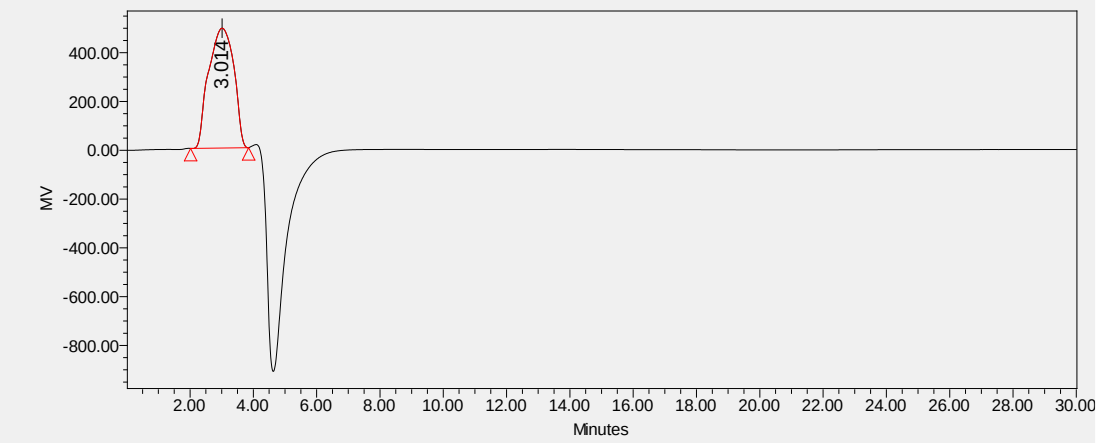

Figure 4.14. SEC chromatogram of **mPEG-PLLA** monitored using RI detector.

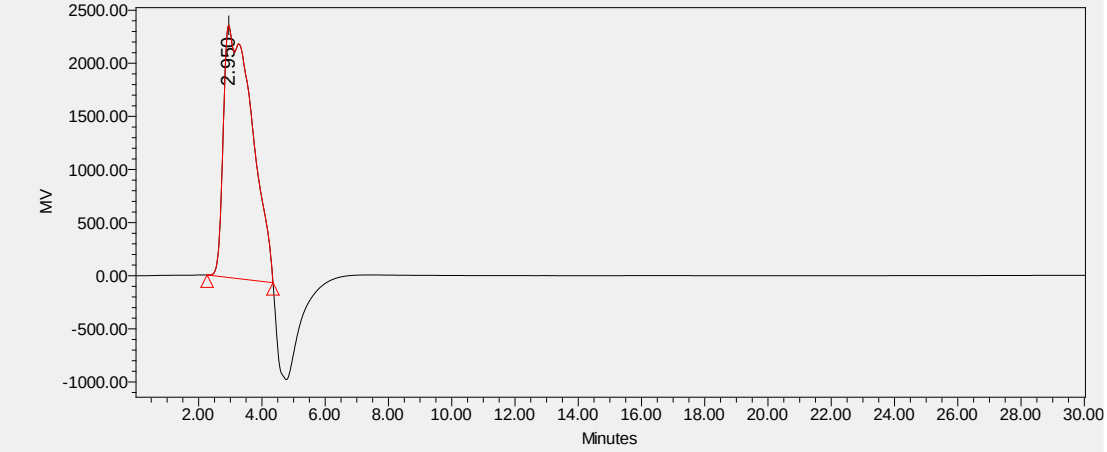

Figure 4.15. SEC chromatogram of **APTMS-PLLA** monitored using RI detector.

4.2.5.3. TEM analysis of IONP@PLLA

Energy dispersive X–ray (EDX) spectrum was measured using a transmission electron microscope (TEM) equipped with an EDX facility. The elemental composition and relative abundance are given in Table 4.4.

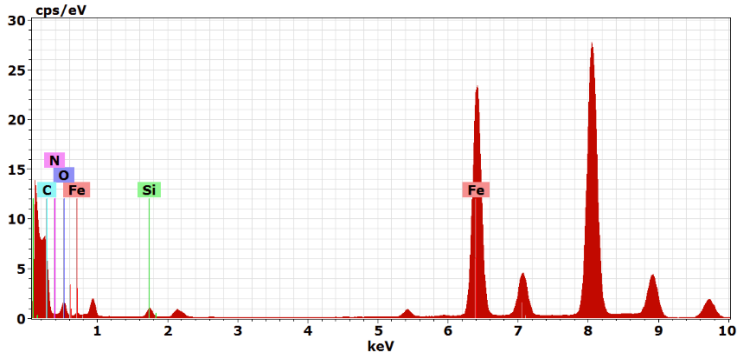

Figure 4.16. Energy dispersive X-ray (EDX) spectrum of **IONP@PLLA**.

Table 4.4. TEM-EDX spectrum measurement of **IONP@PLLA**.

Element	K_{value}	**Weight (%)**
Carbon (C)	0.277(Kα)	54.19
Iron (Fe)	6.398 (Kα); 0.705 (Lα)	26.01
Oxygen (O)	0.525(Kα)	10.57
Nitrogen (N)	0.392(Kα)	5.50
Silicon (Si)	1.739 (Kα)	3.73

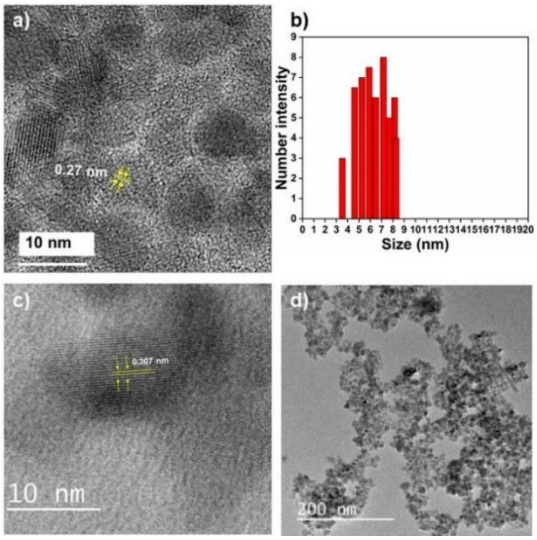

Figure 4.17. HR–TEM imaging and size distribution analysis of a,b) **IONP,** c,d) **IONP@PLLA**.

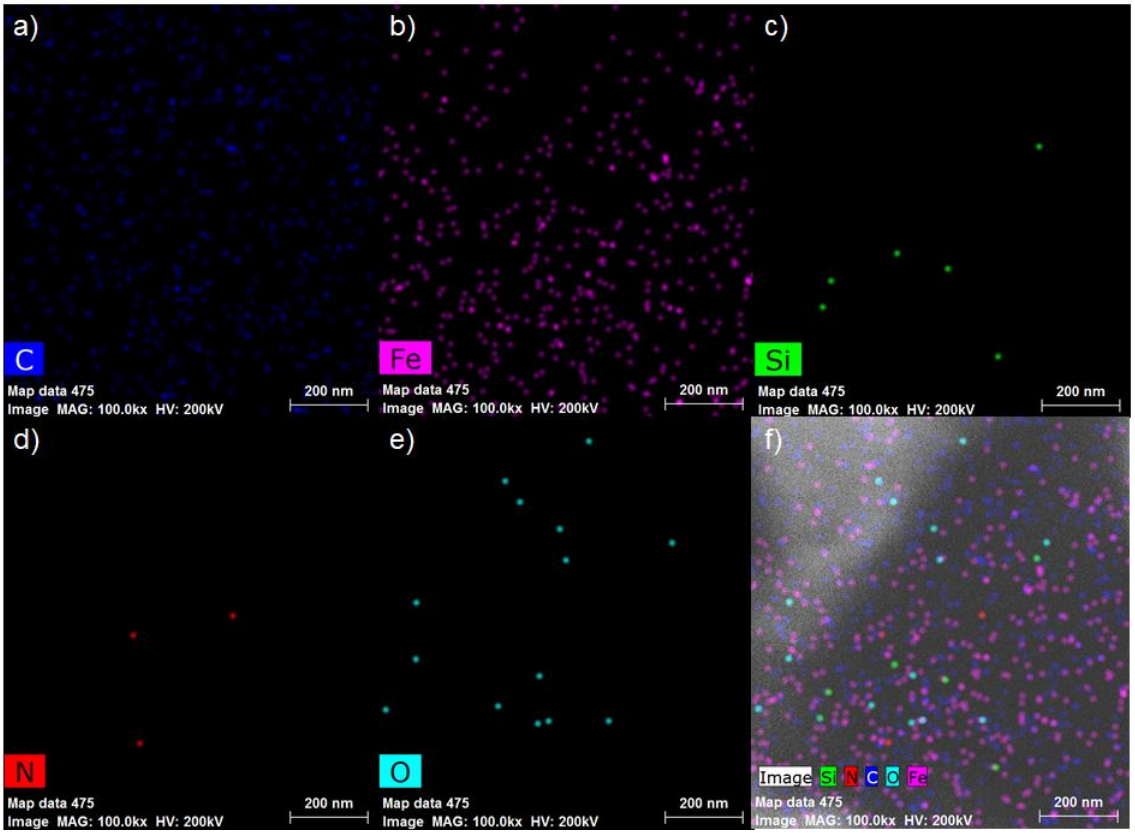

Figure 4.18. TEM mapping of the portion selected for a) C, b) Fe, c) Si, d) N, e) O, and f) combined image for all.

***4.2.5.4. XPS survey of IONP@PLLA*:** To determine the chemical compositions and electronic structure of **IONP@PLLA**. XPS measurements were carried out, and a broadly scanned XPS spectrum can be seen in Figure 4.19a. The spectrum indicates the presence of iron (Fe $2p_{1/2}$), carbon (C 1s), oxygen (O 1s), nitrogen (N 1s), and silicon (Si $2p_{3/2}$) emerging from the PLLA-coated iron oxide nanoparticles. In Figure 4.19b,c, and d, the individual fitted curves for the binding energies of iron, oxygen, and silicon, respectively, have been provided.

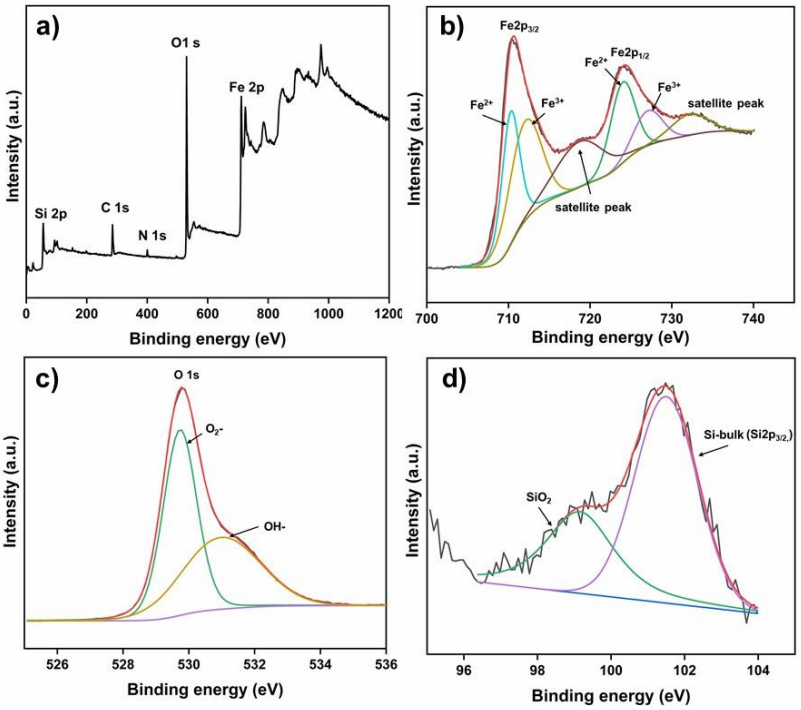

Figure 4.19. XPS survey of **IONP@PLLA** a) broad XPS scan, and the high-resolution spectra of b) Fe 2p, c) O 1s, d) Si $2p_{3/2}$.

4.2.5.5. Thermal degradation by thermogravimetric analysis.

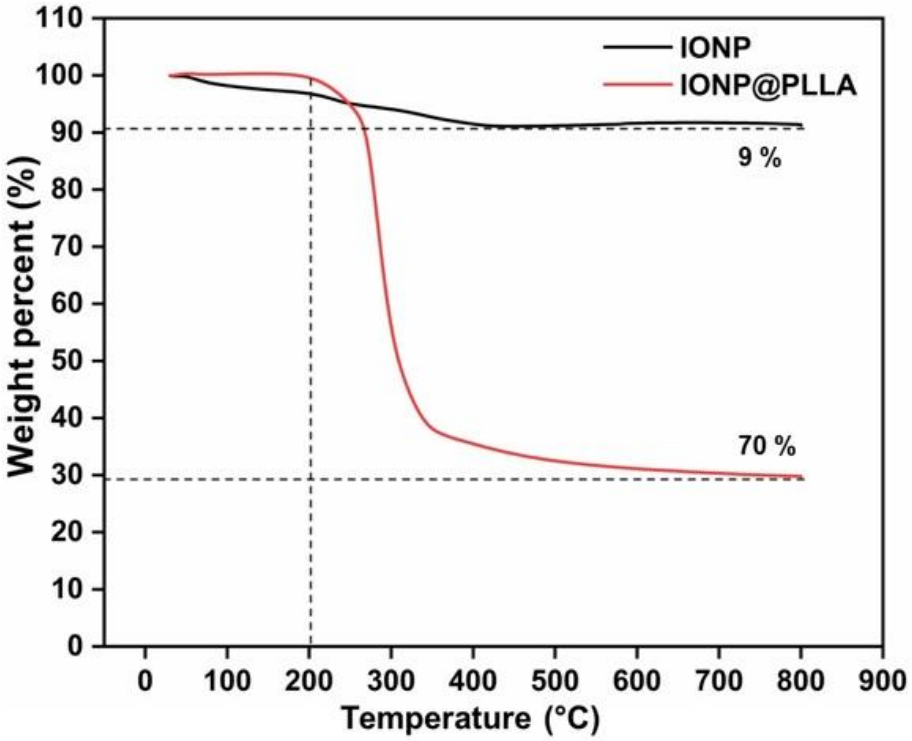

Figure 4.20. Thermogravimetric analysis (TGA) of **IONP** and **IONP@PLLA**.

4.2.5.6. Differential scanning calorimetry (DSC) thermograms

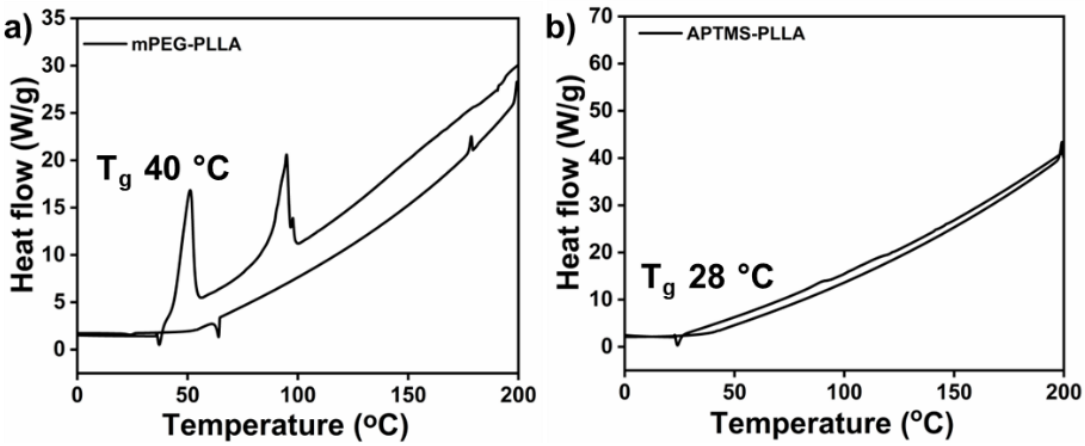

Figure 4.21. DSC thermograms of a) **mPEG-PLLA**, b) **APTMS-PLLA**.

4.2.6. Size analysis using TEM and DLS studies

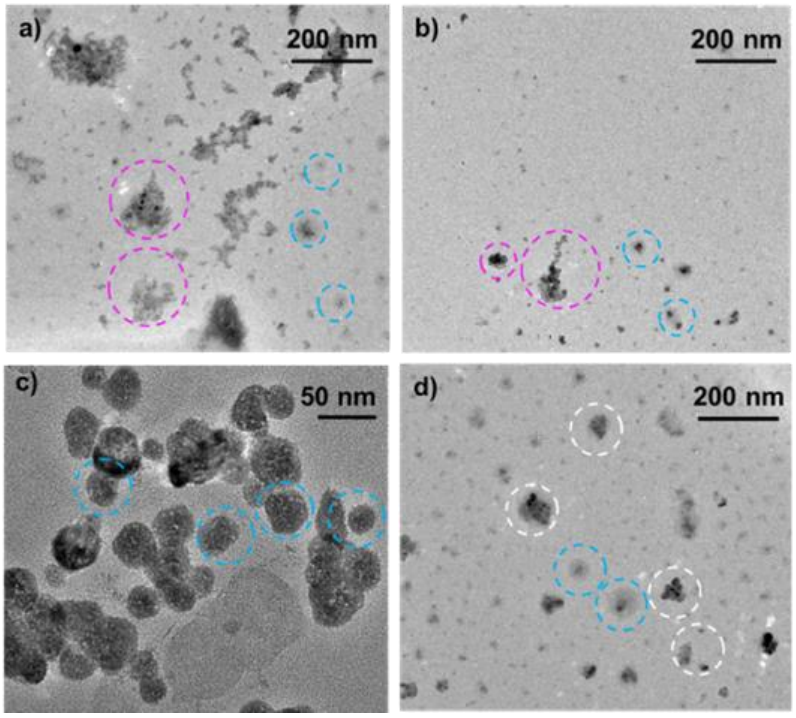

Figure 4.22. TEM imaging of **SS-NC** with different ratios of **IONP@PLLA/mPEG-PLLA** a) 0.05:0.01 mg/mL b) 0.05:0.05 mg/mL. c) 0.05:0.25 d) 0.05:0.35. Samples encircled with blue, pink, and white are corresponding to **SS-NC**, **IONP@PLLA**, and **NS-NC**, respectively.

Table 4.5. Observation of concentration-dependent self-sorting system TEM and DLS.

IONP@PLLA/ mPEG-PLLA	The concentration of mPEG-PLLA in IONP@PLLA/mPEG-PLLA	Product

(mg/mL)	(mM)	
0.05:0.001		-
0.05:0.005		-
0.05:0.01		**SS-NC+IONP@PLLA**
0.05:0.05	2	**SS-NC+IONP@PLLA**
0.05:0.10	2.3	**SS-NC+IONP@PLLA**
0.05:0.15	3.5	**SS-NC**
0.05:0.20	4.7	**SS-NC**
0.05:0.25	5.9	**SS-NC**
0.05:0.30	7.0	**SS-NC+NS-NC**
0.05:0.35	8.0	**SS-NC+NS-NC**
0.05:0.45	9.4	**SS-NC+NS-NC**

Table 4.6. Observation of concentration-dependent self-sorting system DLS.

S. No.	Compound	Z-Average (nm)
a)	**IONP**	34
b)	**IONP@PLLA**	51
c)	**NS-NC**	452
d)	**SS-NC**	227

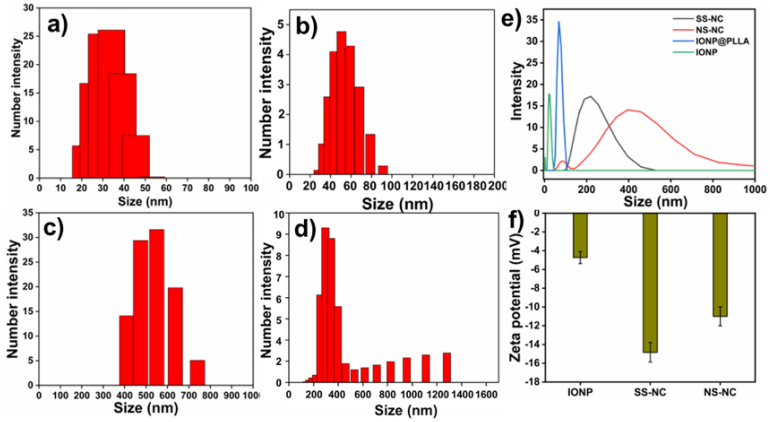

Figure 4.23. Size distribution data by DLS. a) **IONP**, b) **IONP@PLLA**, c) **NS-NC** (0.15 mg/mL), d) **SS-NC (IONP@PLLA/mPEG-PLLA** 0.05:0.15 mg/mL (w/v)), e) Size intensity graph, f) Zeta potential data at pH 7.4.

4.2.7 Drug loading and release behavior of DOX-SS-NC: Though the **SS-NC** was formed in the weight ratio ranging between 0.05:0.05 (1:1) and 0.05:0.25 (1:5) **IONP@PLLA/mPEG-PLLA**, we have chosen 0.05:0.15 (1:3) mg/mL as the optimized concentration ratio and the obtained **SS-NC** is used for further drug loading (DL) and release studies. For loading of doxorubicin (DOX) to **SS-NC** was performed with a 1:3 (21 mg) ratio of **IONP@PLLA/mPEG-PLLA**, in a 10 mL PBS solution. Then a 1mL solution of DOX (4 mg) in DMF was added to the **SS-NC** solution. After stirring for 7 h, the resulting mixture was dialyzed using a dialysis membrane bag (MWCO: ~3.5 kDa) against distilled water (2 × 500 mL) for 48 h to wash any unloaded DOX and DMF solvent. **SS-NC** encapsulated with DOX (**DOX-SS-NC**) was freeze-dried and re-dissolved in DMF (2 mg/mL), accompanied by UV–vis spectral analysis. A calibration curve was obtained using various concentrations of DOX in DMF (Figure 4.24), and the drug (DOX) loading content was determined by the ratio of the amount of loaded DOX to that of the dried sample using eq.4.4. Encapsulation efficiency was calculated by eq.4.5. The percentage of the content or total mass of drug in micelles was estimated as the difference between the initial drug quantity and unentrapped or free drug quantity in the supernatant with respect to the total quantity incorporated in the polymeric nanocarrier preparation. DOX release studies from **SS-NC** were investigated at 37 °C and 40 °C in PBS. AMF was applied at 24 kA m^{-1} and 409 kHz for 30 min.

The loading efficiency was calculated by the given formula in equation (eq.)

$$Drug\ Loading\ Efficiency\ (DLE)\ \% = \frac{Mass\ of\ drug\ in\ micelles}{Total\ mass\ of\ micelles} \times\ 100 \quad \text{(eq. 4.4)}$$

$$Encapsulation\ Efficiancy\ (EE, w/w)\ \% = \frac{Mass\ of\ drug\ in\ micelles}{Initial\ amount\ of\ drug\ loaded} \times\ 100 \quad \text{(eq. 4.5)}$$

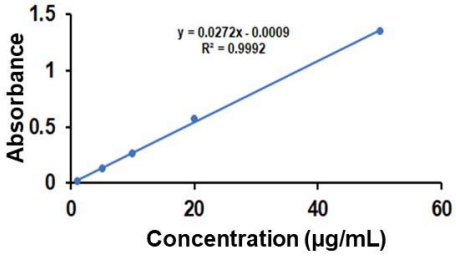

Figure 4.24. Calibration curve for doxorubicin (DOX).

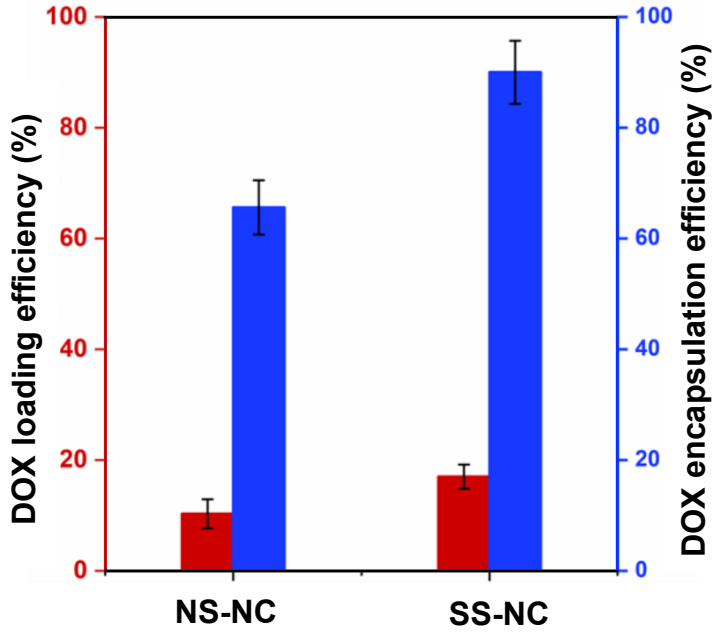

Figure 4.25. DOX encapsulation efficiency (EE) and loading efficiency (LE) of **SS-NC** and **NS-NC**. Readings were recorded in triplicate.

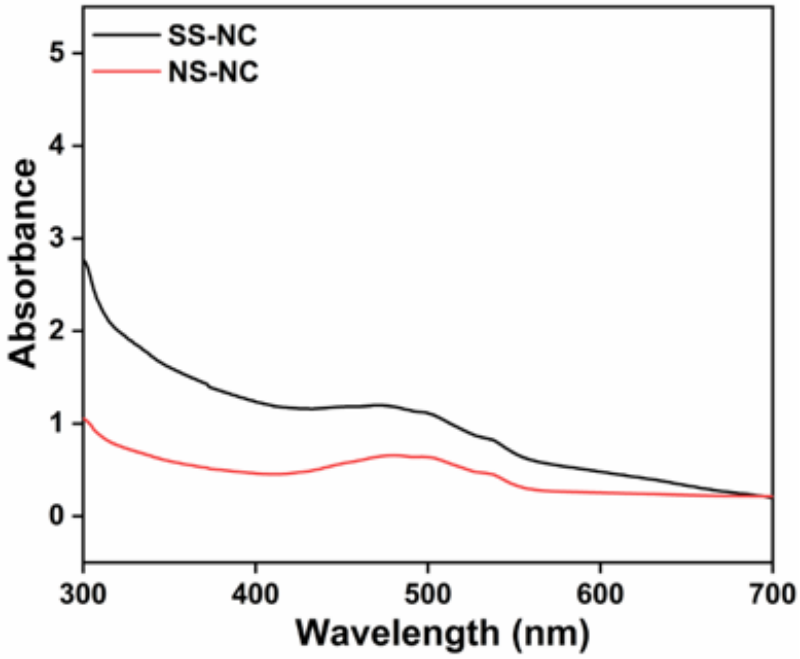

Figure 4.26. Comparison of UV−vis spectra of DOX encapsulated **SS-NC** and **NS-NC (**0.15 mg/mL **mPEG-PLLA** in PBS**)**.

4.2.8. Magnetic properties: Hysteresis loops diagrams for naked **IONP**, **IONP@PLLA**, and **SS-NC** were obtained in the solid state using a physical property measurement system (PPMS) at 300 K.

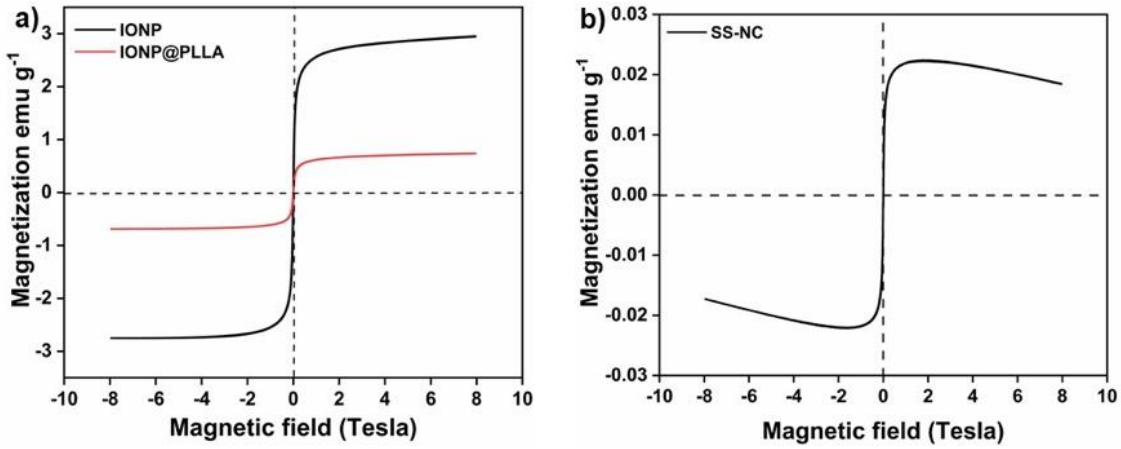

Figure 4.27. M-H hysteresis curve for a) **IONP**, **IONP@PLLA**, b) **SS-NC**.

4.2.9. Magnetic hyperthermia of DOX-SS-NC: Magnetic hyperthermia setup was used by applying an alternate magnetic field (AMF) at a frequency of 409 kHz and a magnetic field amplitude of 24 kA m^{-1} for 30 min on a sample solution of 500 µg/mL in PBS. The magnetic field amplitude (kA) and frequency (kHz) were optimized for the heat rise to 45-46 °C (Figure 4.28) as it is the optimal temperature for hyperthermia application on biological systems.[63] After applying the magnetic field, the sample was kept at 37 °C and aliquots were taken at different time intervals for 24 h and measured by UV–vis spectrophotometer at 599 nm.

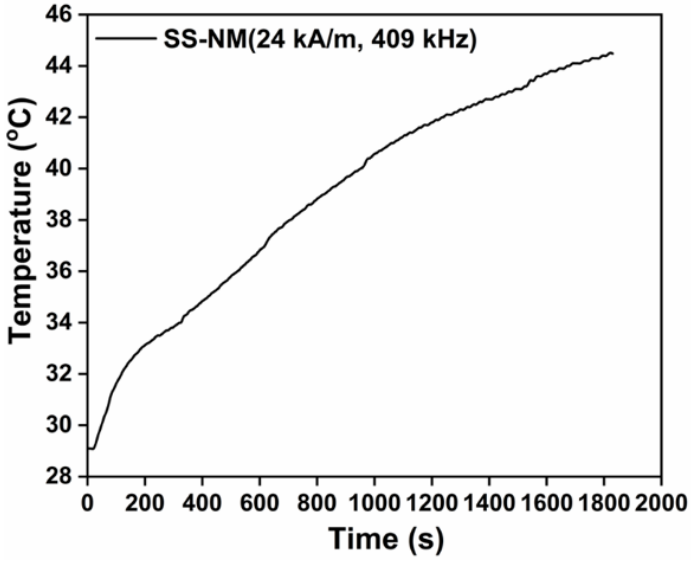

Figure 4.28. Heat rise in hyperthermia at 24 kA, 409 kHz.

4.2.10. Separation of SS-NC and NS-NC using External magnet

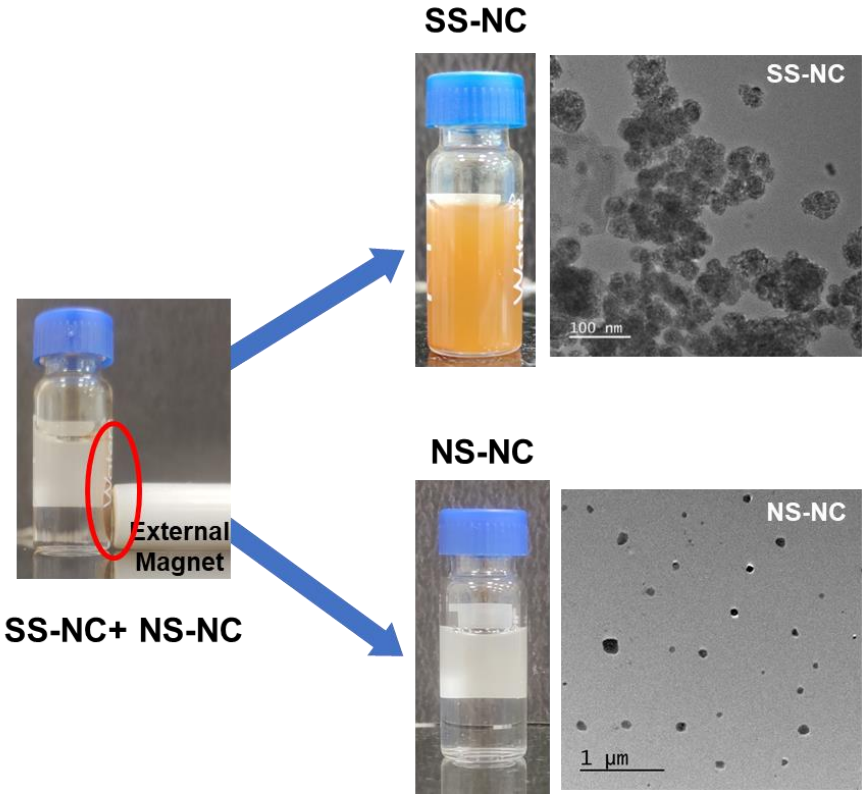

Figure 4.29. External magnetic separation of **SS-NC** and **NS-NC** with corresponding TEM images.

4.3. Possible pathways for the observation of the broad size range of SS-NC

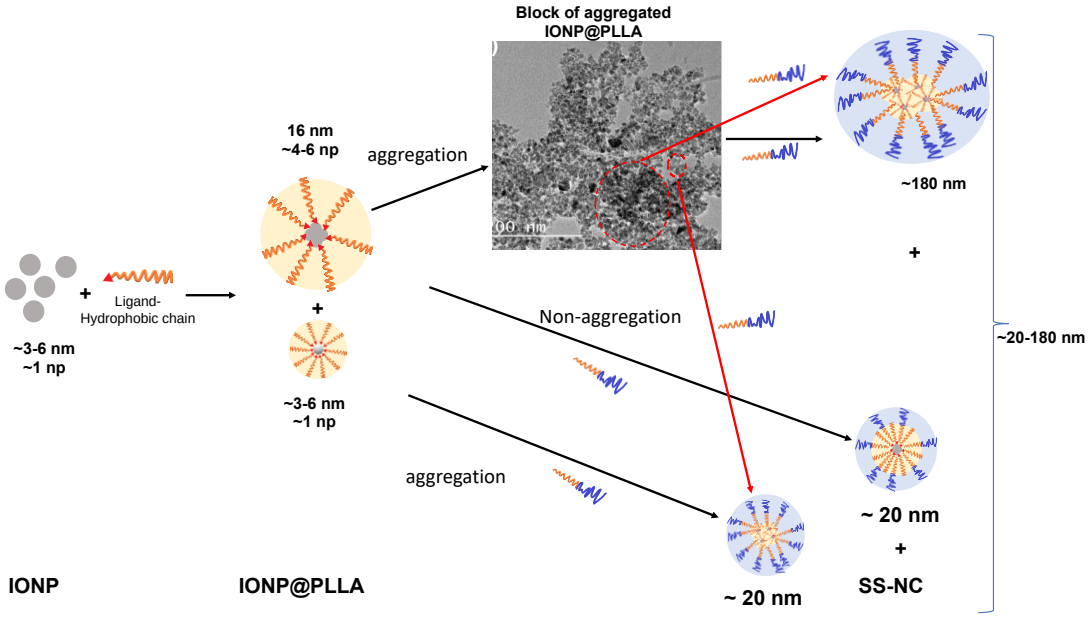

Figure 4.30. Broad size of **SS-NC** resulting from aggregated and non-aggregated **IONP-PLLA** upon self-assembly with **mPEG-PLLA**.

4.4. Conclusions

We demonstrate for the first time, the self-sorting behaviour of hydrophobic PLLA-conjugated **IONP** and amphiphilic **mPEG-PLLA** polymers in a competitive environment to produce a stable and novel type of core-shell nanocarrier with a crowded hydrophobic core. Intriguingly, the initiation concentration (0.01 mg/mL) observed for **SS-NC** was lower than the CMC (0.02 mg/mL) found for **mPEG-PLLA**, while the narcissistic self-sorted nanocarrier **NS-NC** formed only at the saturation concentration (0.3 mg/mL) observed for **IONP@PLLA** when maximum uptake was observed. Further TEM and confocal data also revealed **SS-NC** to have a core and shell structure. The drug uptake capability study using DOX for **SS-NC** shows 1.7 and 1.4 fold higher DLE and EE percentages than **NS-NC** which might be due to its higher hydrophobic core than its narcissistic counterpart **NS-NC**. Furthermore, magnetism (AMF) induced drug release has shown a sustained release profile compared to experiments without AMF and has exhibited stable pH profiles between 6 and 8, including the typical pH range of tumour cells (6.4 to 7), with a promising magnetic hyperthermia ability. The present study opens up a new avenue for optimizing the sustained uptake and release properties of other drugs by tuning hydrophobic and hydrophilic component arrangements in nanocarriers.

4.5. References:

1 Heuer-Jungemann, A.; Feliu, N.; Bakaimi, I.; Hamaly, M.; Alkilany, A.; Chakraborty, I.; Masood, A.; Casula, M. F.; Kostopoulou, A.; Oh, E.; Susumu, K.; Stewart, M. H.; Medintz, I. L.; Stratakis, E.; Parak, W. J.; Kanaras, A. G. The Role of Ligands in the Chemical Synthesis and Applications of Inorganic Nanoparticles. *Chem. Rev.* **2019**, *119*, 4819−4880.

2 Arvizo, R. R.; Bhattacharyya, S.; Kudgus, R. A.; Giri, K.; Bhattacharya, R.; Mukherjee, P. Intrinsic therapeutic applications of noble metal nanoparticles: past, present and future. *Chem. Soc. Rev.* **2012**, *41*, 2943−2970.

3 Howes, P. D.; Chandrawati, R.; Stevens, M. M. Colloidal nanoparticles as advanced biological sensors. *Science* **2014**, *346*, 1247390.

4 Zhang, F.; Lees, E.; Amin, F.; Rivera-Gil, P.; Yang, F.; Mulvaney, P.; Parak, W. J. Polymer-coated nanoparticles: a universal tool for biolabelling experiments. *Small* **2011**, *7*, 3113−3127.

5 Elsabahy, M.; Wooley, K. L. Design of polymeric nanoparticles for biomedical delivery applications. *Chem. Soc. Rev.* **2012**, *41*, 2545− 2561.

6 Coti, K. K.; Belowich, M. E.; Liong, M.; Ambrogio, M. W.; Lau, Y. A.; Khatib, H. A.; Zink, J. I.; Khashab, N. M.; Stoddart, J. F. Mechanised nanoparticles for drug delivery. *Nanoscale* **2009**, *1*, 16–39

7 Begines, B.; Ortiz, T.; Pérez-Aranda, M.; Martínez, G.; Merinero, M.; Argüelles-Arias, F.; Alcudia, A. Polymeric Nanoparticles for Drug Delivery: Recent Developments and Future Prospects. *Nanomaterials* **2020**, *10*, 1403.

8 Zhu, K.; Deng, Z.; Liu, G.; Hu, J.; Liu, S. Photoregulated Cross-Linking of Superparamagnetic Iron Oxide Nanoparticle (SPION) Loaded Hybrid Nanovectors with Synergistic Drug Release and Magnetic Resonance (MR) Imaging Enhancement. *Macromolecules* **2017**, *50*, 1113−1125.

9 Zhang, W.; Lyu, X.; Zhang, L.; Wang, W.; Shen, Q.; Lu, S.; Lu, L.; Zhan, M.; Hu, X. Rationally Driven Drug Nonradiative Decay via a Label-Free Polyprodrug Strategy to Renew Tumor Cascade Photothermal-Chemotherapy. *Macromol. Rapid Commun*. **2022**, *43*, 2100918.

10 Hu, J.; Qian, Y.; Wang, X.; Liu, T.; Liu, S. Drug-Loaded and Superparamagnetic Iron Oxide Nanoparticle Surface-Embedded Amphiphilic Block Copolymer Micelles for Integrated Chemotherapeutic Drug Delivery and MR Imaging. *Langmuir* **2012**, *28*, 2073−2082.

11 He, C.; Duan, X.; Guo, N.; Chan, C.; Poon, C.; Weichselbaum, R. R.; Lin, W. Core-shell nanoscale coordination polymers combine chemotherapy and photodynamic therapy to potentiate checkpoint blockade cancer immunotherapy. *Nat. Commun.* **2016**, *7*, 12499.

12 Batista, C. C. S.; Albuquerque, L. J. C.; de Araujo, I.; Albuquerque, B. L.; da Silva, F. D.; Giacomelli, F. C. Antimicrobial activity of nano-sized silver colloids stabilized by nitrogen-containing polymers: the key influence of the polymer capping. *RSC Adv.* **2018**, *8*, 10873−10882

13 Macher, T.; Totenhagen, J.; Sherwood, J.; Qin, Y.; Gurler, D.; Bolding, M. S.; Bao, Y. Ultrathin Iron Oxide Nanowhiskers as Positive Contrast Agents for Magnetic Resonance Imaging. *Adv. Funct. Mater.* **2015**, *25*, 490−494.

14 U. Landman and U. Heiz, *Nanocatalysis*; Springer: Berlin, Heidelberg, New York, 2007.

15 Kanelidis, I.; Kraus, T. The role of ligands in coinage-metal nanoparticles for electronics. *Beilstein J. Nanotechnol.* **2017**, *8*, 2625−2639.

16 Kumar, C. S. S. R.; Mohammad, F. Magnetic nanomaterials for hyperthermia-based therapy and controlled drug delivery. *Adv. Drug Deliv. Rev.* **2011**, *63*, 789−808.

17 Kaur, P.; Aliru, M. L.; Chadha, A. S.; Asea, A.; Krishnan, S. Hyperthermia using nanoparticles--Promises and pitfalls. *Int. J. Hyperthermia* **2016**, *32*, 76−88

18 Ahmad, A.; Gupta, A.; Ansari, M. M.; Vyawahare, A.; Jayamurugan, G.; Khan, R. Hyperbranched polymer-functionalized magnetic nanoparticle-mediated hyperthermia and niclosamide bimodal therapy of colorectal cancer cells. *ACS Biomater. Sci. Eng.* **2020**, *6*, 1102−1111.

19 Kim, H.-C.; Kim, E.; Jeong, S. W.; Ha, T.-L.; Park, S.-I.; Lee, S. G.; Lee, S. J.; Lee, S. W. Magnetic nanoparticle-conjugated polymeric micelles for combined hyperthermia and chemotherapy. *Nanoscale* **2015**, *7*, 16470−16480.

20 Quinto, C. A.; Mohindra, P.; Tong, S.; Bao, G. Multifunctional superparamagnetic iron oxide nanoparticles for combined chemotherapy and hyperthermia cancer treatment. *Nanoscale* **2015**, *7*, 12728−12736

21 Reyes-Ortega, F.; Checa Fernández, B. L.; Delgado, A. V.; Iglesias, G. R. Hyperthermia-triggered doxorubicin release from polymer-coated magnetic nanorods. *Pharmaceutics* **2019**, *11*, 517.

22 Her, S.; Jaffray, D. A.; Allen, C. Gold nanoparticles for applications in cancer radiotherapy: Mechanisms and recent advancements. *Adv. Drug Delivery Rev.* **2017**, *109*, 84−101.

23 Goddard, Z. R.; Marín, M. J.; Russell, D. A.; Searcey, M. Active targeting of gold nanoparticles as cancer therapeutics. *Chem. Soc. Rev.* **2020**, *49*, 8774−8789.

24 Gupta, A.; Ahmad, A.; Singh, H.; Kaur, S.; K M, N.; Ansari, M. M.; Jayamurugan, G.; Khan, R. Nanocarrier Composed of Magnetite Core Coated with Three Polymeric Shells Mediates LCS-1 Delivery for Synthetic Lethal Therapy of BLM-Defective Colorectal Cancer Cells. *Biomacromolecules* **2018**, *19*, 803−815

25 Matsumoto, K.; Terashima, T.; Sugita, T.; Takenaka, M.; Sawamoto, M. Amphiphilic Random Copolymers with Hydrophobic/Hydrogen-Bonding Urea Pendants: Self-

Folding Polymers in Aqueous and Organic Media. *Macromolecules* **2016**, *49*, 7917−7927.

26 Altintas, O.; Barner-Kowollik, C. Single-Chain Folding of Synthetic Polymers: A Critical Update. *Macromol. Rapid Commun.* **2016**, *37*, 29−46.

27 Gonzalez-Burgos, M.; Latorre-Sanchez, A.; Pomposo, J. A. Advances in single chain technology. *Chem. Soc. Rev.* **2015**, *44*, 6122−6142.

28 Albert, S. K.; Thelu, H. V. P.; Golla, M.; Krishnan, N.; Varghese, R. Modular synthesis of supramolecular DNA amphiphiles through host–guest interactions and their self-assembly into DNA-decorated nanovesicles. *Nanoscale* **2017**, *9*, 5425−5432.

29 Adams, M. L.; Lavasanifar, A.; Kwon, G. S. Modular synthesis of supramolecular DNA amphiphiles through host–guest interactions and their self-assembly into DNA-decorated nanovesicles. *J. Pharm. Sci.* **2003**, *92*, 1343−1355

30 Van Nostrum, C. F. Covalently cross-linked amphiphilic block copolymer micelles. *Soft Matter* **2011**, *7*, 3246−3259.

31 Xu, Y.; Qin, Y.; Palchoudhury, S.; Bao, Y. Water-Soluble Iron Oxide Nanoparticles with High Stability and Selective Surface Functionality. *Langmuir* **2011**, *27*, 8990 – 8997.

32 Percástegui, E. G.; Ronson, T. K.; Nitschke, J. R. Design and Applications of Water-Soluble Coordination Cages. *Chem. Rev.* **2020**, *120*, 13480−13544.

33 Shimizu, L. S.; Salpage, S. R.; Korous, A. A. Functional Materials from Self-Assembled Bis-urea Macrocycles. *Acc. Chem. Res.* **2014**, *47*, 2116−2127.

34 Dånmark, S.; Aronsson, C.; Aili, D. Tailoring Supramolecular Peptide–Poly(ethylene glycol) Hydrogels by Coiled Coil Self-Assembly and Self-Sorting. *Biomacromolecules* **2016**, *17*, 2260−2267.

35 Burd, C.; Weck, M. Self-Sorting in Polymers. *Macromolecules* **2005**, *38*, 7225.

36 Smith, M. M.; Smith, D. K. Self-sorting multi-gelator gels—mixing and ageing effects in thermally addressable supramolecular soft nanomaterials. *Soft Matter* **2011**, *7*, 4856.

37 Chakrabarty, R.; Mukherjee, P. S.; Stang, P. J. Supramolecular Coordination: Self-Assembly of Finite Two- and Three-Dimensional Ensembles. *Chem. Rev.* **2011**, *111*, 6810−6918.

38 Foster, J. A.; Parker, R. M.; Belenguer, A. M.; Kishi, N.; Sutton, S.; Abell, C.; Nitschke, J. R. Differentially Addressable Cavities within Metal–Organic Cage-Cross-Linked Polymeric Hydrogels. *J. Am. Chem. Soc.* **2015**, *137*, 9722−9729.

39 Safont-Sempere, M. M.; Fernandez, G.; Würthner, F. Self-Sorting Phenomena in Complex Supramolecular Systems. *Chem. Rev.* **2011**, *111*, 5784−5814.

40 Darling, S. B. Directing the self-assembly of block copolymers. *Prog. Polym. Sci.* **2007**, *32*, 1152–1204.

41 Smith, D. K. Lost in translation? Chirality effects in the self-assembly of nanostructured gel-phase materials. *Chem. Soc. Rev.* **2009**, *38*, 684−694.

42 Imai, S.; Takenaka, M.; Sawamoto, M.; Terashima, T. Self-Sorting of Amphiphilic Copolymers for Self-Assembled Materials in Water: Polymers Can Recognize Themselves. *J. Am. Chem. Soc.* **2019**, *141*, 511−519.

43 Wang, H.; Zhao, Y.; Wu, Y.; Hu, Y. L.; Nan, K.; Nie, G.; Chen, H. Enhanced anti-tumor efficacy by co-delivery of doxorubicin and paclitaxel with amphiphilic methoxy PEG-PLGA copolymer nanoparticles. *Biomaterials* **2011**, *32*, 8281−8290.

44 Wu, X. L.; Kim, J. H.; Koo, H.; Bae, S. M.; Shin, H.; Kim, M. S.; Lee B. H; Park, R. W.; Kim, I. S.; Choi, K.; Kwon, I. C.; Kim, K.; Lee, D. S. Tumor-Targeting Peptide Conjugated pH-Responsive Micelles as a Potential Drug Carrier for Cancer Therapy. *Bioconjugate Chem.* **2010**, *21*, 208–213.

45 Cagel, M.; Tesan, F. C.; Bernabeu, E.; Salgueiro, M. J.; Zubillaga, M. B.; Moretton, M. A.; Chiappetta, D. A. Polymeric mixed micelles as nanomedicines: Achievements and perspectives. *Eur. J. Pharm. Biopharm.* **2017**, *113*, 211−228.

46 Mishra, B.; Patel, B. B.; Tiwari, S. Colloidal nanocarriers: a review on formulation technology, types and applications toward targeted drug delivery. *Nanomed.: Nanotechnol., Biol. Med.* **2010**, *6*, e9–e24.

47 Fan, M.; Han, Y.; Gao, S.; Yan, H.; Cao, L.; Li, Z.; Liang, X.-J.; Zhang, J. Ultrasmall gold nanoparticles in cancer diagnosis and therapy. *Theranostics* **2020**, *10*, 4944−4957.

48 Qian, H.; Wohl, A. R.; Crow, J. T.; Macosko, C. W.; Hoye, T. R. A Strategy for Control of “Random” Copolymerization of Lactide and Glycolide: Application to Synthesis of PEG-b-PLGA Block Polymers Having Narrow Dispersity. *Macromolecules* **2011**, *44*, 7132−7140.

49 Tan, C. H.; Ahmad, A.; Anur, F. H. Investigation of the synthesis of poly-D,L-lactide-co-poly(ethylene glycol) flexible thermoplastic. *Int. J. Polym. Anal. Charact.* **2016**, *21*, 104-111.

50 Kammiyada, H.; Ouchi, M.; Sawamoto, M. Ring-Expansion Living Cationic Polymerization of Vinyl Ethers: Optimized Ring Propagation. *Macromol. Symp.* **2015**, *350*, 105−116.

51 Yokozawa, T.; Yokoyama, A. Chain-Growth Condensation Polymerization for the Synthesis of Well-Defined Condensation Polymers and π-Conjugated Polymers. *Chem. Rev.* **2009**, *109*, 5595− 5619.

52 Silva, V. A. J.; Andrade, P. L.; Silva, M. P. C.; Bustamante, A. D.; Valladares, L. D. S.; Albino Aguiar, J. Synthesis and characterization of Fe_3O_4 nanoparticles coated with fucan polysaccharides. *J. Magn. Magn Mater.* **2013**, *343*, 138–143.

53 Shameli, K.; Ahmad, M. B.; Yunis, W. Z.; Ibrahim, N. A.; Rahman, R. A.; Jokar, M.; Darroudi, M. Silver/poly (lactic acid) nanocomposites: preparation, characterization, and antibacterial activity. *Int. J. Nanomed*. **2010**, *5*, 573−579.

54 Johnson, L.; Gray, D. M.; Niezabitowska, E.; McDonald, T. O. Multi-stimuli-responsive aggregation of nanoparticles driven by the manipulation of colloidal stability. *Nanoscale* **2021**, *13*, 7879−7896.

55 Zhong, Y.; Yu, L.; Chen, Z.-F.; He, H.; Ye, F.; Cheng, G.; Zhang, Q. Microwave-Assisted Synthesis of Fe_3O_4 Nanocrystals with Predominantly Exposed Facets and Their Heterogeneous UVA/Fenton Catalytic Activity. *ACS Appl. Mater. Interfaces* **2017**, *9*, 29203−29212.

56 Ananthapadmanabhan, K. P.; Goddard, E. D.; Turro, N. J.; Kuo, P. L. Fluorescence probes for critical micelle concentration. *Langmuir* **1985**, *1*, 352−355.

57 Jongpaiboonkit, L.; Zhou, Z.; Ni, X.; Wang, Y.-Z.; Li, J. Self-association and micelle formation of biodegradable poly(ethylene glycol)-poly(L-lactic acid) amphiphilic di-block co-polymers. *J. Biomater. Sci., Polym. Ed.* **2006**, *17*, 747-763.

58 Cao, Y.; Yang, S.; Li Y.; Shi, J. Cooperative organizations of small molecular surfactants and amphiphilic block copolymers: Roles of surfactants in the formation of binary co-assemblies. *Aggregate* **2021**, *2*, e49.

59 Blanco, E.; Shen, H.; Ferrari, M. Principles of nanoparticle design for overcoming biological barriers to drug delivery. *Nat. Biotechnol.* **2015**, *33*, 941−951.

60 Ge, Y. Q.; Zhang, Y.; Xia, J. G.; Ma, M.; He, S. Y.; Nie, F.; Gu, N. Effect of surface charge and agglomerate degree of magnetic iron oxide nanoparticles on KB cellular uptake in vitro. *Colloids Surf. B* **2009**, *73*, 294 –301.

61 Tufa, L. T.; Jeong, K. J.; Tran, V. T.; Lee, J. Magnetic-Field-Induced Electrochemical Performance of a Porous Magnetoplasmonic Ag@Fe_3O_4 Nanoassembly. *ACS Appl. Mater. Interfaces* **2020**, *12*, 6598−6606.

62 Maeda, H.; Matsumura, Y. Tumoritropic and lymphotropic principles of macromolecular drugs. *Crit. Rev. Ther. Drug Carrier Syst.* **1989**, *6*, 193−210.

63 Roti Roti, J. L. Cellular responses to hyperthermia (40-46 degrees C): cell killing and molecular events. *Int. J. Hyperthermia* **2008**, *24*, 3–15.

64 Swietach, P.; Vaughan-Jones, R. D.; Harris, A. L.; Hulikova, A. The chemistry, physiology and pathology of pH in cancer. *Philos. Trans. R. Soc., B* **2014**, *369*, 20130099.

65 Zhang, Y.; Huo, M.; Zhou, J.; Zou, A.; Li, W.; Yao, C.; Xie, S. DDSolver: An Add-In Program for Modeling and Comparison of Drug Dissolution Profiles. *AAPS J.* **2010**, *12*, 263−71.

66 Mahajan, R.; Selim, A.; Neethu, K. M.; Sharma, S.; Shanmugam, V.; Jayamurugan, G. A systematic study to unravel the potential of using polysaccharides based organic-nanoparticles versus hybrid-nanoparticles for pesticide delivery. *Nanotechnol.* **2021**, *32*, 475704–475716.

67 Makoid, M.; Dufoure, A.; Banakar, U. M.; Michael, D. A.; Banakar, U. Modelling of Dissolution Behaviour of Controlled Release Systems. *STP Pharma*. **1993**, *3*, 49−58.

68 Cohen, S.; Yoshioka, T.; Lucarelli, M.; Hwang, L. H.; Langer, R. Controlled delivery systems for proteins based on poly(lactic/glycolic acid) microspheres. *Pharm. Res.* **1991**, *8*, 713−720.

69 Dash, S.; Murthy, P. N.; Nath, L.; Chowdhury, P. Kinetic modeling on drug release from controlled drug delivery systems. *Acta Polym. Pharm.* **2010**, *67*, 217−223.

70 Zhan, S.; Wang, J.; Wang, W.; Cui, L.; Zhao, Q. Preparation and in vitro release kinetics of nitrendipine-loaded PLLA–PEG–PLLA microparticles by supercritical solution impregnation process. *RSC Adv.* **2019**, *9*, 16167−16175.

71 Alba, A.; du Boullay, O. T.; Martin-Vaca, B.; Bourissou, D. Direct ring-opening of lactide with amines: application to the organo-catalyzed preparation of amide end-

capped PLA and to the removal of residual lactide from PLA samples. *Polym. Chem.* **2015**, *6*, 989−997.

Chapter 5: *Overall summary and conclusion of the thesis*

5.0. Summary

As a result of the limitations and uncertainties associated with traditional drug discovery, researchers have been able to investigate the biological profile of natural as well as synthetic macromolecules.[1-3] This unfolded the importance of polymeric materials in the biological system and incidentally promoted the research and development in the field of bioactive synthetic polymers both commercially and academically.[4, 5] In chapter 1 of this thesis, we have discussed the diversity and role of bioactive synthetic polymers and their potential applications. The inert polymers chitosan, peptides, and pluronics, which had previously been reported as inactive, were discovered to be bioactive or chemically modified in order to generate therapeutic responses.[6, 7] This made polymeric drugs a preferable choice as sequestrants to bind with multivalent receptors. Further conjugating one or more bioactive moiety with an inert polymer backbone to enhance solubility and improve drug pharmacological behavior has evolved the branch of polymer-drug conjugates, which occupied the field of controlled and site-specific drug delivery application.[7, 8] As the major attention was given to improve the bioactivity of existing natural or synthetic polymers, as in the case of polymeric drugs or polymer-drug conjugates, the need of new bioactive synthetic polymers while exploiting existing bioactive small molecules for therapeutic application cannot be denied. Here, the journey started to transform existing small molecules into prodrug polymers by polymerizing small molecules *via* complementary functional groups.[9] It is possible with drug polymers to uncover new drugs and extend drug delivery in ways that are not presently possible with small molecules and chemically inert polymer-drug conjugates. On the other hand, this thesis focuses on the development and definition of drug polymers, which are still at the pioneering stage and have never been satisfactorily defined in the past.

The ongoing COVID-19 pandemic and the overuse of antibiotics diverted our attention toward the future antibiotic crisis. Antimicrobial polymers (APs) have been

reported many times as a method for managing microbial infections more effectively, and they are discussed in chapter 1 in detail. Antibiotic alternatives have become so vital that they have sometimes replaced classical antibiotics.[10] Biocidal polymers (BP), polymeric biocide (PB), and biocidal releasing polymers (BRP) are the most common types of APs, according to the classification provided recently. All classes of antimicrobial polymers reported to date possess unique features of their structures and applications, but they also contain a significant amount of non-drug spacer units. This gap has been exploited by putting forward a hypothesis on how to develop a model for synthesizing a polymer without any non-drug spacer or linker using ciprofloxacin (antibiotic), a second-generation fluoroquinolone.

This unique structure of ciprofloxacin (**1**) provides two complementary functional groups (NH and COOH), which makes it capable of self-polymerization, as shown in chapter 2. Though the reports on the polymerization of **1** by substituting them with linkers/spacer units have been found, the idea of a self-polymerized drug and the effect of a non-drug spacer unit in the drug-polymer has been realized for the first time by our group.[11] Here we have developed a novel type of drug-polymer **C_0P_1** using ciprofloxacin as a monomer unit, which is introduced as a true drug-polymer due to the 0% non-drug/inert unit in the polymeric structure and the release of only drug unit for the activity upon hydrolysis. For comparison study, two other polymers with different spacer chain lengths **C_2P_2** and **$C_{10}P_3$**, (29 and 53%, respectively), were also synthesized. The antibacterial studies in both solution and suture coating phases indicated that, at least in the present case, the length of the non-drug spacer is inversely proportional to the antibacterial property of the polymer. Polymerization was a crucial factor in achieving uniform coating of **C_0P_1** on nylon threads, as monomer **1** has a poor solubility profile for coating application. Furthermore, the hydrolysis study in an acidic environment indicated that **1** was released slowly and sustainedly from **C_0P_1**, as opposed to two other spacer polymers that showed rapid degradation in the same environment. Considering its higher stability (409 °C melting point), biocompatibility, and better coating properties, **C_0P_1** offers great potential for therapeutic applications, especially in suture coatings.

Additionally, the structural stability of **C_0P_1** stored in solid state in closed vial at atmospheric conditions (with temperature range 20-40 °C for 6 months) was analyzed by ^{1}H-NMR spectroscopy in DMSO-d_6. Most of the peaks remained unchanged after storage, with some hydrolyzed product detected by increase in COOH-peak intensity at

15.3 ppm. The storage in N_2 atmosphere may resolve the stability issue as the polymer is prone to hydrolyse by small amount of moisture content. Further, no degraded product was observed in the NMR spectrum.

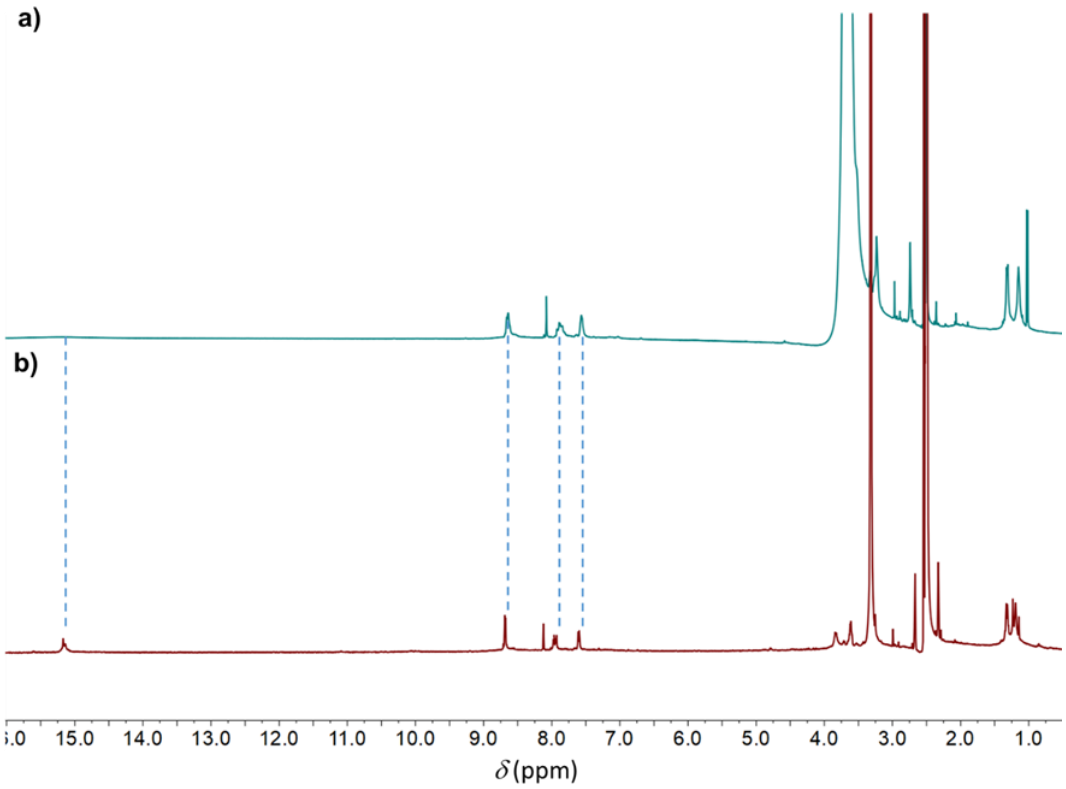

Figure 5.0. Time-dependent storage stability study by 400 MHz ^{1}H NMR spectra of **C_0P_1** in DMSO-d_6 a) 0h b) 6 months.

The concept of a true drug polymer may lead to the unraveling of many new drug polymers and their application as advanced biomaterials. This means that we believe **C_0P_1** can provide a new direction in drug polymer synthesis. Due to the rising incidence of antibiotic resistance and the antimicrobial crisis, the need for biocidal materials has greatly increased. New drug discovery can be enhanced by using existing biocidal small molecules to make better-performing bioactive materials. Nanotechnology has prospered greatly since the discovery of carbon nanomaterials, especially carbon dots, and we believe there are many more exciting results to come in this diverse field. In this area, another subclass of carbonized polymer dots (CPDs) has been introduced in the past decade. There is a brief description of this in chapters 1 and 3 of this thesis. As a result of CPD's unique properties and nano effect, it is also being exploited for antimicrobial purposes. To explore the better antibacterial properties of the synthesized true drug-polymer **C_0P_1**, it has been carbonized and transformed by the solvothermal synthetic

route to CPD (**CPD-C_0P_1**), and the synthetic conditions have been optimized in such a way that the near white light emission property is enhanced with a modest quantum yield of 23%. Additionally, the **CPD-C_0P_1** retained its broad spectrum antimicrobial activity and was highly cytocompatible even at unexpectedly high concentrations (500 mg/mL), with up to 90% of cells remaining unaffected. The biocompatible, antibacterial, and bioimaging properties of **CPD-C_0P_1** were subsequently demonstrated by embedding them in a biocompatible matrix (PMMA) for the manufacture of RGB emissive nanofiber mats (NFMs) and further studied their antibacterial properties. Based on the mechanistic study of **CPD-C_0P_1**, a series of mechanisms, including adhesion of **CPD-C_0P_1** to bacterial cell walls, ROS generation, and cell wall damage, may contribute to its biocidal activity. Moreover, the NFM has shown efficient antibacterial properties due to the release of **CPD-C_0P_1** from it in PBS buffer. Even though the field of CPDs is emerging with the unfolding of many exciting properties within, we believe that this work contributes towards the direction of exploring carbon nanomaterial for antimicrobial applications more efficiently.

As nanocarriers for drug delivery, polymers have played a crucial role, primarily as a delivery agent to cancer cells because of their size, inertness, stimuli-responsive behavior, and extraordinary capacity to contain large quantities of bioactive molecules. The fourth chapter of this thesis explores the use of stimuli-induced polymeric nanocomposites for drug delivery. Our proposal involves the development of a water-soluble magnetic field-induced drug delivery system obtained by preferential molecular marriage that avoids narcissistic self-sorting. This work utilized the self-sorting behavior of hydrophobic PLLA-capped IONPs and amphiphilic **mPEG-PLLA** to create **SS-NC**, a novel core-shell type nanocarrier. The traditional self-assembled micelles formed as a result of the narcissistic self-sorting of an amphiphilic **mPEG-PLLA**, known as **NS-NC**, were also produced for comparison. Moreover, the IC (0.01 mg/mL) observed for the **SS-NC** met the CMC (0.02 mg/mL) at the time of maximum uptake, like the CMC for **mPEG−PLLA**, while the **NS-NC** formed only at the saturation concentration (0.3 mg/mL) observed for **IONP@PLLA** at the time of maximum uptake. In addition, UV−vis, TEM, DLS, and confocal studies were conducted to characterize the newly formed **SS-NC**. These studies revealed the formation of a core-shell-type structure. It has been found that **SS-NC**, a micellar system built using **IONP@PLLA** and **mPEG−PLLA**, was able to form a more dense hydrophobic core when compared to

traditional micellar system **NS-NC**, which has been studied using Pyrene encapsulation as the probe. The **SS-NC** has been utilized for the loading and encapsulation of hydrophobic drugs (doxorubicin/DOX) due to the denser hydrophobicity of the core of the material. In accordance with our expectations, we observed a 1.7-fold increase in drug loading and a 1.4-fold increase in encapsulation efficiency of **SS-NC** over **NS-NC**, respectively, when assayed against **NS-NC**. The presence of magnetic nanoparticles **IONP** further improved the performance of the **SS-NC** by facilitating a 50% increase in drug release by applying alternate magnetic fields (AMF) as physical stimuli as an alternate mechanism for drug release. The optimal glass transition temperature of **mPEG-PLLA** polymer (40 °C) was found to be responsible for up to 18-20% drug release to be observed on day 8 in the presence of mere temperature (40 °C). At the same time, the nanocarrier has also shown a 6-12% release rate of the drug within the first eight days at 37 °C and is stable at both slightly acidic and basic pH, i.e., pH 6 and 8. The newly formed nanocarrier is capable of delivering drugs precisely when stimuli are applied to it. As this nanocarrier is able to carry a hydrophobic bioactive molecule, it can be further optimized to deliver better performance and deliver a wide variety of hydrophobic bioactive molecules by altering the length of the polymer chains, using di, tri, or multiblock copolymers, or replacing the metal nanoparticles in the core of the nanocarriers. As far as generating core-shell nanocarriers can be concerned, if these systems are synthesized with inert polymers and metal nanoparticles, it can lead to many applications, such as combining hyperthermia, photothermal and photo-induced smart drug delivery systems for cancer cells, which is the combination of chemotherapy and hyperthermia.

Though, two newly obtained nano systems **CPD-C_0P_1** and **SS-NC** are completely individual system both are obtained for a common cause of therapeutic application i.e., to be used as bioactive polymeric nanocomposite. On one hand biocompatible polymer self-assembled nanostructure **SS-NC** facilitate drug delivery for hydrophobic drug doxorubicin and on the other hand polymer originated carbonized polymer dot **CPD-C_0P_1** acts as an individual therapeutic agent by showing antibacterial and bioimaging properties. Despite their individuality these nano systems fall under same class of therapeutically active polymers i.e., polymeric nanocomposites.

5.1. Conclusion

Overall, this thesis contributes and provides valuable insights towards the development of highly biocompatible polymers and polymeric nanocomposites with enhanced physical properties, biocidal activity, and stimuli-responsive drug delivery behavior. A future study is likely to explore the synthesis of cyclic polymers and oligomers of antibacterial molecules and their potential antibacterial activity against bacteria that are resistant to antimicrobial agents.

5.2. References

1. Drews, J. Drug Discovery: A Historical Perspective. *Science* **2000,** *287*, 1960–1964.
2. Dickson, M.; Gagnon, J. P. Key factors in the rising cost of new drug discovery and development. *Nat. Rev. Drug Discov.* **2004,** *3*, 417–429.
3. Berdigaliyev, N.; Aljofan, M. An overview of drug discovery and development. *Future Med. Chem.* **2020,** *12*, 939–947.
4. Jung, K.; Corrigan, N.; Wong, E. H. H.; Boyer, C. Bioactive Synthetic Polymers. *Adv. Mater.* **2022,** *34*, 2105063.
5. Bolívar-Monsalve, E. J.; Alvarez, M. M.; Hosseini, S.; Espinosa-Hernandez, M. A. et al. Engineering bioactive synthetic polymers for biomedical applications: a review with emphasis on tissue engineering and controlled release. *Adv. Mater.* **2021,** *2*, 4447–4478.
6. Li, J.; Yu, F.; Chen, Y.; Oupický, D. Polymeric drugs: Advances in the development of pharmacologically active polymers. *J. Control. Release* **2015,** *219*, 369–382.
7. Ekladious, I.; Colson, Y. L.; Grinstaff, M. W. Polymer–drug conjugate therapeutics: advances, insights and prospects. *Nat. Rev. Drug Discov.* **2019,** *18*, 273–294.
8. Senapati, S.; Mahanta, A. K.; Kumar, S.; Maiti, P. Controlled drug delivery vehicles for cancer treatment and their performance. *Curr. Signal Transduct. Ther.* **2018,** *3*, 7.
9. Li, X.; Liu, P. Acid-triggered degradable polyprodrug with drug as unique repeating unit for long-acting drug delivery with minimal leakage. *Mater. Sci. Eng. C.* **2021,** *128*, 112317.
10. Kenawy, E.-R.; Worley, S. D.; Broughton, R. The Chemistry and Applications of Antimicrobial Polymers: A State-of-the-Art Review. *Biomacromolecules* **2007,** *8*, 1359–1384.

11. Sartaliya, S.; Gowri, V.; Chopra, V.; Roy, H. S.; Ghosh, D.; Jayamurugan, G. Unraveling the Effect of Nondrug Spacers on a True Drug-Polymer and a Comparative Study of Their Antimicrobial Activity. *ACS Appl. Polym. Mater.* **2022**, *4*, 3952–3961.

List of publications

Publications included in the thesis

1. **S. Sartaliya**, V. Gowri, V. Chopra, H. S. Roy, D. Ghosh, G. Jayamurugan, Unraveling the Effect of Nondrug Spacers on a True Drug-Polymer and a Comparative Study of Their Antimicrobial Activity *ACS Appl. Polym. Mater*. **2022**, *4*, 3952–3961.
2. **S. Sartaliya**, R. Mahajan, R. Sharma, A. H. Dar, G. Jayamurugan, New Water-Soluble Magnetic Field-Induced Drug Delivery System Obtained Via Preferential Molecular Marriage over Narcissistic Self-Sorting *Langmuir* **2022**, *38*, 8999–9009.
3. **S. Sartaliya**, R. Sharma, A. Sharma, V. Chopra, K. M. Neethu, D. Ghosh, G. Jayamurugan, Biocidal polymer derived near white light-emitting carbonized polymeric dots for antibacterial and bioimaging applications, (manuscript under review).

Other publications

1. A. H. Dar, V. Gowri, A. Gopal, A. Muthukrishnan, A. Bajaj, **S. Sartaliya**, A. Selim, Md. E. Ali, G. Jayamurugan,* Designing of Push−Pull Chromophores with Tunable Electronic and Luminescent Properties Using Urea as the Electron Donor, *J. Org. Chem.* **2019**, *84*, 8941–8947.
2. S. Kaur, A. Mukhopadhyaya,† A. Selim,† V. Gowri, K. M. Neethu, A. H. Dar, **S. Sartaliya**, Md. E. Ali,* G. Jayamurugan,* Tuning the Hetero-selectivity in Cross-coupling of Terminal Alkynes through Rational Designing of Catalyst, *Chem. Commun.* **2020**, *56*, 2582–2585.
3. A. Selim, K. M. Neethu, V. Gowri, **S. Sartaliya**, S. Kaur, G. Jayamurugan*, Thiol-Functionalized Cellulose Wrapped Copperoxide as a Green Nano Catalyst for Regiospecific Azide–Alkyne Cycloaddition Reaction: Application in Rufinamide Synthesis *Asian J. Org. Chem.* **2021**, *10*, 3428–3433.
4. A. Selim, S. Kaur, A. H. Dar, **S. Sartaliya**, G. Jayamurugan, Synergistic Effects of Carbon Dots and Palladium Nanoparticles Enhance the Sonocatalytic Performance for Rhodamine B Degradation in the Absence of Light, *ACS Omega* **2020**, *56*, 22603–22613.
5. R. Sharma, A. Selim, B. Devi, S. M. Arumugam, **S. Sartaliya**, S. Elumalai, G. Jayamurugan, Realizing direct conversion of glucose to furfurals with tunable selectivity utilizing a carbon dot catalyst with dual acids controlled by a biphasic medium. *Biomass Convers. Biorefin.* **2022.**

Shaifali Sartaliya
Ph.D. Research Scholar
Institute of Nano Science and Technology (INST) &
Indian Institute of Science Education and Research (IISER) Mohali
Punjab, 140306 India

Shaifali Sartaliya completed B. Pharma (Hons.) from Rajiv Gandhi Technical University, Bhopal, M.P., India, in 2014 and M.S. Pharma from National Institute of Pharmaceutical Education and Research (NIPER) Kolkata, West Bengal, India, in 2016. She joined Institute of Nano Science and Technology (INST) in January 2017 and registered with Indian Institute of Science Education and Research (IISER) Mohali for the Ph.D. program. Her current research interests include the development and synthesis of new types of polymeric biomaterials with enhanced physical properties, biocidal activity, and stimuli-responsive drug delivery behavior. She authored several research articles in reputed international journals. She has presented her research work at several national and international conferences.